Stretch forming of thermoplastic fibre–metal laminates

Anthony Sexton

June 2014

A thesis submitted for the degree of Doctor of Philosophy

of the Australian National University

Declaration

This thesis is an account of research undertaken between February 2010 and June 2014 at The Research School of Engineering, College of Engineering and Computer Science, Australian National University, Canberra, Australia.

Except where acknowledged in the customary manner, the material presented in this thesis is, to the best of my knowledge, original and has not been submitted in whole or part for a degree in any university.

Publications

Journal Papers

1. A. Sexton, W. Cantwell, S. Kalyanasundaram. Stretch Forming Studies on a Fibre Metal Laminate based on a Self-Reinforcing Polypropylene Composite. *Composite Structures*, 94:431-437, 2012.

2. S. Kalyanasundaram, S. DharMalingam, S. Venkatesan, A. Sexton. Effect of Process Parameters during Forming of Self Reinforced-PP based Fiber Metal Laminate. *Composite Structures*, 97:332-337, 2013.

3. A. Sexton, W. Cantwell, M. Doolan and S. Kalyanasundaram. Investigation of the deformation behaviour of a thermoplastic fibre metal laminate. *Materials Science Forum*, 773-774:503-511, 2013.

4. A. Sexton, S. Venkatesan, S. Davey, N. Akhavan, W. Cantwell and S. Kalyanasundaram. Simulation of the forming behaviour of a thermoplastic fibre metal laminate. *Manuscript in preparation*

5. A. Sexton, S. Venkatesan, W. Cantwell and S. Kalyanasundaram. Numerical modelling of the room temperature formability of a glass fibre reinforced thermoplastic fibre metal laminate. *Manuscript in preparation*

Conference Papers

1. A. Sexton, W. Cantwell, S. Kalyanasundaram. Stretch Forming Studies on a Fibre Metal Laminate based on a Self-Reinforcing Polypropylene Composite. 16th International Conference on Composite Structures (ICCS16), Porto, Portugal, June 2011.

2. A. Sexton, S. Venkatesan, W. Cantwell, S. Kalyanasundaram. Experimental and numerical characterisation of the out-of-plane stretch forming of a fibre metal laminate based on a self-reinforced polypropylene composite. 15th European Conference on Composite Materials (ECCM15), Venice, Italy, June 2012.

3. A. Sexton, W. Cantwell, S. Kalyanasundaram. Development of a forming limit diagram for a fibre metal laminate based on a glass fibre reinforced polypropylene composite. International Conference on Mechanics of Nano, Micro and Macro Composite Structures, Turin, Italy, June 2012.

4. A. Sexton, W. Cantwell, M. Doolan and S. Kalyanasundaram. Investigation of the deformation behaviour of a thermoplastic fibre metal laminate. 15th International Conference on Advances in Materials and Processing Technologies (AMPT2012), Wollongong, Australia, September 2012.

5. A. Sexton, W. Cantwell, M. Doolan and S. Kalyanasundaram. Experimental Characterisation of the Formability of a Thermoplastic Fibre Metal

Laminate. 7th Australasian Congress on Applied Mechanics (ACAM7), Adelaide, Australia, December 2012.

6. A. Sexton, S. Davey, W.J. Cantwell, S. Kalyanasundaram. Finite Element Simulation of the Stretch Forming of Annealed Aluminium Sheets. 7th Australasian Congress on Applied Mechanics (ACAM7), Adelaide, Australia, December 2012.

7. S. DharMalingam, A. Sexton, S. Venkatesan, S. Kalyanasundaram. Numerical investigation of the effect of temperature on the formability of a thermoplastic fibre metal laminate. 7th Australasian Congress on Applied Mechanics (ACAM7), Adelaide, Australia, December 2012.

Acknowledgements

I would like to thank A/Prof. Shankar Kalyanasundaram, my principal supervisor, for the opportunity to be a part of this research. I would also like to thank my advisers Dr. Matthew Doolan and Prof. Wesley Cantwell for their support throughout this project.

This project would not have been successful without the advice, support and knowledge provided by Sudharshan Venkatesan and Sivakumar Dhar Malingam. I am forever indebted to them for getting me started with equipment and software and for putting up with my constant questions in the beginning.

Thank you to my colleagues Sebastian Davey, Nima Akhavan Zanjani and Wentian Wang for their discussions, distractions, moral support, and help in overcoming problems.

I would also like to thank my parents, my brothers Chris and Michael, and my sister Olivia for all of the support throughout the last few years and beyond. I can never thank my Mum and Dad enough for their encouragement, without which I never would have achieved so much in life.

Finally, my biggest thanks are to my partner Becky. She is the reason I started the PhD and, most importantly, she is the reason I finished. Her love, support, and encouragement during the PhD were, and are, indescribable. Thank you for listening to me, caring for me, and pushing me to finish.

Abstract

Fibre–metal laminates are sandwich materials comprised of altering layers of fibre-reinforced composites and metal alloys. These materials can offer superior properties compared to the monolithic constituents such as superior specific strength compared to metals and better impact and fatigue resistance than composite materials. The use of fibre–metal laminates is currently restricted to specialised applications where the superior properties justify the high cost. This is due to the increased manufacturing time and cost over conventional materials. A method for mass production of fibre–metal laminates would allow them to be integrated more easily into existing production facilities and greatly reduce the cost associated with their use.

This thesis investigates the stamp formability of fibre–metal laminates using two distinct materials; one laminate based on a self-reinforced polypropylene composite and the other based on a glass-fibre reinforced polypropylene composite. Specimens of varying geometry were stretched over a hemispherical punch to elicit different deformation modes in the fibre–metal laminates and a non-contact optical measurement system was used to measure the surface strain during deformation. These experiments analysed the effect of the deformation mode on the formability of the laminates. The results from the experimentation were used to assess the deformation behaviour of the fibre–metal laminates and to identify

the safe forming limits of the materials. It was found that the fibre–metal laminates can be formed in a similar manner to monolithic metals. The self-reinforced polypropylene laminate was found to exhibit superior formability to monolithic aluminium whereas the glass-fibre reinforced polypropylene laminate showed reduced formability. In addition, the effect of temperature on the formability of the laminates was investigated. The temperature did not have a significant effect on the deformation behaviour during the forming process in either fibre–metal laminate and no increased formability was exhibited by the glass-fibre reinforced polypropylene based laminate. However, the self-reinforced polypropylene based laminate showed improved formability at elevated temperatures. Two significant findings were identified; the friction interaction between the specimens and the tooling has a major effect on the forming of the laminates, and the forming limits of the aluminium are improved when bonded to a self-reinforced polypropylene composite.

The finite element analysis software ABAQUS/Standard was chosen for simulation of fibre–metal laminate forming. Tensile tests were performed to obtain the mechanical behaviour of the constituent materials, where the composites were simulated using non-linear elastic orthotropic material models and the aluminium using an elastic-plastic model. The experimental forming results were compared to the simulation and it was found that the simulation could accurately represent the general forming behaviour of the laminates. There was difficulty in matching some of the glass-fibre reinforced polypropylene laminates due the non-

homogeneous behaviour of the composite. Results from the simulated specimens were used to assess the deformation of the composite, which could not be directly observed in the experiments, and to determine a preliminary failure condition of the composite experiencing stretch forming using the predicted strain in the failure region.

Nomenclature

CGA Circle Grid Analysis

FEA Finite Element Analysis

FML Fibre Metal Laminate

GMT Glass Mat Thermoplastic

LDH Limiting Dome Height

CLT Classical Laminate Theory

μ Coefficient of friction

DSC Differential Scanning Calorimetry

FLC Forming Limit Curve

FLD Forming Limit Diagram

LDR Limiting Draw Ratio

ϵ_1 Major Strain

MVF Metal Volume Fraction

ϵ_2 Minor Strain

NLO Nonlinear Orthotropic

PEI Polyetherimide

PML Polymer Metal Laminate

PTFE Polytetrafluoroethylene

GFRP Glass-Fibre Reinforced Polypropylene

SRPP Self-Reinforcing Polypropylene

β Strain ratio

Contents

List of Figures

List of Tables

Chapter 1

Introduction

1.1 Motivation

Evidence of human-driven climate change is motivating research into advanced materials. Such materials are primarily of interest to the transport industry which is attempting to reduce the fuel consumption (and therefore emissions) of aircraft and vehicles through the reduction of weight. According to the International Energy Agency (2011), the transport sector is currently responsible for 23% of energy-related CO_2 emissions and the Agency expects that the transport sectors of emerging economies will drive all net growth in demand for oil. This means that significant reductions in greenhouse gas emissions can be achieved by targeting the transport industry for improvement. Alternative fuels, improved engine efficiency, and reduction of vehicle weight are some of the methods proposed for reducing fuel consumption. Reduced vehicle weight is seen as a precursor for further efficiency improvements through the principle of 'mass decompounding' [1]. Lower vehicle mass allows the use of smaller, more efficient engines or alternative power sources such as hybrids or fuel cell technologies. The lifetime fuel savings from mass reduction alone are impressive: analysis by IFEU (Institute for

Energy and Environmental Research) has shown that for every 100kg reduction in the mass of passenger vehicles there is a saving of 300-800L of fuel over the lifetime of the vehicle. For mass transportation vehicles such as buses and taxis this saving increases to over 2500L. Innovative design, which involves the optimisation of components to attain higher performance from existing materials, and material substitution, where the existing material is replaced by a higher performance material, are two of the major methods proposed for mass reduction. The most prominent materials presented for the substitution of steel in vehicles are metals such as aluminium and magnesium. In addition to material substitution using alternative metals, polymer composite materials are also gathering interest. Composite materials have both advantages and disadvantages when compared to steel in their potential for use in vehicles. One of the major challenges in the adoption of composite materials in vehicles is finding a suitable rapid manufacturing technique. Traditionally, composite materials were manufactured using thermoset matrices, and these materials require careful handling, storage, and a labour-intensive procedure, all which increase manufacturing time and cost. These difficulties limit the potential of composite parts to applications where the superior properties of the composite justify the cost. It has been estimated that the reduction in mass using composite materials is 20-35% and 40-65% using glass-fibre and carbon-fibre reinforced composite materials respectively [2]. The advent of low cost thermoplastic composites has led to studies of how existing low cost rapid manufacturing techniques, unavailable to thermoset composites,

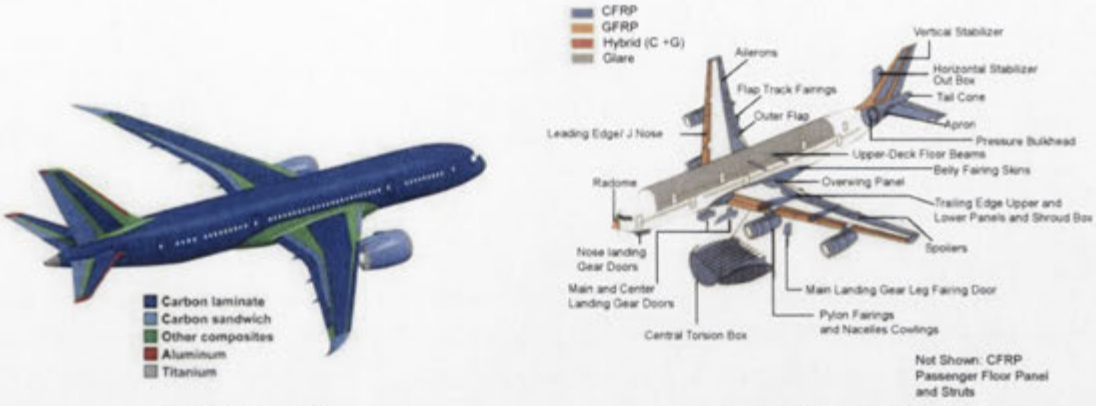

(a) Boeing 787 (b) Airbus A380

Figure 1.1: Composite materials and fibre-metal laminate systems in the Boeing 787 and Airbus A380 [3]

can be applied to them. The application of rapid forming processes to composite materials, which were originally developed for metal components, would allow composites to be integrated more easily into existing production facilities. The use of composite materials in the Boeing 787 and Airbus A380, shown in Figure 1.1, allow these aircraft to transport larger quantities of passengers and cargo for lower fuel costs. This is significant when the highest cost to airlines is fuel.

Fibre–metal laminate (FML) systems are a composite material consisting of alternating layers of fibre-reinforced composite and metal. The development of laminated structures can be traced to Germany after the Second World War. The bonding of metal layers was introduced due to the lack of heavy machinery to create built-up metal structures [4]. It was found later that, due to this lamination, the laminated parts exhibited good fatigue properties. The first generation of FML systems utilised an aramid fibre reinforced thermoset composite called ARALL. This FML system was developed in the 1970s by TU Delft and Fokker.

Studies of this material on F-27 wing panels showed great promise. A weight reduction of 25% was achieved while maintaining strength, and loads which would cause failure in monolithic aluminium caused only minor damage in the FML [4]. However, it was found that the blunt notch strength of the ARALL FML was critical, and premature fatigue cracks appeared at doublers when layers were bonded together to increase strength. Other deficiencies were also found in the ARALL FML systems, such as poor bonding between the aramid fibres and matrix material, moisture absorption and failure of the fibre/matrix interface, and fibre failure under tension–compression fatigue loading [5]. These problems led to the development of FML systems such as GLARE, which contains a glass-fibre reinforced thermoset composite. Studies showed that the GLARE FML was not only less expensive than the ARALL FML but also resulted in greater weight reductions and had superior fatigue resistance. This culminated in the use of GLARE in the Airbus A380 upper fuselage [4]. The disadvantage of these FML systems is that they utilise thermoset polymers for the matrix material, and these require complicated and time-consuming manufacturing procedures which restricts their use to high-cost, low-volume applications such as aircraft.

Thermoplastic polymers offer the ability to form preconsolidated sheets of material with a manufacturing time comparable to metals, a facility which would allow composite materials to be used in automotive applications. These materials also have the advantage that they can be heated and reformed repeatedly. Woven-fibre composites are gaining increasing interest compared to unidirectional

composites due to their superior stability and deformation characteristics in thermoforming [6].

The most common method for mass production of components is stamp forming. This process makes use of a die, blankholder, and punch. The die and punch are designed according to the desired final shape and the blankholder is used to control the amount of stretching and drawing of material into the die. The most common material system used in stamp forming is metal alloys. Stamp forming of materials such as steel is a well understood process. However, the application of stamp forming to FML sheet materials has not yet been investigated thoroughly; only recently have studies begun to investigate the formability of FML systems when stamp forming is used. These studies, which will be reviewed in the following chapter, have found that it is possible to form FML systems. One of the major conclusions from these studies is that heating of the FML prior to forming can improve formability.

Production of components using stamp forming often involves a costly and time-consuming die design and die tryout process. In recent times, this process has been streamlined by using predictive modelling techniques involving finite element analysis (FEA). FEA allows relatively rapid and inexpensive determination of material formability and reduces the number of trials needed. The validation of a finite element model against established forming experiments, and which covers all deformation modes, allows the modelling of a range of complex components.

1.2 Aims and Contributions

This thesis investigates the formability of two fibre–metal laminate systems, one based on a self-reinforced polypropylene composite and the other on a glass-fibre reinforced polypropylene composite. This investigation uses a real-time strain measurement system to measure the strain throughout the forming process, and assesses the effect of the deformation mode on the forming behaviour of the two fibre–metal laminates. The aim of the experimental investigation is to provide a fundamental understanding of the formability of the fibre–metal laminate by:

- comparing the formability of fibre–metal laminates to monolithic aluminium,
- assessing and analysing the forming behaviour of fibre–metal laminates,
- determining the effect of temperature on the formability of fibre–metal laminates, and
- developing a failure limit for fibre–metal laminates for all deformation modes and temperatures.

The experimental work contributes to understanding the formability of fibre–metal laminates, including the development of a comprehensive predictive finite element model for the forming of fibre–metal laminates.

1.3 Thesis Outline

This chapter is followed by Chapter 2, which details the theory and literature relevant to the materials used in this study and their forming. Studies into metal, composite, and laminate forming are discussed and the methods to determine formability are outlined. In addition, an overview of the finite element method is provided. Chapter 3 outlines the mechanical properties and behaviour of the materials used in this study and also details the methodology for the experimental work. This includes the manufacture of laminates and specimens, the parameters and strain measurement techniques used for the experimental work, and the estimated properties of the laminates used in this study. Chapter 4 details development of the finite element model for simulation of the experimental work. This includes boundary conditions, the user-defined material model, modelling the adhesive layer, and the effect of temperature. An overview of the theory used by the finite element analysis software is also provided. Chapter 5 presents the results of the experimental and finite element analysis performed using isothermal room-temperature conditions on the self-reinforced polypropylene composite-based FML. This is followed by Chapter 6 which details the effect of temperature on the forming of the self-reinforced polypropylene composite-based FML and details the FE simulation results for these experiments. Chapters 7 and 8 present the results of experimental and numerical work performed on the glass-fibre reinforced FML under isothermal and non-isothermal conditions respectively. All the experimental results use the strain on the surface of the specimen to determine the

forming behaviour of the FML under different deformation modes. Results from the experiments are compared to the forming of monolithic aluminium, and are used to calculate the forming limits of the laminates, which are compared to the FE simulation. In addition, the quality of the formed parts and results of investigations into how failure occurred are detailed. Finally, Chapter 9 summarises the conclusions found in this study and makes recommendations for future research into the forming of FML systems.

Chapter 2

Literature Review

2.1 Introduction

This chapter outlines relevant theory for the constituent materials used in this study, being aluminium and a fibre-reinforced composite, as well as the theory for fibre–metal laminates in general. An overview of the properties, current uses, and previous research on the manufacture of each material is presented. This includes the techniques used to determine the formability of sheet materials. The use of optical strain measurements to assess material properties and behaviour is then reviewed. Finally, the development of finite element simulations of the materials, particularly of fibre–metal laminates and their forming, are detailed.

2.2 Materials

2.2.1 Aluminium

Aluminium is the most abundant metal in the world. However, pure aluminium does not occur naturally and complicated procedures, such as the Hall process, are required to obtain pure aluminium from bauxite. Aluminium generally exhibits

Alloy series	Major alloying element
1xxx	Aluminium (99%)
2xxx	Copper
3xxx	Manganese
4xxx	Silicon
5xxx	Magnesium
6xxx	Magnesium and Silicon
7xxx	Zinc
8xxx	Other elements

(a)

Temper designations	
O	annealed
H	strain hardened
T	thermally treated
W	solution heat treated
F	as fabricated

(b)

Table 2.1: Aluminium alloy (a) and temper (b) designations

a high strength-to-weight ratio, good weldability, machinability, formability, and good corrosion resistance [7]. Due to its high specific strength, aluminium has found uses in the aerospace and automotive industries. Aluminium is not generally used in its pure form. Different alloying elements are added to improve stiffness, strength, ductility, and other mechanical and electrical properties. The different alloying elements can be identified by the designation of the aluminium alloy. Alloys are also separated into different tempers depending on their properties. The alloy designations and temper designations are shown in Table 2.1.

The aluminium alloys most commonly used in sheet applications are the 5xxx and 6xxx series. The 5xxx series has good formability, moderate strength, and good corrosion resistance. However, they suffer problems in their appearance due to strain markings such as Lüders lines [8]. Therefore, the 5xxx series alloys are generally used for internal structural components. The 6xxx alloys exhibit improved formability, surface appearance, and corrosion resistance for external

automotive applications.

2.2.2 Composites

Composite materials are made up of two or more distinct materials, creating a new material with enhanced characteristics. Generally, composite materials are comprised of a high strength, high stiffness reinforcement which is supported by a softer and more ductile matrix. The fibres provide strength and stiffness and the matrix transfers the load between the fibres and protects them from environmental damage. The most popular composite materials are fibre reinforced polymer matrix composites. Figure 2.1 shows the combination of matrix and fibre reinforcement materials which can be used to create polymer composites. The reinforcement can be continuous, woven, or chopped fibre; polymer composites generally contain 20–50% by weight of reinforcement [9]. There are two main types of polymer matrix material: thermoset and thermoplastic. The difference between the two is determined by the type of polymer used to create the matrix.

Currently, thermoset polymers are the most common form of matrix material used for polymer composites. Thermoset polymers are formed from a low viscosity liquid which becomes cross-linked by a curing process. The curing process is either by combination with a catalyst or solvent, or through the application of energy, usually heat and pressure or UV light. The high degree of cross-linking in thermoset polymers means that they generally cannot be melted and reformed

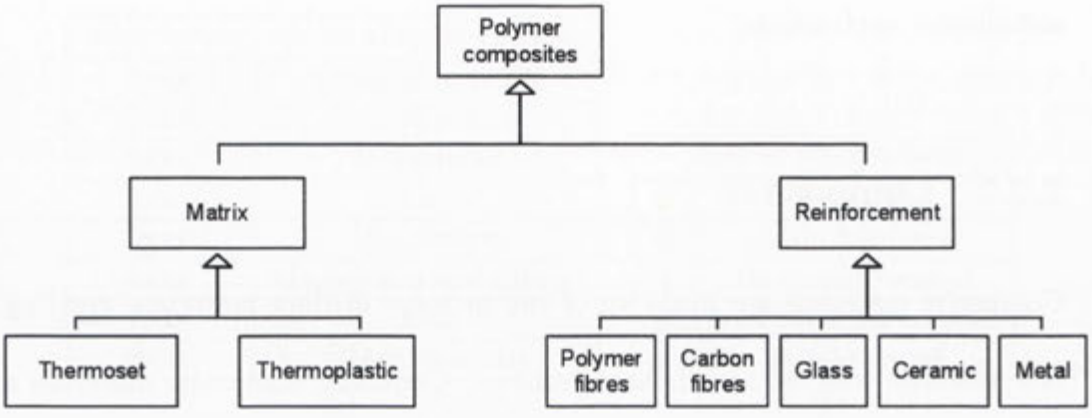

Figure 2.1: Polymer composite materials

after curing. An advantage of thermoset polymers is the low viscosity polymer, which provides good wet-out with the fibres. Also, the polymers maintain their mechanical characteristics at high temperatures and have good chemical resistance. However, thermoset composites suffer from limited shelf-life and recyclability, are time-consuming and expensive to manufacture, and have low strain to failure. These limitations have led to the increased use of thermoplastic composites. Thermoplastic composites can be rapidly manufactured using techniques such as injection molding and thermoforming, are recyclable, and have an infinite shelf-life [10, 11]. Despite these advantages, difficulties exist with coating continuous reinforcement fibres with a thermoplastic matrix due to the high viscosity of the polymer and the high temperatures required for melt processing [12]. Several processes have been developed to impregnate fibre reinforcements into thermoplastic matrices including melt, solvent, or powder impregnation, co-weaving, and commingling [13].

The ability to tailor the orientation of the fibre reinforcements in composite

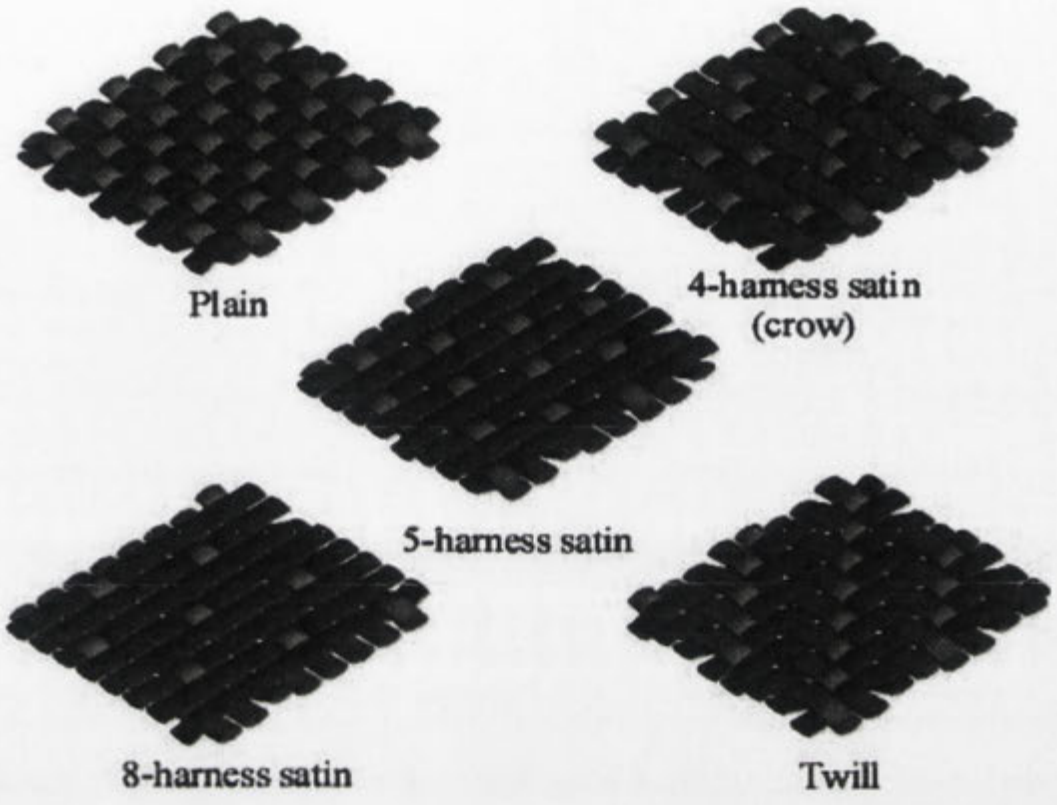

Figure 2.2: Typical weave patterns for woven fibre composites [14]

materials is the major reason for their advantage over monolithic metals. Tailoring allows different mechanical properties to be created using the same constituents. Strength and stiffness characteristics in the material can be oriented in the desired direction only, which allows for more efficient use of material. Therefore, different reinforcement techniques are used for different applications. For example, unidirectional composites are used when strength and stiffness are important in a single direction. By stacking different layers of these reinforcements in different directions it is possible to have different mechanical properties in different directions.

A unique reinforcement scheme for fibre reinforced composite materials is wo-

ven fibre. Woven fibre composites offer significant advantages over unidirectional and random fibre composites due to their superior damage tolerance, which in turn is due to the resistance to crack propagation offered by the woven fabric [15]. In addition, woven composites are capable of deforming through stretching of undulated fibres and trellising of the yarns [6], which allows a small extension of the composite without damaging the fibres.

Interest in the application of fibre reinforced composite materials for structural components is growing. Recently, the Boeing 787 became the first commercial aircraft to contain 50wt% composites. The automotive industry is also showing an interest in applying thermoplastic composite materials to their vehicles. Manufacturers such as Mercedes, BMW, Peugeot, Nissan, and others have begun to use thermoplastic composites [16]. The Mercedes A Class utilises a glass mat thermoplastic (GMT) to replace steel in the rear hatch, which has resulted in a 25% reduction in the mass of the component [17]. The BMW M3 uses a glass fibre reinforced thermoplastic composite for the front and rear bumpers. These bumpers show improved crash performance and reduced weight when compared to a metal bumper system [16]. In addition to the aerospace and automotive industries, the consumer products and renewable energy industries have begun to create products using thermoplastic composite materials. An example of this is the Samsonite Cosmolite range of luggage.

Currently, thermoplastic composites are manufactured through time- and labour-intensive methods. Adaptation of thermoplastic composites to mass pro-

duction industries requires the development of techniques to rapidly manufacture parts.

2.2.3 Laminated Structures

There are four basic types of laminate materials:

- metal laminates, consisting of bonded sheet metal;
- composite laminates, consisting of composite layers bonded together;
- polymer–metal laminates, comprising metal bonded to non-reinforced polymers; and
- fibre–metal laminates, consisting of metal bonded to fibre-reinforced polymers.

The development of bonded structures derived from studies which found that adhesive bonding of aluminium sheets provided significant improvement in their fracture toughness, fatigue resistance, and damage tolerance over the monolithic metal [18]. Schijve et al. [19] studied the fatigue properties of metal laminates comprised of 2024-T3 aluminium. According to this study the reasons for increased fatigue and fracture resistance in laminated structures involve four separate mechanisms. Firstly, crack growth in thin sheets is slower than in thicker sheets; therefore, sheets of a certain thickness which have been built up from thinner layers exhibit slower crack growth than a single thick sheet. Secondly, there is a delay in the peak load under variable amplitude loading. This occurs

due to high loads causing larger plastic zones in the thin sheet. Thirdly, there is an arresting of a crack through the full thickness by the adhesive and non-cracked layers. Finally, the fracture toughness for a thin sheet is higher than for a thick sheet and this applies even if the sheets have been laminated. The study found that crack growth in the laminated structure was slower than in the solid material, and that this was more significant for natural cracks as opposed to artificial ones. It also found that the thickness and stiffness of the adhesive layer is of particular importance for the cracks that propagate through the full thickness. Adhesives with low stiffness and high thickness provide limited support to the cracked layer from the non-cracked layers. However, crack initiation in these layers is delayed. High stiffness and low thickness adhesives reduce the crack opening but allow more rapid initiation of cracks in subsequent layers. Kim and Johnson [20, 21] found that metal laminates also have advantages for acoustic damping and can be formed in a similar manner to monolithic metals.

Polymer metal laminates (PML) were the next iteration in the design of laminated structures. These laminates exhibit similar bending stiffness to monolithic metal sheets but have less weight. This is due to the low density polymer significantly increasing the specific moment of inertia of the laminate [22]. Burchitz et al. [23] discussed the invention of a new PML system, termed Hylite, and the challenges associated with introducing this new material into industry. The long term availability, costs, processing, material behaviour, the methods required to design structures, and the end of life predictions are all identified as keys areas

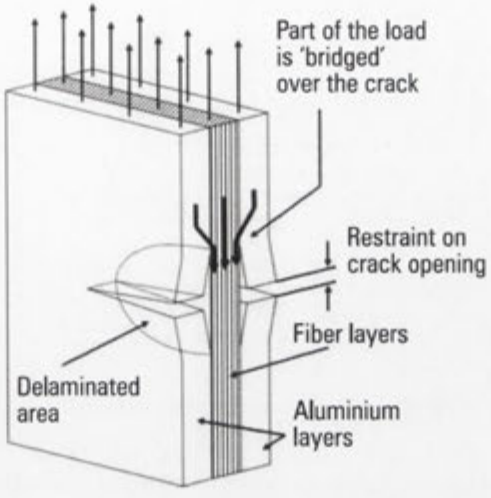

Figure 2.3: Fibre bridging in the region of a crack in an FML [26]

needing to be addressed for new materials such as PML systems to be considered for industrial use.

Vogelesang et al. [24, 25] determined that, by adding a fibrous reinforcement with high strength and stiffness to the polymer layer of these systems, the mechanical properties could be improved. This first generation FML (ARALL) consisted of a high-strength aluminium alloy and a unidirectional aramid fibre reinforced composite. It was found that excellent fatigue resistance was provided through the mechanism of fibre-bridging, which is shown in Figure 2.3. This mechanism is one of the main advantages of FML systems as opposed to monolithic materials, metal laminates, and PML structures.

Vlot et al. [26, 27] investigated the applicability of FML systems for aircraft by assessing the fatigue behaviour, impact resistance, corrosion, and flame resistance of the GLARE FML system. It was found that, as crack length increased, the rate of growth of the crack in the laminate was almost constant, compared to

increased growth rates in monolithic materials. It was also found that laminates exhibited crack growth rates 10–100 times slower than monolithic aluminium and that fatigue damage due to riveted lap joints never occurred in FML structures under realistic conditions.

The impact behaviour of the laminate was also found to be superior to aluminium, with the energy required for first failure in the GLARE FML being 1.3–4 times higher than monolithic aluminium of the same thickness [26, 27]. This impact behaviour was coupled with only minimal damage (matrix cracking and delamination) from impacts which did not cause failure. No fibre failure was found to occur prior to failure of the aluminium layer. In addition, moisture resistance of the laminate structure was shown to be superior compared to monolithic composites, since the composite layers in the laminate are only exposed to moisture at the edges (which can be easily sealed). Corrosion of the metal through the thickness of the laminate is also prevented due to the barrier created by the composite.

Finally, the flame resistance of a laminate used in a fuselage was found to be superior to aluminium in two ways [26, 27]. Firstly, the burn-through time of the laminate was found to be 6 times longer than 2024-T3 aluminium, a result due to the high melting point of the glass fibres (which protects the second layer of aluminium) and delamination (which causes an insulating effect in the laminate). Secondly, unlike metal structures which have to combined with a firewall to help prevent burn-through, the structure of the laminate simultaneously re-

tards the spread of fire and maintains strength even if some of the layers have been compromised.

Determining the properties of the FML systems is a major undertaking due to the complexity of the material. Wu et al. [28] studied the applicability of the rule of mixtures for determining the mechanical properties of FML systems. This study tested several GLARE specimens of different metal volume fractions to determine the strength and modulus of the material. It was found that some mechanical properties of the laminate, such as the elastic (E) and shear (G) stiffnesses, could be predicted using classical laminate theory (CLT) in the linear elastic material response region through the metal volume fraction (MVF), shown in equations 2.1 and 2.2.

$$E_{lam} = MVF \cdot E_{metal} + (1 - MVF)E_{composite} \tag{2.1}$$

$$\frac{1}{G_{lam}} = \frac{MVF}{G_{metal}} + \frac{1 - MVF}{G_{composite}} \tag{2.2}$$

where the subscripts lam, metal, and composite indicate the properties for the laminate, metal, and composite respectively.

Cortés and Cantwell [29] investigated the tensile failure of FML systems comprised of a carbon-fibre/PEEK composite and titanium. Symmetric cross-ply laminates were created by using layers of unidirectional composites to build up the structure. The orientation of the composite fibres was adjusted to assess the

effects of fibre orientation on the mechanical properties of the laminate. CLT was used to predict the modulus of the laminate, and excellent agreement was found with the experimental data. As expected, the laminate failed due to fibre fracture when the fibres were oriented along the longitudinal axis and by debonding of the fibre–matrix interface when the fibre orientations exceeded 15°. In addition, the strength and first-ply failure of the laminate were predicted using the maximum stress, Tsai–Hill, and Tsai–Wu failure criteria. It was found that Tsai–Hill and Tsai–Wu successfully predicted the failure more accurately and the maximum stress criterion was not as good.

Further investigations into the mechanical properties of a FML system based on aluminium and a self-reinforced polypropylene composite were performed by Carillo and Cantwell [30]. Single cantilever beam, tensile, flexural, and impact tests were performed on the FML and the constituent materials. The SCB experiments showed that the adhesive used had a higher interlaminar fracture toughness than the composite. The tensile experiments highlighted an improved strength in the FML specimens over monolithic composite, coupled with increased strain to failure in the ±45° laminates compared to plain aluminium. This study found that failure did not occur in the flexural testing specimens and that fibre orientation had only a secondary effect on the flexural properties. Finally, the impact testing showed a high level of energy absorption.

Reyes and Cantwell [31] conducted similar experiments on a FML based on a glass-fibre reinforced polypropylene composite. This study found that strength

and elastic modulus followed the MVF and that the laminate absorbed significant energy by plastic deformation of the aluminium and localised microcracking in the composite. The residual strength of the laminates after impact was found to only reduce by 15% following a 20J impact, highlighting the advantage of the laminate structure. Carillo and Cantwell [32, 33] also investigated the effects of scaling on the tensile and impact behaviour of thermoplastic FML systems. The laminates used in these studies were developed using a self-reinforced polypropylene composite and an aluminium alloy in four specimen sizes. It was found that specimens scaled in one dimension (thickness) or all dimensions exhibited reduced tensile strength as specimen size increased; this reduction was found to be caused by increased edge delamination and debonding in the larger specimens. In contrast, the specimens scaled in two dimensions (length and width) were found to display increased tensile strength. This was again found to be due to delamination and debonding but with the smaller specimens being more severely affected. The elastic modulus of the laminates was found to remain constant for all specimen sizes. The impact results of the scaling experiments showed that damage was more severe in the thicker composite layers due to difficulties in scaling the weave of the fibres and that the energy to initiate failure did not depend on size. Finally, it was determined that simple scaling laws could be used to predict the impact response of larger FML structures.

Recently, Sinke [34] and Sinmazçelik et al. [35] reviewed the history, bonding types, and experimental testing methods applied to FML systems. Sinke

emphasised the importance of a combination of experimental tests. This study highlighted that experiments were needed to optimise, certify, and qualify FML systems and that predictive numerical tools are needed to accurately simulate and reduce the number of experimental tests required. In particular, more general and versatile FEA models, which correctly describe the unique structure of the FML (encompassing the material behaviour of the composite, metal, and adhesive), are needed to improve the development of new FML structures. The review by Sinmazçelik et al. identified the importance of the surface treatment of the aluminium for good adhesion between the layers of the FML and identified the various testing methods used to analyse the mechanical properties of the laminate.

The application of materials such as composites and FMLs in mass production industries requires the use of rapid manufacturing techniques, such as stamp forming. The following sections will provide a review of the literature regarding the forming techniques and analyses for metals, composites, and laminate structures.

2.3 Sheet Metal Forming

Sheet metal forming is a widely used manufacturing technique in the automotive industry for the rapid production of components. This manufacturing process makes use of a die, blankholder, and punch as shown in Figure 2.4. The die and punch are designed according to the desired final shape, and the blankholder

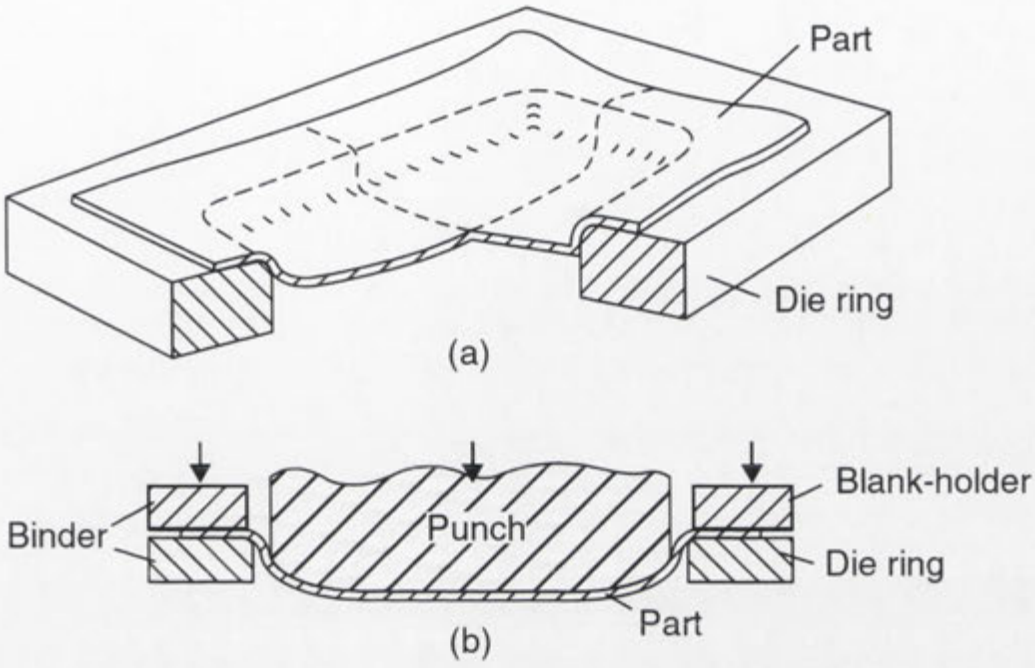

Figure 2.4: Typical stamp tooling [36]

is used to control the flow of metal into the die. The study of metal forming requires knowledge about the mechanical properties of the material which affect formability, the stress and strain inherent to the particular forming process, and the failure limits of the metal experiencing a particular forming process.

2.3.1 Strain Measurement

The forming of sheet metal is often assessed through principal strains. The principal strains are made up of the major, minor, and thickness (or third principal) strains. Circle grid analysis (CGA), developed by Keeler [37] and Goodwin [38], is historically used for measuring the strain on the surface of a material by assessing the degree of deformation of a circle to an ellipse, as shown in Figure 2.5. The terms major and minor strain are derived from the major and minor axes of

this ellipse. The major and minor strain are found by

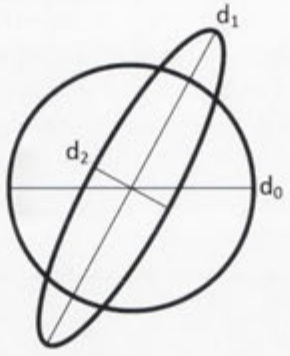

Figure 2.5: Deformation of a circle

$$\epsilon_1 = \ln\left(\frac{d_1}{d_0}\right), \epsilon_2 = \ln\left(\frac{d_2}{d_0}\right) \tag{2.3}$$

The third principal strain can be found by measuring the change in thickness of the sheet (equation 2.4) or using the constant volume formula (equation 2.5).

$$\epsilon_3 = \ln\left(\frac{t}{t_0}\right) \tag{2.4}$$

$$\epsilon_1 + \epsilon_2 + \epsilon_3 = 1 \tag{2.5}$$

The principal strains are used to determine the type of deformation experienced by a sheet material by analysing the strain ratio.

2.3.2 Strain Ratio

The strain ratio describes the ratio of the minor and major strain at a point on the surface of a material.

$$\beta = \frac{\epsilon_2}{\epsilon_1} \tag{2.6}$$

The value of the strain ratio β determines the deformation mode of the sheet metal. All possible deformation modes lie between $-2 < \beta < 1$.

- $\beta = 1$ - Equal Biaxial Stretch
- $\beta = 0$ - Plane Strain
- $\beta = -\frac{1}{2}$ - Uniaxial Tension
- $\beta = -1$ - Draw
- $\beta = -2$ - Uniaxial Compression

The strain ratio is used to create a forming limit diagram (FLD). The forming limit diagram was developed by Keeler and Backofen [39] and is used to visualise the state of strain of the surface of a material undergoing a forming process. A sheet cannot be deformed by compressive forces and therefore at least one of the principal strains must be positive. An FLD and the associated deformation modes are shown in Figure 2.6.

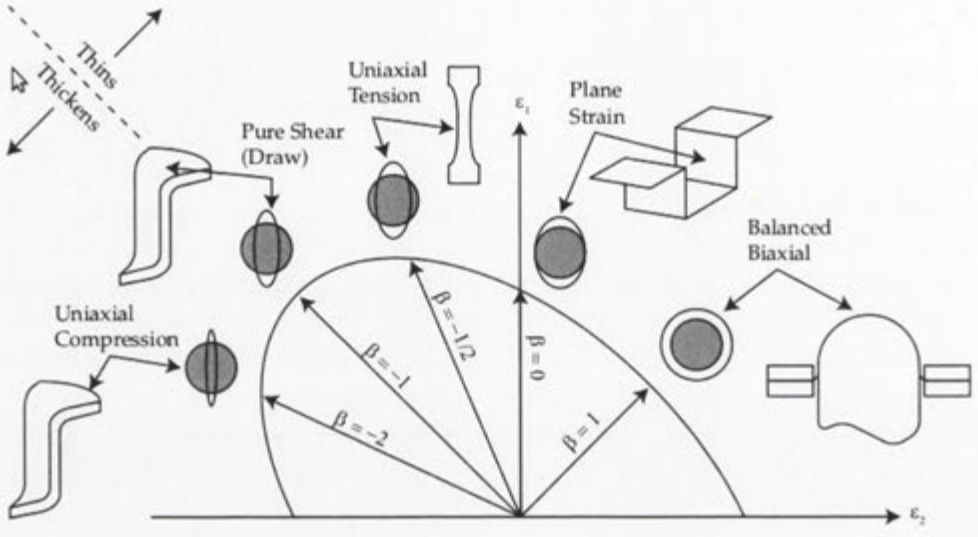

Figure 2.6: Forming modes are shown on a forming limit diagram [40]

2.3.3 Limiting Strain Conditions

The FLD is also useful because it allows the construction of a forming limit curve (FLC). The FLC is a line on the FLD which corresponds to the limiting strain condition at each deformation. The FLC is one of the most useful tools in the analysis of the formability of sheets. It can be used to determine the proximity to failure in a sheet material and to visualise the forming window for a sheet material. Each deformation mode experiences different failure characteristics; these failure modes are shown in Figure 2.7.

Since the introduction of the FLD there have been many studies into the forming of metals. This was aided significantly with the introduction of a simple method to obtain the FLD and FLC. Various methods have been proposed to develop FLDs for materials; these include adjusting the blank holder force, altering the lubrication of the sample, and varying the geometry of the sample.

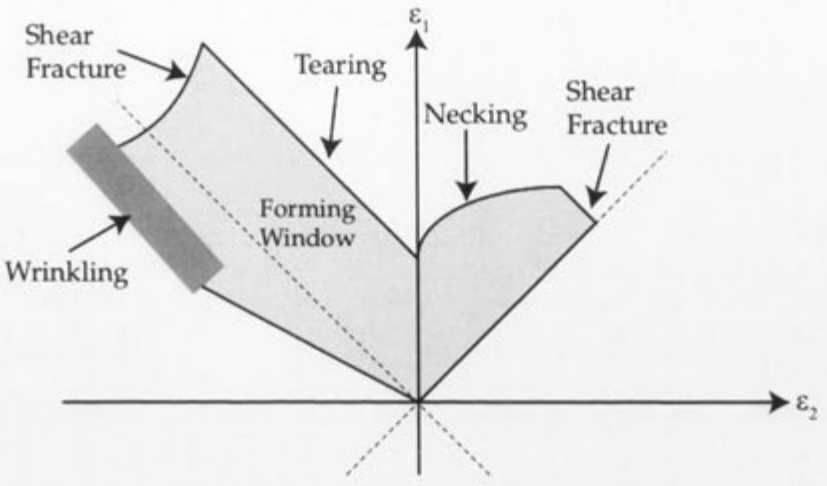

Figure 2.7: The failure associated with different forming modes [40]

The method proposed for the determination of the FLD and FLC was developed by Nakajima[41] and Hecker [42]. They proposed stretching rectangular specimens of varying width over a hemispherical punch; by decreasing the width of the specimen, the lateral constraint can be reduced. This means that the sides of the specimen are not subjected to high levels of stretch and are instead allowed to partially "draw" into the die, which will lead to more negative values of minor strain. The stretching of specimens over a hemispherical punch is called the limiting dome height (LDH) method, and using this method the failure limit of the material can be found for strain ratios from –0.5 to 1. In addition to the method proposed by Nakajima and Hecker, another method using the same simple principle was created by Raghavan [43]. This method uses specimens which have a radius cut out of them to ensure that failure does not occur at the die but instead occurs in the unsupported region of the specimen. All these methods are recognised by the ASTM and ISO as methods for determining the FLD for

sheet materials. Recently, studies have begun investigating the ability to determine the forming limit for materials experiencing pure shear ($\beta = -1$) [44]. This study used a novel specimen geometry to ensure that a region of the material experiences pure shear under proportional loading conditions.

Numerous studies have been performed on the formability of metallic materials. Buakaew et al. [45] investigated the formability of two steel sheets, SPCC and SPCE. This study used specimens of varying geometry, stretched over a hemispherical punch, to determine the FLC; CGA was used to obtain the surface strain distribution. This paper also compared the FLC determined using experiments with the FLC developed by the FEA program AutoForm. It was found that the FE results agreed with the experimentally determined FLC. The difference between the FLC determined using FEA and experiments was found to be 7% and 11% for the SPCC and SPCE steel respectively, with the FEA reporting a lower forming limit.

There is also interest in assessing the formability of metals at high temperatures. This type of forming is aimed at achieving greater formability by permitting different mechanisms to provide deformation, such as more slip systems, diffusion, grain boundary sliding, and dislocation climb.

Li and Ghosh [46] investigated the effect of temperature on the forming behaviour of aluminium alloys. Three aluminium alloys were tested at room temperature and between 250 and 300°C under isothermal and non-isothermal conditions. The post-forming tensile properties of the formed parts were also examined

to determine the effect that the elevated forming temperature had on mechanical properties. It was found that the temperature had a significant effect on the formability, with vastly improved forming depth compared with room temperature forming. At higher temperatures, increasing the punch temperature to between 250 and 300°C decreases the forming depth. However, by setting the die temperature to approximately 50°C higher than the punch temperature, greater forming depths can be achieved. The higher forming temperatures were not found to have an effect on the strength of the formed part.

Hsu et al. [47] investigated the development of a forming limit diagram for aluminium and magnesium alloys at elevated temperatures. Two aluminium alloys and a magnesium alloy were experimentally deformed using blanks of varying geometry to obtain various deformation paths. The FLD_0 for the aluminium alloys at room temperature was found to be in the region of 18–23% strain and that at 300°C the FLD_0 was increased to 28–36%. Forming of the magnesium alloy was not possible at room temperature due to fracture in the specimens caused by the application of force on the lock ring. It was found that the formability of the magnesium was significantly improved at elevated temperatures with the FLD_0 occurring at 67% strain at 300°C.

2.3.4 Effect of lubrication

In the LDH test the lubrication of the punch, die, and blankholder has a significant effect on the state of strain in a specimen. Higher levels of lubrication of the

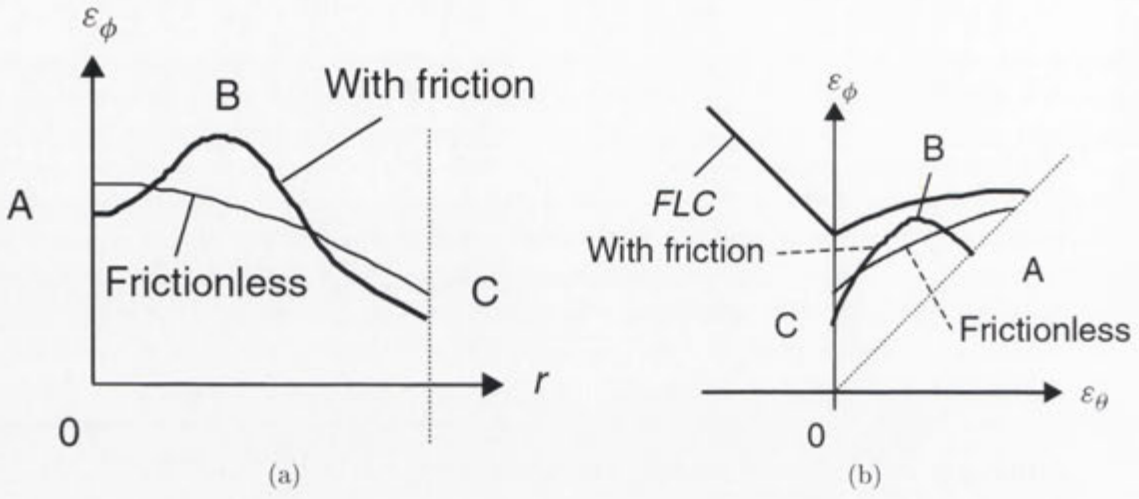

Figure 2.8: Effect of friction at the punch on the surface strain along a meridian [36]

punch and blank allow for more biaxial stretch in the pole region as shown in Figure2.8b [36]. In contrast, low friction in the flange region allows the sample to draw into the die cavity and, depending on the specimen geometry, affect the deformation mode experienced by the specimen. An improvement on the LDH test using the Hecker or Nakajima methods is the Marciniak test [48]. This test was developed by Marciniak and Kuczyński by assessing the limit strains in sheet metal using a flat-bottomed punch and a "carrier blank". The carrier blank is a sheet with a circular region of material removed from the centre. This allows the actual specimen to form over the surface of the punch as if no friction were present. The Marciniak test was further improved by Raghavan [43], who combined the Hecker and Nakajima methods with the Marciniak test to obtain material behaviour for all deformation modes. This was achieved through the use of the varied geometries suggested by Hecker and Nakajima, with the carrier

blank altered accordingly. Raghavan showed that the Marciniak test could be used to determine the FLC for sheet material in a similar manner to the LDH test. Further advances in the Marciniak test were made by Foecke et al. [49] who proposed the use of a recessed punch, which eliminated the need for a carrier blank. The main advantage of the Marciniak test over the LDH test is that it is not affected by friction, bending, and normal pressure on the sheet. However, the results of formability from the LDH test have been shown to provide better correlation with actual panel stamping [47]. In addition, Hsu et al. found at high temperatures that no combination of lubrication or carrier blank allowed the determination of the FLC using the Marciniak test.

2.4 Composite Forming

There are numerous methods by which composite materials can be manufactured into components. Historically, composite structures were manufactured using a complicated layup procedure, which required the laying of fibres in the desired shape by hand and then applying the matrix resin. However, due to a rise in the use of thermoplastic composite sheets there is now increased interest in the direct formability of composites. Generally, composite materials are formed using a process called thermoforming, where the material is heated beyond the melting point of the matrix, formed using vacuum molding or diaphragm forming, and then cooled [50]. However, there is interest in using the same procedures as in metal forming.

The first study into the forming of preconsolidated composite sheets was performed by Hou and Friedrich [51]. This study used a unidirectional and quasi-isotropic preconsolidated carbon fibre reinforced polypropylene to assess the formability of composite materials. The composite sheets were heated above the melting temperature of the polypropylene matrix and formed using cold, matched 90° bend tools. It was posited that there were four basic flow processes in the deformation of a continuous fibre reinforced composite: resin percolation, transverse fibre flow, interply shear-cooperative flow, and intraply shearing. It was found that the temperature range required for stamping was within a few degrees above the melting temperature of the polypropylene. If the forming speed was high enough, this temperature range was found to allow interply slipping throughout the forming process, which prevents buckling of the fibres on the inside of the bend radius and subsequent fibre breakage outside the bending region. It was found that at higher forming speeds the bend angle differed from 90° and the thickness was not uniform; however, it was found that the stamping pressure had significantly more influence on these parameters than forming speed.

Hou [52] studied the stamp forming of woven fabric composite which was a glass fibre reinforced polyetherimide (PEI). This study investigated the tensile strength and forming of the composite above the glass transition temperature of the PEI matrix. The tensile experiments showed that the maximum extension of the composite in the warp or weft direction was approximately 0.6%, whereas the extension in the 45° direction was ~40%. This was possible due to the trellis

effect of the woven fabric, where the angle between the warp and weft fibre bundles reduced from 90° to 35°. It was observed that the trellis effect may aid in the prevention of wrinkling in formed specimens due to the effective reduction in compressive force. This study used a 54mm diameter hemispherical punch to deform specimens into a 30mm diameter mould and a blankholder to control the draw of material into the die. The blankholder force was found to have a significant effect on the amount of wrinkling in the composite; it should be sufficient to prohibit wrinkling but not too severe as to cause tearing.

Hou [53] also studied the hemispherical forming of a unidirectional continuous glass fibre reinforced polypropylene. This work used the same experimental equipment used in [52] to analyse the forming. Again, this study found that the optimal temperature range for stamping was above the melting temperature of the polypropylene. Therefore, the specimens were preheated to 190° and closing speeds of 70–230mm/s were used to keep the temperature above 170° during the forming process. It was found that the major parameters affecting part quality were temperature, forming speed, and blankholder force.

Further studies by Friedrich and Hou [54]investigated the stamp forming of preconsolidated sheets of unidirectional glass fibre reinforced polypropylene composite. Semicircular tubes were formed using different forming speeds and specimen temperatures. In addition, a novel rod-bed mold was used to create complex three-dimensional parts. This study found that high preheat temperatures and closing speeds were essential for good formability. This was because intraply

slipping, rotation, and shear cause the majority of deformation at higher temperatures, and this reduces the strain experienced by the glass fibres. It was also found that at temperatures above 180°C, out-of-plane fibre wrinkling was eliminated

Breuer and Neitzel [55] investigated the forming of thermoplastic composite sheets which were heated slightly above the melting temperature of the matrix. The samples were stamped under non-isothermal conditions and cooled through contact with the punch and die. This study found that the transfer of the heated composite to the tools must be rapid, or else the temperature in the composite cooled below the matrix recrystallisation temperature. During the forming of the composite it was found that to reduce wrinkling in the composite sheet the stress should be applied at 45° to the fibre direction to induce shear deformation, and the fibres should be allowed to draw into the die. The study also investigated the efficiency of the method – radiation, convection, or conduction – used to heat the composite. It was found that heating in a convection oven is the slowest process, but it is preferable to conduction due to problems associated with contact heating such as adhesion and the need for a contact fluid.

Lee et al. [56] investigated the biaxial stretch forming of glass-fibre reinforced thermoplastic composites with a random fibre orientation. This study analysed the forming of the composite under various forming parameters such as punch speed, temperature, and fibre volume fraction. A finite element simulation of the process was developed using an anisotropic linear viscoelastic material model and

it was found that the difference between experimental and numerical results was caused by the inability of the material model to incorporate the effect of strain rate on the mechanical properties. It was also found that, by selecting the optimal forming conditions, the composite exhibited formability equivalent to metals.

Cabrera et al. [57, 58] investigated the non-isothermal stamping of all polypropylene and glass-fibre polypropylene composites. It was found that as the temperature of the all-PP composite was increased, the strength of the composite was reduced and the strain at failure was increased. The effect of increased strain rate was shown to have a similar effect to lowering the temperature, with increased strength and lower strain at failure. It was also found that deconsolidation in the thermoplastic layers, observed by a thickening of the laminate, was present in the composite after heating but prior to stamping. It was also observed that analysing the magnitude and direction of the major strain allows the contribution of intraply shear and fibre drawing to be determined. If the major strain is aligned at 45° to the fibres then deformation primarily occurs due to intraply shear; in addition, if the major strain is oriented along the fibres then the sheet was deformed by drawing of the fibres.

Trudel-Boucher et al. [59] examined the effect of stamp forming process parameters on flexural strength, flexural modulus, and void content of a glass-fibre composite. The process parameters examined were stamping pressure, material temperature, mold temperature, loading rate, holding time, and use of multiple forming steps. Unconsolidated commingled fabric was stamped in a non-

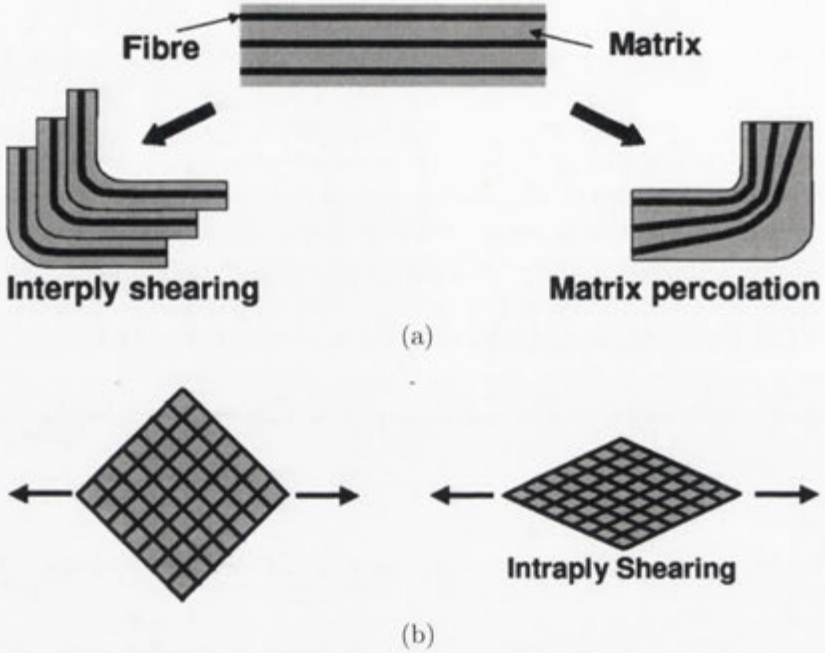

Figure 2.9: Forming mechanisms in woven fibre composites. (a) Interply slip and matrix percolation. (b) Intraply shear [58]

isothermal configuration by heating plies of the fabric to above the melting temperature of the matrix in a convection oven and then rapidly transferring it to a stamping press. The forming operation was carried out in a fast stamping step to achieve the desired shape (while keeping the matrix above the melting temperature) and then cooling the part under constant pressure. It was found that the most significant factor affecting the mechanical properties was the void content; that is, the flexural strength and modulus reduced with increasing void content. Thus, by optimising the process parameters to reduce the void content the flexural properties can be improved. The optimal forming parameters were found to be a loading rate of 25kN/s, a holding time such that the part temperature was below the matrix crystallisation temperature, and a material stamping temper-

ature of 140–170°C. Multiple forming steps were found not to have a significant effect.

Nakamura et al. [60] performed tensile and deep drawing tests on a fully green composite comprised of a woven fabric of ramie fibres and a biodegradable resin. An increase in temperature in the tensile tests was found to allow greater deformation of the composite and a temperature range of 115–130°C was deemed suitable for deep drawing. The tensile tests also showed that by treating the fibres with an alkaline solution a more ductile composite could be created. This more ductile composite was shown to give greater forming depths than a comparable untreated composite; in other words, by correct tailoring of the composite stiffness and ductility, these green composites can produce excellent deep drawing products.

Venkatesan et al. [61, 62, 63, 64] performed a comprehensive study of the hemispherical dome forming of two thermoplastic composites. These composites were woven fabric thermoplastic composites including a self-reinforced polypropylene (SRPP) and a glass-fibre reinforced polypropylene (GFRP). This study investigated the effect of feed rate, forming temperature, and blankholder force on the forming behaviour of composite materials. A 100mm hemispherical punch was used to deform 180mm diameter circular specimens to various depths. Preheat temperatures ranged from 20 to 140°C to deform the specimens under non-isothermal conditions using three different feed rates (20, 40, and 60mm/s) and blankholder forces (2, 7, and 14kN). A non-contact optical measurement system

was used to measure the strain throughout the forming process. It was found that the feed rate had no significant effect on the forming behaviour of the composite materials. It was found that in the SRPP composite, due to low stiffness and high extensibility of the fibres, stretching along the fibre direction was the dominant deformation mechanism. In contrast, the high stiffness glass fibres showed drawing behaviour. It was also found that in order to deform high stiffness woven composites trellising of the fabric must be allowed; moreover, higher stiffness fibres suffer from wrinkling, whereas lower stiffness fibres do not. The SRPP was shown to deform using a combination of stretch and draw and the GFRP deformation was dominated by trellising. In addition, it was found that the magnitude of stretch experienced by the specimen was increased by a phase change from solid to soft semi-solid at 80–100°C and by near melt conditions. This temperature increase also reduces the work required to deform the material. The most significant conclusion of this work was that, by using the optimal combination of process parameters, composite materials can exhibit forming behaviour superior to that of metals.

2.5 Forming of Laminate Structures

In addition to the study of the formability of composite materials there is increasing research into the forming of laminate structures. Studies have been conducted on the forming of the four different laminate systems discussed earlier, with most investigating the drawing behaviour of the material and only one investigating

the forming limits. Some novel forming methods of laminate structures have also been investigated and these will be discussed briefly.

Kim and Johnson [20] studied the forming of steel sheets bonded by a polymeric adhesive. This study used a four-point bending test to examine the formability of a steel sheet laminate. It was found that a high forming speed was favourable because it increased the ability of the adhesive to transmit shear forces, which increased the flexural rigidity of the laminate but also increased its springback. Increased stiffness of the adhesive also increased the rigidity of the laminate but was found to promote delamination. In addition, thicker adhesives were found to reduce deep drawability and improve the acoustic damping properties of the laminate. High temperatures decreased the rigidity of the laminates and improved the shape error of the completed specimen.

Takuda et al. [65] investigated the tensile properties and formability of a laminate comprised of dissimilar metals. The metals included a mild steel and three different aluminium alloys which were roll bonded using a polyurethane resin. Tensile experiments, a cylindrical deep drawing test, and the Erichsen test were performed to elucidate the properties of the laminates. It was found that the yield stress, tensile strength, and elongation of the laminates could be predicted accurately by the rule of mixtures. It was found that the strength coefficient and strain hardening exponent were more difficult to predict but values were in the range between the values of the different metals used in the laminate. The forming parameters of the laminate were significantly more complicated, with parameters

such as the limiting draw ratio (LDR) and Erichsen value not only affected by the composition but also by which material was in contact with specific tools (such as the punch or die). It was concluded that aluminium alloys with high ductility should be used in 2-ply laminates that are set such that the steel is in contact with the punch, whereas low ductility aluminium alloys should be sandwiched between two sheets of steel.

The formability of PML sheets was examined by Kim et al. [66]. This study used a polypropylene core sandwich between two sheets of 5182 alloy aluminium. It was found that the FLC of the sandwich sheet was superior to that of an aluminium sheet of similar thickness, and while the modified Marciniak—Kuczynski theory did not accurately predict the individual material behaviour, it did predict the laminate would exhibit the superior FLC found in the experiments. It was postulated that the FLC could be improved by adjusting the value of four parameters: the shape of the yield function, the strain hardening exponent, the strain rate sensitivity, and the initial defect parameter. If the last three of these parameters are high, and the curvature of the yield surface in the region from biaxial tension to plane strain and from uniaxial tension to plane strain are small, then an improvement is found in the FLC. The strain rate sensitivity and initial defect parameter of the laminated sheet are higher than that of the monolithic aluminium sheet, whereas the strain hardening exponent of the laminate is relatively lower, with the most significant influence coming from the defect parameter (due to the high core thickness). All this leads to the improved formability of the

laminate.

Weiss et al. [67] also investigated a 5182 aluminium and polypropylene laminate to determine the effect of different temperatures on its tensile properties and formability. It was found that the laminate exhibited slightly lower forming limits at 60°C than at room temperature, which could also have been caused by noise in the results. The shear and tensile experiments showed a significant decrease in strength for the polypropylene core and it was therefore suggested that the core had only minimal effect on the forming limit curve. However, this study did not attempt to analyse forming at temperatures where the bond or core stiffness could be affected. It was also found that the laminate required higher blankholder forces in the deep drawing tests than aluminium to prevent wrinkling, due to a lower load carrying capability of the core. These higher blankholder forces led to an earlier onset of tearing in the specimens. Finally, it was found that that higher temperatures reduced springback but increased wrinkling in the specimens, suggesting that a softer core can have a significant effect on final part quality.

Sokolova et al. [68] studied the forming of polymer–metal laminates with a local metal reinforcement. The reinforcement was a small circular disc, which was either solid or a mesh, substituted for the polymer core. It was found that the drawing depth for the specimens with the steel inlays showed an increased forming depth for larger inlay diameters, but still exhibited lower forming depths than the non-reinforced laminate. It was suggested that this was caused by the stiffening and strengthening of the non-stress-critical areas, whereas lower inlay

sizes allowed for more deformation around these areas. The inlays also helped to reduce the thinning associated with the forming process.

Asnafi et al. [69] investigated the forming of fibre–metal laminates which were not laminated prior to forming. It was claimed that this is an advantage because the materials can be handled separately prior to forming. The process involved stamping two layers of metal at the same time and then stamping the metal again, this time with a composite inbetween the layers, and then rapidly heating the tools to consolidate the laminate and to adhere the composite to the metal layer. The study used a woven glass-fibre reinforced polypropylene composite and stainless steel as the constituents. The FML was found to exhibit a smaller stiffness and a larger dent resistance than aluminium after forming, with a weight increase of 46%. It was also found to have a higher stiffness and dent resistance than carbon steel (but not stainless steel); however, the laminate was 60% lighter.

The first comprehensive study of the stamp forming of thermoplastic fibre–metal laminates was conducted by Mosse et al. [70, 71, 72, 73]. This study used an FML made up of a woven glass-fibre reinforced polypropylene composite, aluminium, and a modified polypropylene adhesive to investigate the forming of rectangular cups. The effect of process variables was investigated to determine how these materials could be adequately formed without causing damage to the laminate structure. In addition, a comprehensive model for the adhesive properties of the laminate was developed through the investigation of the shearing behaviour of the laminate. It was found that elevated temperatures led to a re-

duction in the occurrence of the drawing, plane strain, and uniaxial compression forming modes and an increase in the magnitude of biaxial stretch. Increase in temperature also allowed for greater forming depths before failure; however, crack growth was faster in specimens formed at higher temperatures once fracture had initiated. It was also found that damage was introduced in the composite layer (in the side wall) at higher temperatures and that if failure did not occur then specimens formed at higher temperatures showed less shape error. Finally, a small range of temperature was found where the adhesive melted but the composite did not, allowing the FML to form more easily. Compston et al. [74] investigated the difference between surface strain on laminates and monolithic aluminium using formed channel sections. It was found that laminates exhibited lower strain than the aluminium and were not as sensitive to changes in tool radii.

Gresham et al. [75, 40] continued the study of thermoplastic FML forming with an investigation of the hemispherical dome forming of a FML based on a self-reinforced polypropylene. The influence of the aluminium alloy, core material, and surface treatment on adhesion between the layers was investigated. Two composites and a modified polypropylene adhesive were used with three aluminium alloys, employing three different surface treatments to create an FML. The three aluminium alloys were 2024-O, 2024-T3, and 6061-T6 and the composites were an SRPP and a GFRP. The surface preparations trialled were: no treatment, cleaning with a solvent, and etching the surface of the aluminium in an NaOH bath. It was found that, due to a thin coating of pure aluminium on the surface,

the 2024-O and 2024-T3 provided much better bonding than the 6061-T6 in all instances. In fact, it was found that the solvent preparation did not improve the bond and the NaOH treatment did not significantly improve the bonding of the 2024 aluminium. However, the NaOH treatment improved the bonding between the 6061-T6 and the core material to make it equal to that of the 2024 aluminium. In forming experiments, it was found that a combination of 2024-O aluminium and SRPP provided the greatest depth at failure and lowest work required to form. It was also found that low blankholder force led to greater instances of wrinkling and higher blankholder forces in tearing; high temperatures were also found to lead to higher levels of wrinkling. The formed FML specimens were shown to have a more uniform strain distribution and required 30% less work to form than monolithic aluminium.

Dhar Malingam et al. [76, 77] studied the effect of blankholder force, feed rate, and temperature of the forming of two thermoplastic FMLs. A full factorial experimental plan was developed to investigate three blankholder forces, eight temperatures, and three feed rates. It was found that the feed rate had no effect on the formability but that temperature and blankholder force significantly affected results. The effect of temperature showed two distinct behaviours: those at low temperatures (20–100°C) and high temperatures (130–150°C). These temperature regions correspond to the melting/recrystallisation temperatures of the adhesive used in the FML so that at high temperatures the FML behaves as if there are three independent layers which do not interact, and at low temperatures

it behaves as one continuous layer. It was also suggested that the fibre orientation may affect the development of the FLC. Finally, the results from tensile characterisation experiments conducted by Venkatesan et al. were used to develop an FE simulation of the draw forming process for the FML. Excellent agreement was found between the experimental surface strain and the FE simulation.

Carradò et al. [78] recently studied the formability of laminates constructed using different techniques, and containing both reinforced and non-reinforced polymer cores and different metal layers. The different manufacturing methods used were heat press consolidation, continuous roll bonding, and laminates bought directly from an industrial manufacturer. Several tests including differential scanning calorimetry (DSC), adhesion, tensile, and two forming tests (Erichsen and deep drawing) were performed on the laminates. The metals used were steel and aluminium; the polymers were a glass-fibre reinforced polypropylene and a polyolefin (PP-PE) sheet. It was found that the bond produced by the roll bonding process was 1.4 times stronger than the bond created by the heat press consolidation; in fact, delamination occurred in all of the heat press laminates during the Erishsen tests. However, the roll bonded laminate exhibited excellent forming and tensile properties which were comparable to metals.

Reyes and Kang [79] performed preliminary investigations into the stretch forming of fibre metal laminates. This is the only study which has investigated the forming limits of FML structures using techniques developed for metals. It was found that in the lead up to failure that interlaminar failure began to occur

in the composite layer, indicating that the bond strength between the composite and metal remained throughout the forming process. The FML based on the SRPP was found to exhibit forming limits comparable to aluminium, whereas the GFRP laminate showed poor formability.

In addition to the investigation of stamp forming of laminates, Jackson et al. [80] investigated single point incremental forming (SPIF) of sandwich panels including two PMLs, an FML, and an aluminium foam laminate. Two tool paths were used to assess the forming of the laminates, a line and a spiral. This study found that the PMLs were able to be formed using the SPIF process due to the ductile and incompressible core and metal layers which could withstand local indentation without crushing the core.

Another novel method was proposed by Edwardson et al. for the forming of laminates using laser forming [81]. This study attempted to use the method of inducing a thermal gradient in a small area of material to induce a bending moment which would cause the material to deform. However, it was found that due to the dissimilar thermal properties of the constituent materials it was necessary to apply heat to only the outer aluminium layer to induce the required bending moment. It was proposed that this method could be used to correct shape errors resulting from conventional forming operations.

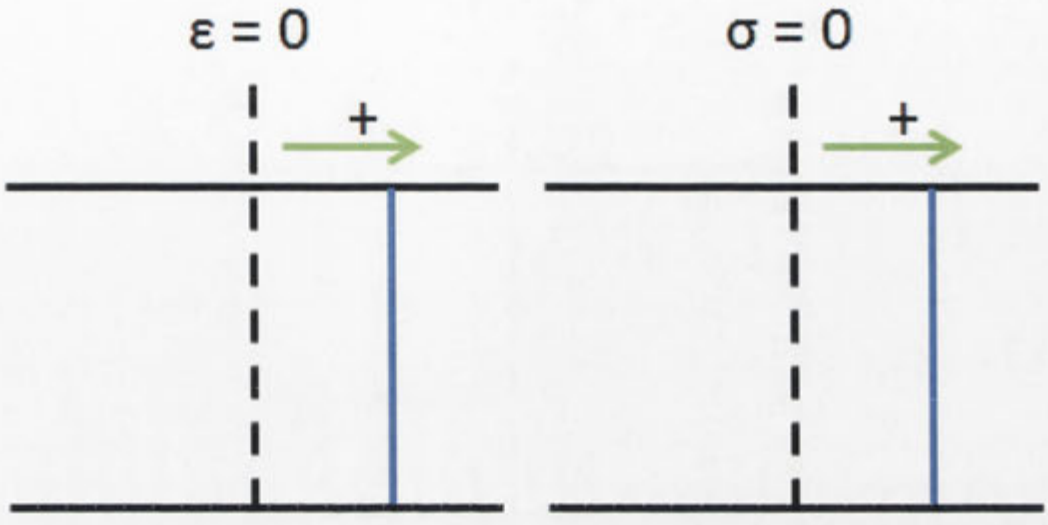

Figure 2.10: Strain (a) and stress (b) in a sheet material experiencing a tensile load

2.5.1 Strain in laminate structures

A sheet experiencing a tensile load will exhibit an in-plane strain distribution as shown in Figure 2.10. In the case of a perfectly bonded laminated sheet the strain distribution will be identical to that shown in Figure 2.10(a); however, due to different stiffnesses, each layer of the laminated sheet will exhibit different magnitudes of stress. This is particularly true for materials such as thermoplastic FMLs where the stiffness of the metal (aluminium) can be up to 17x the stiffness of the composite (SRPP), which means that the stress in the metal layer is much higher than that in the composite, as shown in Figure 2.11 [73]. This discontinuity of stress will need to be counterbalanced by an interfacial shear stress between the layers in order to maintain equilibrium. Therefore, it can be seen that if the strength of the adhesive is lower than the interfacial shear stress then the layers

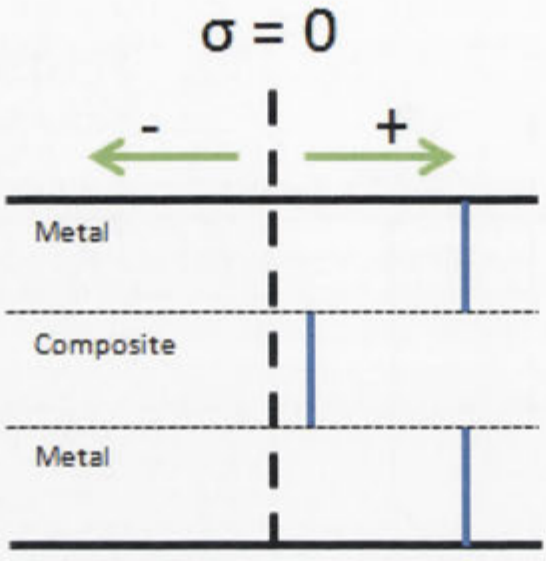

Figure 2.11: Difference in stress in a perfectly bonded laminate

will delaminate.

However, this is just a simple tensile load applied to the sheet which creates a uniform strain through the thickness. The bending of sheet material causes a non-uniform state of strain to exist in the material, as shown in Figure 2.12 [36]. In this case part of the sheet will experience tension, another compression, and there will be a neutral axis about which bending occurs. In the case of combined loading (in-plane and bending), the neutral axis may not coincide with the centre of the material, as in Figure 2.12(a). If the material remains elastic then the stress distribution will remain in a line, such as Figure 2.12(b), whereas if plastic deformation occurs the distribution will taper off towards the edges of the specimen in both directions if the tensile and compressive properties of the material are assumed to be similar. A perfectly bonded laminate will also exhibit this strain distribution; however, the stress in each layer of the laminate will be

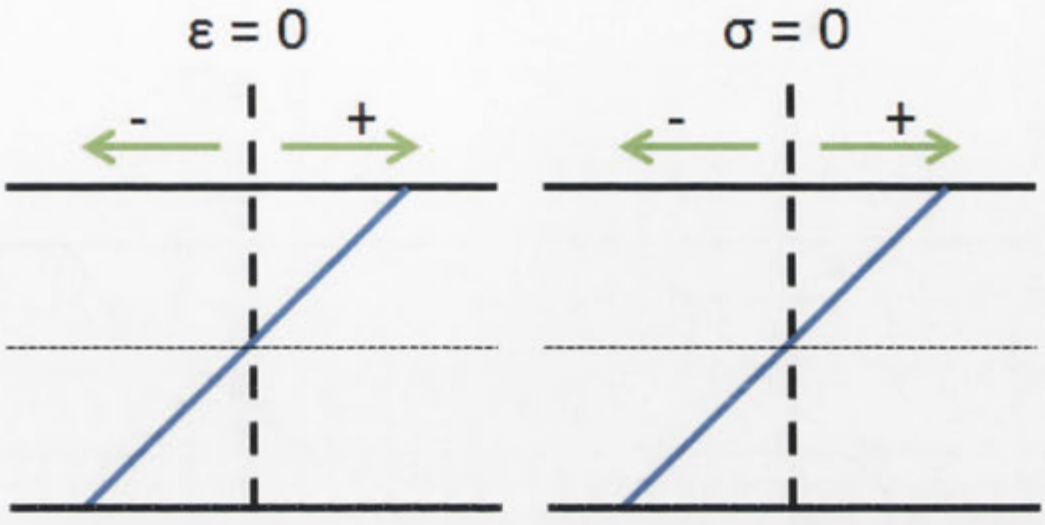

Figure 2.12: Bending strain (a) and stress (b) in an elastic sheet [36]

different if the materials have dissimilar stiffnesses. Figure 2.13 shows the strain and stress distributions in a perfectly bonded laminate. It can be seen from Figure 2.13(b) that there is a discontinuity in the stress through the thickness.

If no bond exists between the layers of the laminate then the strain distribution appears as shown in Figure 2.14. The strain and stress in the layers act independently of the other layers, with each layer having its own neutral axis.

The concept of bending strain in a bonded material is of significant importance to the study of the forming of FML sheet materials, because if the radius of curvature of the sheet, the strain on the outer surface, and the state of the bond (either perfect or failed) is known then the strain in the composite layer can be easily determined.

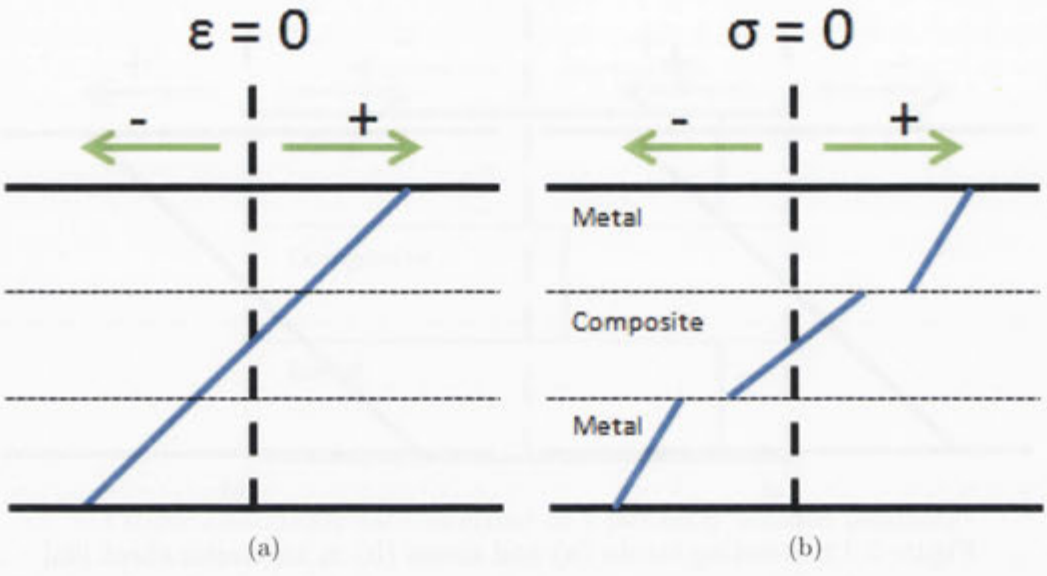

Figure 2.13: Bending strain (a) and stress (b) in a perfectly bonded laminate

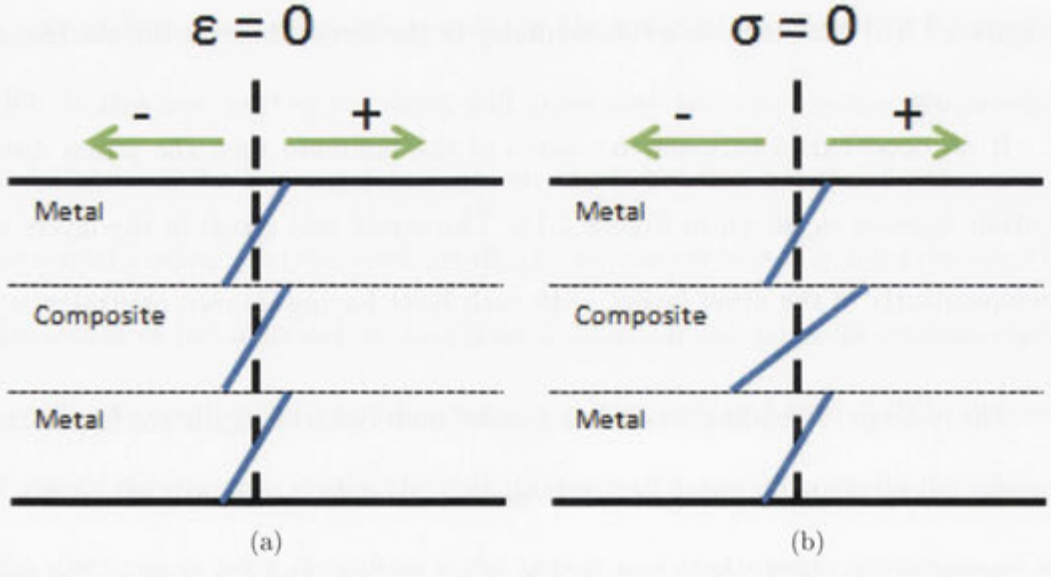

Figure 2.14: Bending strain (a) and stress (b) in a laminate where no bond exists between the layers.

2.6 Optical Strain Measurement

Full-field optical measuring techniques are finding increasing use in engineering research and development. This is due to better computing power, high resolution cameras, and to the ability to assess not only the final strain in a complex specimen (which is performed using mechanical measurement equipment) but also the evolution of strain over the entire surface of the specimen. Schmidt et al. [82] discussed the introduction and use of 3D image correlation using high speed cameras for optical deformation and strain measurement on the NASA 'Return to Flight' program. It was found that optical strain measurement was an invaluable tool for testing and that the strain data was in agreement with mechanical gauges. It also highlighted the significant ease with which results from optical strain measurement can be compared with FE simulations using programs such as LS-Dyna. In addition, Tyson et al. [83] found that full-field optical measurement systems offer significant advantages over conventional measurement techniques such as strain gauges. The higher data resolution and three-dimensional display of results allow for a better understanding of material behaviour.

Historically, the forming of sheet materials was assessed using CGA. This method requires the electrochemical etching of small circles onto the surface of the material and measuring the deformation of these circles into ellipses. The resolution of the surface strain is limited by the minimum size of the circles and the reliability of the surface strain is limited by the accuracy of the measurement system used. However, optical measurement techniques have been developed

to automatically determine the surface strain using CGA; while this overcomes the problems associated with measurement accuracy, it does not improve the resolution of the surface strain. Carasusan [84] proposed the use of CGA and applied structured white light to the surface of the material. A non-contact optical method, shown in Figure 2.15b, was used to obtain the 3D mapping of the specimen's deformation and for determining the surface strain (and therefore the forming limit curve of a material). This study showed that non-contact optical techniques allow for more rapid determination of FLCs and allow for more data to be collected on the surface of the sample. The major limitation of this approach is that it still displays only a limited resolution of the surface strain and shows only the strain at failure.

The most efficient technique to rapidly obtain the surface strain is to use photogrammetry and a stochastic pattern applied to the surface. This method combines the ease of use of CGA, the accuracy of optical measurement techniques, and very high resolution. Three-dimensional photogrammetry uses two or more two-dimensional images taken from different angles to triangulate the positions of the points in a three-dimensional environment. Figure 2.15a shows a diagrammetric arrangement of the cameras. If the position and corresponding angles of the two cameras and the two points $p_1\,(x_1, y_1)$ and $p_2\,(x_2, y_2)$ are known, the point $P\,(X, Y, Z)$ on the surface of the observed specimen can be determined. The determination of the displacement of the point depends on the undeformed point $P\,(X, Y, Z)$ being able to be found for all deformed states $P\,(X_t, Y_t, Z_t)$.

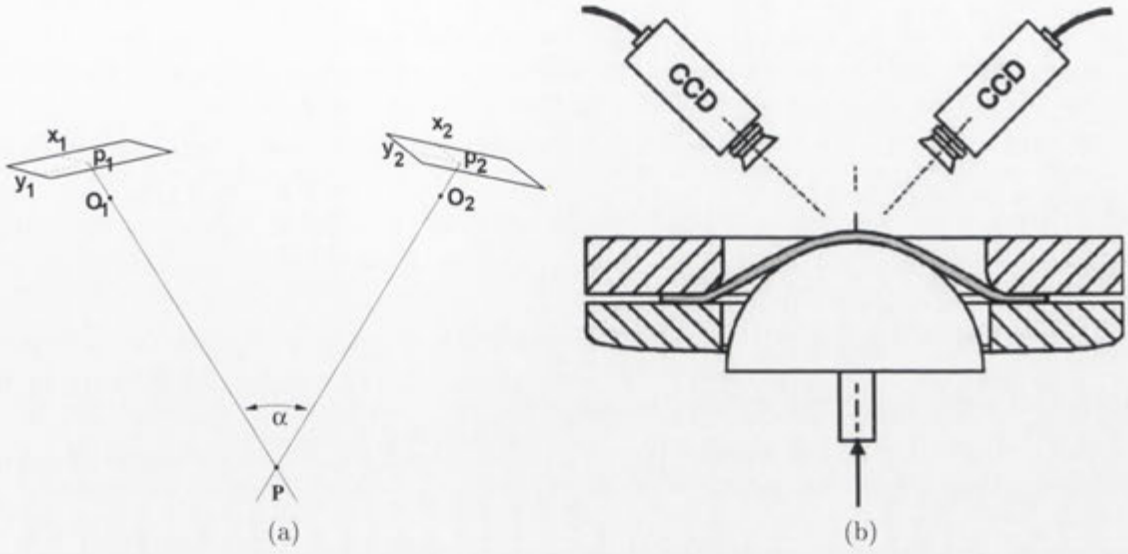

Figure 2.15: Diagrammetric arrangement [85] (a) and schematic setup for optical deformation measurement [86] (b)

Lewison and Lee [87] used optical strain measurement and a 2mm by 2mm grid to determine the forming limits of aluminium-killed drawing quality (AKDQ) steel sheets. The Marciniak test and a single camera were used to reduce the difficulty of obtaining continuous strain measurements; hemispherical dome forming was also performed but the evolution of strain throughout this process was not recorded. They found that the forming limit could be determined visually by carefully examining the captured images for the first signs of a developing neck, or by finding the intersection of a least-squares regression line through the strain values considered safe and another through the points where the strain ratio begins to approach plane strain. It was also found that these methods encounter difficulty if both the major and minor strain were positive as the onset necking developed too rapidly; however, this could be overcome by increasing the image capture rate. Geiger and Merklein [86] showed a procedure for determining the

forming limit diagram of materials using a stochastic pattern. They proposed determining the onset of localised necking by analysing any instabilities in the surface strain: an instability was determined to be a large strain difference between two time steps and a large strain gradient between two points on the surface of the material.

Kalyanasundaram et al. [88] developed a methodology for measuring the surface strain of a laminate during forming using a non-contact optical measuring system. This methodology involved the mounting of the camera system to the stamping press as shown in Figure 2.16. This study found that the optical measurement system was useful in characterising the formability of materials throughout the forming process, especially where simulation of the materials is non-trivial.

2.7 Finite Element Analysis

Finite element (FE) simulations are becoming increasingly popular with engineers and scientists due to the relative ease with which they can analyse a complex system. It also complements this study as the use of optical strain measurement allows direct comparison of experimental results with FE models.

In general, there exist three methods for modelling fibre–metal laminates [89]: the micro-level method, which models the individual fibre and matrix interfaces in the composite layer; the meso-level approach, in which the individual plies are modelled as separate homogeneous layers; and the macro-level method, which

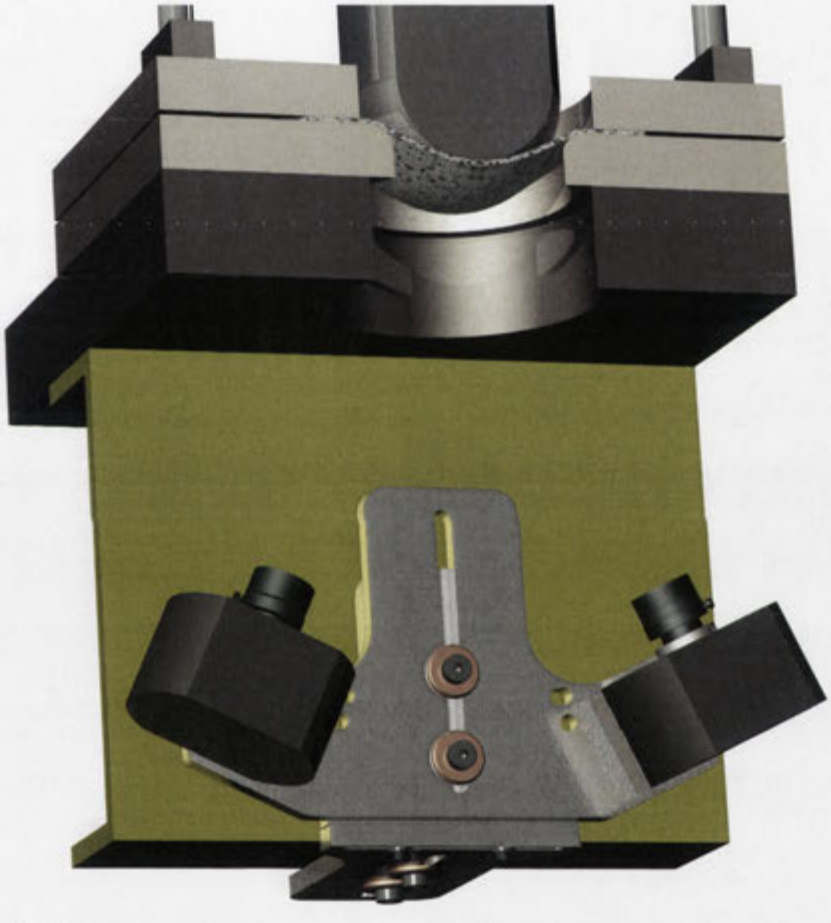

Figure 2.16: Mounting of non-contact optical measurement system to stamping press [88]

models the homogenised response of the complete laminate. There also exists multi-scale modelling, which incorporates the different levels into a single model. However, this terminology can be confusing as it depends on the system under consideration. For example, in composite material analysis the micro-, meso-, and macro- prefixes are used to describe the individual fibre and matrix interfaces, the unit cell of fibre structure, and the homogenised composite respectively.

The modelling of FMLs is a non-trivial process requiring the modelling of the metal layer, the composite layer, and the adhesive layer. Therefore, a brief overview of the methods used in modelling both the constituents and the laminate, with particular emphasis on forming, is provided.

Ozturk and Lee [90] performed numerical and experimental investigations into the out-of-plane stretch forming aluminium killed drawing quality (AKDQ) steel. This study used ABAQUS/Standard to model the forming process of specimens of different width to assess their deformation behaviour. Lubrication of the system was identified as a critical parameter for forming and therefore for accurate simulation of the process. The study found that a refined rectangular mesh should be used to achieve good results and that the element size should be larger than the sheet thickness. The strain paths obtained by the FE simulation were found to represent the FLD with reasonable accuracy.

The modelling of composite materials in forming analyses has been studied using various techniques. Yu et al. [91] developed a non-orthogonal constitutive model for modelling woven composites; this model uses a non-orthogonal pin-

jointed network of fabric, with an imaginary spring used to prevent excess shear deformation. This model was incorporated into a user-defined material model in ABAQUS/Explicit and compared with in-plane shear, pure shear, uniaxial tension, and 3D draping experiments. It was found that the results of the simulation accounted for differences in fibre strength and changes in orientation.

Cao et al. [92] expanded on the work performed by Xue et al. [6] to develop a model for woven composite fabrics which also included the effect of temperature on the response of the material. The model uses a non-orthogonal constitutive model which again represents the composite as a pin-jointed network. In particular, the trellising behaviour of the composite was affected by increased temperatures. Experiments found that the temperature of the heated specimen experienced negligible cooling when not in contact with the tools, but cooled almost instantaneously to the tool temperature upon contact. Therefore, two temperature states were used to model the composite: a high temperature behaviour for regions not in contact with tools and a low temperature response for the contacted regions. A difficulty existed in the representation of the tools, since deformable solid elements with a temperature degree of freedom were used (instead of rigid bodies) in order to allow heat transfer out of the composite material; however, this choice incurs significant computational increases. Hence, the behaviour of the material is not directly affected by temperature but is instead "switched" between the low and high temperature responses using the contact status. This model showed that temperature had a significant effect on the be-

haviour of the simulation but was not compared to experimental work.

The modelling of FMLs has been the subject of numerous studies primarily focused on impact or blast loading conditions. Hashagen et al. [93] developed a procedure for the modelling of FMLs using solid-like shell elements. This paper discusses the procedures required for the representation of the different aspects of the laminated material, such as the need to model the material layers as separate elements in order to examine the interfacial behaviour, or modelling all layers as a continuous element with integration points through the thickness, which is useful if interfacial behaviour is not desired. This study found that the solid-like shell elements yielded similar results to conventional shell elements and showed good agreement with experimental tensile results.

Guan et al. [94] investigated the impact loading of FMLs using an FE simulation. Fibre–metal laminates based on a SRPP and 2024-O and 2024-T3 aluminium were used in conjunction with a nitrogen gas gun to determine the impact response at intermediate velocities. A numerical model was created using ABAQUS/Explicit to compare and analyse the deformation, failure modes, and impact energy. The FML was modelled using separate shell element layers to represent the aluminium and SRPP; the aluminium was modelled as a rate-dependent elasto-plastic material with shear and tensile failure limits, and the SRPP was modelled as an isotropic elastic material with element deletion upon reaching a failure strain. The interaction between the layers of the FML were modelled using rough contact (no sliding between the surfaces in contact). The

results from the simulation were compared to experiments and it was found that the errors in the simulation were less than 5% when considering the total out-of-plane displacement. The failure modes of the FML were also simulated using the FE model, with the high velocity failures manifesting as perforations of the laminate and localised thinning appearing in low velocity impacts.

Guan et al. [95] also examined the numerical simulation of the blast response of FMLs. This study used similar aluminium to the previous study (including the FE model) and a GFRP composite. The composite was modelled as an orthotropic elastic material incorporating Hashin's failure criteria and a damage model based on the negative slope of the stress–displacement relation after damage initiation. In this model the error between total displacement in the experiments compared to FEA was reduced to 2%, and the delamination and failure of the composite layers was modelled reasonably well. However, the deformation mode of the aluminium was not reproduced due to the non-uniform shock pressure and high strain rates.

Fan et al. [89, 96] continued the development of a finite element model to assess the structural and perforation behaviour of an FML subjected to a low velocity impact. In both these studies a woven glass-fibre prepreg and 2024-O aluminium was used to create the FMLs, with the first paper [89] also investigating the effect of laminate configuration. The modelling procedure for each of these investigations involved the meso-level approach, with the layers of the FML considered as separate parts and modelled using shell elements, which are

connected using an interaction property. The GFRP layer was modelled as an orthotropic elastic material with limited ductility until the initiation of failure, which was determined using Hashin's failure criteria. Following the initiation of failure, a degraded stiffness matrix is constructed to represent the reduced performance of the composite. The interface between the FML layers was modelled using a high friction coefficient ($\mu = 100$) to reduce the relative displacement between the surfaces, providing the appearance of a strong bond. The results obtained using this method of simulation agreed well with experimental results, even with the simplified material models and interaction properties.

In conjunction with the material behaviour, the other major parameter which affects the simulation of forming procedures (particularly for FML forming) is the interaction between the individual material surfaces. As discussed in Section section §2.5 an interfacial shear stress develops in laminates containing materials which have differing stiffnesses. There are two major ways to model this in FEA: a comprehensive cohesive model and an interfacial friction model. Cohesive element modelling requires knowledge of delamination energies and crack opening/growth information. The friction method models the interfacial shear using a simple "stick–slip" analysis [73]. The "stick–slip" analysis means that below a certain maximum shear stress the layers are considered to be "stuck" together with the friction force equal to μp. If the maximum shear stress is exceeded the layers are considered to act in an independent manner.

The studies on the simulation of FMLs discussed previously all used either

rough contact (no sliding) or high friction coefficients (greatly restricted sliding) to represent perfect bonds between the layers of the FML. However, studies by Mosse et al. [73, 97] and a model incorporating the cohesive effects of the adhesive layer by Vo et al. [98] offer significantly more complex representations of the interfacial behaviour. Mosse et al. incorporated the effect of temperature on the behaviour of the adhesive in the FML. This model used results from double-lap shear experiments to determine the strength of the adhesive at different temperatures. In addition, the effect of pressure applied to the bonding area was determined to see if contact pressure between the surfaces affected bond strength. It was found that both the temperature and applied pressure had a significant effect on the adhesive strength. In order to model the interfacial behaviour, a user-defined friction routine was incorporated into the LS-DYNA model. This model predicted a high friction coefficient ($\mu = 100$) when the bond was considered intact and a frictionless condition after failure (where failure was determined using the maximum shear stress determined by the experiments as a function of temperature). Another significant benefit to this model is that the bond is able to reform if failure occurs above the melting point of the adhesive, which yields improved results compared to experimental forming. Vo et al. [98] used the material models developed by Guan et al. [95] and Fan et al. [89, 96] with the addition of strain rate dependency in the composite and a cohesive model for the adhesive layer. Excellent agreement with experiments was found. The cohesive element was defined using a linear elastic traction–separation behaviour with a

quadratic nominal stress criterion for failure and a linear softening law for damage evolution based on energy conjunction. The traction–separation behaviour uses an uncoupled elastic stiffness matrix which relates the traction stress to the traction strain.

The final consideration when developing a finite element model of forming is the interaction between the specimen and the tools. Studies have been performed which have investigated the tribological conditions between tools and specimens during forming. Ghosh [99] investigated a method for determining the coefficient of friction between the tools and specimens in forming processes. This study recognised the phenomenon of friction between the specimen and the punch retarding deformation in the centre of the specimen and shifting it to the unsupported regions. By analysing the contact pressure between the punch and the specimen, ignoring the effect of pressure on the coefficient of friction (that is,$\tau = \mu p$), and that the inflection point in the load-displacement diagram represents the maximum deformation of the pole region and therefore maximum contact pressure, the coefficient of friction can be determined. It was found that the coefficient of friction between a polished steel punch and steel sheets was 0.22–0.26 and for aluminium and brass sheets it was 0.3–0.4. Javadi and Tajdari [100] investigated the coefficient of friction between aluminium and steel and found that the friction coefficient between non-lubricated steel and aluminium varied between 0.2 to 0.9 as the contact stress was increased.

2.8 Summary

This chapter presents a comprehensive review of the literature regarding the constituent materials of fibre–metal laminates, their processing, and finally their simulation using finite element analysis. It can be seen that while extensive research has been conducted into the forming of metals and composites, comparatively little has been performed on the forming of FMLs, particularly its modelling. The properties and advantages of the constituent materials has been discussed and the research into manufactured FMLs has been detailed. The review has shown that FMLs exhibit admirable properties when used in applications requiring damage and fatigue tolerance, but there is a barrier to their widespread adoption due to the focus on thermoset laminates which cannot be easily manufactured. The studies which did, however, analyse thermoplastic FMLs and their formability did not address the limitations to forming and the behaviour of the laminates in different deformation modes. In addition, the methods used to obtain experimental results and to model forming behaviour have been discussed. This study seeks to address the lack of information on the forming limits of two distinct fibre–metal laminates. The two different laminates will help to show the effect of stiffness, temperature, failure strain, and failure mode on the behaviour of a novel material undergoing a conventional forming process.

Chapter 3

Experimental Method

3.1 Introduction

Fibre–metal laminates are combinations of materials with different chemical compositions, strengths, and other properties. This chapter briefly discusses the properties of the constituent materials and describes the manufacturing process used to create FMLs from these constituents. In addition, the method for characterising the constituent material behaviour, and the process for determining the FLD and FLC of the final laminate, are outlined. This includes how the specimens were chosen and the standards used to design the experimental procedure. Finally, the use of the ARAMIS measurement system to provide strain data and its incorporation with stamp forming equipment is discussed.

3.2 Materials

Thermoplastic composites exhibit a wide range of mechanical properties depending on the reinforcement and the matrix. In order to give an overview of the mechanical behaviour of the varied thermoplastic composites, two distinct com-

posite materials were used in this study:

- a self-reinforced polypropylene composite (SRPP), and
- a glass-fibre reinforced polypropylene composite (GFRP).

These materials were chosen so as to compare the observed behaviour of two very different composites. The SRPP has a relatively low stiffness and a high strain to failure whereas the GFRP has a high stiffness and low strain to failure.

Due to its high strength-to-weight ratio, good weldability, machinability, formability, and good corrosion resistance the metal chosen for the outer layer of the fibre–metal laminate was aluminium. In particular, the aluminium layer in the fibre–metal laminates used in this study was 5005-O aluminium. This grade is considered a general structural metal with good formability, is strain hardenable, has moderately high strength, and has excellent corrosion resistance. The annealed temper was achieved by heating 5005-H34 aluminium in a muffle furnace to 400°C, holding it there for at least 2 hours, then furnace cooling. In general, aluminium has a stiffness of $69.8GPa$, a density of $2.7g/cm^3$ and a Poisson's ratio of 0.33.

The SRPP used in this study was Curv®, from Propex Fabrics, which is produced by heat compacting layers of woven, highly aligned tapes of polypropylene. It forms a matrix through melting of the outer fibre layers. This process provides a fibre volume fraction of 55–65%. The resulting composite has a density of $0.92g/cm^3$, a coefficient of thermal expansion of $6.8 \times 10^{-5}K^{-1}$ and a notched Charpy impact energy of $120KJ/m^2$.

The GFRP used in this study was a consolidated plate comprised of a balanced 2/2 twill weave of glass fibres which made up 60% of the composite by weight (35% by volume). The GFRP had a density of $1.485 g/cm^3$. This composite is called Twintex®, from Fiber Glass Industries Inc. The glass fibres provide high stiffness coupled with brittle failure, with a failure strain, according to the manufacturer, of approximately 2.5%.

3.3 Laminate Manufacture

The fibre–metal laminates used in this study were created using a combination of a 1.0mm thick composite and 2 layers of 0.6mm thick 5005-O aluminium. Two distinct fibre–metal laminate systems were developed, one based on GFRP and the other on SRPP. A $50 \mu m$ thick modified polypropylene (Gluco) adhesive layer was placed between the aluminium and the composite resulting in a nominal laminate thickness of 2.2mm. In order to facilitate a strong bond, the aluminium was etched in a 5% NaOH solution for 5 minutes prior to manufacture and the surfaces of the composite and adhesive were cleaned using isopropyl alcohol to remove contaminants.

The laminate stacking arrangement is illustrated in Figure 3.1. Laminates of 230mm by 240mm were placed in a hydraulic press and heated to 155°C. This temperature is high enough to melt the adhesive without affecting the SRPP or the GFRP. Once the temperature was achieved, a pressure of 1MPa was applied for 5 minutes after which the laminate was rapidly water cooled. The heat press

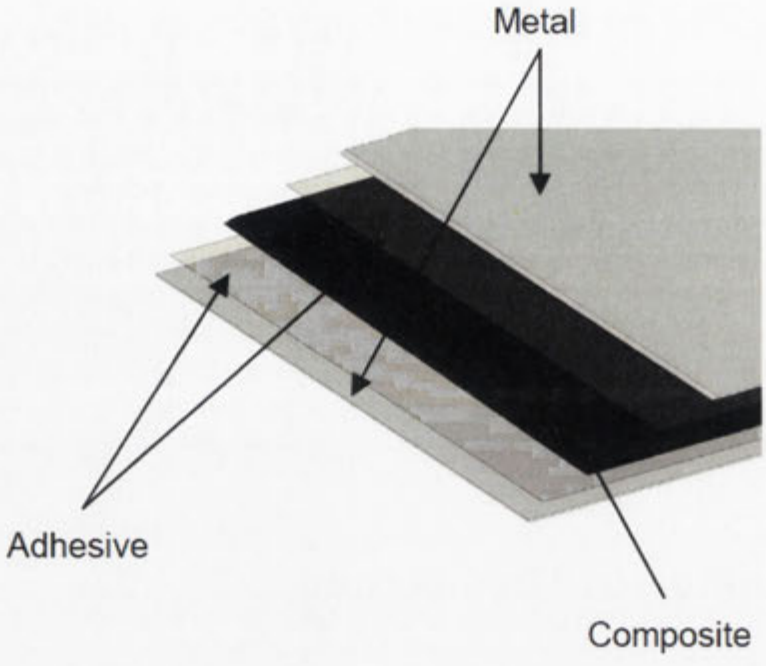

Figure 3.1: Laminate stacking arrangement

is a single-ram manually-actuated hydraulic press with two heated steel platens which contain water heat exchangers to control the cooling rate. This allows rapid cooling of the specimens leading to high degrees of crystallinity in the adhesive layer which is beneficial for bond strength [101]. In order to prevent degradation of the laminates during manufacture water jet cutting was then used to obtain the desired experimental geometries. Water jet cutting uses high pressure and velocity water containing abrasive particles and therefore does not suffer from the same problems inherent to other cutting methods (such as heat-affected zones in laser cutting and the defects introduced into composite materials from shearing using milling and cutting tools).

3.4 Experimental Method

The experimental component of this work consisted of characterisation experiments and forming experiments. The characterisation experiments aid the analysis of results from complex experiments, such as forming, and help the development of modelling. The major focus is the forming experiments, which will provide real time information into the forming behaviour of the FMLs and allow determination of the failure limits of the FMLs in forming processes.

3.4.1 Characterisation experiments

The characterisation experiments to obtain the stress–strain behaviour of the composite materials were carried out in accordance with ASTM D3039. The dimensions of the experimental tensile specimens are shown in Figure 3.2. These

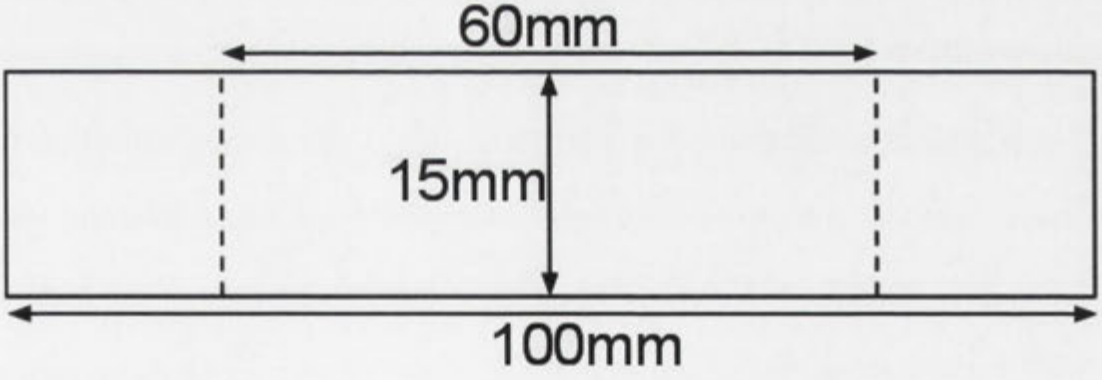

Figure 3.2: Characterisation tensile specimens for the SRPP and GFRP

tests were conducted with the in collaboration with S. Venkatesan [64] on an Instron 1416 at the University of New South Wales at the Australian Defence Force Academy. Eight temperatures consisting of room temperature (20–25 °C),

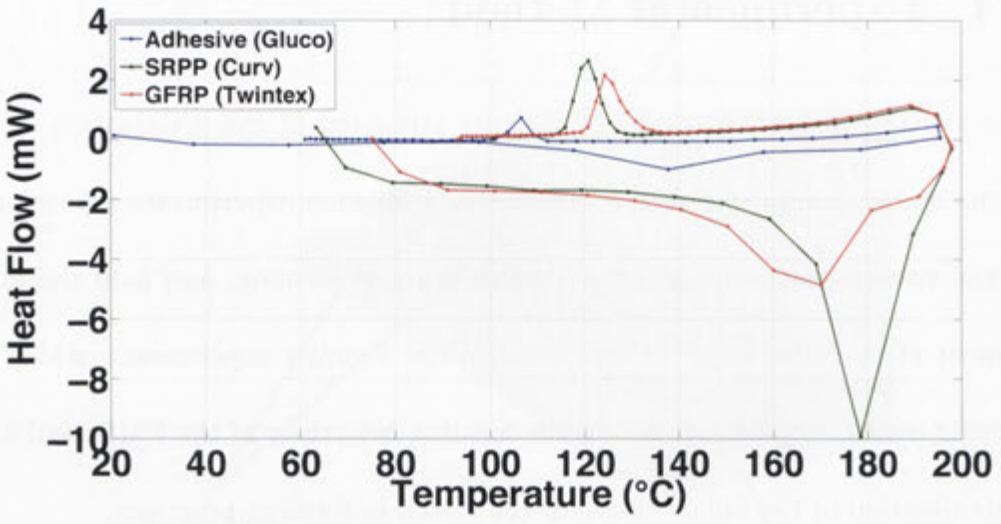

Figure 3.3: Differential scanning calorimetry results for the adhesive, SRPP, and GFRP

40°C, 60°C, 80°C, 100°C, 120°C, 140°C, and 160°C were used to elicit the effect of temperature on the composites. The tensile tests were performed at a constant crosshead displacement rate of 5mm/min and a laser extensometer was used to measure the deformation of the specimens. This deformation was then used to determine the stress–strain behaviour.

In addition, differential scanning calorimetry (DSC) was performed on the composites and adhesives to determine the melting and recrystallisation characteristics. DSC involves measuring the heat flow into and out of the material during the heating and cooling of the material; during a phase transition such as melting or recrystallisation more or less heat flow is needed to continue heating the specimen as rapidly as a reference material. Figure 3.3 shows the heat flow for the composites and adhesive as the specimens were heated from room temperature to 200°C and then cooled. The figure shows that the adhesive, SRPP,

Material	Melting temperature	Recrystallisation temperature
Aluminium 5005-O	650°C	N/A
Adhesive (Gluco)	120°C to 160°C	100°C to 110°C
SRPP (Curv)	150°C to 190°C	115°C to 125°C
GFRP (Twintex)	150°C to 180°C	120°C to 135°C

Table 3.1: Melting and Recrystallisation Temperatures

and GFRP begin to require more energy at temperatures of 120°C, 150°C, and 150°C respectively, indicating the onset of melting. Recrystallisation occurs at 110°C, 125°C, and 135°C in the adhesive, SRPP, and GFRP respectively. Table 3.1 summarises the key points of the materials. It can be seen that there exists a region of temperature where the matrix of the composites has recrystallised but the adhesive remains in a melted state. This condition had been shown to allow the deformation of the FML as three separate consolidated layers [73, 77].

3.4.2 Stretch forming experiments

The stretch-forming experiments in this study were conducted in accordance with ASTM2218 and ISO12004. These standards dictate the parameters required to determine the forming limits of sheet metals – such as the specimen and tool geometry, feed rate, lubrication, and data extraction methods. The specimen geometries required by these documents utilise the specimens developed by Hecker, Nakajima, and Raghavan [42, 41, 43]. Hecker and Nakajima [42, 41] proposed the use of rectangular specimens varying from approximately 25mm in width to 200mm combined with a 100mm hemispherical punch. Raghavan [43] suggested using "waisted" specimens, specimens with an hourglass appearance, to ensure

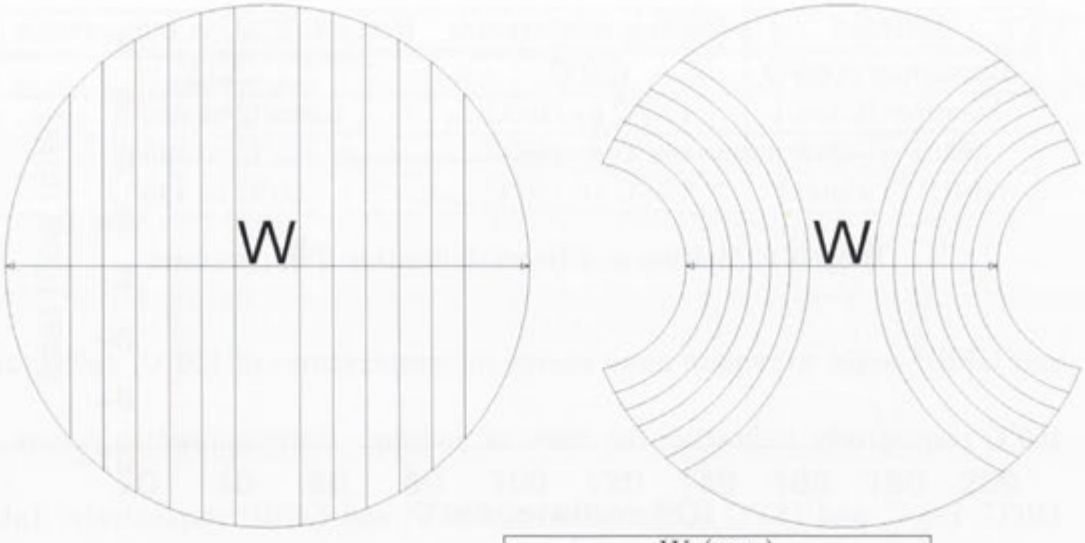

	W (mm)
Rectangular specimens	25, 50, 75, 100, 125, 150, 200
Hourglass specimens	25, 40, 55, 70, 85, 100, 120

Figure 3.4: Experimental geometries

that failure occurred close to the centre. Using these specimens it is possible to obtain all deformation modes from uniaxial tension $\left(\beta = -\frac{1}{2}\right)$ to balanced biaxial stretch ($\beta = 1$). Only one study has been performed on the forming of fibre–metal laminates using different specimen geometries [79] and no information was provided about the behaviour of each FML specimen compared to monolithic metal forming. Therefore, this study performed a pilot experiment at room temperature using the rectangular specimens developed by Hecker and Nakajima and the hourglass specimens developed by Raghavan to determine the optimal combination of specimen geometries. Figure 3.4 shows the specimens used in the room temperature pilot study. The nomenclature of the experimental specimens was chosen to reflect the specimen geometry and the width of the specimen at its thinnest point. Hence, the rectangular specimens were named, in order from thinnest to largest,

25mm, 50mm, 75mm, 100mm, 125mm, 150mm, and 200mm and the hourglass specimens were named 25mmHG, 40mmHG, 55mmHG, 70mmHG, 85mmHG, 100mmHG and 120mmHG. After the pilot study at room temperature, five specimen geometries were selected for the evaluation of the effect of temperature. The reduced "width" direction is termed the lateral direction and the "length" direction is called the longitudinal direction.

All experimental forming specimens had the fibre orientation aligned along the longitudinal direction of the specimens. This had the effect of reducing the amount of deformation available to the laminates due to failure at the fibres. Other studies [102] have shown that the formability of composites can by altered by orienting the fibres at 45° to the longitudinal direction. This effect was not assessed in this work.

A custom designed 300kN stamp press with a 100mm diameter hemispherical punch and 105mm open die, shown in Figures 3.5 and 3.6, was used to evaluate the forming of the fibre–metal laminate. The forming was performed using a hydraulic punch with a stroke length of 200mm. The blankholder constrains the blank through the use of a lock ring, shown in Figure 3.6(b). The lock ring has a radius of 82.5mm which is less than the specimen radius and therefore forces the specimen into a bend–unbend which prevents any material from outside the lock ring from drawing into the die region. The amount of locking applied by the blankholder was controlled through torque applied to six bolts surrounding the lock ring. The amount of blankholder force applied to the experimental specimens

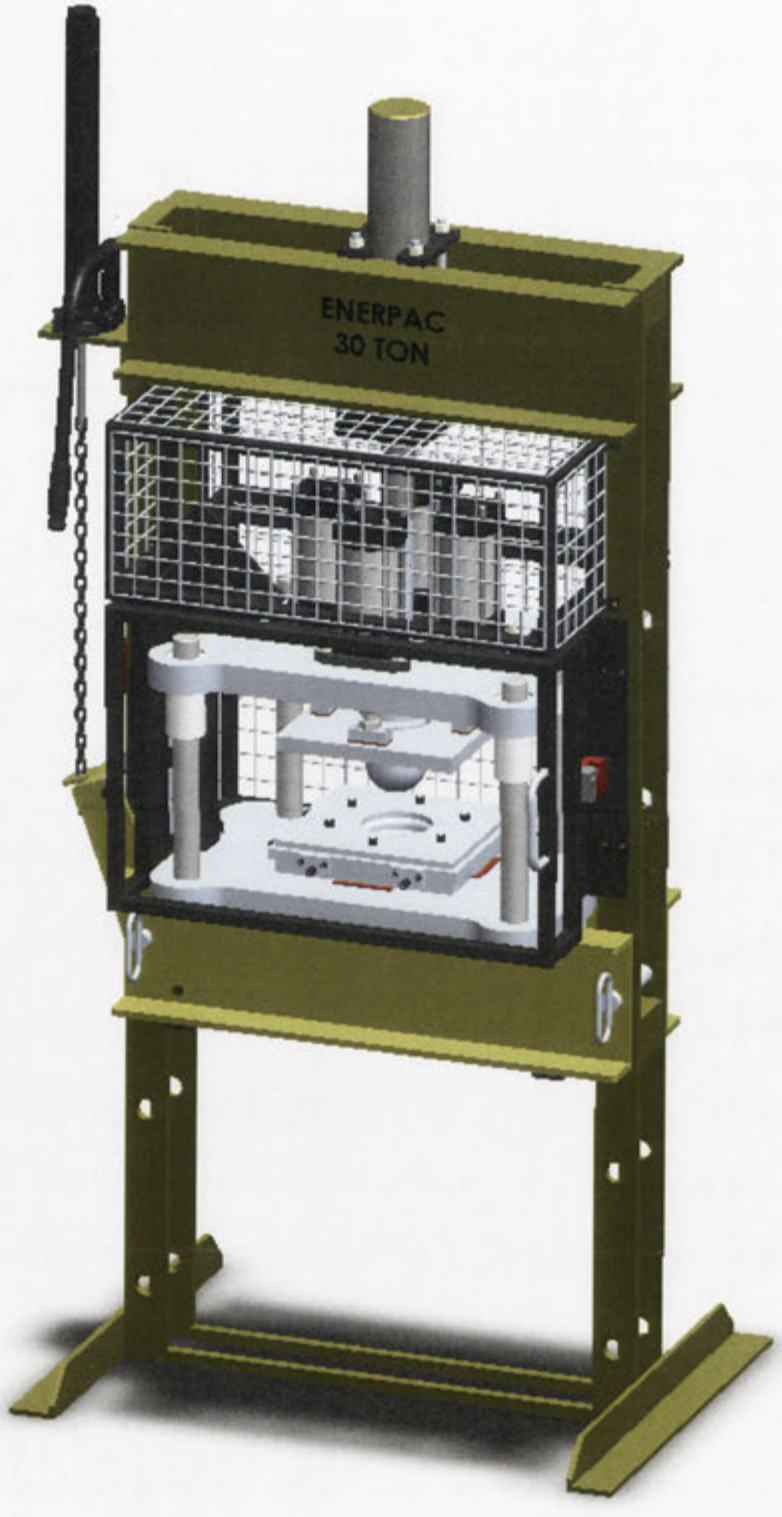

Figure 3.5: Press setup

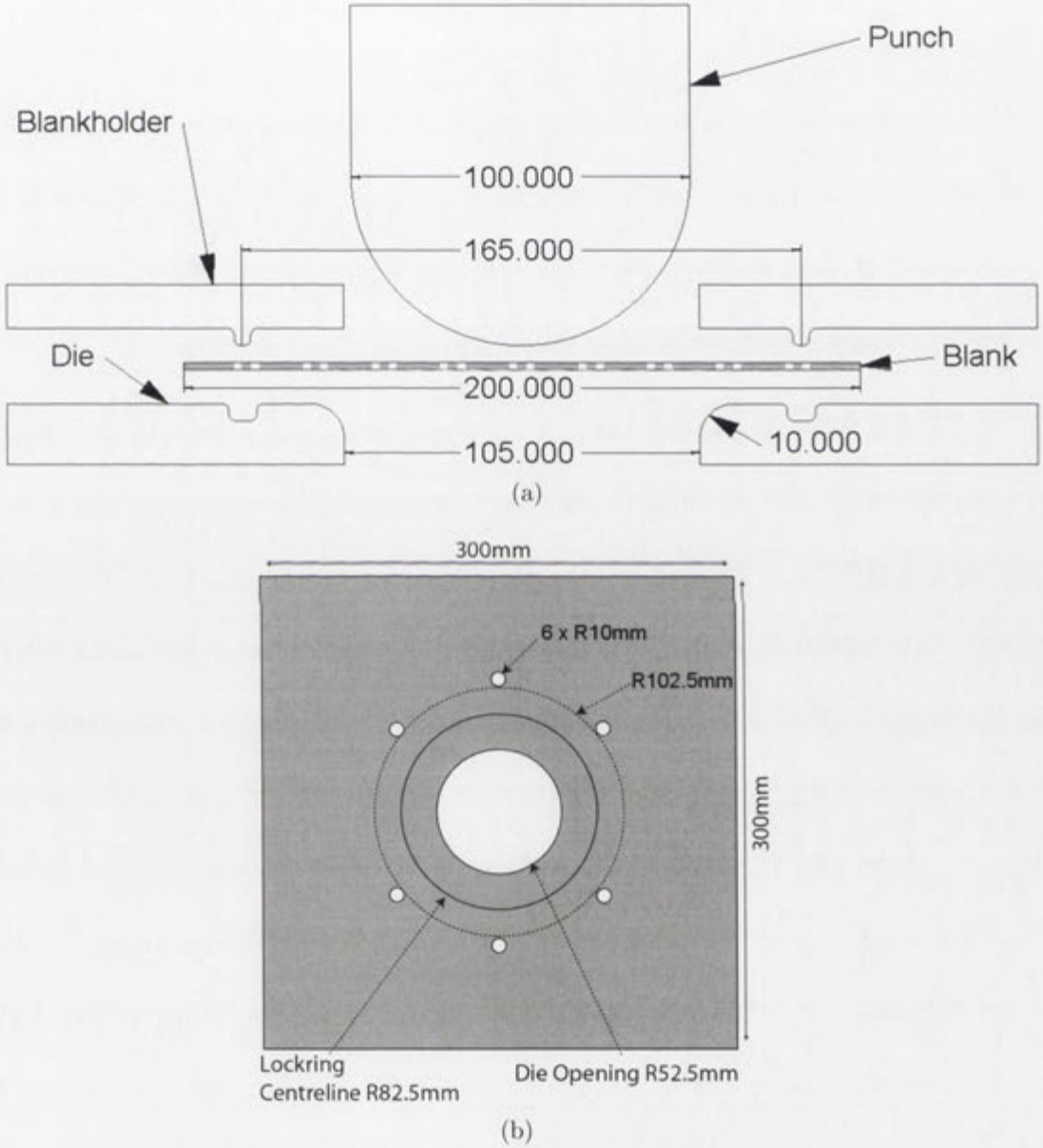

Figure 3.6: Press schematic (a) and design of lock ring and securing bolts (b)

Parameter	Value
Feed rate	5-10mm/s
Blankholder torque	10-30Nm
Temperature	20-140°C
Lubrication	Teflon (PTFE) film

Table 3.2: Process parameters for the experimental formability studies

depended on the specimen geometry. Higher torques, and therefore blankholder forces, were required to lock the 200mm specimen than the 25mm specimen. In addition, as discussed in subsequent chapters, the lock ring induces a strain in the material which must be controlled to prevent premature failure.

Table 3.2 summarises the key process parameter values used in the forming experiments. The ASTM2218 and ISO12004 standards require a feed rate of 1.5mm/s for the evaluation of formability. However, the experimental press at the ANU was not capable of maintaining the punch force required to deform specimens at low feed rates, therefore a feed rate of 10mm/s was selected for the experiments. This should not have an effect on the results as the low feed rate is to ensure the rapid determination of localised necking in sheet metals, which is not an issue when using the strain measurement system chosen for this study. The lowest torque values (10Nm) were used for the 25mm GFRP FML specimens and the highest (30Nm) for the 200mm SRPP FML specimens. In addition, Teflon release film was used to reduce friction between the punch and the specimens. Finally, in order to determine the effect of temperature on the forming of the FML systems, experiments were conducted at 20°C intervals from room temperature up to 140°C, resulting in 7 temperature levels. The 160°C

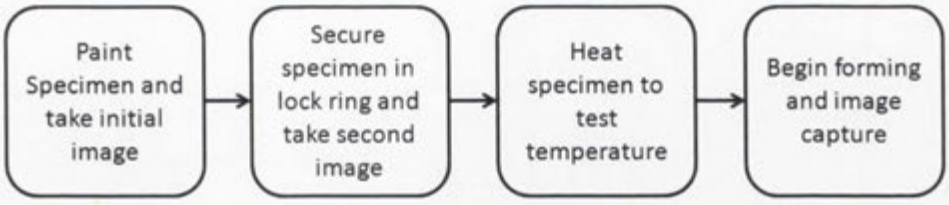

Figure 3.7: Experimental Procedure

test was not conducted as it was found that the behaviour at 140°C adequately described the behaviour at 160°C.

The experimental procedure used in this study is shown in Figure 3.7. After the specimen had been manufactured and cut to the desired geometry it was placed on the press and an image taken of the surface. This image served as the reference for all other images in the experiment and provided the state of 0% strain. After the initial image was taken, the specimen was then secured in the blankholder and lock ring and a second image taken; this image determined the effect of the lock ring on the surface strain. The specimen, die, and blankholder were placed in an oven (unless a room temperature experiment), heated to the test temperature, and replaced on the press. The press was then actuated and the image capture started when the punch was 10mm away from the specimen.

The specimens were heated to the test temperature through the use of an oven which was heated to the desired temperature. The time required to heat the specimens to the test temperature, called the soak time, was calculated by placing the die, blankholder, and specimen in the oven with a thermocouple placed in the specimen to determine when the test temperature had been achieved. The soak time for all specimens was found to be 2–3 hours.

A local data acquisition PC allowed the design of process parameters and controlled the feed rate and punch displacement. A 150kN compression load cell was used to measure the punch force and a linear potentiometer provided the punch displacement. The experiments were conducted at a feed rate of 10mm/s and the depth at failure was determined by a 2% drop from maximum load. An open die was used to facilitate measurement of the strain on the surface of the material throughout the forming process using the ARAMIS strain measurement system.

3.5 Strain Measurement

The measurement of the strain on the surface of the experimental specimens was facilitated by the ARAMIS 3D real-time strain measurement system, manufactured by GOM GmbH. Figure 3.8 shows the configuration of the ARAMIS system and the measuring volume. This measuring volume is the region of space in which displacement and strain measurements can be conducted. By changing the focal length, slider distance, camera angle, and measuring distance the ARAMIS strain measurement system can be used to analyse a number of measurement volumes, shown in Table 3.3. Due to the standardised equipment setup used in the study, a measuring volume of 180 x 160 x 150 mm was used. This measuring volume was chosen to ensure measurements of all points on the surface of the specimens, that the specimen remained inside the measuring volume at all forming depths, and to allow the correct placement of the cameras. The parameters for this volume

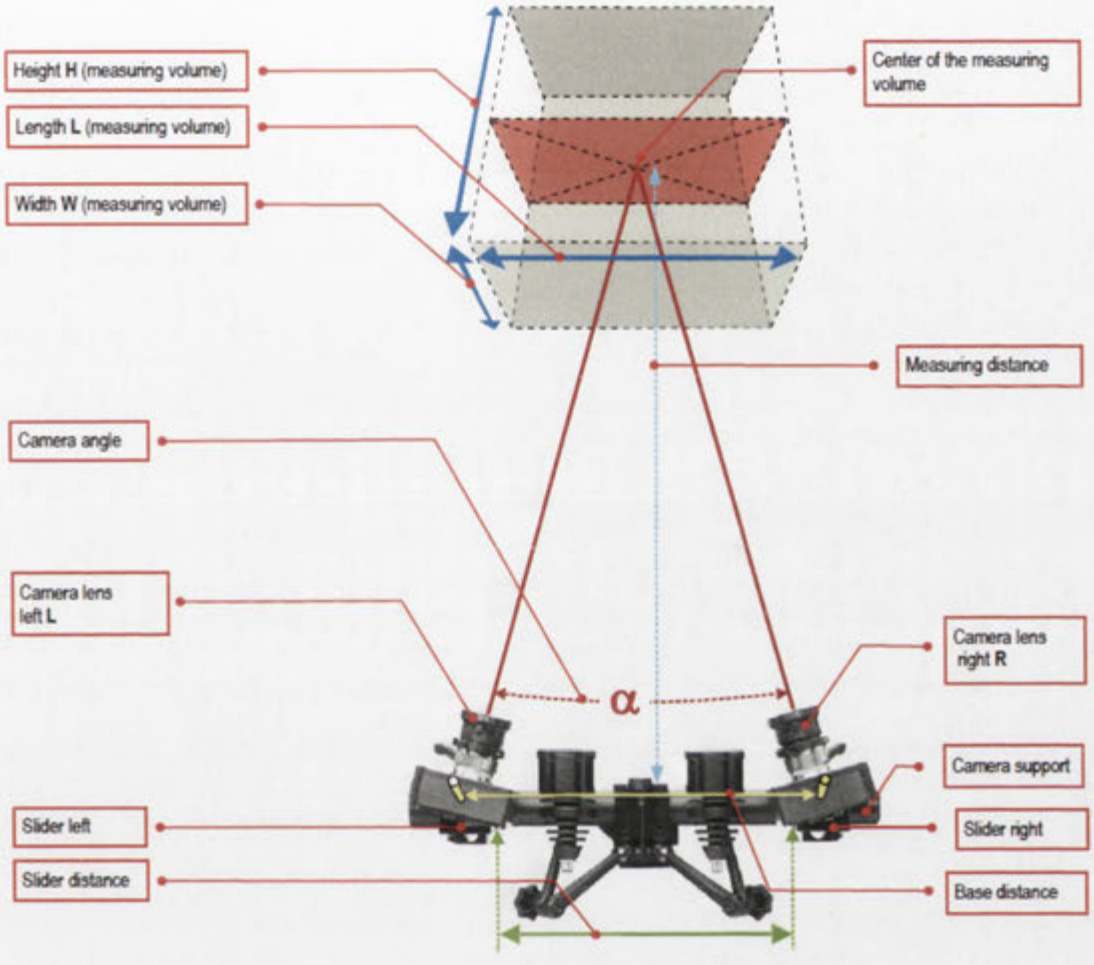

Figure 3.8: ARAMIS Configuration [103]

Parameter	Specification
Measuring volumes	10 x 8 to 5000 x 4150 (mm)
Resolution	2448 x 2050 (pixels)
Max. frame rate	24 (Hz)
Shutter time	0.1ms to 2s
Strain range	0.02 to >100%
Accuracy	up to 0.01%

Table 3.3: Specifications of the ARAMIS system [103]

were a focal length of 17mm, a camera angle of 25°, a slider distance of 136mm, and a measuring distance of 395mm. These parameters control the width and length of the measuring volume, but the height, or depth of field, is controlled by the aperture settings. A fully open aperture provides a shallow depth of field and therefore restricts the height of the measuring volume; this is unsuitable for stamp forming experiments especially when the forming depth could be large for specimens tested at high temperatures. To provide a large measuring height for the experiments the aperture was set to its lowest setting; however, this restricted the amount of light available to the sensor, so in the region surrounding the open die external lighting was used and the shutter time of the cameras adjusted accordingly.

The system used the random pattern applied to the surface of the specimens shown in Figure 3.9 to determine both the undeformed and deformed coordinates of points on a 2D plane. There is, however, a trade-off between the resolution of the calculations and the ability to fully resolve the pattern. When larger surface characteristics are used in the pattern the calculations become more coarse due to less points being assigned to the surface, resulting in more interpolation required between points. Smaller surface characteristics may not have enough contrast to be identified by the cameras, which results in no calculations being possible. The surface pattern must have low reflectivity and high contrast and adequate lighting must be used to allow full determination of all the points.

The required stochastic pattern was applied using a thin coating of matte

Figure 3.9: High contrast stochastic pattern applied to the surface of a specimen

white paint to serve as the base layer and black paint to create the surface characteristics. The white paint was chosen as the base layer to enhance the lighting conditions under the stamp press. The random pattern of black surface characteristics was created through the use of an aerosol spray. The surfaces of the specimens were cleaned with isopropyl alcohol to prepare them for painting. In applying the paint its extensibility was particularly important. It was found that certain paints would exhibit good characteristics if tested immediately but would flake off the surface during forming if allowed to cure for too long; other paints were found to only be suitable for small extensions and would peel off at higher forming depths. The chosen paint was a high temperature engine enamel manufactured by Septone.

Using the stochastic pattern, the ARAMIS system divides the surface into $15 \times$

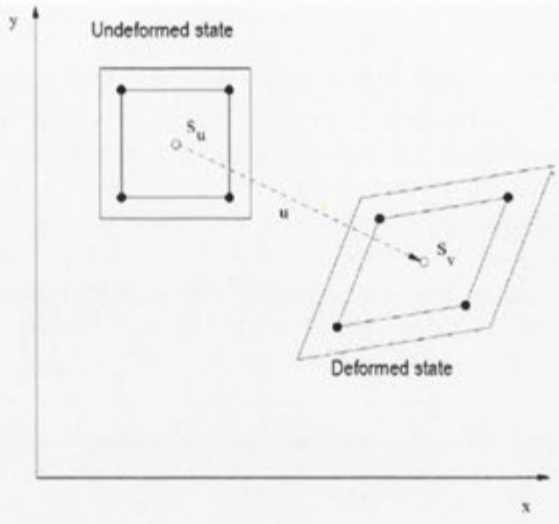

Figure 3.10: Four-sided facet [103]

15 pixel correlation areas known as facets which have an additional overlap of 2 pixels. Figure 3.10 shows the deformation of a four-sided facet [103]. The deformation gradient tensor is calculated for the virtual centre of gravity of each facet using the four points of the facet. The deformation gradient tensor is split into two separate tensors: a purely rotational tensor and a stretch tensor. The strain can be directly read from the stretch tensor. In this study the techniques developed by Kalyanasundaram et al. were used to assess the formability of the thermoplastic FML systems.

3.6 Analysis of results

In this study, the formability of the experimental specimens was assessed using several key indicators:

- the strain behaviour at the pole,

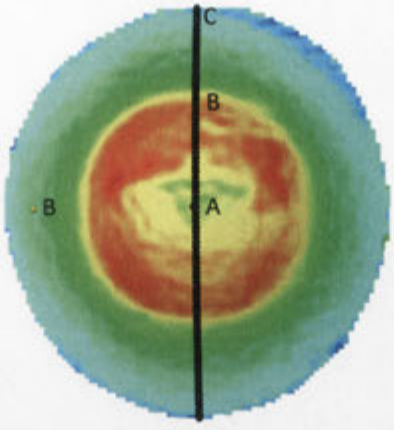

Figure 3.11: Points of interest on the experimental specimens

- the strain behaviour in the region of failure,
- the strain along the meridian,
- the overall surface strain behaviour, namely the FLD and strain contours.

These indicators were chosen because they provide all the information required to describe the formability of a material. Figure 3.11 shows the indicators used to assess formability. Point A represents the pole region, Point B represents the region of failure, and Point C represents the die edge. The failure region (Point B) always occurs along the fibre direction, which means that in the case of the 200mm specimen it can occur in either the longitudinal or the lateral direction. The meridian line is also shown in the figure. Finally, points at 45° to the fibre direction were assessed (in those specimens that could be analysed) to confirm findings by previous researchers of the effect of trellising in the woven fabric.

The strain at the pole is important as it shows the expected deformation mode from the experimental specimen. It is also desired that the region of failure

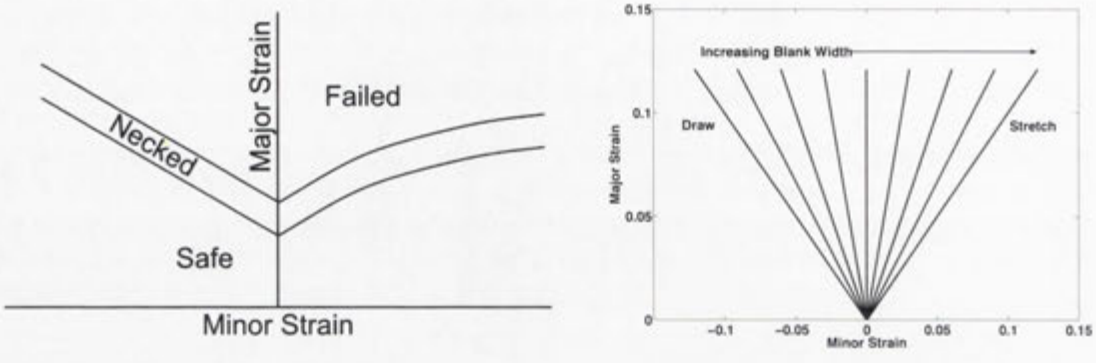

(a) (b)

Figure 3.12: Regions of the FLC (a) and the effect of specimen geometry on the forming mode (b)

coincides with the pole region, preferably within 25mm. However, due to the effect of friction this may not occur and therefore the region of failure will be considered separately even when the points do coincide.

In general, the formability of a material is determined using the major and minor strain experienced by the material under certain forming conditions. These strains are then used to create the FLC where three regions are present: the safe, marginal, and failed regions, shown in Figure 3.12(a). By varying the specimen geometry different forming modes can be obtained, shown in Figure 3.12(b). In order to determine the safe, marginal, and failed regions of the FLC the images captured by the measuring system must be assessed. Figure 3.13 shows how such points can be identified from the ARAMIS images. Figures 3.13(a) and (b) show the specimen immediately before and after failure and Figure 3.13(c) shows an overlay of the major strain on Figure 3.13(a). Using this major strain it can be seen that the red region can be used to obtain the failed data points, the

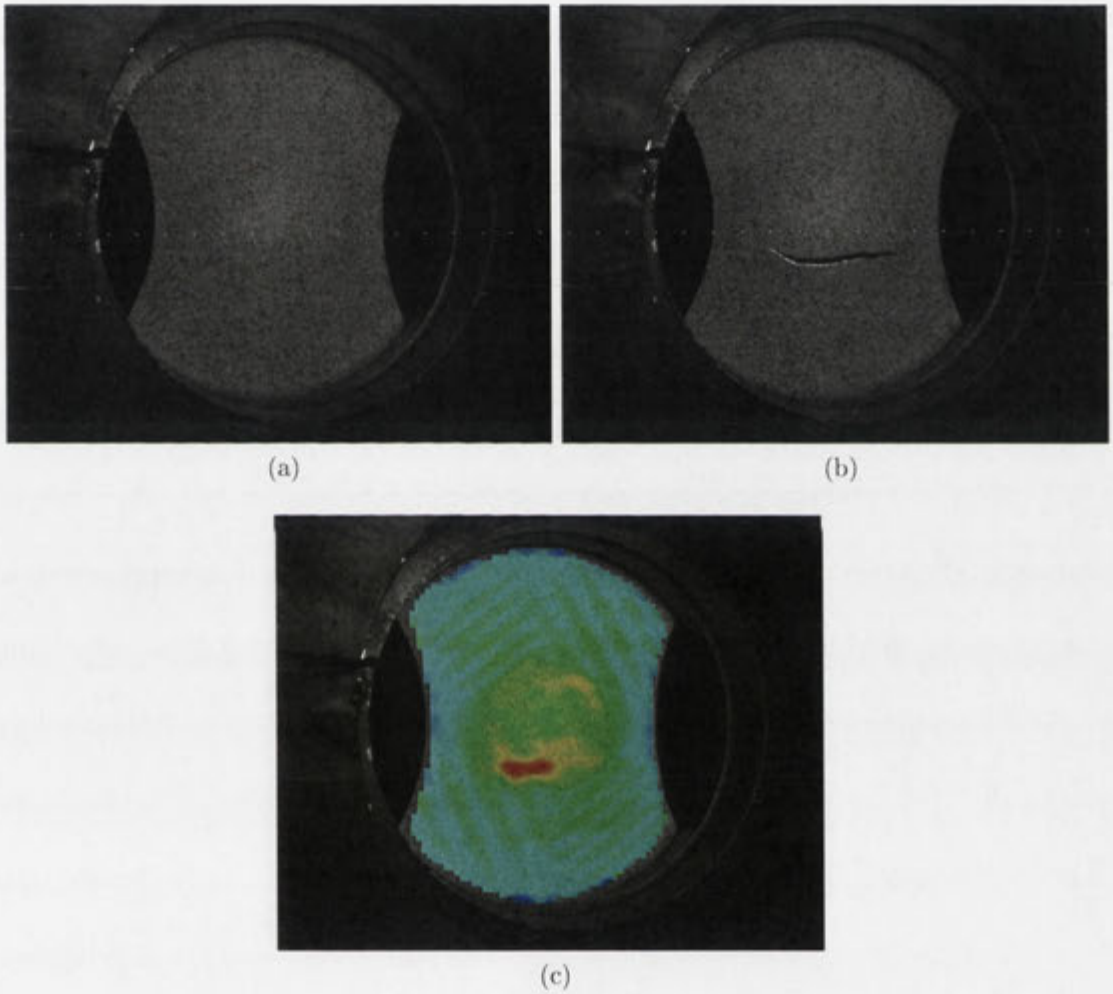

(a) (b)

(c)

Figure 3.13: Identification of areas of interest for FLC creation

orange/yellow for the marginal region, and the green/blue for the safe region.

3.7 Summary

This research sets out to investigate the formability of two different FML systems based on thermoplastic composites. The method for manufacturing and preparing the experimental specimens and the mechanism for measuring the resulting strains has been detailed. A total of 14 geometries were used in a pilot study at room temperature to determine which specimens would give the desired forming behaviour; 5 geometries were chosen for the evaluation of the effect of temperature. This resulted in 98 experiments comprised of 2 material systems, 14 geometries at room temperature, and 5 geometries at temperatures ranging from 40°C to 160°C. The experiments were conducted using a stamp press with an open die to facilitate strain measurement using the ARAMIS system. Stretching of the specimens was enforced through the use of a lock ring and blankholder. The aim is to use the strain results to determine the formability of the laminates by assessing the evolution and distribution of surface strain and the strain state at failure to develop a forming limit curve. Chapter 4 will detail the development of a finite element model for comparison with experimental results. Subsequent chapters will use the methods outlined in this chapter to obtain a range of experimental results, which are then discussed.

Chapter 4

Development of the Finite Element Model

4.1 Introduction

A major aspect of this thesis is the development of a finite element model. Such a model is important as it allows analysis of regions and parameters unavailable to experimental study. This is useful for materials such as FMLs because the composite layer is not visible to external measurement equipment. It also provides the capability to rapidly adjust forming parameters – such as stiffness, friction, and other boundary conditions – and get insight into their effect on the mechanical behaviour of materials during forming.

This chapter first outlines the finite element methods implemented by the finite element analysis software. It describes how the constitutive models for the composites used in the characterisation experiments described in Chapter 3 were developed. In addition, the constitutive models for the aluminium and adhesive layers are also discussed. Finally, the procedure for determining the boundary conditions, setting up the simulation, and modelling the forming process is pro-

vided.

4.2 Finite Element Method

Finite element analysis is a numerical method for solving problems which can be described by differential equations. Using this analysis technique the problem is discretised into a number of elements which can then be solved algebraically for a range of displacements and forces. This representation of the problem yields a number of simultaneous algebraic equations which are able to be solved. This method determines values of displacement at the discretised points in the continuum; interpolation is used to determine values at other points. This is especially useful for complicated geometries, loadings, and material properties where it is generally not possible to obtain an analytical solution. For nonlinear problems there are two methods for obtaining a solution, the explicit and the implicit.

4.2.1 Explicit Method

The equations of motion for a body integrated using a central difference integration rule are given in equation 4.1 [104].

$$\begin{aligned} \mathbf{u}^{i+1} &= \mathbf{u}^{i} + \Delta t^{(i+1)} \dot{\mathbf{u}}^{i+\frac{1}{2}} \\ \dot{\mathbf{u}}^{i+\frac{1}{2}} &= \dot{\mathbf{u}}^{i-\frac{1}{2}} + \frac{\Delta t^{(i+1)} + \Delta t^{(i)}}{2} \ddot{\mathbf{u}}^{i} \\ \ddot{\mathbf{u}}^{i} &= \mathbf{M}^{-1} \cdot \left(\mathbf{F}^{i}_{ext} - \mathbf{F}^{i}_{int} \right) \end{aligned} \tag{4.1}$$

where $\mathbf{M}$ is the mass matrix, $\mathbf{F}_{ext}$ is the externally applied force vector, and $\mathbf{F}_{int}$ is the internal force vector. To ensure numerical stability, the time-step required for solution has to be controlled. If the time-step is too large, divergence from the correct solution will occur. Therefore, the method is deemed to be conditionally stable. The optimum time-step size is calculated according to equation 4.2.

$$\begin{aligned} \Delta t &\approx \frac{L_s}{C_d} \\ C_d &= \sqrt{\frac{E}{\rho(1-\nu)}}, \end{aligned} \tag{4.2}$$

where L_s is some characteristic element dimension and C_d is the dilatational wave speed of the material [104]. Because there is no requirement to check for equilibrium, the explicit solution has been successfully used for metal forming analysis [105]. Mattiasson found that the explicit method was less computationally expensive than the implicit method for metal forming simulations.

4.2.2 Implicit Method

When considering a quasi-static problem, the equilibrium conditions (assuming the solution for time t is known) can be expressed as [106]

$$^{t+\Delta t}\mathbf{F}_{ext} - {}^{t+\Delta t}\mathbf{F}_{int} = \mathbf{0}, \tag{4.3}$$

where $^{t+\Delta t}\mathbf{F}_{ext}$ is the vector of externally applied forces at time $t + \Delta t$ and

${}^{t+\Delta t}\mathbf{F}_{int}$ is the vector of internal forces derived from the stress. The solution is known for time t, therefore the internal forces can be expressed as

$$ {}^{t+\Delta t}\mathbf{F}_{int} = {}^{t}\mathbf{F}_{int} + \mathbf{F}_{int}, \tag{4.4} $$

where ${}^{t}\mathbf{F}_{int}$ are the internal forces at time t and $\mathbf{F}_{int}$ is the increment in the internal force between t and $t + \Delta t$. The increment in the internal forces can be approximated using the tangent stiffness matrix ${}^{t}\mathbf{K}$ at time t

$$ \mathbf{F}_{int} \approx {}^{t}\mathbf{K}\mathbf{U} \tag{4.5} $$

The tangent stiffness matrix, also called the Jacobian matrix of the system [107], is defined by the relationship between the derivative of the internal forces with respect to the displacement

$$ {}^{t}\mathbf{K} = \frac{\partial {}^{t}\mathbf{F}_{int}}{\partial {}^{t}\mathbf{U}}. \tag{4.6} $$

Substituting equations 4.5 and 4.4 into equation 4.3, the equilibrium equation becomes

$$ {}^{t}\mathbf{K}\mathbf{U} = {}^{t+\Delta t}\mathbf{F}_{ext} - {}^{t}\mathbf{F}_{int} \tag{4.7} $$

where, by inverting the stiffness matrix and solving for $\mathbf{U}$, an approximation of the displacement at $t + \Delta t$ can be determined

$$ {}^{t+\Delta t}\mathbf{U} \approx {}^{t}\mathbf{U} + \mathbf{U} \tag{4.8} $$

Using the solution obtained in equation 4.8, the force and stress at each node can be determined. However, the assumption in equation 4.5 and the size of the

time-step may cause the value of the displacement to be incorrect. This leads to equation 4.3 resulting in an "out of balance" load vector $\mathbf{\Delta F}_{ext}^{(i-1)}$

$$^{t+\Delta t}\mathbf{F}_{ext} - {}^{t+\Delta t}\mathbf{F}_{int} = \mathbf{\Delta F}_{ext}^{(i-1)}. \tag{4.9}$$

Therefore, an iteration scheme must be used until the value of $\mathbf{\Delta F}_{ext}^{(i-1)}$ is sufficiently small. The Newton–Raphson iteration scheme aims to find the solution to the nonlinear equation (Equation 4.10) which is equivalent to equation 4.3.

$$\begin{aligned} \mathbf{f}(\mathbf{U}) &= \mathbf{0} \\ {}^{t+\Delta t}\mathbf{F}_{ext} - {}^{t+\Delta t}\mathbf{F}_{int} &= \mathbf{0}. \end{aligned} \tag{4.10}$$

Equation 4.10 can be linearised by a Taylor series expansion about the approximate solution determined in previous iterations:

$$\mathbf{f}(\mathbf{U}) = \mathbf{f}\left({}^{t+\Delta t}\mathbf{U}^{(i-1)}\right) + \left[\left.\frac{\partial \mathbf{f}}{\partial \mathbf{U}}\right|_{t+\Delta t\mathbf{U}^{(i-1)}}\right]\left(\mathbf{U} - {}^{\mathbf{t+\Delta t}}\mathbf{U}^{(\mathbf{i-1})}\right) + \text{higher order terms.} \tag{4.11}$$

By neglecting the higher-order terms an updated displacement increments vector $\mathbf{\Delta U}^{(i)}$ can be determined:

$$^{t+\Delta t}\mathbf{K}^{(i-1)}\mathbf{\Delta U}^{(i)} = {}^{t+\Delta t}\mathbf{F}_{ext} - {}^{t+\Delta t}\mathbf{F}_{int}^{(i-1)} \tag{4.12}$$

$$^{t+\Delta t}\mathbf{U}^{(i)} = {}^{t+\Delta t}\mathbf{U}^{(i-1)} + \mathbf{\Delta U}^{(i)}. \tag{4.13}$$

The initial conditions for this iteration scheme are given in equation 4.14:

$$^{t+\Delta t}\mathbf{U}^{(0)} = {}^{t}\mathbf{U}; \quad ^{t+\Delta t}\mathbf{K}^{(0)} = {}^{t}\mathbf{K}; \quad ^{t+\Delta t}\mathbf{F}_{int}^{(0)} = {}^{t}\mathbf{F}_{int}. \tag{4.14}$$

Kim et al. [108] investigated the use of implicit and explicit finite element methods in the hydroforming simulation of an automotive lower arm made from a power-law plastic steel. LS-DYNA was used to perform the explicit analysis and HydroFORM-3D was used to perform the implicit analysis. It was found that both methods accurately represented the forming. However, the implicit method had a relatively long computation time and the treatment of friction between the blank and tools must be carefully considered. The explicit method required less computation time, but it was found that reasonable results could only be obtained with careful selection of time increments and mass scaling.

As it has been found that either the implicit or the explicit method can be used to simulate forming, this study uses ABAQUS/Standard finite element analysis software due to its ready availability. This software uses an implicit method to obtain a solution.

4.3 Development of constitutive material models

The first step in the development of the finite element simulation for the forming of FMLs is the development of constitutive material models. In this simulation it is required that the aluminium, both composites, and adhesive layers be modelled.

4.3.1 Constitutive Model for Aluminium Layer

The 5005-O aluminium used in this investigation was modelled as a rate-independent isotropic hardening plastic material with isotropic thermal properties. This was based on experiments conducted by Mosse [73]. The thermal conductivity and heat capacity of the aluminium are 200W/mK and 0.9J/g°C respectively. The lack of strain rate dependency is considered valid due to the use of the model at temperatures less than half the melting temperature and a low strain rate. The strain decomposition can therefore be expressed as:

$$\epsilon = \epsilon^{el} + \epsilon^{pl}. \tag{4.15}$$

The elastic response of the material is linear and isotropic and can therefore be represented using the bulk (K) and shear (G) moduli which are determined using Young's modulus and Poisson's ratio:

$$K = \frac{E}{3(1-2\nu)} \tag{4.16}$$

$$G = \frac{E}{2(1+\nu)}. \tag{4.17}$$

The modulus and Poisson's ratio for the aluminium were $69.8GPa$ and 0.3 respectively. The yield condition is given by,

$$q = \sigma^0 \tag{4.18}$$

	Thermal conductivity (W/mK)	Heat capacity (J/g°C)
SRPP	0.22	2
GRFP	0.35	1.3

Table 4.1: Thermal properties of the composite materials

where $\sigma^0\left(\bar{\varepsilon}^{pl}, \theta\right)$ is the stress as a function of the equivalent plastic strain $\left(\bar{\varepsilon}^{pl}\right)$ and temperature (θ), and q is the Mises equivalent stress. The stress of the aluminium can then be given as a tabular function of the equivalent plastic strain, where a plastic strain of zero refers to the yield point. This is provided in Appendix A.

4.3.2 Constitutive Model for Composite Layer

There are two composite materials which were considered in this study, the GFRP and the SRPP. The thermal properties for both of the materials can be described by their isotropic thermal conductivity and were derived using the rule of mixtures. However, for the SRPP, as it is 100% polypropylene, the material was modelled using the polypropylene thermal properties. The values used for simulation are shown in Table 4.1 . Due to the significant difference in material properties the mechanical models for the SRPP and the GFRP are considered separately. The basis for the model of both materials was decided to be an orthotropic material with the resulting stiffness matrix:

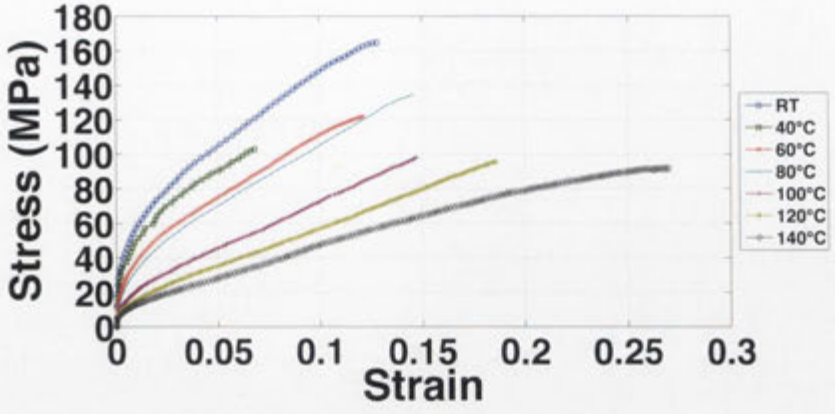

(a) Stress–strain behaviour for the SRPP composite

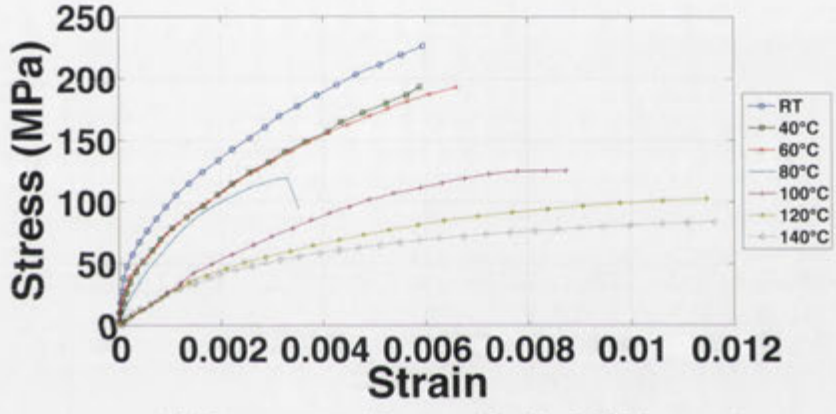

(b) Stress–strain behaviour for the GFRP composite

Figure 4.1: Stress–strain behaviour for the composite materials

$$\begin{bmatrix} \sigma_1 \\ \sigma_2 \\ \tau_{12} \end{bmatrix} = \begin{bmatrix} C_{11} & C_{12} & 0 \\ C_{12} & C_{22} & 0 \\ 0 & 0 & C_{33} \end{bmatrix} \begin{bmatrix} \epsilon_1 \\ \epsilon_2 \\ \gamma_{12} \end{bmatrix}. \tag{4.19}$$

The characterisation experiments described in Chapter 3 were used to obtain the stress–strain behaviour for the SRPP and GFRP composites at different temperatures. The stress–strain curves are shown in Figure 4.1. The most important finding of the characterisation experiments is that both the SRPP and

GFRP composites exhibit non-linear stress–strain behaviour. Previous studies have shown that the materials remain elastic at all strain values [73]. It is also shown that the stiffness of the materials decreases with increasing temperature. Hence, the models for the SRPP and GFRP were developed using a user-defined material subroutine (UMAT), implementing the tangent modulus method to define the instantaneous modulus of the material. Therefore, a two-part non-linear curve was determined to be the best model of the stress in the material as a function of strain. Matlab® was used to determine these equations and it was found for the SRPP composite that an exponential function, given in equation 4.20, best describes the stress–strain behaviour in the region $0 < \epsilon < 0.02$, and a straight line, given in equation 4.21, describes the subsequent behaviour. The equations are called the constitutive material equations:

$$\sigma = Ae^{B\epsilon} + Ce^{D\epsilon} \tag{4.20}$$

$$\sigma = Y\epsilon + H. \tag{4.21}$$

These equations were chosen as they provided an accurate representation of the stress–strain behaviour at each temperature. In addition, using the same equation for each temperature allowed the rapid determination of stress–strain behaviour at other temperatures, as the coefficients A, B, C, D, Y, and H are all dependent on temperature. Table 4.2 shows the coefficients for the constitu-

	A	B	C	D	Y	H
RT	40.46	31.02	-33.47	-908.3	883.24	51.4
40°C	35.08	31.08	-34.05	-897.6	799.79	48.6
60°C	27.02	33.42	-23.44	-509.8	714.42	37
80°C	24.02	32.74	-22.2	-403.5	707.01	31.7
100°C	15.03	33.54	-13.09	-418.4	546.61	17.6
120°C	10.91	35.65	-8.958	-551.7	444.33	12.81
140°C	9.073	34.45	-7.478	-633.5	296.74	11.63

Table 4.2: Coefficients for the constitutive material equations for the SRPP composite

tive equations at each temperature. It can be seen that no trend exists in the coefficients B and D which would provide a simple temperature relation. However, there is a negative trend for the coefficients A and Y with the trend in Y highlighting the reduction in stiffness, and a positive trend in the coefficient C. Therefore, a piecewise linear function, provided in equation 4.22, was used to determine the effect of temperature on each coefficient. This ensured that the coefficients used in Equations 4.20 and 4.21, which were determined by Matlab®, were used at each experimental temperature level and the interpolation is given by

$$\#\,(T) = P_1 T + P_2, \tag{4.22}$$

where # indicates the coefficients (A, B, C, D, Y, and H) from Equations 4.20 and 4.21, and P_1 and P_2 are the interpolation coefficients. These full equations (equation 4.22) are provided in Appendix B.

The stress–strain relationship for the GFRP shown in Figure 4.1 presented difficulties when attempting to use curve-fitting software with the two-part non-

	A	B	C	D
RT	116.6	115.8	-98.84	-1281
40°C	94.53	123.5	-84.02	-1061
60°C	-92.67	-896	104.3	97.42
80°C	-136	-641.6	140	-7.455
100°C	30680	-83.54	-30680	-82.64
120°C	79.99	24.73	-78.15	-332.3
140°C	-59.28	-498.5	59.47	31.52

Table 4.3: Coefficients for the constitutive material equations for the GFRP composite

linear functions. This is because the maximum strain is only 0.12%. Therefore, only equation 4.20 was required to describe the behaviour. The coefficients are again functions of temperature, with relationships according to equation 4.22. These coefficients are given in Table 4.3 and the effects of temperature are given in Appendix C.

These stress–strain equations are then used to calculate the tangent modulus of the material at each strain value according to equation 4.23.

$$E = \frac{d\sigma}{d\epsilon}|_{\epsilon=\epsilon_i} \tag{4.23}$$

This results in the stiffness of the material being described by equation 4.24 for the SRPP composite and equation 4.25 for the GFRP composite.

$$E = \begin{cases} ABe^{B\epsilon} + CDe^{D\epsilon} & \text{if } \epsilon \leq 0.02 \\ Y \end{cases} \tag{4.24}$$

$$E = ABe^{B\epsilon} + CDe^{D\epsilon}. \tag{4.25}$$

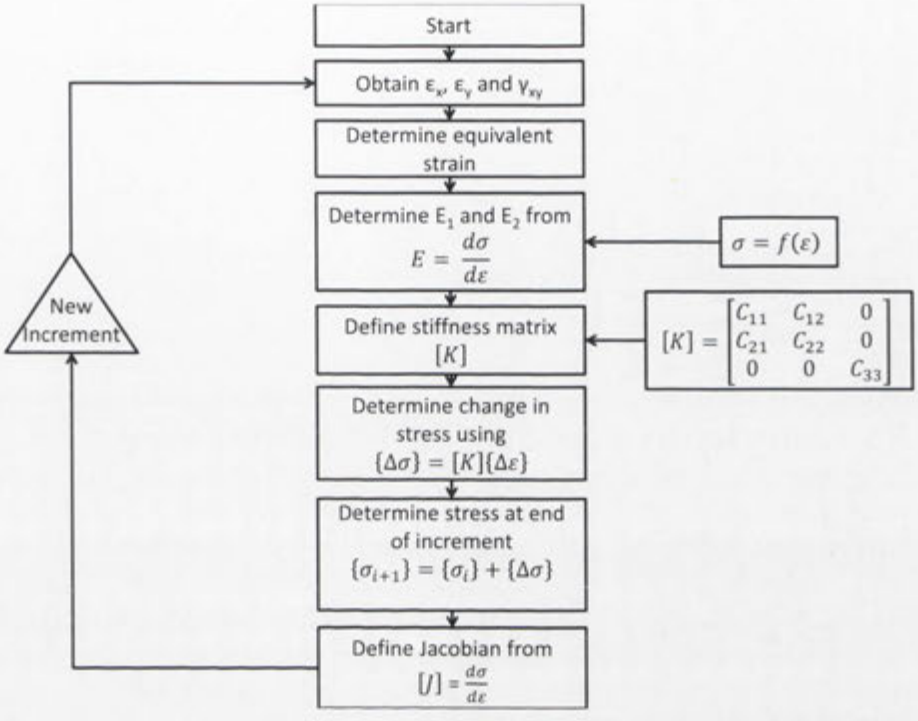

Figure 4.2: Flow chart for the composite constitutive model

The process for determining the mechanical response of the material in the user-defined material model is given in Figure 4.2. The strain in the element is obtained and substituted into equations 4.24 or 4.25 from which the stiffness of the material is calculated. This stiffness is then used to define the components of an orthotropic stiffness matrix as shown in equation 4.19, where

$$C_{11} = \frac{E_1}{1 - \nu_{12}^2}, C_{12} = \frac{E_1 \cdot \nu_{12}}{1 - \nu_{12}^2}, C_{22} = \frac{E_2}{1 - \nu_{12}^2}, \tag{4.26}$$

$$C_{33} = \frac{E}{2\,(1 + \nu_{12})}. \tag{4.27}$$

The change in stress over the increment and the stress at the end of the

increment is then determined using the tangent stiffness matrix. In order to increase the convergence rate the constitutive Jacobian is then specified using the relationship

$$[J] = \frac{d\sigma}{d\epsilon}. \tag{4.28}$$

4.3.3 Constitutive Model for Adhesive Layer

There were two constitutive models considered for the simulation of the adhesive layer. They were the perfect contact model and the friction model developed by Mosse [73, 97].

The friction model developed by Mosse [73, 97] assesses the interaction at every contact point between the two surfaces and assumes that no relative motion occurs between the two surfaces if the equivalent stress

$$\tau_{eq} = \sqrt{\tau_1^2 + \tau_2^2} \tag{4.29}$$

is less than the critical stress τ_{crit}. In the Coulomb friction model, the critical stress is either proportional to the contact pressure or, in the case of a critical stress limit, the limiting stress τ_{max}.

$$\tau_{crit} = \mu p$$

$$\tau_{crit} = min\left(\mu p, \tau_{max}\right)$$

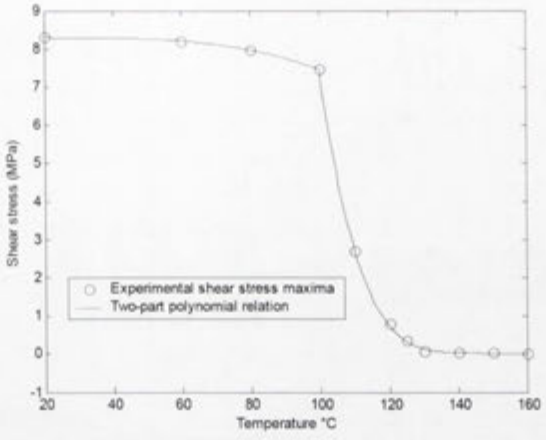

Figure 4.3: Effect of temperature on the shear stress limit [73]

If the equivalent stress is greater than or equal to the critical stress then slip occurs. Figure 4.3 shows the results obtained by Mosse on the effect of temperature on the shear strength of the adhesive between aluminium and the polypropylene based composites. A two-part function of temperature, given in Equation 4.30 and Equation 4.31, was then developed to allow the shear strength to be modelled for non-isothermal forming conditions.

$$\tau = \frac{-1}{457143}T^3 + \frac{3}{16000}T^2 - \frac{47}{8000}T + 8\frac{9}{25} \; for \; 0 \leq T \leq 100 \tag{4.30}$$

$$\tau = \frac{1}{570291}T^4 - \frac{16}{15647}T^3 + \frac{475}{2126}T^2 - 21\frac{83}{122}T + 788\frac{23}{51} \; for \; 100 < T \leq 130 \tag{4.31}$$

The analysis procedure for the constitutive adhesive model is described in Figure 4.4 . At the start of each increment the model checks if the bond has already been broken and, if so, the temperature at which the bond previously failed. If the previous failure occurred above 130^{o}C or failure has not occurred,

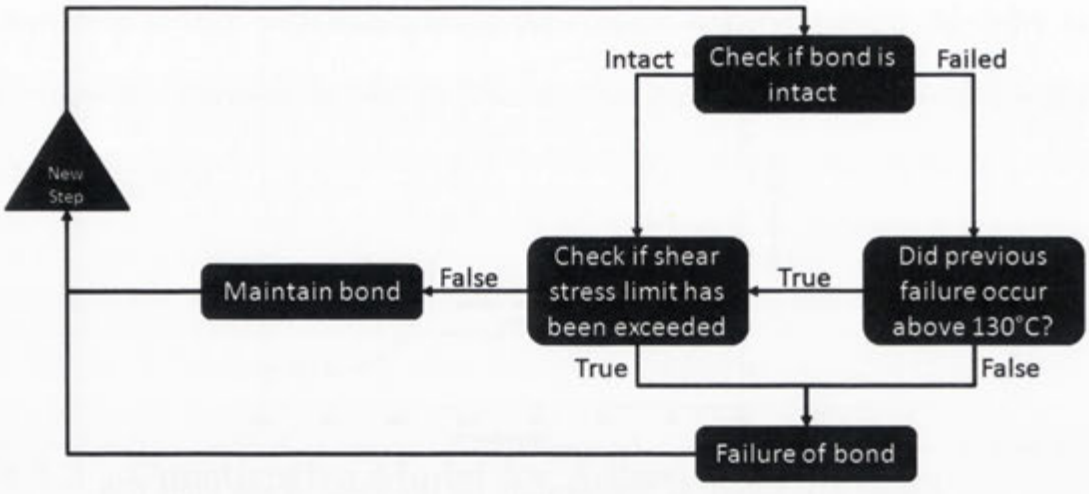

Figure 4.4: Flow chart for friction subroutine

then the bond is considered intact, the shear strength of the bond is calculated, and the bond is checked for its current condition. This provides the facility that if failure occurs above the adhesive melting temperature of the adhesive then the bond between the layers can be reformed. If the equivalent stress does not exceed the critical stress then no relative motion occurs; however if the equivalent stress exceeds the critical stress then the layers are free to slide over each other.

The perfect contact model assumes that there is no sliding between the layers in contact. This is implemented using the "rough" contact model in ABAQUS which allows no relative motion between two layers in contact. This effectively sets the friction coefficient to infinity, that is, $\mu = \infty$. This model and the Mosse model provide the same effect if the adhesive bond remains unbroken.

Similarly to the contact with the tools, the normal contact between the layers of the FML are considered to be hard contact, with the prevention of separation after initial contact in either case.

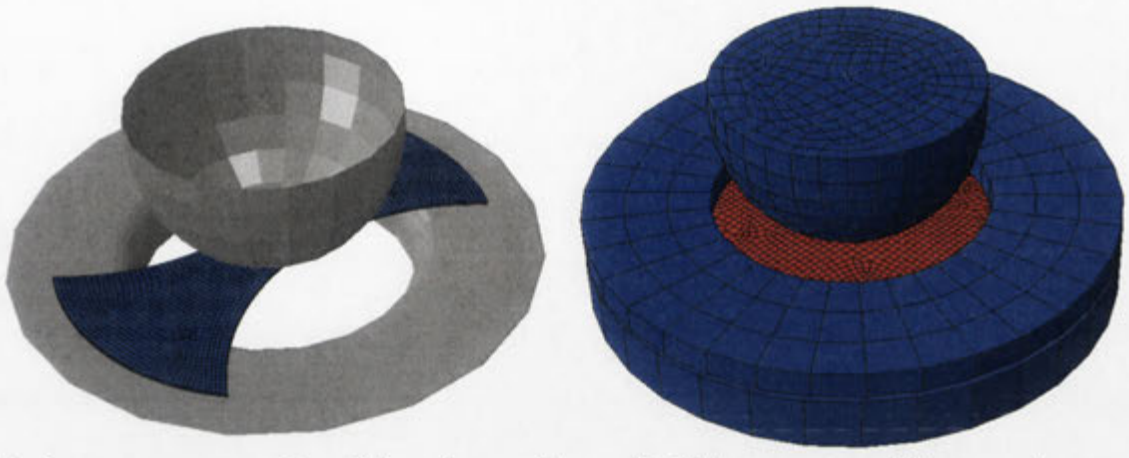

(a) Room temperature 25mmHG specimen with blankholder omitted

(b) High temperature 200mm specimen

Figure 4.5: FEA models used for simulation

4.4 Simulation Procedure

The setup of the models used to simulate the forming of the FML systems in ABAQUS/Standard is shown in Figure 4.5. Figure 4.5(a) shows the modelling of the room temperature forming where the tools, comprised of punch, blankholder, and die are modelled as analytical rigid bodies due to the model only requiring mechanical analysis. Analylitcal rigid bodies do not contain elements and can accurately represent geometries with increased computational efficiency [109]. At high temperatures, shown in Figure 4.5(b), the tools are modelled using deformable 3D elements with a rigid body constraint (the mesh size was determined automatically by the software to accurately represent the geometry of the tools). This means that structural calculations are ignored for all of the elements in the tools and that the elements can only translate as a rigid body in accordance with the part's reference point. Using this method, the tools still require mechanical

properties to be assigned, which are essential for contact stiffness calculations between the tools and the specimens. This modelling technique, however, allows the application of thermal boundary conditions to the tools and heat transfer, conditions which were not available when using analytical rigid surfaces or discrete rigid bodies.

The element type chosen to model the experimental specimen was the shell. The ABAQUS/Standard FE software uses a shell element called S4 or S4R, meaning a 4-node shell element with reduced integration (when the R designation is used).

The thermal properties in the FE simulation are set up in two ways: for the tools there is an isothermal temperature and for the FML layers a predefined field is used. These boundary conditions are used to allow the change in temperature in the specimen but to reduce calculation difficulty. The tools are modelled as isothermal because the tools used in the experiments are manufactured from steel and have a much greater mass than the experimental specimens; therefore, no appreciable temperature rise will occur in the tools during the short forming operation. The punch was set to a temperature of 20°C to simulate room temperature and the die and blankholder were set to the same temperature as the specimen.

The dimensions of the tools were taken from Figure 3.6 to accurately reflect the experimental forming procedure. The mesh of these bodies was designed to allow the accurate representation of the tool geometry, with a finer mesh being

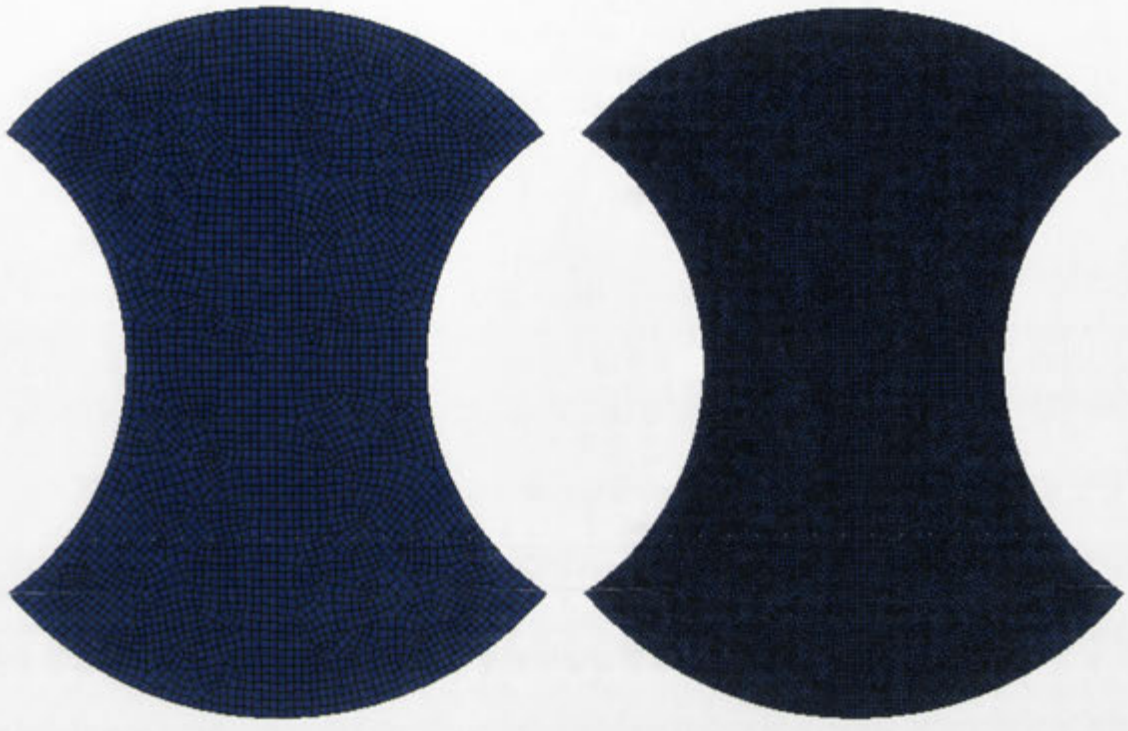

(a) Aluminium layer (b) Composite layer

Figure 4.6: Typical finite element model mesh

used around the curved surfaces. The aluminium and composite were modelled as three layers of shell elements meshed using S4R elements. Individual shell layers were used so that the material characteristics of the composite and the aluminium could be accurately represented. A typical meshing of the finite element model is illustrated in Figure 4.6. The mesh used to represent the composite layer is more refined than the aluminium layer due to the lower stiffness in the composite layer, which means it will act as the slave surface when in contact with both the top and bottom aluminium layers. The maximum element size for the aluminium layer was 2mm by 2mm and for the composite layer it was 1mm by 1mm. The layers were also partitioned to allow easier selection of regions of interest (such

Part	Number of elements
25mmHG composite layer	9453
25mmHG aluminium layers	2266
70mmHG composite layer	17036
70mmHG aluminium layers	4162
200mm composite layer	11127
200mm aluminium layers	3005

Table 4.4: Number of elements in the simulated specimens

as the pole and meridian) and to provide a more regular mesh. The number of elements used to simulate the specimens is shown in Table 4.4.

The contact between the tools and the specimen was modelled using surface-to-surface contact with finite sliding allowed between the surfaces. The surface-to-surface contact discretisation was used because it provided more accurate stress and pressure results than a node-to-surface discretisation, primarily because the surface-to-surface contact resists penetration over an average region near slave surface nodes compared to only considering penetration at the node. In addition, the surface-to-surface contact allows for double-sided contact, which is a requirement for all of the contact entities in a forming simulation. The Coulomb friction model used to describe the sliding behaviour is discussed in Section 4.3.3. The contact pressure between the tools and the specimen was defined as hard contact with separation allowed after the initial contact; that is,

$$\begin{aligned} p &= 0 \qquad \text{for } h < 0 \qquad \text{(open)} \\ h &= 0 \qquad \text{for } p > 0 \qquad \text{(closed)}, \end{aligned} \tag{4.32}$$

where p is the contact pressure between the surfaces and h is the "overclosure"

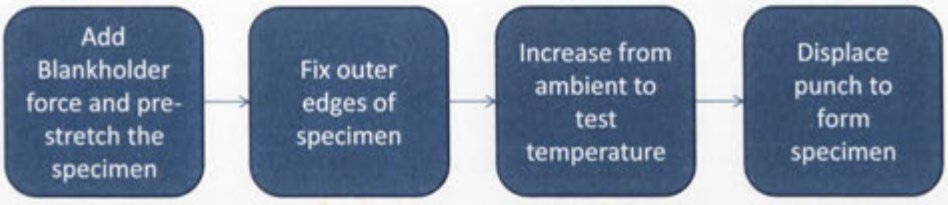

Figure 4.7: Analysis procedure for the FE simulation

of the surfaces. The thermal properties for the transfer of heat between the surfaces in contact was taken from experiments and simulations conducted by Mosse [73]. The gap conductance, the coefficient of thermal conduction between two surfaces in contact, was modelled as a clearance-dependent variable: that is, 0 for clearances over 0.05mm and 0.08W/mK for clearances below 0.05mm.

The analysis procedure used for the simulation follows the experimental procedure. First, the blankholder force and initial stretching of the specimen caused by the lock ring is applied, then the outer edges of the specimen are fixed, the specimen is then heated, and finally the punch is displaced. The procedure for analysis is shown in Figure 4.7. The method used to model the lock ring was to model the specimens to the middle of the lock ring (that is, each specimen had a radius of 82.5mm rather than the 100mm radius of the physical specimens) and fix the outer edges in all degrees of freedom. The stretch induced by the lock ring is modelled using a shell edge load which is applied perpendicular to the edge of each layer in the model, with the magnitude of the load being determined by matching the resulting surface strain with the experimental results. To ensure that the specimen layers maintained interaction during the pre-stretch process, a friction coefficient was specified between the layers. The heating of the specimen

was a more difficult endeavour due to the thermal expansion of both the specimen and the tools and the differences in the expansion coefficients. It was also found in the experiments that the specimens experienced a positive strain increase, probably due to the expansion of the blankholder and die which increased the strain in the specimens. The punch displacement and time-step were matched such that the final displacement of the punch matched that obtained in the experiments and the feed rate was 10mm/s.

4.5 Summary

This chapter outlined the justification for using the chosen simulation procedure and software, outlined how the simulation was designed, and detailed the development of the constitutive models required to model the forming of a fibre–metal laminate. The model used for simulation considers the effect of temperature on the mechanical properties of the constituent materials, their interactions, and the change in specimen temperature as a consequence of the forming process. An implicit formulation is used to ensure the stability and accuracy of the results obtained in the simulation for direct comparison with experimental results.

Chapter 5

Isothermal Stretch Forming of an SRPP-based Fibre–Metal Laminate

5.1 Introduction

This chapter details the stretch forming of a fibre–metal laminate based on a self-reinforced polypropylene composite and analyses the effect of deformation mode on the formability of the laminate. The chapter consists of two sections, the experimental work and the finite element simulation of the experiments. The formability of the SRPP FML is assessed under isothermal conditions using 14 specimens, comprised of two different specimen geometries (hourglass and rectangular), according to the parameters outlined in Chapter 3. These experiments were assessed at room temperature to discover the effect of specimen geometry on the forming mode and to provide information about the general forming behaviour of the laminate. Several aspects of the experimentally formed FML specimens were analysed and compared to the results of monolithic aluminium to extract the forming behaviour, which includes:

- the evolution of strain as a function of forming depth at two selected regions

on the surface of the specimens,

- the general strain behaviour over the entire surface of the specimens including the state of strain for all points at various forming depths,
- assessment of the strain along the longitudinal axis of the specimens,
- the determination of the forming limits for the SRPP FML, and, finally,
- using the bending strain relation to determine the behaviour of the sub-surface layers.

These results will provide a comprehensive description of the forming behaviour of the SRPP FML at room temperature.

Secondly, the experimental geometries were modelled using ABAQUS/Standard as outlined in Chapter 4. In this section the FE simulation was verified and the sub-surface behaviour analysed to determine the behaviour of those layers which are not visible to the ARAMIS strain measurement system.

5.2 Experimental work

5.2.1 Effect of the lock ring

The blankholder force is applied to each specimen prior to the forming process which, due to the nature of the lock ring, causes each specimen to experience a "pre-stretch". This pre-stretch appears not only as an induced strain on the surface of the specimen but also as a slight alteration of the specimen geometry

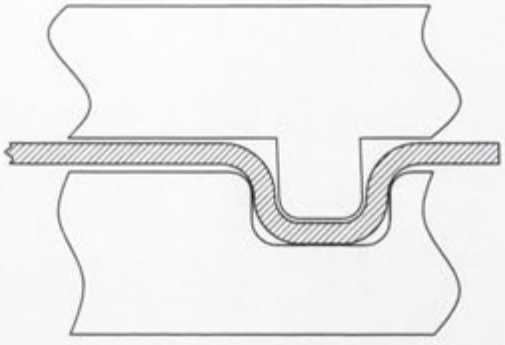

Figure 5.1: Deformation of material into the lock ring

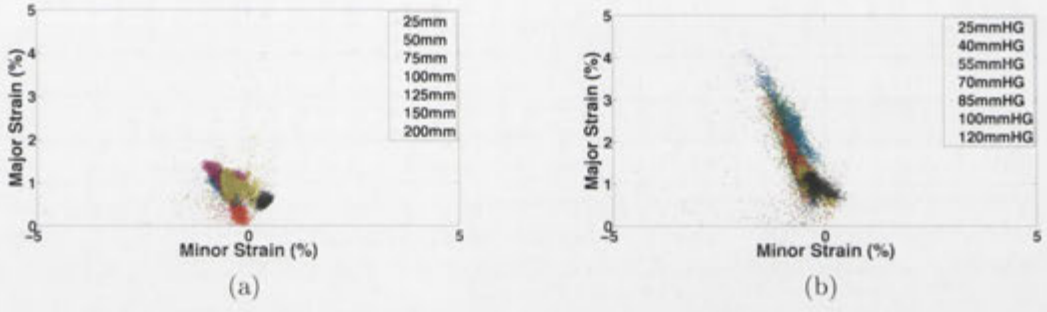

(a) (b)

Figure 5.2: The effect of the lock ring on the surface strain for the rectangular (a) and hourglass (b) geometries

prior to forming; it is caused by the lock ring used to secure the specimens against draw during forming. As the blankholder force is increased the specimen is forced to deform into the lock ring, shown in Figure 5.1, causing stretching of the specimen. This data was captured by taking an image with the optical strain measurement system before and after the application of blankholder force and the securing of the lock ring.

Figure 5.2 shows the results of the strain calculations for the effect of the lock ring on the experimental geometries. These figures are the FLD for the specimens at this stage and show the state of major and minor strain for every

point on the surface of the experimental specimens. All geometries experienced approximately the same effect from the lock ring. It can be seen that the lock ring applies a small positive increase in major strain and a generally negative increase in minor strain. The difference in the "pre-stretch" behaviour of the rectangular and hourglass specimens is entirely a consequence of the specimen geometry. The rectangular specimens exhibit a clustered strain behaviour because at this stage of the process there is only an apparent pulling on either edge of the specimen causing the specimen to elongate in one direction only and therefore a fairly uniform state of strain. However, because of the tapered shape of the hourglass specimens, the thinner centres of the specimens experience a higher state of strain than the wider regions closer to the die edge. The strain ratio for the "pre-stretch" in the thinner specimens, for both specimen types, is approximately 0.3. The larger blanks such as the 100mmHG, 120mmHG, 150mm and 200mm specimens experience deformation akin to plane strain and biaxial stretch due to lateral directions being constrained or stretched.

Care had to be taken with the smaller specimens, such as the 25, 50, 75 and 100mm rectangular specimens, to prevent the pre-stretch from causing premature failure. Figure 5.3 shows the failure of a 100mm rectangular specimen at the lock ring. In addition to the failure shown in Figure 5.3, the lock ring on the other side had also induced tearing in the specimen, that is, it failed at both ends. Although not as significant, the blankholder force in the hourglass specimen also had to be carefully controlled. For example, if a high blankholder force was used with the

Figure 5.3: Failure of a rectangular specimen due to lock ring

25mmHG specimens, tearing in the centre of the specimen initiated due to the increase in strain. This effect is assessed because it is present in all specimens and must be accounted for when analysing the strain state and modelling the forming behaviour.

5.2.2 Evolution of strain in selected regions

In this study, prior to the analysis of the strain behaviour of the entire surface of the specimen, two regions of interest were selected to provide detailed local deformation behaviour of the specimens. These regions are

- the pole region, and
- the failure region.

These two regions were selected because they exhibit forming behaviour of significant interest for the assessment of formability and their comparability to previous studies. The pole region is the centre of the specimen, the point of initial contact with the punch and experiences the largest forming depth. The failure region is the region in which failure occurs in the specimen and can provide detailed

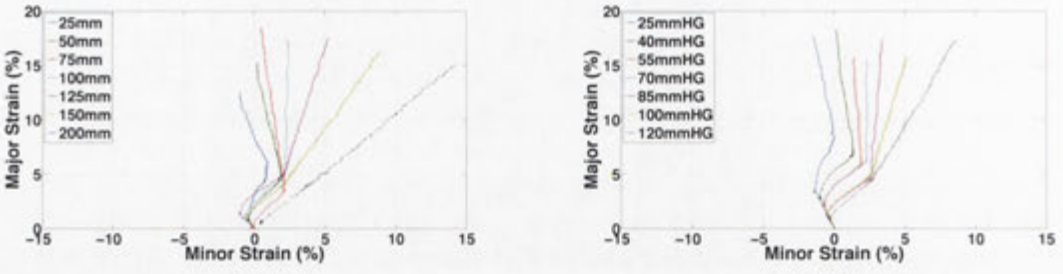

(a) (b)

Figure 5.4: Evolution of strain in the pole region for the rectangular (a) and hourglass (b) geometries

information about the conditions required for failure.

5.2.2.1 Pole region

Figure 5.4 shows on a forming limit diagram (FLD) the evolution of surface strain at the pole of both the rectangular and hourglass experimental specimens. The points on each line correspond to the state of strain at increasing forming depths. These figures illustrate the idea that by altering the geometry of the specimen it is possible to obtain different deformation modes. Figures 5.4 and 5.5 also show that, in both the FML and aluminium specimens, three separate deformation behaviours occur: pre-stretch, biaxial deformation, and proportional loading. The initial region is characterised by the effect of the lock ring on the surface strain of the specimen, which is discussed in the preceding section.

The biaxial deformation is caused by the shape of the punch. The hemispherical punch begins to deform only the pole region of the specimen which leads to that region experiencing biaxial stretch. This behaviour disappears as soon as the reduced specimen width in the lateral direction and the lower lateral con-

Specimen	25mm	50mm	75mm	100mm	125mm	150mm	200mm
Strain ratio (β)	-0.08	0.01	0.22	0.13	0.30	0.55	0.95

(a)

Specimen	25mmHG	40mmHG	55mmHG	70mmHG	85mmHG	100mmHG	120mmHG
Strain ratio (β)	-0.08	0.01	0.1	0.15	0.2	0.33	0.5

(b)

Table 5.1: Strain ratio of the experimental rectangular (a) and hourglass (b) specimens using only the strain at the failure depth

straint retards stretch in that direction, at which point material in this direction is permitted to partially draw into the die (depending on the specimen geometry; the 200mm specimen obviously maintains biaxial stretch). The final behaviour observed depends on the geometry, and leads to a continuous strain path in which the ratio of major and minor strain can be used to determine the deformation mode.

A specimen's deformation mode in the final strain behaviour region can be calculated using two methods. Firstly, if only the strain state at the final stage of deformation (the failure depth) is considered, as is the case when primitive methods such as circle grid analysis (CGA) are used, then the strain ratio, and therefore the deformation mode, of the specimen is shown in Table 5.1. These values ignore the evolution of strain at the pole prior to failure, which showed a consistent ratio between the major and minor strain. The strain ratios calculated based on the evolution of strain in this region, which follows a straight line, are shown in Table 5.2. This shows that the specimens exhibit deformation from uniaxial tensions to biaxial stretching at the pole.

Specimen	25mm	50mm	75mm	100mm	125mm	150mm	200mm
Strain ratio (β)	-0.31	-0.16	-0.11	0.01	0.26	0.56	0.94

(a)

Specimen	25mmHG	40mmHG	55mmHG	70mmHG	85mmHG	100mmHG	120mmHG
Strain ratio (β)	-0.15	-0.1	-0.05	0	0.06	0.23	0.46

(b)

Table 5.2: Strain ratios for the rectangular (a) and hourglass (b) geometries using the evolution of strain

Table 5.2 shows that the 25mm and 25mmHG specimens can be used to approximate uniaxial tension, the 100mm and 70mmHG specimens show the plane strain deformation mode, and the 200mm specimen exhibits biaxial stretch deformation. The data presented in Table 5.2 is useful because it shows that the forming limits for the SRPP FML can be determined over the full range of deformation modes from uniaxial tension to balanced biaxial stretch. It also leads to the important finding that there is significant overlap of the strain ratios for the 14 hourglass and rectangular specimens. This means that fewer specimens for analysis at higher temperatures need to be selected. The specimens selected for analysis at high temperatures, and the preferred specimens for more detailed analysis in this chapter, include the 25mmHG, 40mmHG, 70mmHG, 150mm and 200mm specimens. These were chosen because they exhibit a wide variety of deformation modes between uniaxial tension and biaxial stretch.

Figure 5.5 shows the evolution of the major and minor strain in monolithic aluminium specimens. These figures show that, even though the final major strain in the aluminium is generally lower compared to SRPP FML, the strain

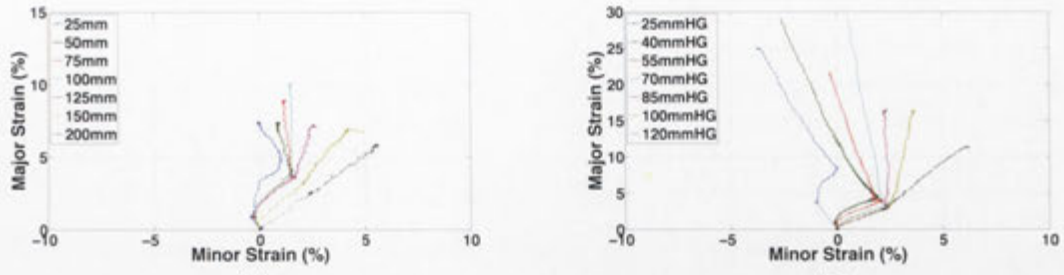

(a) (b)

Figure 5.5: Evolution of strain for aluminium specimens in the pole region for the rectangular (a) and hourglass (b) geometries

Specimen	25mm	50mm	75mm	100mm	125mm	150mm	200mm
Strain ratio (β)	-0.43	-0.2	-0.07	0	0.27	0.6	1

(a)

Specimen	25mmHG	40mmHG	55mmHG	70mmHG	85mmHG	100mmHG	120mmHG
Strain ratio (β)	-0.22	-0.16	-0.12	-0.06	0	0.09	0.45

(b)

Table 5.3: Strain ratios for the aluminium rectangular (a) and hourglass (b) geometries using the evolution of strain

behaviour of the SRPP FML is very similar to the monolithic aluminium. The monolithic aluminium specimens also show the three deformation behaviours: pre-stretch, biaxial deformation, and a strain path to failure. Table 5.3 shows the strain ratios of the aluminium specimens for the final behaviour, calculated using the evolution of strain, and it can be seen that the SRPP FML strain ratios agree well with the aluminium specimens. However, the 25mm aluminium specimen shows a more negative strain ratio, closer to the ratio of –0.5 expected of an ideal uniaxial tension specimen, and there is a difference in the hourglass specimens where the aluminium specimens are again more negative than the SRPP FML specimens. These results show the validity of using specimens of different width

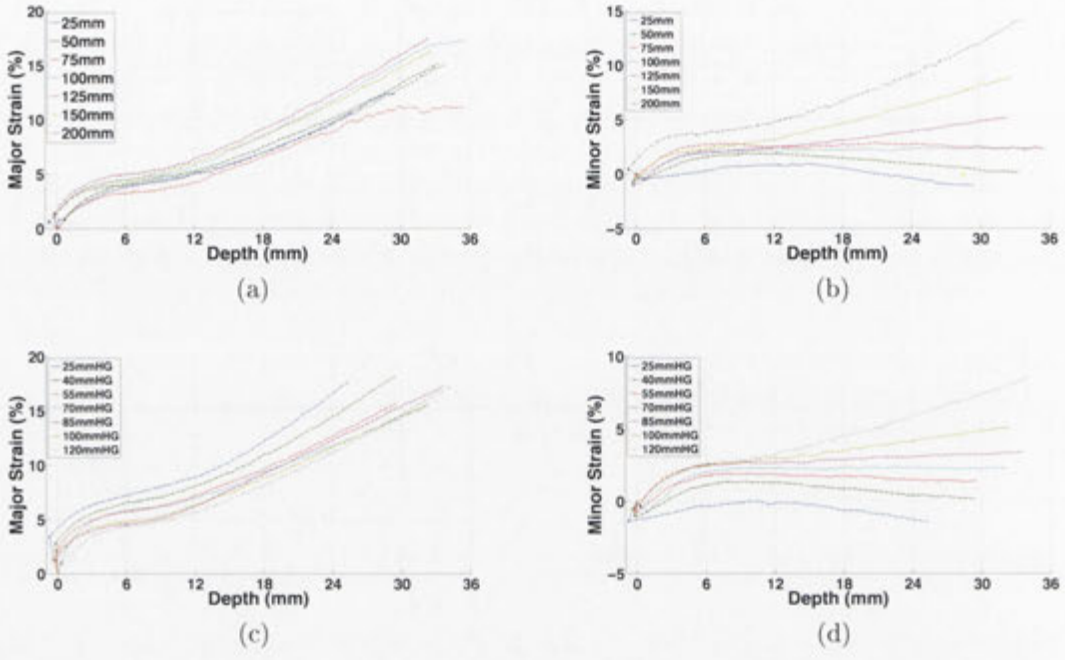

Figure 5.6: Evolution with forming depth of major (a) and minor (b) strain at the pole of the rectangular specimens, and evolution of major (c) and minor (d) strain at the pole of the hourglass specimens

to elicit the various deformation behaviours – in not only metals but also in more advanced materials such as FMLs. The difference in the major strain magnitude between the aluminium and FML specimens is due to the forming behaviour of the FML compared to the aluminium; this will be discussed further in subsequent sections of this chapter.

Figure 5.6 shows the evolution with forming depth of the major and minor strain in the FML specimens. These figures display the effect of specimen geometry on strain ratio. It can be seen that the evolution of major strain in all specimen geometries is similar, but that the difference in strain ratio and therefore deformation behaviour is caused by the evolution of the minor strain. The initial evolution of the minor strain mimics the major strain behaviour until the

lateral constraint causes a change, with the larger specimens experiencing some restriction in movement in the lateral direction, thus creating more positive minor strain values. The figures also show that the hourglass specimens show a trend in how the major strain magnitude evolves. In contrast to the rectangular specimens, the hourglass specimens show, with increasing blank width, a decrease in the magnitude of major strain at the pole of the specimen. In addition, the hourglass specimens show increased major strain values compared to rectangular specimens of similar width at equivalent depths.

The major and minor strain are equivalent to the first and second principal strains and are therefore comprised of the strains in the longitudinal (ϵ_y), lateral (ϵ_x), and shear strains (ϵ_{xy}) at each point. The composition of strain at each point is an important indication of what underlying deformation the composite is experiencing. It has been shown in previous studies that, when the fibre directions are aligned with the x and y axes, the longitudinal and lateral strains represent strains along the fibre, while shear strains are the result of matrix deformation and fibre trellising. These studies also found that it is possible for composites to have larger forming depths if the material is permitted to undergo large amounts of shear deformation. Figure 5.7 shows the evolution of these strains at the pole of the uniaxial tension, plane strain, and biaxial stretch FML specimens. The figures show that the major strain evolution at the pole corresponds to the longitudinal strain (ϵ_y) (or ϵ_x in the 200mm case as ϵ_x and ϵ_y are similar), which is the strain along the fibres in the composite layer. In addition, the nature of the specimen

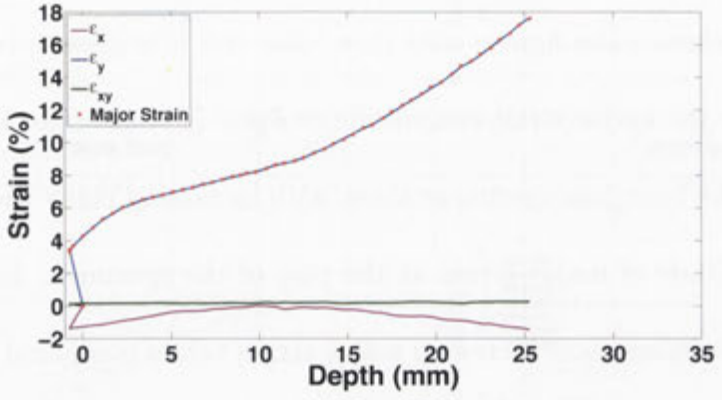

(a) 25mmHG

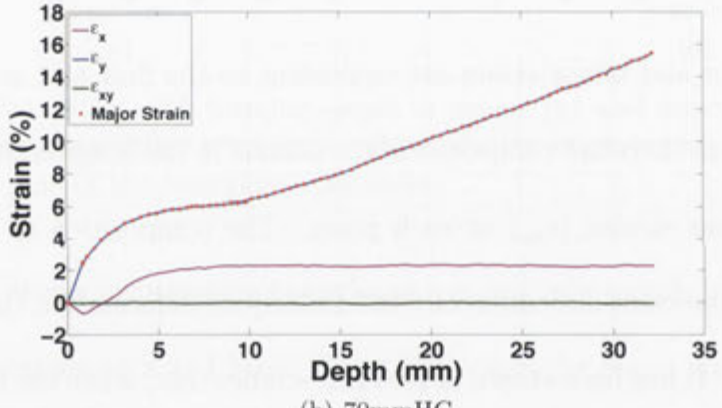

(b) 70mmHG

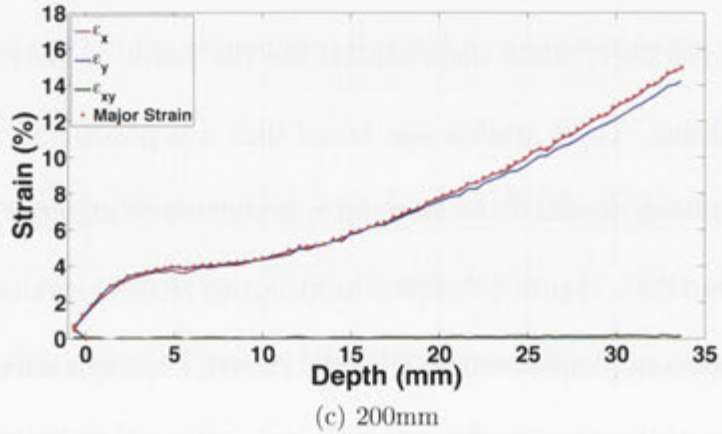

(c) 200mm

Figure 5.7: Evolution of longitudinal, lateral, and shear strain at the pole

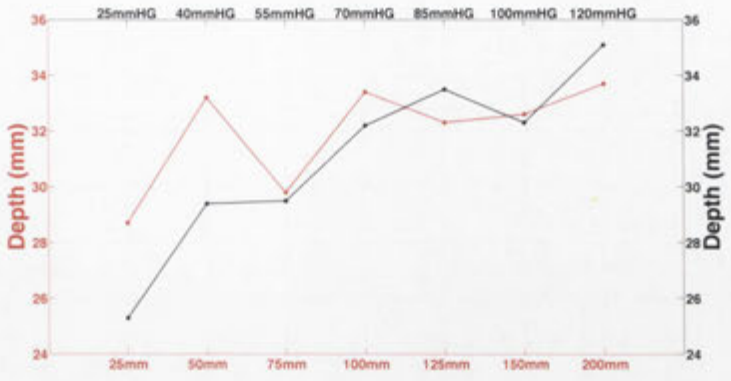

Figure 5.8: Failure depths in the experimental specimens. Hourglass specimens are shown in black and the rectangular specimens are shown in red.

geometry ensures that elongation occurs along this axis. This figures also show that the pole experiences no shear strain.

5.2.2.2 Failure region

The region of failure in formed specimens is primarily determined by the region of highest strain. In some cases, the failure of the experimental specimens occurs in the unsupported region, the region between the punch and the die. The evolution of the strain in this region can be markedly different from the behaviour at the pole. Failure occurs in this region for one reason only, friction between the tools and the experimental specimen. As discussed in the literature review, in the absence of friction, the highest strain and therefore failure will occur in the centre of the specimen. This is particularly applicable to the hourglass specimens where not only will symmetry cause high strain at the pole but the reduced width will also lead to higher stresses. The depth of failure for the experimental specimens is shown in Figure 5.8. This figure shows a clear trend in the hourglass specimens

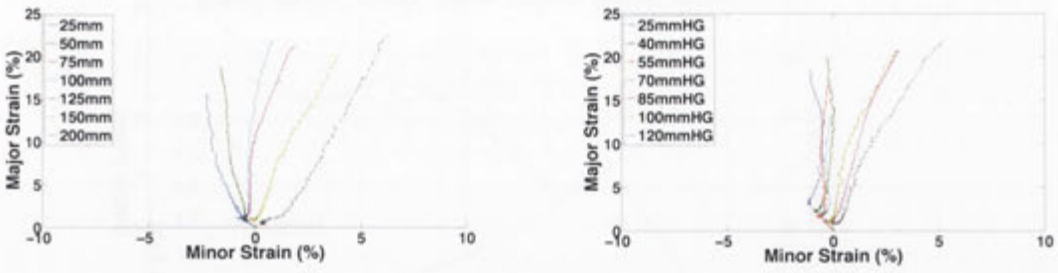

(a) (b)

Figure 5.9: Evolution of strain at the failure region for the rectangular (a) and hourglass (b) geometries

towards an increased failure depth in the larger specimens. The rectangular specimens show no trend in failure depth in the smaller specimens, with a transition to the expected behaviour in the 125mm and larger specimens. The difference between the specimens of widths 100mm and below and the larger specimens is that the former fail at the lock ring and the latter in the visible region. This implies that the smaller rectangular specimens are beginning to fail at the lock ring with no noticeable effect on the strain evolution at the pole, except for the 75mm specimen which shows a plateau in the major strain evolution in Figure 5.6(a). It is not necessary, however, for a trend to exist in the failure depth of the specimens. Because the effect of the specimen geometry is to induce different deformation behaviour in the material, it is entirely possible that different failure depths may occur for different deformation modes, such as the rapid failure of metals in plane strain.

Figure 5.9 shows the evolution of strain in the regions of failure of the experimental specimens. It was difficult to observe the region of failure in some of the thinner rectangular specimens, such as the 25mm through to the 100mm

Specimen	25mm	50mm	75mm	100mm	125mm	150mm	200mm
Strain ratio (β)	N/A	N/A	N/A	N/A	0.18	0.22	0.23

(a)

Specimen	25mmHG	40mmHG	55mmHG	70mmHG	85mmHG	100mmHG	120mmHG
Strain ratio (β)	0.03	0.04	0.01	0.01	0.16	0.15	0.23

(b)

Table 5.4: Strain ratios in the failure region for the rectangular (a) and hourglass (b) geometries using the evolution of strain

specimens. Therefore, the analysed region of these specimens in Figure 5.9 occurs at a distance of 25mm from the pole, midway between the pole and die, which should see the most rapid increase in strain. There is also evidence of the effect of deformation mode on the failure of the specimen by looking at Figures 5.9(a) and 5.9(b) where certain specimens experience different magnitudes of major strain at failure which vary depending on the strain ratio. Table 5.4 shows the strain ratio of the FML specimens and it can be seen that, compared to the strain ratio of the pole, for all geometries (excluding the thin rectangular ones, which did not exhibit visible failure, and the 85mmHG specimen) the failure region experiences a deformation mode more closely associated with plane strain, where the minor strain experiences a low or nil increase/decrease. This aligns with the theory of metal forming that metals will fail quicker in plane strain than any other forming mode. This is especially apparent in the 70mmHG specimen which experiences the largest proportion of plane strain deformation.

Figure 5.10 shows the strain path evolution of the aluminium specimens. It is obvious from these figures that the failure behaviour of the materials is signifi-

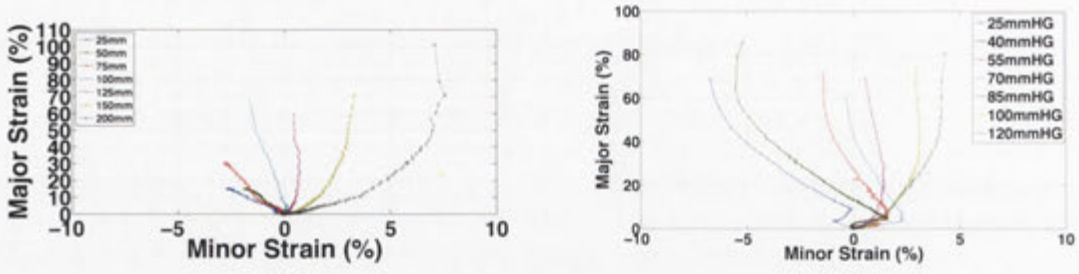

(a) (b)

Figure 5.10: Evolution of strain at the failure region for the rectangular (a) and hourglass (b) geometries

cantly different. The aluminium seems to be able to withstand higher strains than the SRPP FML before a visible through-thickness tear appears in the specimen. However, the failure in the FML specimens appeared as rapid fracture of all three layers without any prior indication of proximity to failure (such as the formation of a localised neck), whereas the failure of the aluminium involved the formation of a localised neck with subsequent thinning and a rapid increase in strain until failure. In fact, the reason that the strain at the pole in the aluminium (Figure 5.5) is lower than the equivalent SRPP FML specimens (Figure 5.4) is because the failure region in the aluminium has formed a localised neck and all other regions have ceased deformation. The lack of a localised neck in the SRPP FML specimens is an indication of improved formability as it shows that no region of the specimen is preferentially deforming compared to other regions and therefore leads to a more uniform strain distribution in the specimen. However, the sudden failure of all layers simultaneously along the fibre direction indicates fracture of the composite fibres as the initiator of failure.

Figure 5.11 shows the evolution of strain at the two regions of interest in the

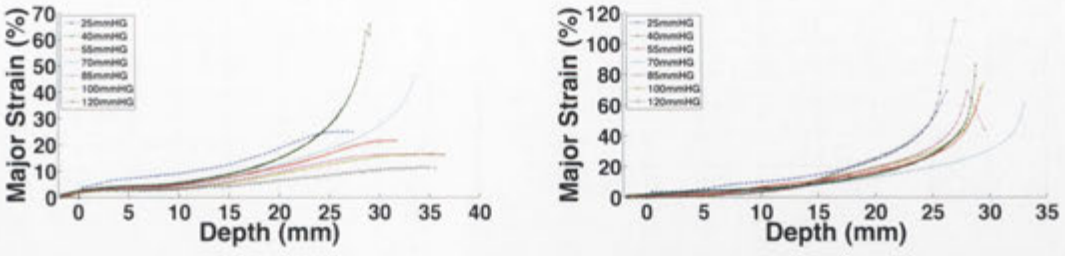

(a) (b)

Figure 5.11: Evolution of the major strain at the pole (a) and failure (b) region for the aluminium hourglass specimens as a function of forming depth

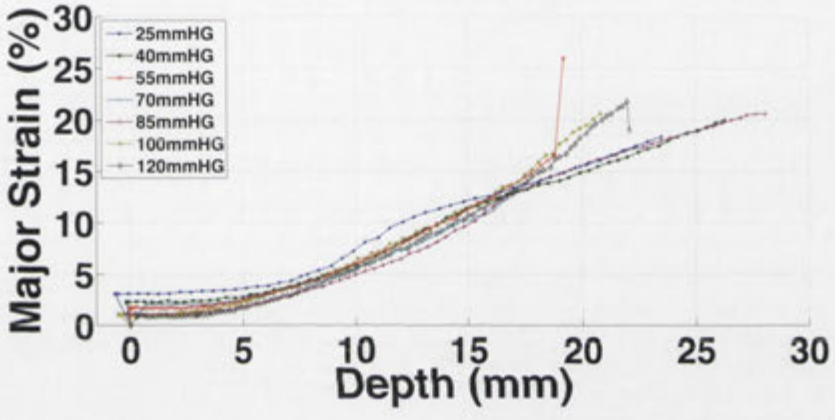

Figure 5.12: Evolution of the major strain in the failure region of the SRPP FML hourglass specimens as a function of forming depth

aluminium hourglass specimens as a function of depth. It can be seen that the major strain in the failure region, shown in Figure 5.11, exhibits an exponential increase in strain as the forming depth increases, whereas a plateau occurs at the pole. Two specimens do not show this behaviour, the 40mmHG and the 70mmHG; this is because the failure region occurs at, or in close proximity to, the pole which means that the pole and failure region coincide. When this is compared to the strain at the pole and failure regions in the SRPP FML hourglass specimens, shown in Figures 5.6(c) and 5.12 respectively, it can be seen that the FML does not exhibit the plateau at the pole nor the exponential increase at the region

of failure, which further demonstrates the improved distribution of strain in the FML specimens.

Figure 5.13 shows the composition of the major and minor strain and the evolution of the lateral, longitudinal, and shear strains in the region of failure of the uniaxial tension, plane strain, and biaxial stretch specimens respectively. Due to the lack of shear strain in the failure region, primarily because it occurs in the fibre direction, the major and minor strain are again the same as the longitudinal and lateral strain, meaning that the maximum extension of the fibres is the limiting factor in the formability of the laminate. A recent study by Zanjani and Kalyanasundaram [102] found that the failure strain and depth of a SRPP composite was greatly improved by orienting the fibres at 45° to the longitudinal direction. The figure shows that, unlike the 25mmHG and 70mmHG, the 200mm specimen has the major strain in the lateral direction. This is caused by the biaxial nature of the 200mm specimen which introduces the possibility of failure in either the lateral or longitudinal directions.

5.2.3 Surface strain behaviour

The surface strain contours for the experimental rectangular specimens corresponding to uniaxial tension, plane strain, and biaxial stretch, as identified in Table 5.2, are shown in Figure 5.14 and Figure 5.15. This figure shows the strain contours for the 25mm, 100mm, and 200mm FML specimens at 10mm depth increments. It can be seen from the figure that the optical measurement system

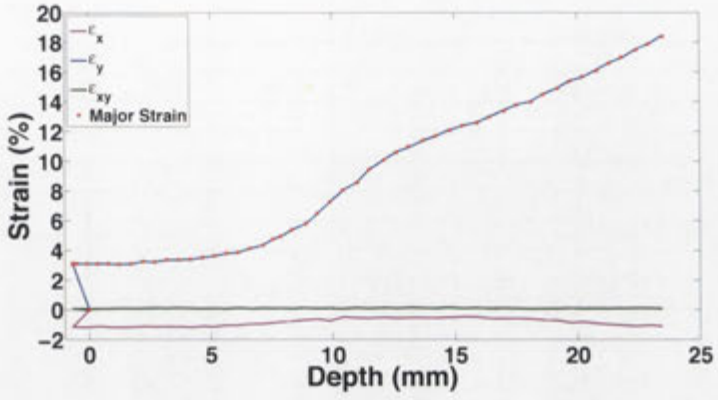

(a) 25mmHG

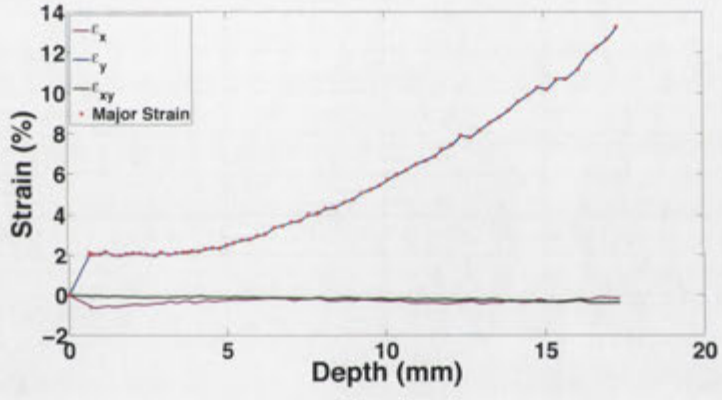

(b) 70mmHG

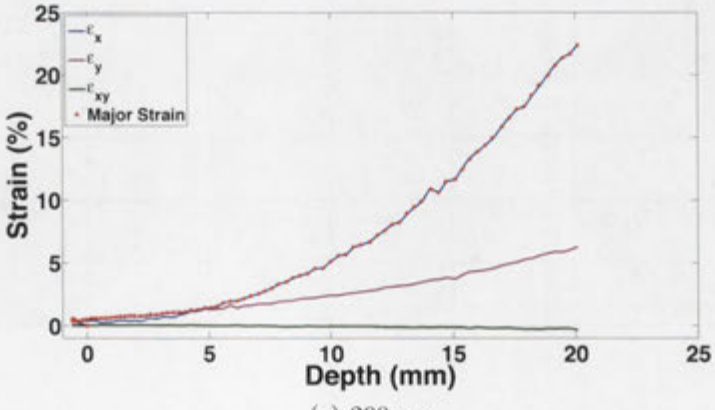

(c) 200mm

Figure 5.13: Evolution of longitudinal, lateral, and shear strain in the failure region

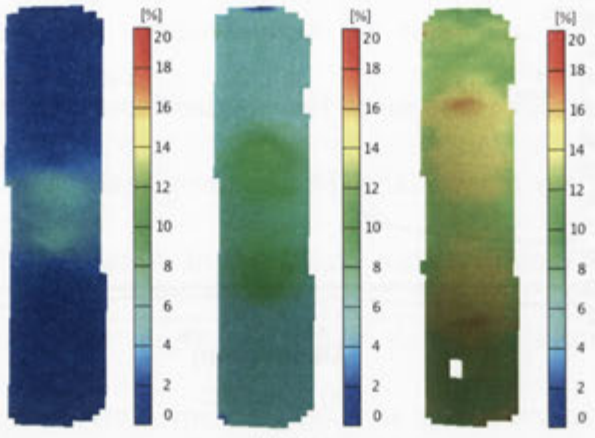

(a) 25mm

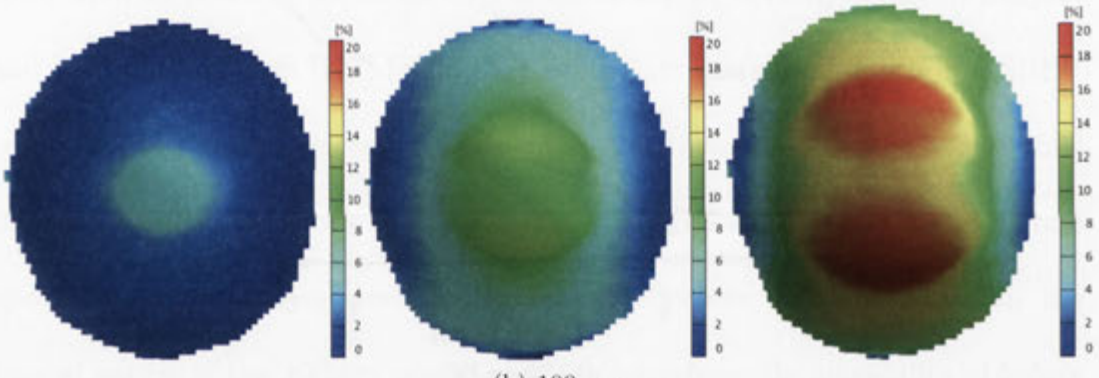

(b) 100mm

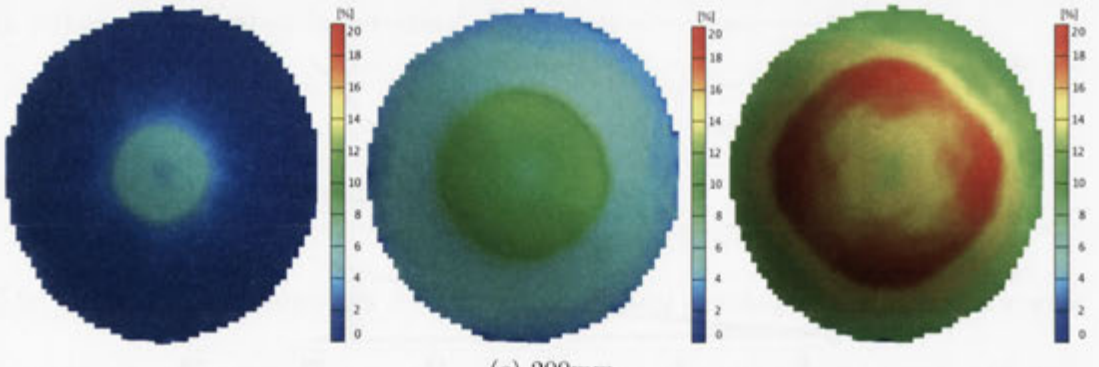

(c) 200mm

Figure 5.14: Strain contours for the selected rectangular specimens at 10mm, 20mm and 30mm depths

provides superior strain resolution compared to CGA. In addition, the ability of the system to provide full-field strain information at any forming depth, rather than just at failure, is highlighted. This ability allows the identification of any regions that may be experiencing unusual behaviour and also permits the calculation of strain ratio and other important forming parameters in regions of interest. These images illustrate forming process of the FML specimens. Initially, only the pole region of each specimen deforms, resulting in the state of initial biaxial stretch shown in Figure 5.4. However, after the contact pressure and area between the punch and specimen increase to a certain level, the high strain region in the specimen "separates" and begins to increase to the side of the contact area with the punch. This again highlights the effect of friction on the forming of sheet materials. The material in contact with the punch is not able to deform as easily as the region to the side, causing an inequality in strain levels and a reduced rate of increasing strain at the pole at larger depths. The hourglass specimens, shown in Figure 5.15, exhibit a lower tendency for the strain to increase in the unsupported regions. This is because the narrower width in the centre of the hourglass specimens aids in the concentration of strain in the centre.

Figure 5.16 shows the contours of the strain ratio on the surface of selected specimens at the failure depth. The strain ratio for the 25mmHG and the 200mm FML specimens are completely negative and positive respectively, whereas the 70mmHG FML specimen is centred around 0. Compared to aluminium, it can

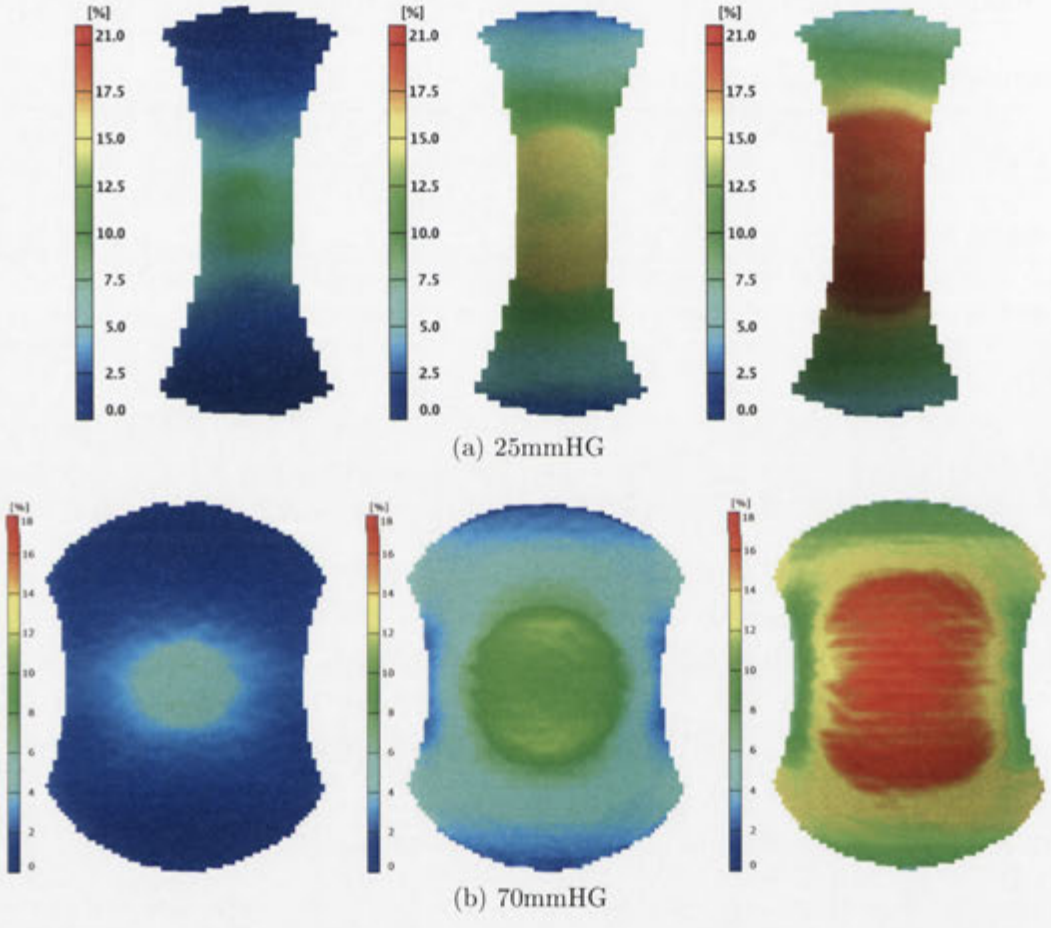

(a) 25mmHG

(b) 70mmHG

Figure 5.15: Strain contours for the selected hourglass specimens at different forming depths (10mm, 20mm, and 25mm for the 25mmHG; 10mm, 20mm, and 30mm for the 70mmHG)

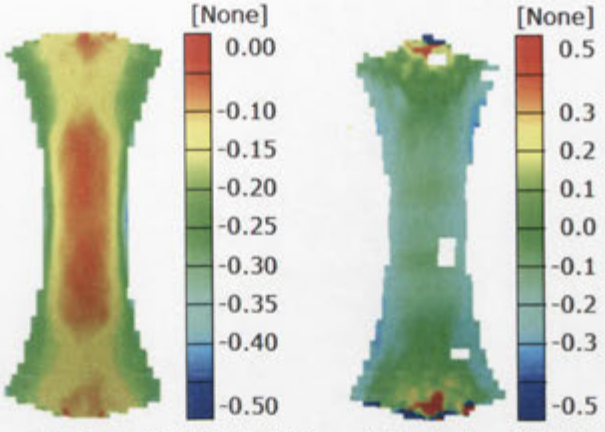

(a) 25mmHG, FML (left) and aluminium (right)

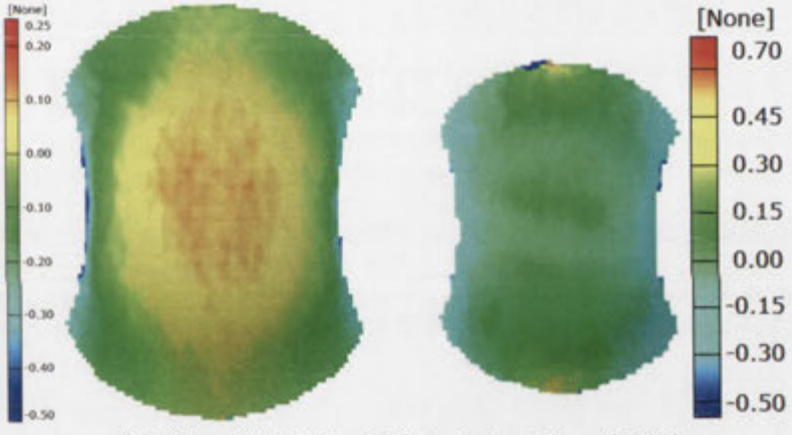

(b) 70mmHG, FML (left) and aluminium (right)

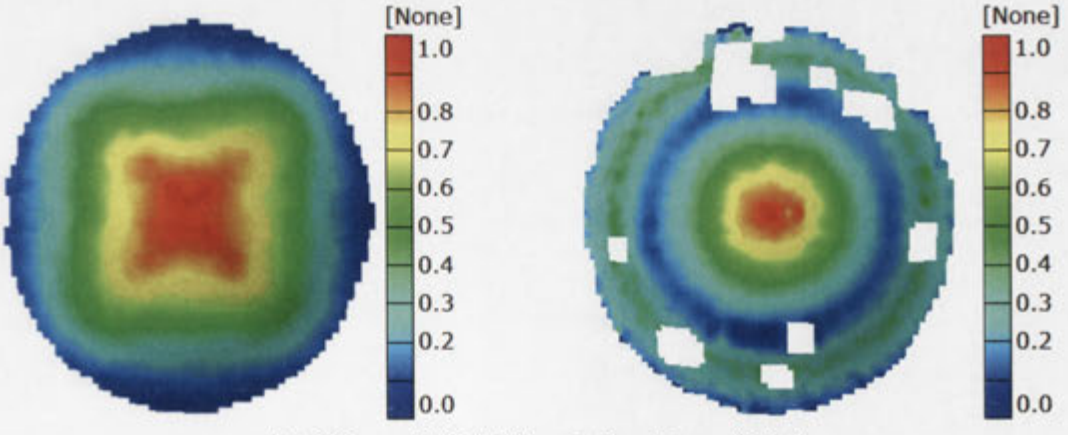

(c) 200mm, FML (left) and aluminium (right)

Figure 5.16: Surface contour of the strain ratio (β) in selected specimens at the failure depth

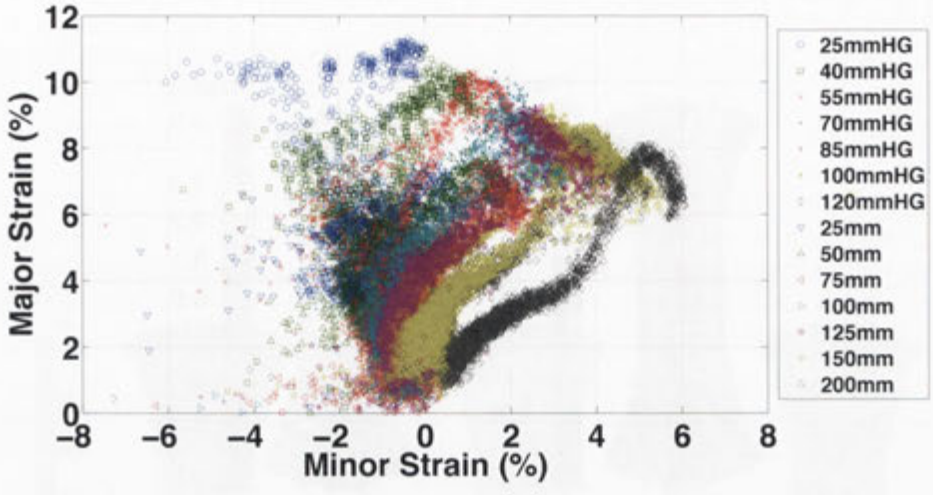

Figure 5.17: FLDs for all specimens at a depth of 15mm

be seen that the FML specimens exhibit much greater variation of strain ratio across the surface, even with the large difference in strain in the aluminium due to the formation of a localised neck. In both materials, particularly the 200mm FML specimen, the regions of higher (more positive) strain ratio correspond the regions of lower strain when compared to the major strain distribution shown in Figure 5.14.

5.2.3.1 Forming limit diagram at various depths

The data shown in the surface strain contours can also be used to create a FLD, which gives quantitative results about the forming of FMLs in the form of a FLD. Strain data, and therefore the FLD, was obtained for every point on the surface at depth increments of $0.5mm$, which provides a large volume of results. In addition, when all of the geometries tested at room temperature are displayed on the same graph they appear as shown in Figure 5.17 which again highlights the

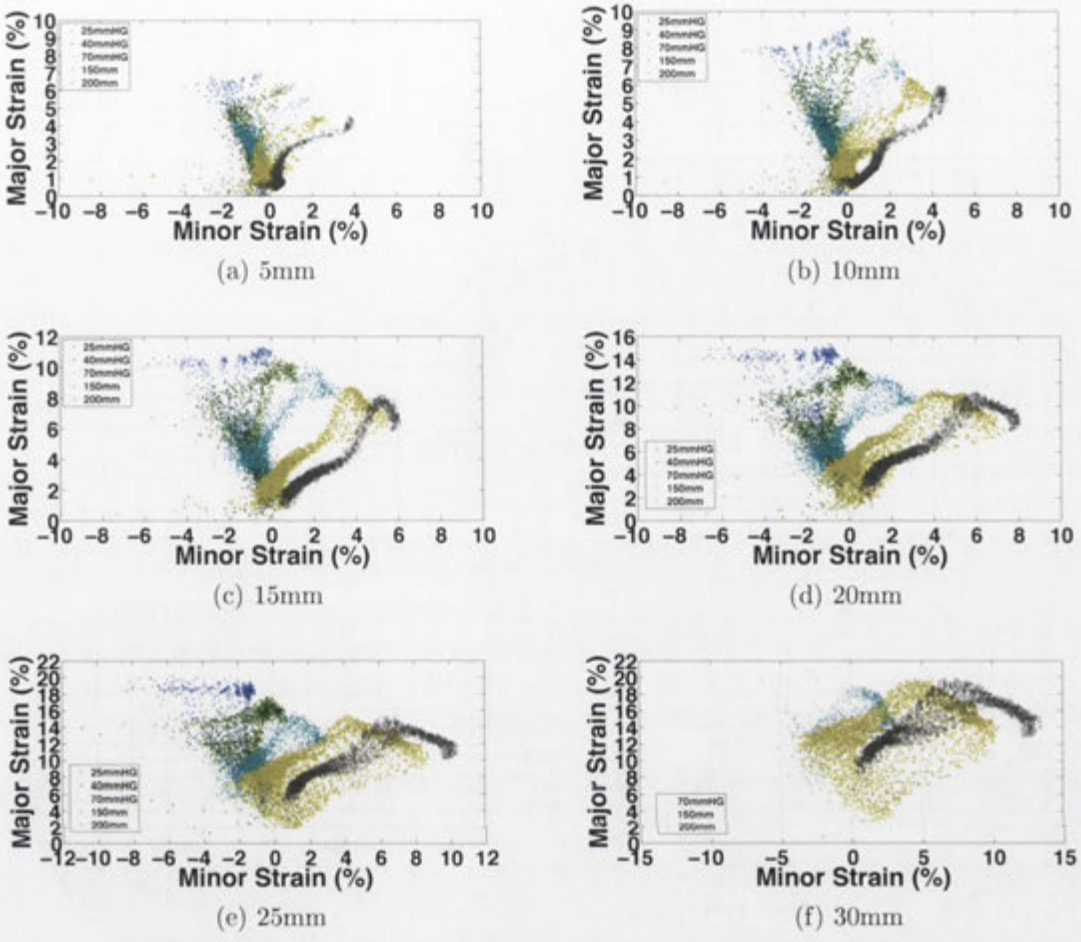

(a) 5mm (b) 10mm

(c) 15mm (d) 20mm

(e) 25mm (f) 30mm

Figure 5.18: Experimental forming limit diagrams for the rectangular geometries at various depths

overlap in deformation modes for many of the specimens. Figure 5.18 shows the FLDs for selected experimental specimens at $5mm$ depth increments. The change in the FLDs with increasing forming depth can be seen as increased maximum and mean major and minor strain values. The strain envelopes for the FML specimens also show, with increased forming depth, an increasing range for the major and minor strain. For example, from 5mm to 10mm the minor strain limits increase from <–1.5%,4.5%> to <–2%,4.75%> while the major strain limits change from <0%,5%> to <0%,6.75%>, which is an increase of 12.5% in the

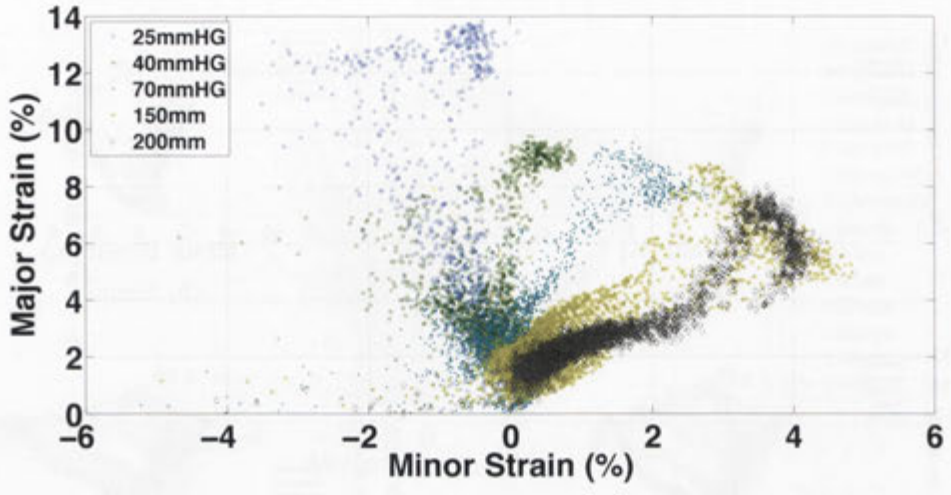

Figure 5.19: FLD for aluminium specimens at a forming depth of 15mm

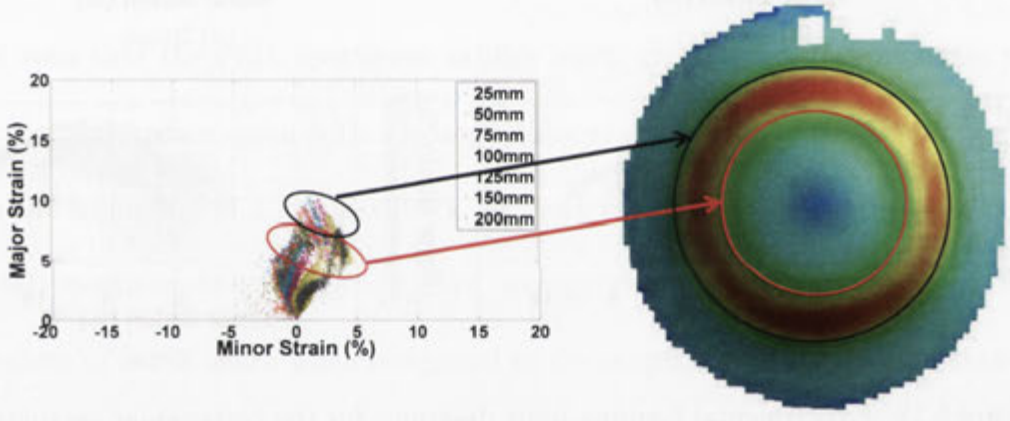

Figure 5.20: Regions of the aluminium FLD shown on an indicative contour plot

minor strain envelope and 35% in the major strain envelope. A key discovery from the FLDs of the FML specimens is the improved strain distribution when compared to aluminium specimens. Figure 5.19 shows the FLD for aluminium specimens at a 15mm forming depth. When this figure is compared to Figure 5.18(c) it is clear that the FML strain distribution shows less stratification of the major strain values and a wider range of minor strain values. This is important because the difference in major strain elucidates the rapid deterioration of the quality of the formed aluminium part. Figure 5.20 shows where the regions

of the aluminium FLD occur on a formed specimen. As the depth increases the discrepancy between the strain in these regions increases. In addition, once the neck has formed in the high strain region of the aluminium, the material deforms in a plane strain deformation mode, which leads to rapid failure. This is shown by again assessing the increases in the major and minor strain limits. For the evolution from 15mm to 20mm forming depth, the minor strain envelope in the aluminium and FML increase by 29% and 33% respectively, with the major strain envelope increasing by 72% and 30%. This shows that the FML specimen is undergoing a more uniform deformation, since the rapid increase in the major strain in the aluminium, caused by necking, is not significantly changing as the strain envelope increases. This phenomenon is more readily seen using the meridian major strain.

5.2.4 Meridian Strain

The major strain along the longitudinal axis of an experimental specimen is called the meridian strain. These results are of particular interest because they allow the rapid determination of the likely failure points in a material and, especially for axis-symmetric stamping, they provide an easy method for visualising the strain over the entire surface of the specimen.

The meridian strain distribution for the specimens corresponding to uniaxial tension, plane strain, and biaxial stretch are shown in Figure 5.21. These figures show the evolution of the strain distribution on a line along the longitudinal

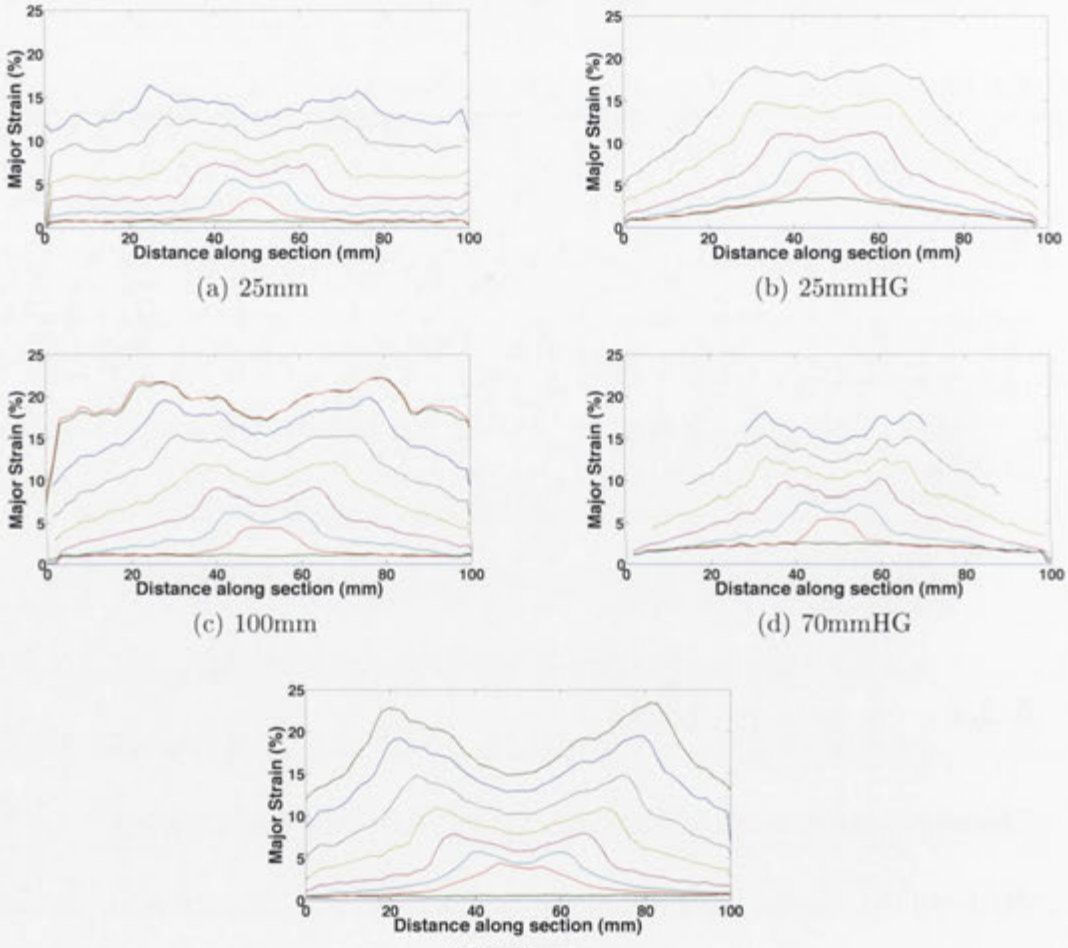

(a) 25mm

(b) 25mmHG

(c) 100mm

(d) 70mmHG

(e) 200mm

Figure 5.21: Meridian major strain at 5mm depths for the specimens corresponding to uniaxial tension, plane strain, and biaxial stretch

axis of the specimens (and therefore the fibre direction in the composite layer). Each graph represents the state of major strain in the specimens at 5mm depth increments, with the first and second distributions corresponding to the initial and pre-stretch stages respectively. The pole region occurs at the 50mm distance and the edge of the die is at 0 and 100mm. These figures make clear the superior forming characteristics of the FML compared to aluminium, shown in Figure 5.22. It can be seen in this figure that the aluminium specimens begin to experience a localised neck; the strain in the regions to the side of the punch also undergoes a rapid increase compared to the pole. Conversely, the FML specimens maintain a roughly equal increase in strain along the entire length of the longitudinal axis.

It can be seen in the aluminium strain distributions that as the localised neck forms to the side of the punch the increase in the major strain at the pole ceases. The 25mm aluminium specimen begins to show necking between 20 and 25mm. The strain increase between these depths is 8.6% at the pole compared to an increase of 95% at a distance of 25mm from the pole. In comparison, the evolution in the FML specimen between these depths is 33% at the pole and 78% at 25mm from the pole. This shows that while some disparity exists between these regions it is not as significant as the aluminium specimen. The onset of localised necking in the 100mm and 200mm specimens also begins between depths of 20mm and 25mm, with increases at the pole and 25mm distance region being 18.8% and 130% respectively (for the 100mm specimen) and 17% and 143% (for the 200mm specimen). The 100mm and 200mm FML specimens show a similar trend to the

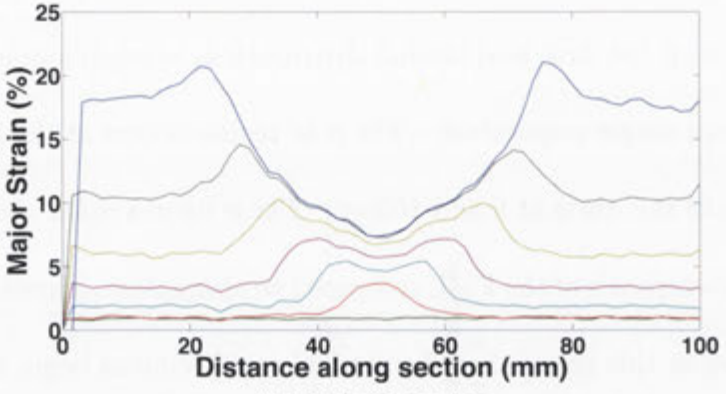

(a) Uniaxial tension

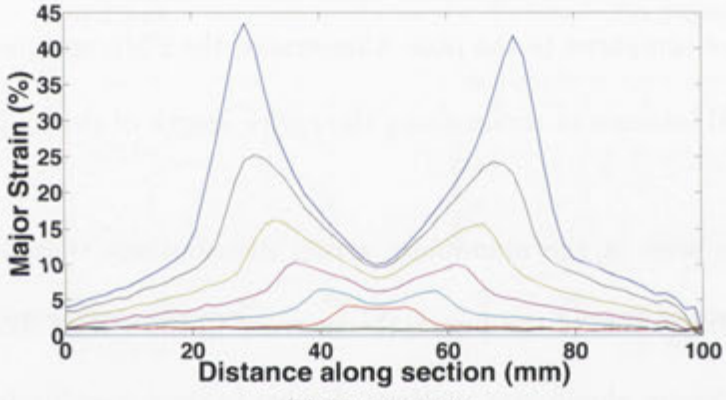

(b) Plane strain

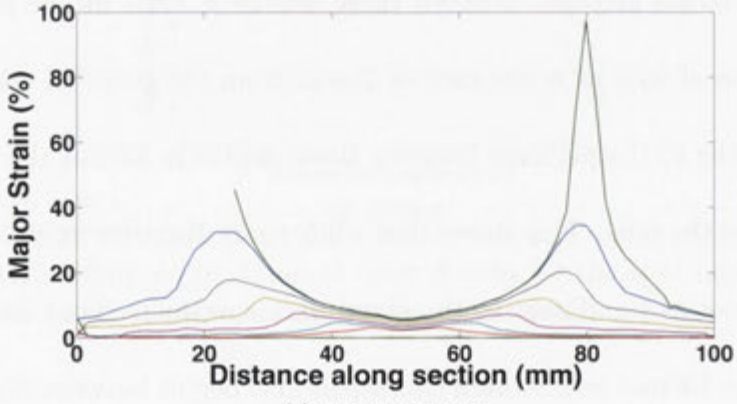

(c) Biaxial stretch

Figure 5.22: Meridian major strain at 5mm depths for selected aluminium specimens

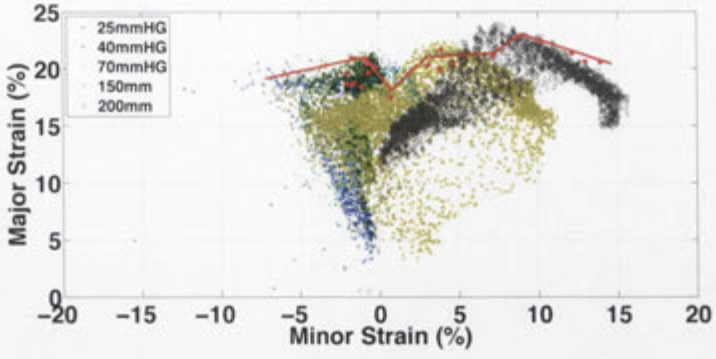

Figure 5.23: Final FLD for selected experimental specimens

25mm specimen, with the strain increases being 31% and 48% for the 100mm specimen and 30% and 70% for the 200mm specimen.

5.2.5 Forming Limit Curve

The FLDs for selected experimental specimens immediately prior to failure are shown in Figure 5.23 with the strain values for the points of failure superimposed. The FLC for the aluminium specimens is shown in Figure 5.24. The FLC is drawn below the points at the onset of localised necking (in the aluminium) and prior to failure (in the fibre–metal laminate samples), which ensures that the safe forming region does not contain points which are necked or are in close proximity to failure. The key difference between the failure behaviour of the FML and the aluminium is the lack of localised necking in the FML specimens prior to failure, which removes the need for the necked or "marginal" points on the FLC. There is no visual or numerical indication of where failure will occur in the FML specimens prior to its catastrophic failure, whereas the failure of the aluminium specimens can determined by assessing the strain behaviour across the surface.

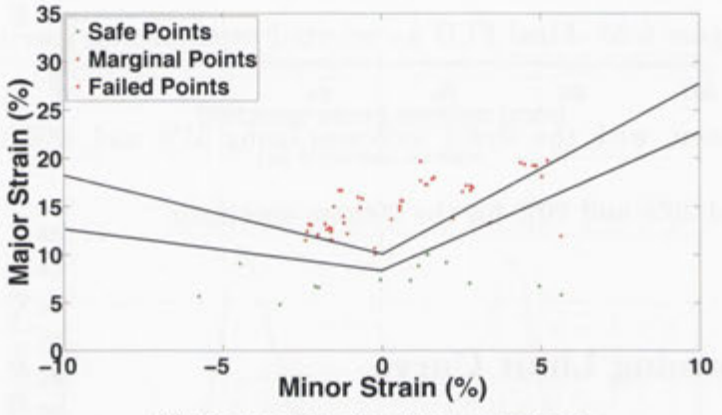

(a) Rectangular aluminium specimens

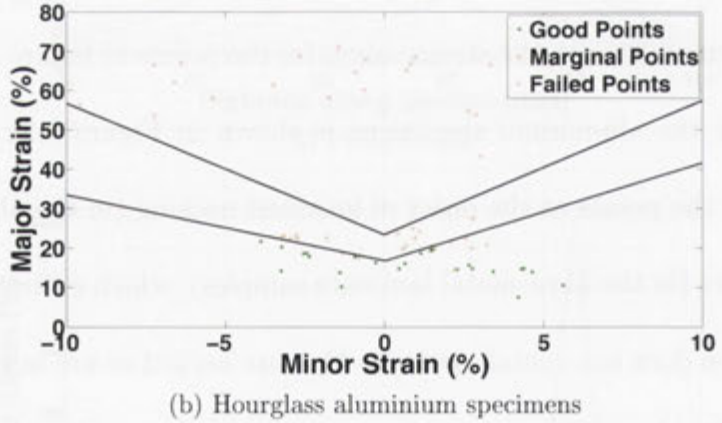

(b) Hourglass aluminium specimens

Figure 5.24: Forming limit curves for aluminium at room temperature

That is, as the neck grows other regions no longer experience increases in strain. This provides an easy way to identify the failure region, but causes problems in determining the exact onset of the localised neck, which reduces the veracity of the predicted strain limits.

In both the aluminium and fibre–metal laminate samples the failure occurred not in the centre of the specimen, as expected by symmetry, but to one side of the punch. However, as stated previously, failure of all rectangular specimens with widths below 125mm occurred at the lock ring which ruled out the accurate determination of the forming limit for their respective deformation modes. This is possibly the cause of the reduced FLC for the rectangular aluminium specimens, shown in Figure 5.24.

Another key aspect of the FML FLC is the fact that certain points of failure are below the maximum major strain experienced for a given minor strain. This is due to the weave of the SRPP layer. In the fibre direction there is a limit to the strain which the fibres can withstand, and, due to the geometry and 0/90 angle of the forming tests conducted in this study, the strain ratio is also controlled in the fibre direction. However, in regions not along the longitudinal and lateral directions the major and minor strain occur not in the fibre direction but at an angle, which causes the matrix to experience deformation. Due to the ductile nature of the matrix it is possible for these regions to withstand greater strain levels than predicted by the FLC.

5.2.6 Sub-surface strain behaviour

The problem with using the surface strain obtained from the optical strain measurement system is that this reports only the strain in the aluminium layer. However, it is possible to determine the strain in the SRPP layer using the bending strain relation [36]. The calculation of the strain at a distance z from the mid surface of the specimen is given by equation 5.1,

$$\epsilon_1 = \epsilon_0 + z\kappa, \tag{5.1}$$

where ϵ_1 is the major strain on the surface, ϵ_0 is the mid surface strain, z is the distance from the mid surface, and κ is the inverse of the radius of curvature of the laminate. The strain measurement provides ϵ_1, the known thickness of the laminate determines z, and the radius of curvature for the failed region can be obtained from assessing the meridian depth profiles, as shown in Figure 5.25. The pole of each specimen will obviously have a radius of curvature of 50mm due to the radius of the punch, resulting in a strain difference of 2.2% between the surface of the aluminium and the mid-surface of the SRPP and a 3.8% difference to the mid-surface of the top aluminium layer.

This technique can be used to assess the major strain in the SRPP and top aluminium layer along the meridian of the FML specimens. Figure 5.26 shows the meridian major strain for all three layers in the 25mmHG, 70mmHG and 200mm specimens. The difficulty in using this method is that the only indication of the

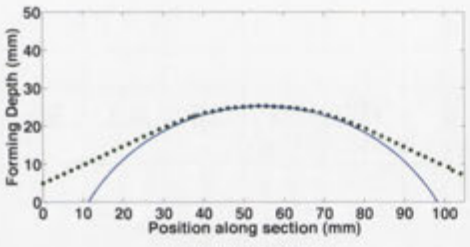

(a) 25mmHG

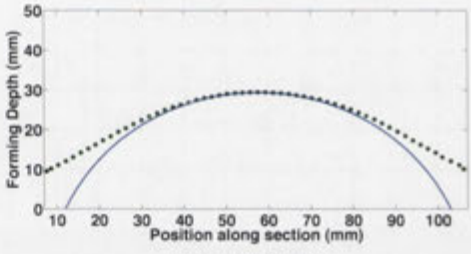

(b) 40mmHG

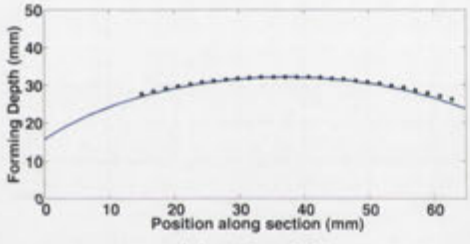

(c) 70mmHG

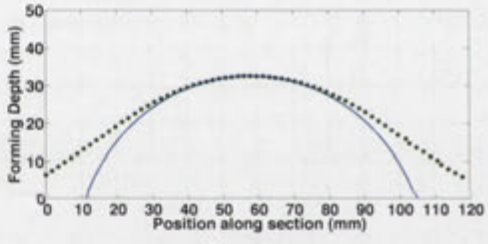

(d) 150mm

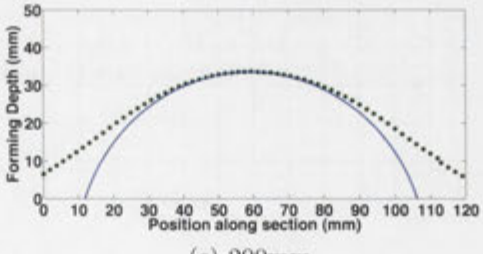

(e) 200mm

Figure 5.25: Meridian depth profiles at the failure depth. The green points indicate the forming depth in the specimen and the blue line represents the geometry of the hemispherical punch

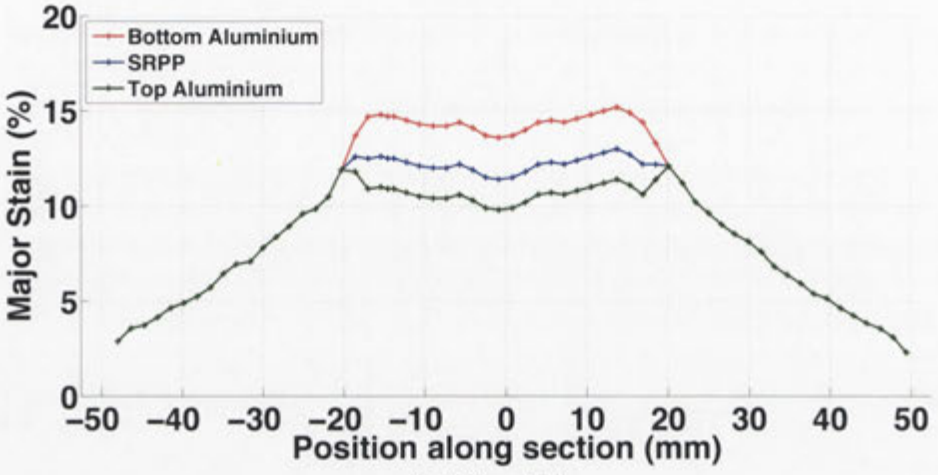

(a) 25mmHG

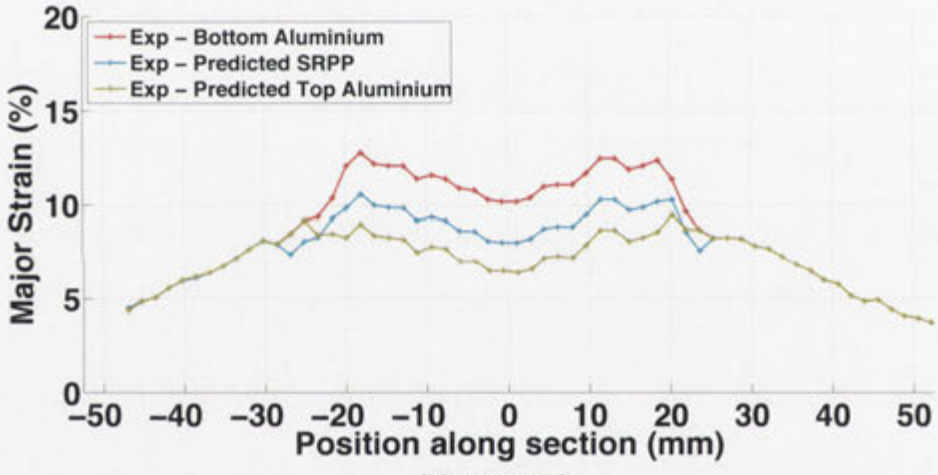

(b) 70mmHG

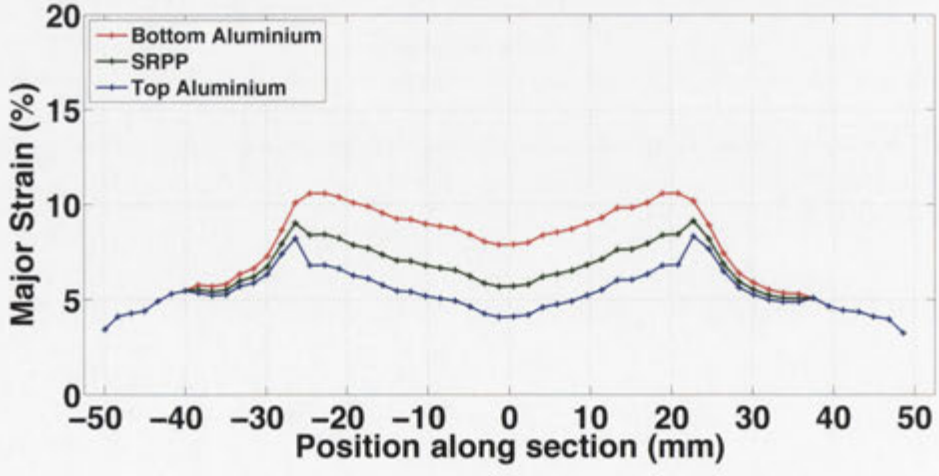

(c) 70mmHG

Figure 5.26: Major strain along the longitudinal axis in the SRPP and top aluminium layers

Figure 5.27: Major and minor strain directions in the 25mmHG specimen. The points represent the failure region

transition from the radius of the punch to the straight line of the unsupported region is where the depth contour of the specimen ceases to conform to the punch dimensions (as shown in the meridian depth profiles). The applicability of using this method therefore depends on the state of the bond between the layers of the FML; that is, if the bond is intact then the equation should produce the correct strains for the subsurface.

Calculating the sub-surface strain in the FML opens up the possibility of determining a preliminary failure criterion of the SRPP layer. By assessing the major and minor strain directions, shown for the 25mmHG FML specimen in Figure 5.27, both the sub-surface major and minor strains can be found for any point in the specimen.

The failure points of each specimen were found to occur along the longitudinal (meridian) axis and were 13mm away from the pole in the 25mmHG, 17mm in the 40mmHG, 27mm in the 70mmHG, 31mm in the 150mm, and 33.7mm in

Specimen	Radius of curvature (ρ) (mm)	Mid Surface Major Strain (%)
25mmHG	50	16.2
40mmHG	50	17.8
70mmHG	≈50	11.1
150mm	0	19.9
200mm	0	22.4

Table 5.5: Radii of curvature and calculated SRPP major strain at the failure depth

200mm specimen. Therefore, the calculated radii of curvature in the longitudinal direction and SRPP major strain are shown in Table 5.5. These show that the strain at failure of the SRPP layer is not in accordance with the predicted value from the tensile characterisation experiments presented in Chapter 4. This is not surprising as every material exhibits different failure limits depending on the deformation mode (hence why the FLC exists). However, the uniaxial tension specimen (25mmHG) agreed with subsequent tensile experiments which showed tensile failure of the SRPP occurring at a major strain of 16.4% and a minor strain of –1.6%. Therefore, the failure of the tensile specimen at approximately 13% strain is most likely caused by premature failure (in that set of experiments) induced by the unique grips used to secure the specimens. The stress/strain behaviour of those specimens was not affected, only the strain at failure.

Using the same specimens in Figure 5.25, the minor strain depth profiles are found by determining the radius of curvature in the minor strain direction. The minor strain depth profile for the 25mmHG specimen is shown in Figure 5.28 and the calculated radii of curvature and SRPP minor strains for all specimens are provided in Table 5.6. It can be seen that the uniaxial tension specimen

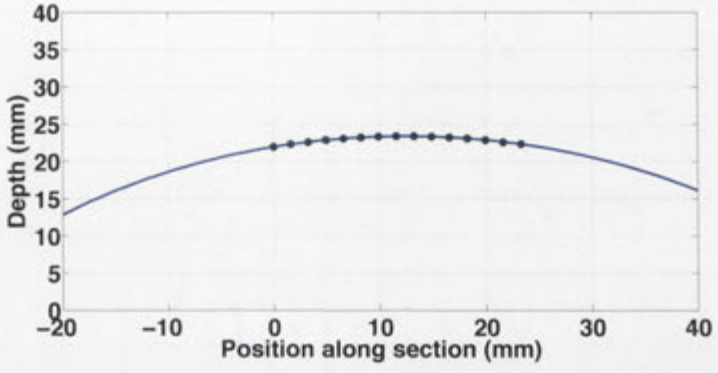

Figure 5.28: Minor strain depth profile for the 25mmHG specimen

Specimen	Radius of curvature (ρ) (mm)	Mid Surface Minor Strain (%)
25mmHG	55.5	-3.04
40mmHG	52.8	-2.4
70mmHG	39.24	-2.96
150mm	68.4	2.23
200mm	41.7	3.6

Table 5.6: Radii of curvature and calculated SRPP major strain at the failure depth

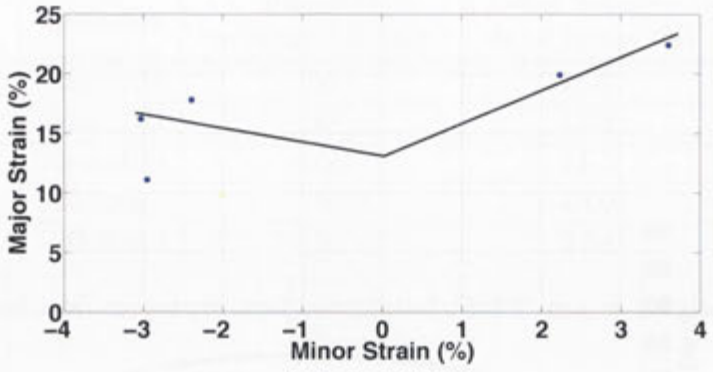

Figure 5.29: Preliminary failure criteria for the SRPP based on calculated failure strains

(25mmHG) does not fail at the expected –1.64% but at a minor strain of –3%. In this instance the discrepancy is most likely due to a difference between the deformation behaviour observed during a uniaxial tension test conducted on a universal testing machine and that observed using a hemispherical punch. Alternatively, it could be due to the effect of the bonding of two materials with dissimilar Poisson's ratios. Therefore, the preliminary failure strains posited for the SRPP layer, shown in Figure 5.29, do not necessarily represent the correct state of failure strain for the material. More research is required to determine the actual forming limits of the composite layer. This is particularly important as previous studies by Hinton et al. [110] found that the current failure theories for composite materials were not useful for practical applications. Research into the forming behaviour of composite materials provides a practical determination of the failure of composite materials experiencing different deformation, as shown by the different forming modes.

5.3 Finite Element Simulation

The two primary objectives of the finite element simulation were to provide information about the forming behaviour of the regions invisible to the ARAMIS measurement system and to create predictive models of any desired forming process. Therefore, the simulation procedure consisted of two aspects: the verification of the FE results by comparing them with experimental data, and analysis of the invisible regions. The development of the FE model was discussed in Chapter 4. Due to the large number of experimental specimens, not all specimens were selected for FE simulation; again, only the specimens corresponding to uniaxial tension, plane strain, and biaxial stretch were chosen for further analysis.

5.3.1 Verification of FE simulation

In order to demonstrate that the FE simulation can accurately predict material behaviour, the model must be verified by experimental findings. The first aspect of the experimental results to be assessed was the "pre-stretch", shown in Figure 5.2. The pre-stretch experienced by the experimental specimens was applied in the simulation by applying a small displacement to the outer edges, shown in Figure 5.30, which corresponds to the surface strain behaviour obtained through experimentation. The magnitude of the force depended on the geometry being examined and the force applied by the blankholder.

Figure 5.31 shows good agreement between the experimental pre-stretch and the results obtained from the force applied in the FE simulation. However, it is

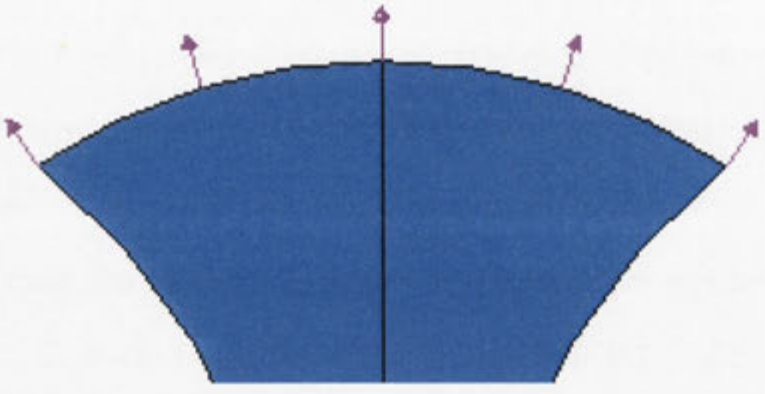

Figure 5.30: Force applied to edge of specimens in the FE model to simulate the effect of the lock ring on surface strain

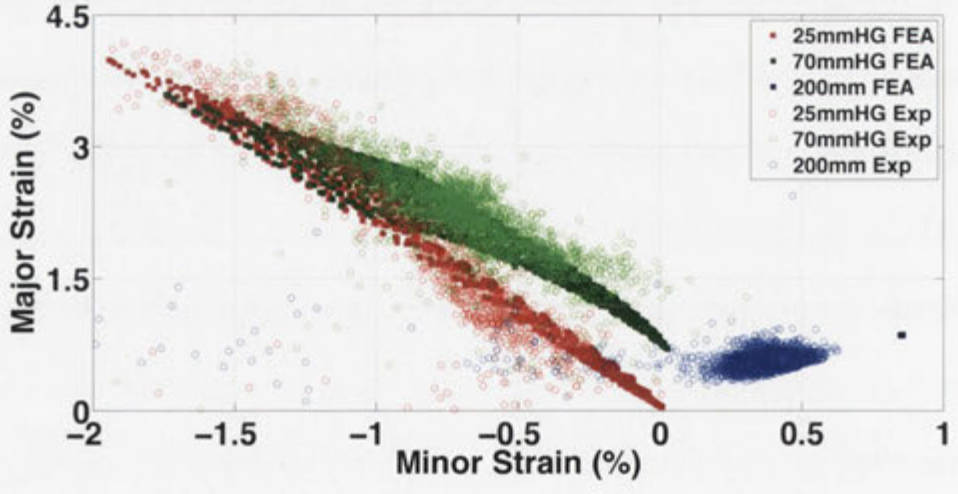

Figure 5.31: FE simulation of the effect of the lock ring on the surface strain

Figure 5.32: Deformed model

difficult to achieve a perfect match in the 200mm simulation. This is because the force applied to the FE model is perfectly symmetrical, as is the geometry, which requires that the major and minor strain are equal at all points.

In addition to the pre-stretch, three other aspects of the forming behaviour were chosen for comparison: the FLD, the meridian strain distribution, and the evolution of the strain at the pole of the specimens. The three specimen geometries were modelled to the failure depth of the experimental specimens and the deformed FE models are shown in Figure 5.32.

Figure 5.33 shows the evolution of major strain at the pole of both the experimental and FE specimens. It is clear that the evolution of strain in the FE model at this point shows excellent agreement with the experimental results. There are, however, some areas of difference between the FE and experimental specimens. It can be seen in the initial strain behaviour that there is a negative change in forming depth coupled with an increase in major strain in the experimental specimens. This change in depth in the experimental specimens is caused by rigid body motion induced by securing the lock ring. The implementation of

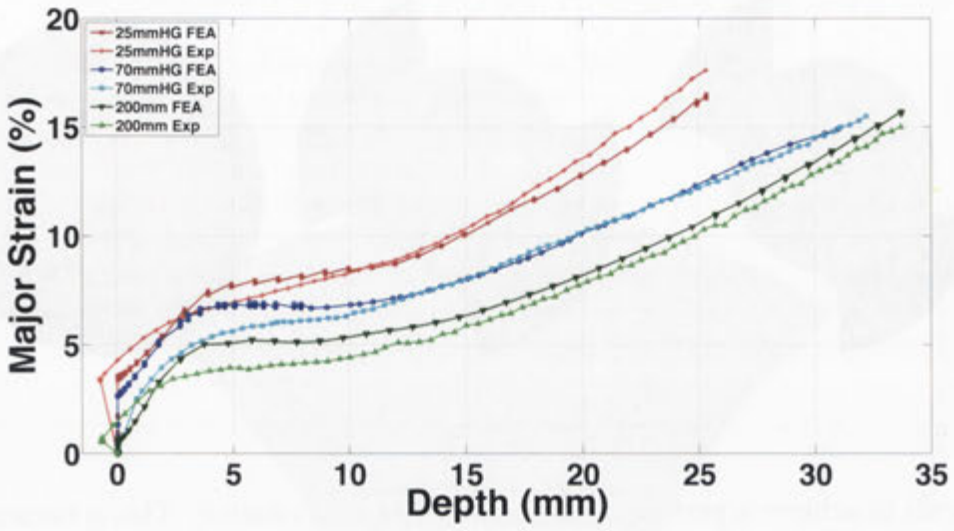

Figure 5.33: Evolution of major strain at the pole

the "pre-stretch" strain in the FE simulation will not cause this change in the forming depth because it can only induce in-plane deformation. There is also a deviation of the FE simulation at the beginning of contact with the punch. In this stage, where only the pole is deforming in biaxial stretch, the FE predicts that the major strain will increase much more rapidly than what was observed in the experimental specimens. In the final stages of deformation the FEA result slightly deviates from the experimental evolution, which may be caused by a difference in stiffness between the SRPP used for characterisation and the SRPP used in the FML, or through damage introduced to the SRPP layer.

Figure 5.34 shows the effect of system parameters on the evolution of strain in the FE model. The parameters investigated were the adhesion between the FML layers and the mechanical response of the internal layer. The figure shows that if the layers of the FML were allowed to move independently of each other with no friction, which is analogous to removing the adhesive, the strain at the pole on

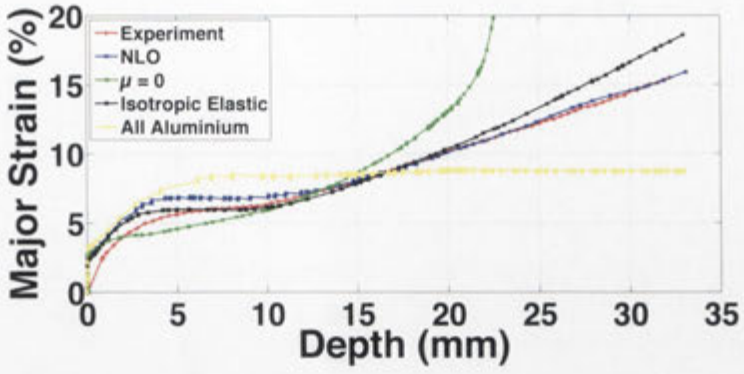

Figure 5.34: Effect of various parameters of the strain evolution at the pole of the 70mmHG specimen

the lower aluminium surface would increase more rapidly than all other models. This is because there is no restriction on the deformation in the pole region. The aluminium fails at a strain of approximately 15%, after which the software applies an apparent stiffness of 0MPa in the aluminium which causes the major strain at the centre of the specimen to rapidly increase. At the failure depth of the specimen the frictionless model exhibited a strain of 180% at the pole, compared to 15.5% in the experimental and the simulated nonlinear orthotropic (NLO) specimens. The all aluminium and isotropic elastic specimens were selected to investigate the effect of composite layer stiffness on FML behaviour. In the all aluminium model, the SRPP properties were substituted with aluminium properties, which should provide similar results to a 2.2mm thick aluminium specimen. This is indeed seen by the relative flattening of the strain evolution at the pole, with an increase in strain occurring in the unsupported region. The isotropic elastic simulation uses the modulus provided by the manufacturer of 4200MPa. This model shows reasonable agreement with the experimental results, with deviation

primarily occurring after a depth of 20mm and a major strain of 11%. The stiffness of 4200MPa for the isotropic elastic model is higher than the stiffness of 1080MPa for the nonlinear orthotropic model, meaning that the higher stiffness of the composite layer in the isotropic elastic model is increasing stretch at the pole.

5.3.1.1 Meridian strain

Figure 5.35 shows the comparison of the meridian major strain observed in the experimental specimens with the strain predicted by the FE model at depths of 10, 20, and 25mm. These figures show that excellent agreement has not only been achieved between the experimental results at the pole but also at all regions along the longitudinal axis. It can be seen, however, that the FE model shows a more gentle transition from the peak in strain towards the lower strain at the die edge, whereas the experimental results show a rapid drop in major strain. In addition, the experimental results show a much earlier onset of the effect of friction with the punch, with the meridian strain at 10mm depth showing lower strain at the pole compared to the outer regions.

It was found during modelling that, apart from the material and adhesive models, the most significant factor affecting the results was the amount of friction between the tools and the aluminium layers. If the friction between the specimen and the punch was too high then the strain at the pole was reduced and the strain in the unsupported region increased more than seen experimentally. Conversely,

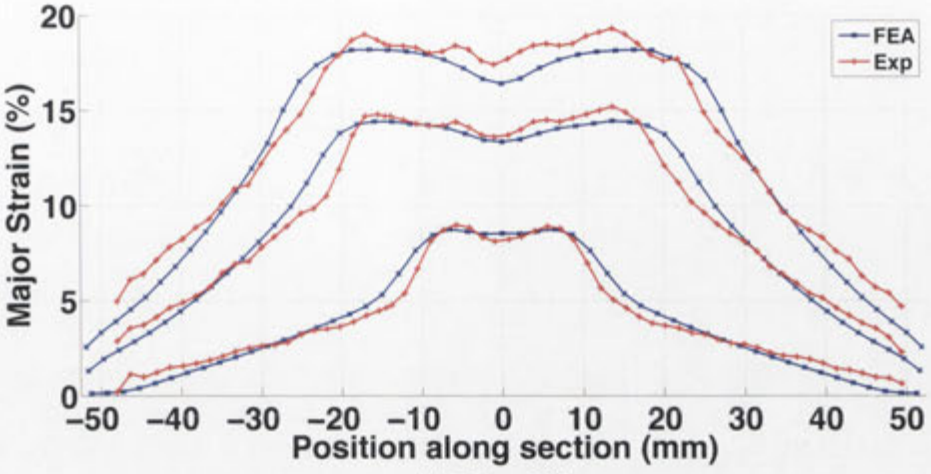

(a) 25mmHG

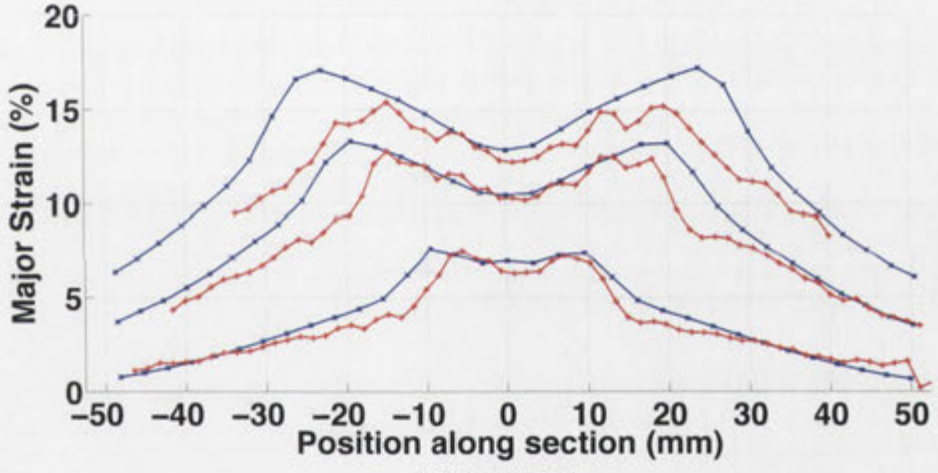

(b) 70mmHG

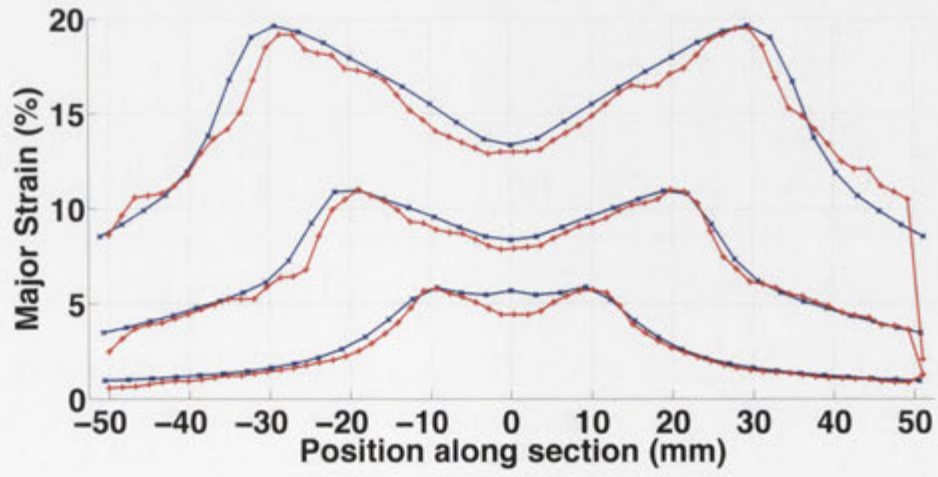

(c) 200mm

Figure 5.35: Comparison of meridian major strain in selected specimens

if the friction was too low then the pole and unsupported region strain values were, respectively, too high and too low.

5.3.1.2 Forming limit diagram

In ensuring model validity, the final component of the surface strain behaviour to be compared was the forming limit diagram. This diagram was chosen because it allows the state of both the major and minor strain on the surface of the FML to be compared. Figure 5.36 shows the comparison of the FLD in the FE simulation and the experimental specimens. It can be seen that the overall surface behaviour of the FE model matches that of the experimental model, including the minor strain. The major area of difference is in the biaxial stretch specimen where it can be seen that the balanced biaxial strain region in the FE simulation, which is the region around the pole of the specimen, has a larger value of minor strain than the experimental specimen. This behaviour could be caused by two factors, a reduced stiffness of the material layers or reduced friction between the specimen and the punch in the FE simulation.

5.3.2 Behaviour of the fibre metal laminate layers

The advantage of the FE simulation over the ARAMIS measurement system is the ability to determine what is occurring in those other layers of the FML which are not visible during experimentation. Figure 5.37 shows the meridian major strain for all three layers calculated in Section 5.2.6 and compares it to

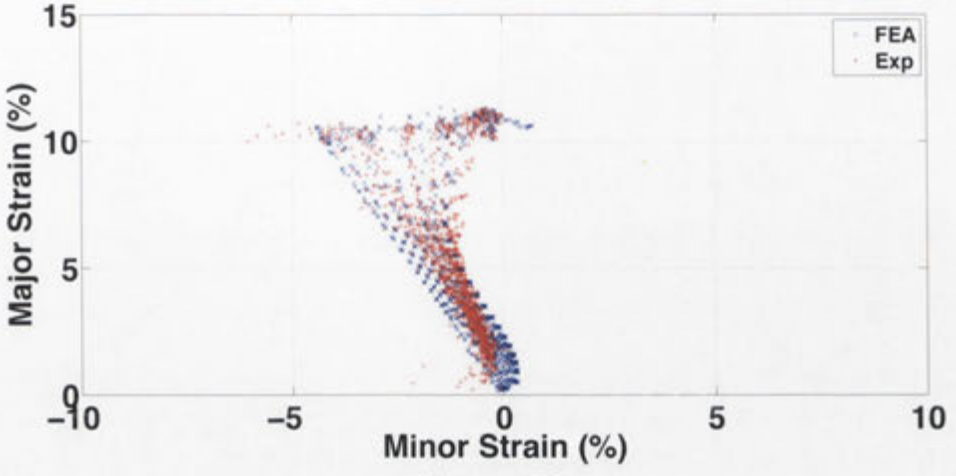

(a) 25mmHG

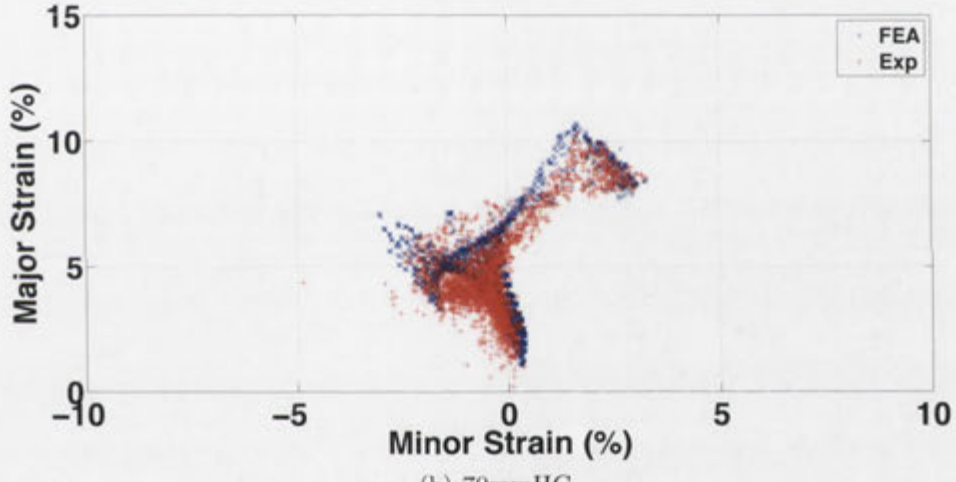

(b) 70mmHG

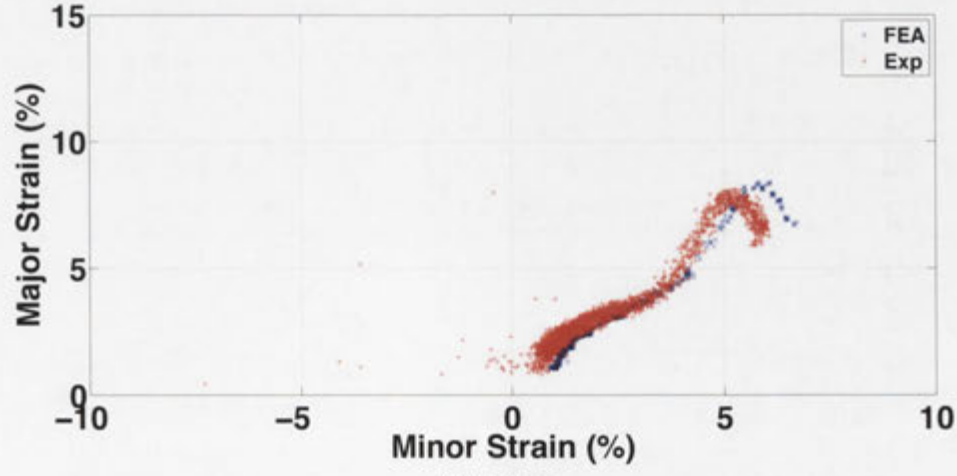

(c) 200mm

Figure 5.36: Comparison of the FLD for the selected specimens at a depth of 15mm

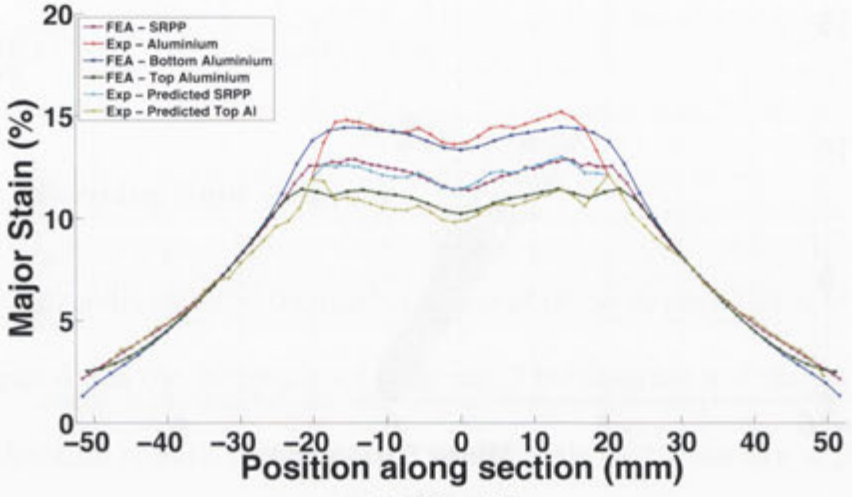

(a) 25mmHG

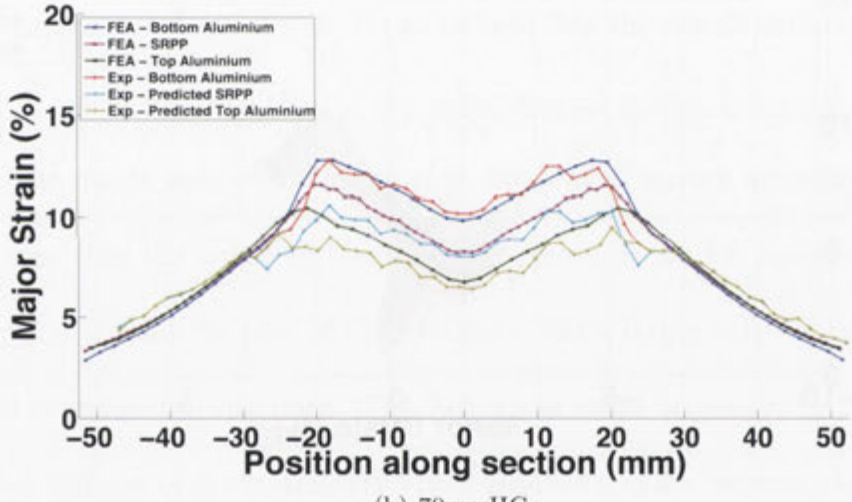

(b) 70mmHG

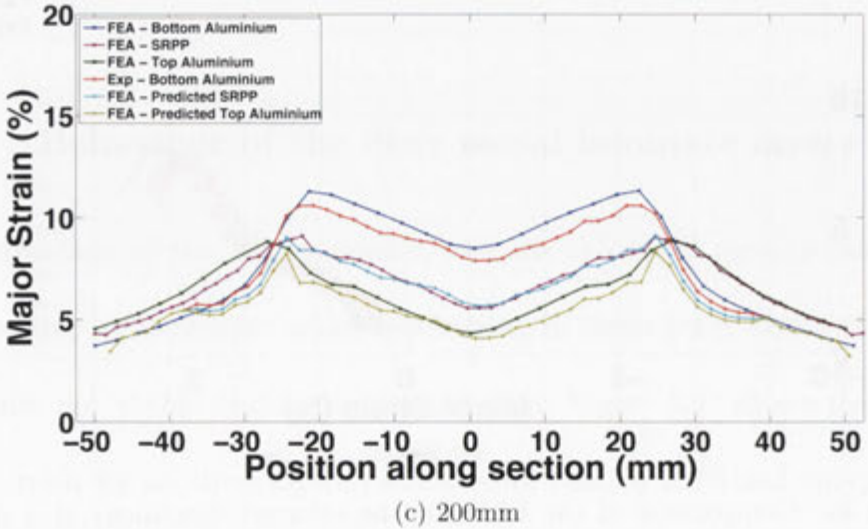

(c) 200mm

Figure 5.37: Meridian major strain in all 3 layers of the specimens

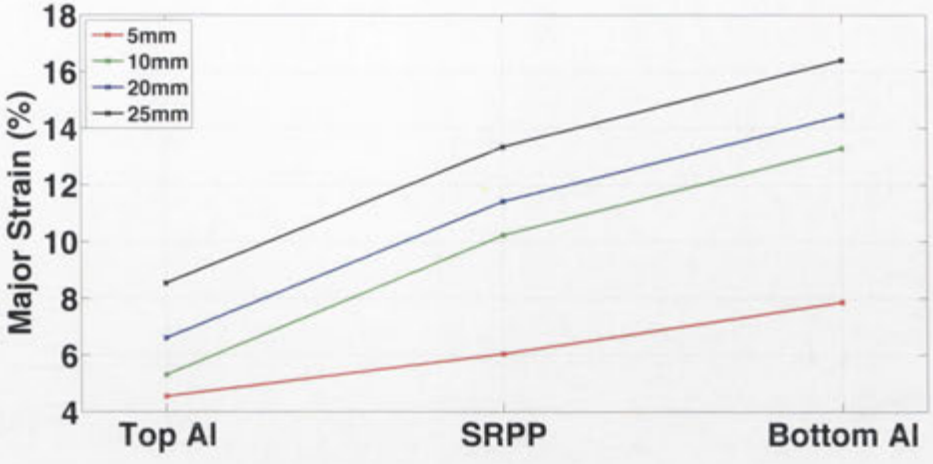

Figure 5.38: Major strain though the thickness

the meridian major strain produced by the FE simulation at a forming depth of 20mm. These figures validate the predicted bending induced in the specimen by the hemispherical punch, with the top aluminium experiencing lower levels of strain than the bottom aluminium layer, showing that the model seems to be accurately representing the behaviour of each layer and not just the surface. Interesting behaviour can be noticed in the 70mmHG and 200mm specimens where the region outside the punch, previously thought to be a straight section, shows a variation in strain through the thickness. The inner layers of the FML in the FE simulation are seen to be experiencing higher magnitudes of major strain compared to the bottom layer; this behaviour could only be due to bending occurring in the opposite direction to that at the pole of the specimen. Figure 5.38 provides further detail of the strain through the thickness of the laminate. Of particular interest is the difference in slope between the top aluminium and SRPP and the SRPP and bottom aluminium layers. In addition, the rise in major strain

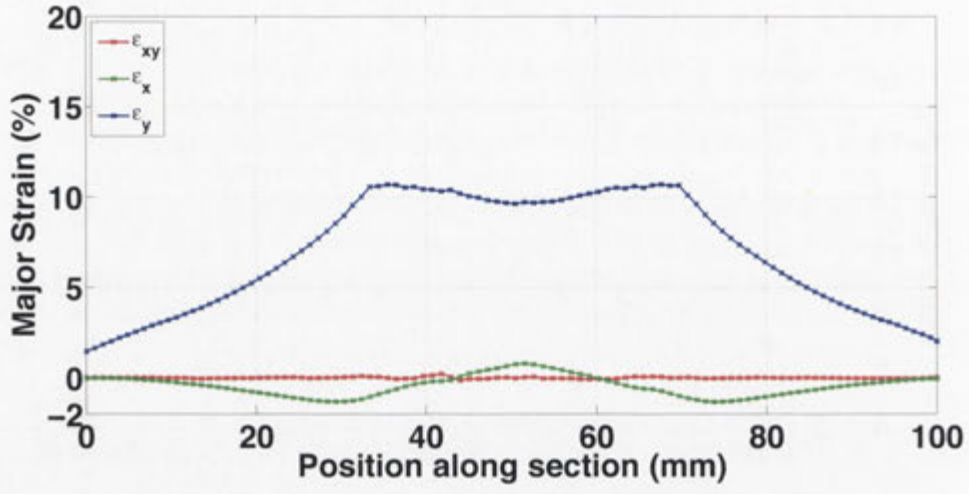

Figure 5.39: ϵ_x, ϵ_y and ϵ_{xy} for the SRPP layer

in the SRPP and bottom aluminium layer between 5mm and 10mm depth is 69% compared to an increase of only 17% in the top aluminium layer. This increase is primarily due to the bending induced in the specimen by the punch and the friction between the punch and the top aluminium which reduces the strain in the top aluminium layer. After the 10mm of forming depth the influence of bending is reduced as the punch fully deforms the pole of the specimen; this can be seen by the constant strain differences at each depth.

In metal forming it is customary to discuss the major and minor strain; however, in composite materials the longitudinal, transverse, and shear strains are more commonly considered because they can be related to the fibre and matrix strains. Figure 5.39 shows these strains along the meridian in the SRPP layer of the 25mmHG specimen as determined by the FE simulation. As expected, the shear strain along this section, which is also oriented along the longitudinal axis of the specimen, is approximately zero. This is because of the geometry and

boundary conditions of the specimen, which means that along the meridian the major strain is oriented along the longitudinal axis (ϵ_y) and therefore the shear strain is zero. Because of this alignment it is also possible to determine the deformation mode of the SRPP layer along the meridian by assessing the longitudinal strain (ϵ_y) and the lateral strain (ϵ_x). At the pole, the SRPP is experiencing a small amount of biaxial stretch (as indicated by the positive strain values); at a distance of approximately 25mm the lateral strain is at its most negative and the strain ratio is –0.15. Finally, at a distance of approximately 20mm from the pole, where the longitudinal strain is at a maximum, the strain ratio is –0.07.

A major aspect of the experimental results was the simultaneous and catastrophic failure of all layers of the laminate, indicating failure of the SRPP layer. In the initial FE simulation the model did not contain a failure criterion and therefore it continues to predict forming well after the failure depth observed in experiments. Figure 5.40 shows the surface strain contours for the SRPP and bottom aluminium layers, with the experimental results for comparison. These figures show that the strain distribution in the SRPP is similar to the aluminium layer but with different strain magnitudes.

Figure 5.41 shows the state of strain in the FE SRPP layer at the failure depth observed in the experiments. Initially, to simulate failure, a simple failure model based on a maximum strain criterion was developed; this model used the failure strain determined in Figure 4.1 for room temperature. This led to a constant maximum strain value of 13%. However, when the FLD of the composite layer

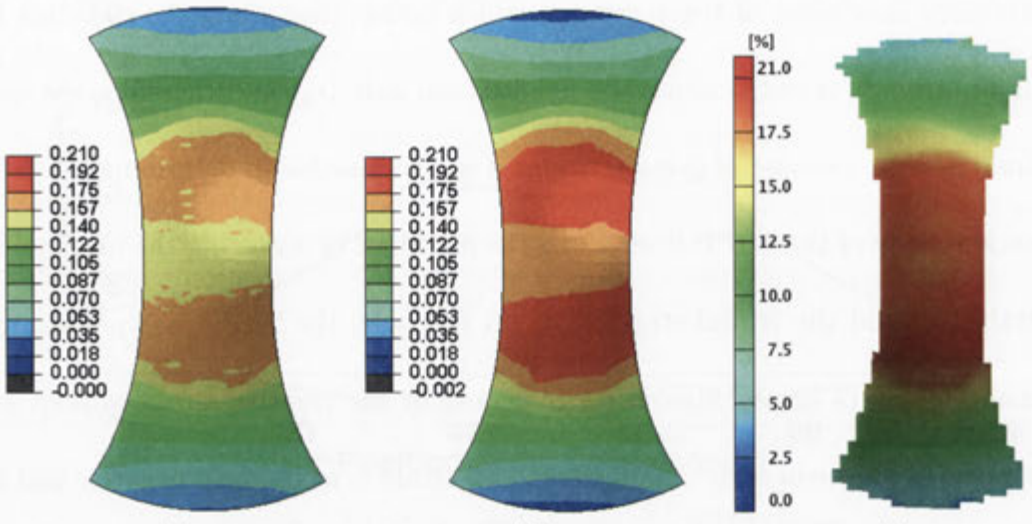

(a) (b) (c)

Figure 5.40: Contour plots for the 25mmHG specimen. SRPP layer (a), bottom aluminium layer (b) and the experimental results (c)

in the FEA is plotted at the failure depth of each specimen (25.3mm for the 25mmHG, 32.2mm for the 70mmHG, and 33.7mm for the 200mm, shown in Figure 5.41, it can be seen that the strain in the formed SRPP exceeds the failure strain obtained in the characterisation experiments. In fact, there are far more points above the determined line in the 70mmHG and 200mm specimens than below, which indicates that failure of the composite layer could not have occurred at 13%. Using the FE simulation it is possible to predict the failure of the SRPP layer by assessing the failed point in the experimental geometry. In the 25mmHG specimen, failure occurred approximately 13mm from the pole along the longitudinal axis; assessing this point in the SRPP layer of the FE simulation it was found that the major and minor strain values at this point were 16.4% and –1.61% respectively. In the 70mmHG specimen, failure was found to occur 27mm from the pole along the longitudinal axis, leading to major and minor

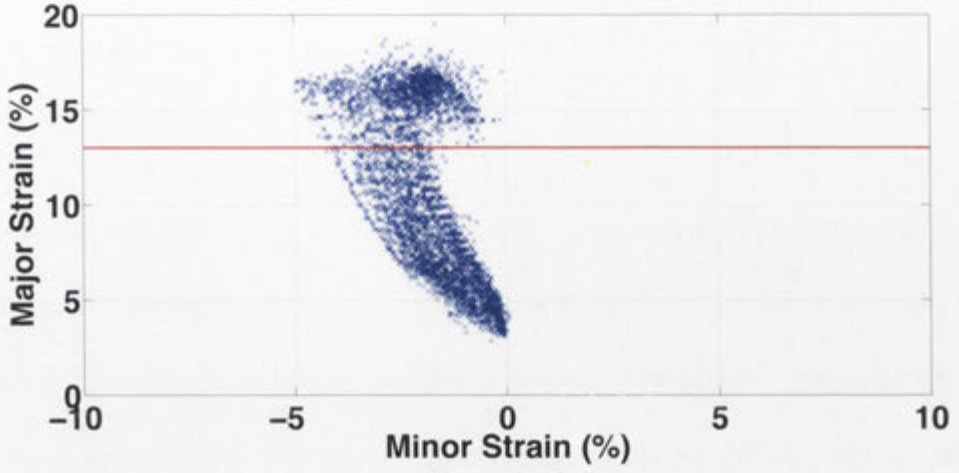

(a) 25mmHG

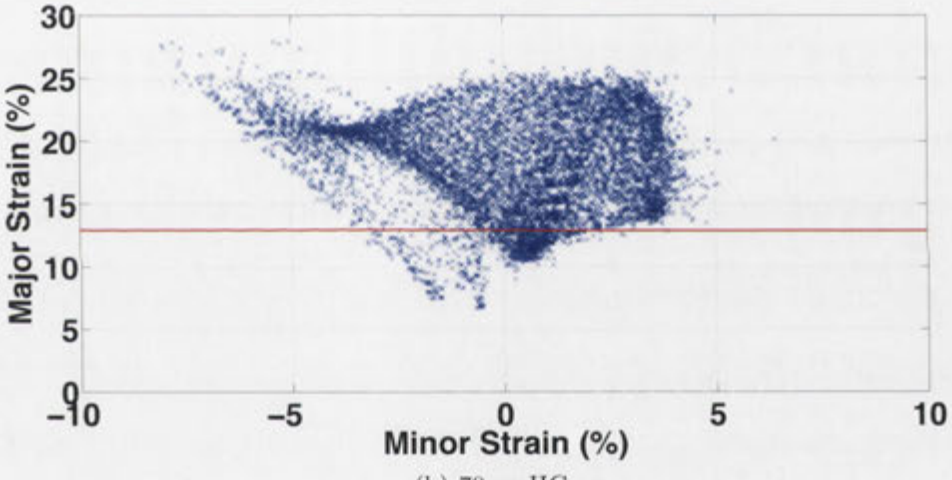

(b) 70mmHG

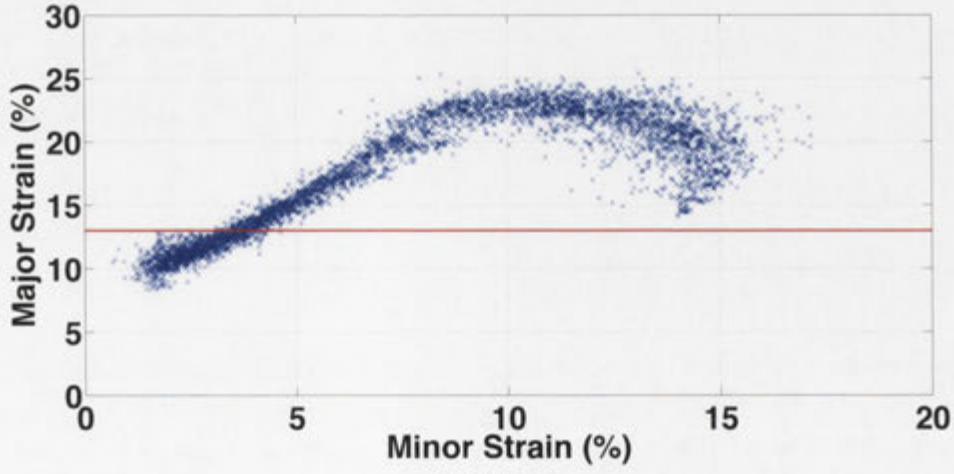

(c) 200mm

Figure 5.41: FLD of the composite layer at the failure depth in the FEA specimens

strain values of 25.7% and 3.9%. Finally, the 200mm specimen failed 35.8mm from the pole along the fibre direction, with major and minor strain values of 22.5% and 7.9%.

When compared to the failure strain values predicted using the bending equation in Section 5.2.6, it is easy to see that the predicted major strains are similar; however, there is significant difference in the minor strain values. It can be seen from the uniaxial tension (25mmHG) specimen that the FE results more closely match the minor strain values found in characterisation tests on the SRPP than the value predicted in the forming experiments using the bending equation. Since the major strain values and, at lower forming depths, the minor strain are shown to match, the difference in the minor strain at greater depths is most likely caused by a lack of information on the biaxial strain behaviour of the SRPP and a possible variation in Poisson's ratio from the value reported by the manufacturer. Herein lies a difficulty in developing a model for a manufacturing process that has not yet been attempted for a particular material: the data available does not allow full simulation of all of the deformation modes. In particular, there is no information about the compressive behaviour of the SRPP, and this parameter can cause significant changes to material behaviour in areas where the strain ratio and/or the minor strain are negative.

However, it is useful to consider the results from the FE simulation as a starting point for the development of a FLC for the SRPP. If the FLDs and failure points for the SRPP layer are combined into a single graph, Figure 5.42, it can

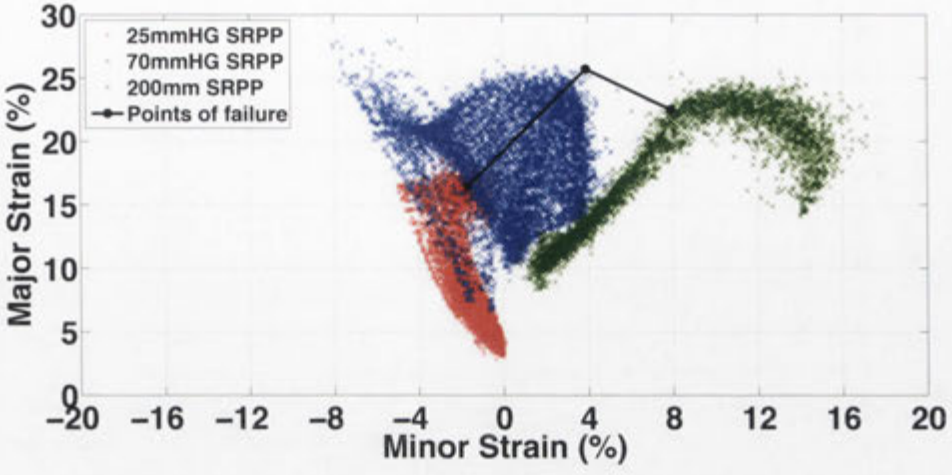

Figure 5.42: Combined FLDs for the SRPP at failure with the failed points superimposed

be seen that the failed data point for the 25mmHG uniaxial tension specimen lies in an unfailed region of the 70mmHG specimen. This agrees with the finding from the experimental specimens that the failure behaviour of the FML is more complex than just considering the major and minor strain magnitudes. If the values of major strain were similar then it could be explained by variability in the composite; however, the difference in the failure major strain for a given minor strain is as large as 9% strain, which could not be due to material variability. Therefore, it is necessary to determine the composition of the major strain at the failed point in the 25mmHG SRPP compared to the unfailed 70mmHG point. Figure 5.43(a) shows the composition of the major strain at the failed point in the SRPP layer of the 25mmHG specimen, where it can be seen that the major strain is composed entirely of longitudinal strain and the minor strain of the lateral strain. This implies that at the failure point the major and minor strain occur in the fibre direction, meaning that the fibres, which are the limiting factor

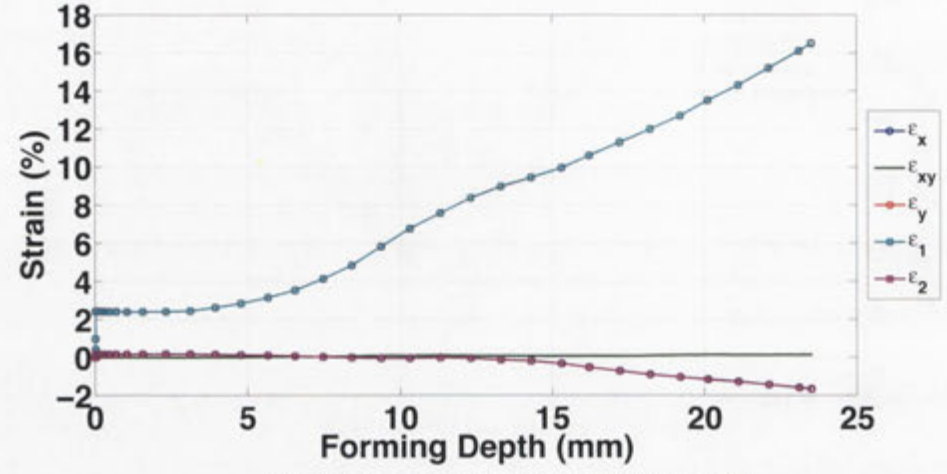

(a) Failed point in the 25mmHG specimen

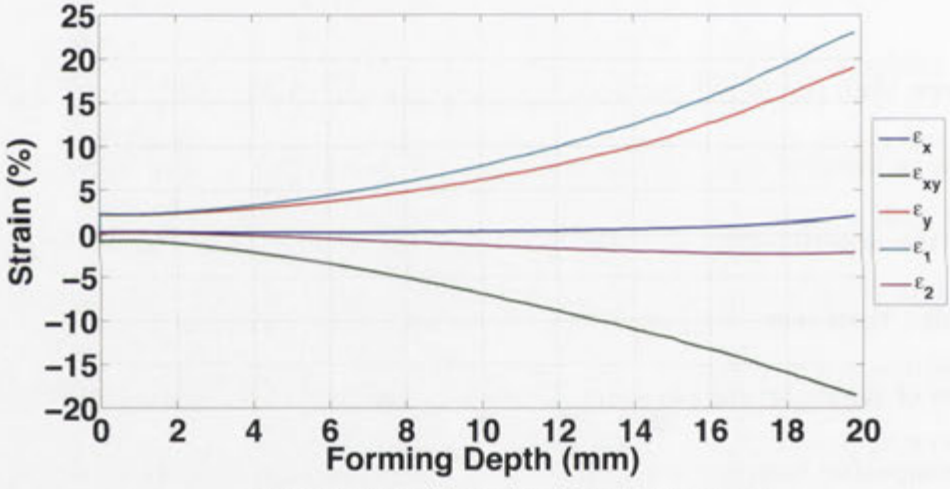

(b) Unfailed point in the 70mmHG specimen

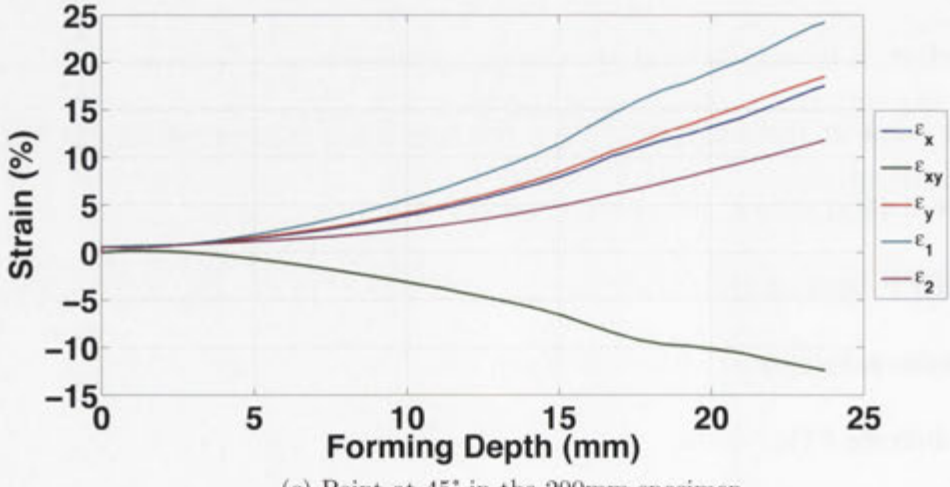

(c) Point at 45° in the 200mm specimen

Figure 5.43: Comparison of strain composition at different points in the specimens

for elongation, are experiencing the highest strain. Figure 5.43(b) shows that the major strain of the unfailed point in the 70mmHG specimen is comprised of longitudinal strain and shear strain. This is the reason the point has not failed: the material is experiencing shear strain which means the fibres are not experiencing the highest strain. The polypropylene matrix can withstand more strain than the aligned polypropylene fibres and therefore has a higher limiting major strain for a similar minor strain. In addition, trellising of the fabric also allows the longitudinal strain (ϵ_y)to be larger than the failure strain of the 25mmHG specimen because the fibres are no longer parallel to the longitudinal axis. Similarly, the point shown in Figure 5.43(c) is a point in the 200mm specimen at 45° to the fibre direction. This point shows that the major and minor strain are comprised of equal amounts of longitudinal, lateral, and shear strain which allows the point to withstand higher major strains. These results are highly significant because they show that a FLC developed from only the state of the major and minor strain in a composite is not complete, and that another variable must be considered. The most suitable variable to complete the description of the failure behaviour of the SRPP, and therefore the FML, is the principal strain angle. This angle defines the angle between the major strain and the longitudinal and lateral axes, which when compared to the fibre directions can be used to determine the limits in all material directions. This is not to say that failure can be induced in the matrix direction at all: just that the strain required to fail the matrix is much larger than that of the fibres or aluminium, and the FLC will show that the equivalent major

and minor strain states may have a different principal angle and therefore failure limit . Figure 5.44 shows the FLD for the SRPP layer in the three specimens. The principal angle is calculated using the equation

$$\tan(2\theta_p) = \frac{\gamma_{xy}}{\epsilon_x - \epsilon_y}, \tag{5.2}$$

where the angles of 0° and 90° correspond to the fibre directions and an angle of 45° corresponds to the matrix dimensions, which is strain caused by trellising.

5.4 Summary

This chapter has identified the forming behaviour of a fibre–metal laminate under isothermal conditions at room temperature. The formability was assessed using 14 specimen geometries to elicit deformation modes ranging from uniaxial tension to biaxial stretch.

In order to quantify the material behaviour, a range of metrics were used – the major and minor strain and their components (longitudinal (ϵ_y), lateral (ϵ_x), and shearing (ϵ_{xy}) strains). These strains were measured at key locations such as the pole and failure regions along the meridian line, helping to give a general overview of the behaviour across the entire surface. Finally, using these metrics, a forming limit curve was developed for the FML.

The deformation behaviour of the SRPP-based FML was found to depend on the specimen geometry and mimicked the behaviour of similar aluminium

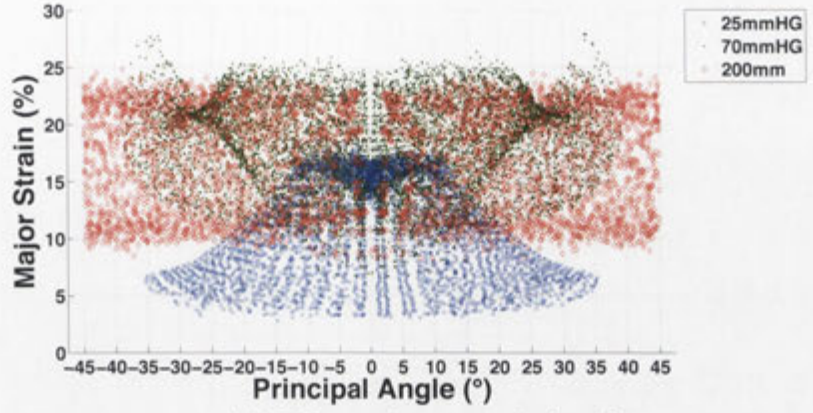

(a) Major strain vs principal angle

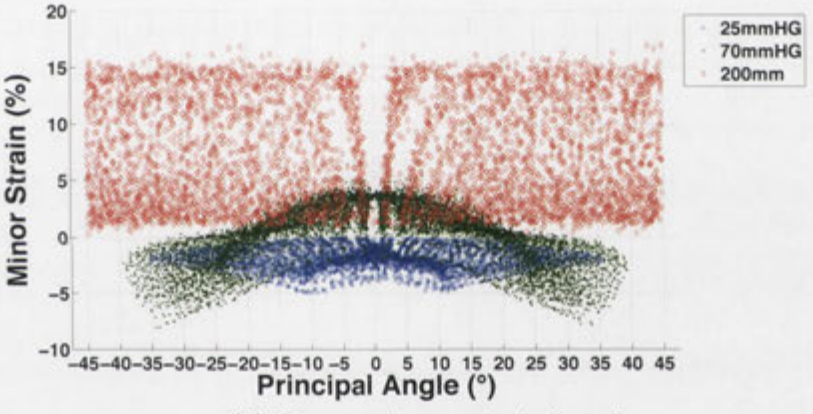

(b) Minor strain vs principal angle

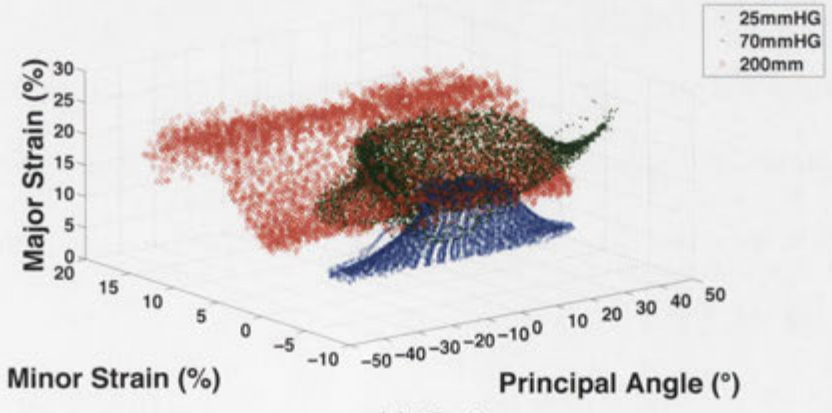

(c) 3D view

Figure 5.44: FLD of the SRPP specimens containing the principal angle

specimens. The deformation occurred through three distinct behaviours: "pre-stretch" caused by the lock ring, forming of the pole region in biaxial stretch, and finally a constant strain path until failure.

The failure of the FML was different to that of the aluminium, with the lack of a localised neck prior to failure and failure occurring as a catastrophic fracture rather than tearing. The lack of a localised neck meant that no indication of the exact failure point was provided by the strain contour; however, failure always occurred in the fibre direction due to the lower extensibility of the fibres. This was also highlighted in the surface strain contours and meridian strain plots of the FML, which showed greater uniformity compared to the aluminium. This indicates that a higher quality part can be produced for similar forming depths.

The FLC for the FML showed that the forming limits were comparable to aluminium but with some interesting results. It was shown that the state of major and minor strain alone did not provide a sufficient failure condition due to the composite's greater extensibility in the 45° direction.

Analysis of the sub-surface of the FML using bending strain equations provided insight into the behaviour of the layers not visible to the strain measurement system and showed that, at least in the case of uniaxial tension, the failure of the composite agreed with experimental testing.

A finite element model was also developed to simulate the forming of the fibre–metal laminate. Three specimens corresponding to the uniaxial tension, plane strain, and biaxial stretch deformation modes were chosen for comparison.

Verification of the models was performed by comparing the evolution of the pole, the FLD, and the meridian major strain. All of these comparisons showed good agreement between experiment and model. In addition, the effect of changing certain process parameters in the FE model, such as the SRPP layer's mechanical and interface behaviour and friction, were analysed and it was found that these changes had a significant effect on the validity of the simulation. The FE model was then used to assess the forming of the non-visible layers of the FML; it was found that the strain predicted in the SRPP and top aluminium layers using the bending equation agreed with the results of the FEA. The state of strain in the SRPP layer in the FEA was then used to assess the failure conditions in the SRPP; this verified that an additional parameter is needed to determine the criterion for failure of the laminate. It was proposed that a good parameter is the principal strain angle which indicates whether high strain occurs in either the fibre or matrix directions. However, experiments performed with the fibre direction not oriented along the longitudinal axis of the SRPP and FML are still needed to develop this failure criterion.

This study has shown that the forming behaviour of the SRPP FML is comparable to aluminium at room temperature. This insight has helped in developing a method for assessing the effect of temperature on formability.

Chapter 6

Effect of temperature on the formability of an SRPP-based FML

6.1 Introduction

The results of the experimental testing at room temperature showed that there is significant redundancy in the results obtained for the deformation behaviour of the FML. Therefore, five specimens were chosen for further analysis at higher temperatures. These specimens were chosen based on the exhibited deformation mode, the ability to observe failure, and to obtain a comprehensive FLC requiring as few experimental specimens as possible. The specimens chosen for further analysis are shown in Figure 6.1. These specimens were chosen because they exhibit deformation modes ranging from uniaxial tension to balanced biaxial stretch without overlap in the results, as shown in Figure 6.2.

This chapter will primarily follow the same format as Chapter 5 to allow easy comparison and to rapidly determine the effects of temperature on the significant aspects of the FML formability including

- the effect of temperature on the evolution of strain in two selected regions

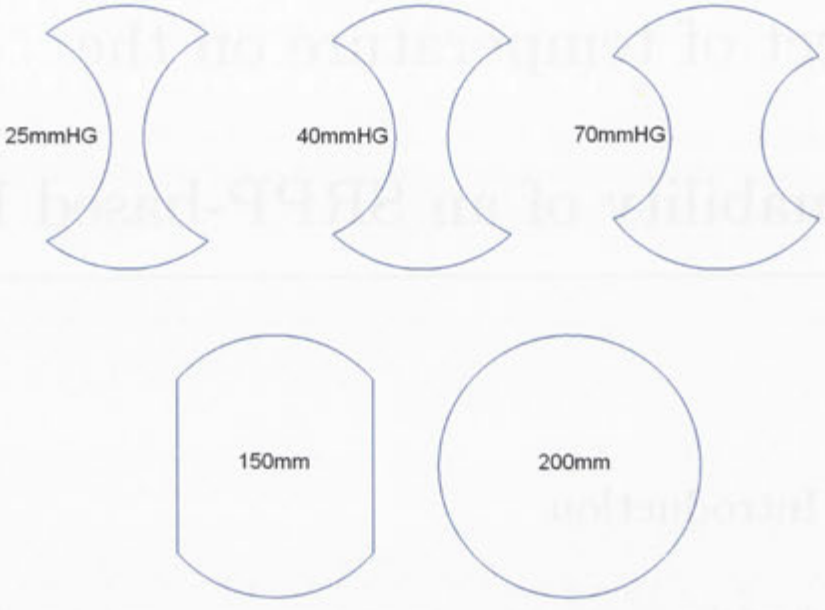

Figure 6.1: Selected specimens for high temperature experiments

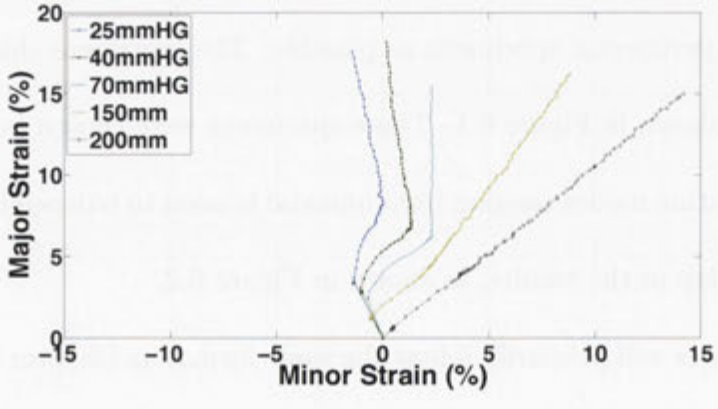

Figure 6.2: Deformation behaviour of the specimens chosen for high temperature analysis

on the surface of the specimens,

- the effect of temperature on the surface strain behaviour at various forming depths,
- the effect of temperature on the strain along the longitudinal axis of the specimens, and, most importantly
- the effect of temperature on the forming limits of the SRPP FML.

A finite element simulation is also conducted to investigate the behaviour of the sub-surface.

6.2 Experimental Work

6.2.1 Effect of temperature on the induced lock ring strain

The effect of temperature on the induced strain caused by the lock ring and preheating is shown in Figure 6.3. These figures show the state of major and minor strain on the surface of the experimental specimens at all temperature levels after applying blankholder force and heating. As all specimens had the blankholder force applied prior to heating, and the applied blankholder force was the same in each experiment, it is obvious that the pre-stretch *should* be the same for all temperatures. However, due to the application of the preheat, there are different amounts of induced thermal strain. Table 6.1 shows how the strain on the surface of selected specimens was affected by the preheat. It was found

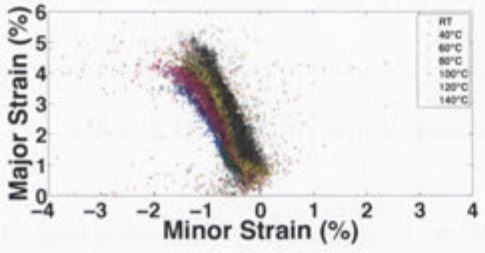

(a) 25mmHG

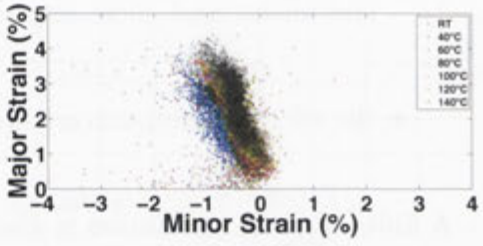

(b) 40mmHG

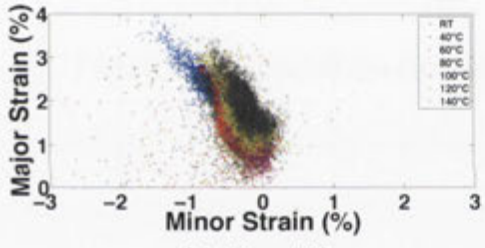

(c) 70mmHG

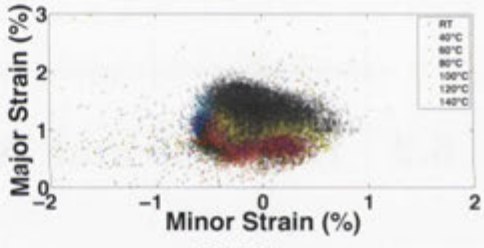

(d) 150mm

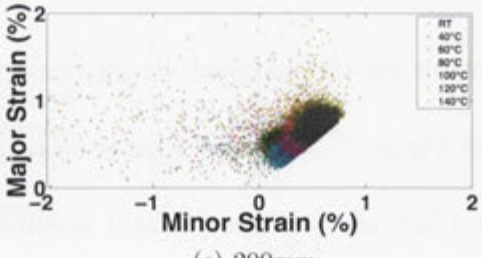

(e) 200mm

Figure 6.3: Effect of temperature on the "pre-stretch" strain in the specimens

	Mean major strain	Mean minor strain
RT	1.93%	–0.89%
40°C	2.18%	–0.75%
60°C	2.37%	–0.68%
80°C	2.49%	–0.65%
100°C	2.22%	–0.7%
120°C	2.27%	–0.46%
140°C	2.75%	–0.56%

(a) 25mmHG

	Mean major strain	Mean minor strain
RT	2.24%	–0.70%
40°C	1.391%	–0.36%
60°C	1.532%	–0.4%
80°C	1.4%	–0.25%
100°C	1.15%	–0.22%
120°C	1.694%	–0.27%
140°C	1.89%	–0.24%

(b) 70mmHG

	Mean major strain	Mean minor strain
RT	0.57%	0.34%
40°C	0.51%	0.2%
60°C	0.71%	0.39%
80°C	0.42%	0.24%
100°C	0.58%	0.39%
120°C	0.77%	0.53%
140°C	0.72%	0.49%

(c) 200mm

Table 6.1: Effect of pre-stretch and pre-heat on the surface major strain

that a generally positive increase in strain occurred in both the major and minor strain directions. The positive increase in both the major and minor strain occurs due to the thermal expansion of the die and blankholder in the longitudinal and lateral directions respectively. The specimens where a positive increase did not occur were caused by a lower initial "pre-stretch" than the room temperature specimen. This lower pre-stretch occurred due to the variability of the process. All specimen geometries had the six bolts tightened to the same torque and in the same pattern for each temperature (e.g. the 70mmHG specimen bolts were each tightened to 25Nm) which should result in a consistent pre-stretch. This variability in the pre-stretch strain is not a significant issue: the only effect is a difference in strain at all stages of deformation which is equal to the difference in pre-stretch strain.

In addition, it was found that as the temperature of the specimen was increased that an unusual effect could occur. The higher temperatures caused softening in the polypropylene matrix of the composite, and in early trials this caused the composite, and therefore the laminate, to be crushed by the blankholder which reduced the constraint applied by the lock ring. Hence, at high temperatures, the torque in the six bolts had to be adequate to fully secure the specimen but not too high to cause squeeze flow of the polypropylene matrix (which would then allow the specimen to draw in from outside the lock ring).

6.2.2 Effect of temperature on the strain evolution

Similarly to the room temperature experiments, two regions were examined for detailed strain information. In this chapter, the effect of temperature on the behaviour is assessed rather than the behaviour itself, which was discussed in the previous chapter.

6.2.2.1 Pole region

The effect of temperature on the evolution of major and minor strain at the pole of the experimental specimens is shown in Figures 6.4 and 6.5 respectively. The chosen specimens were again the uniaxial tension, plane strain, and biaxial stretch specimens. The major strain at the pole in each specimen, illustrated in Figure 6.4, shows that the temperature does not seem to have a significant effect on the evolution of major strain at the pole except to increase the depth of failure. This is because the same deformation process is being created for each specimen regardless of temperature. All specimens are being stretched over a hemispherical punch, which means that for a similar depth and assuming similar boundary and friction conditions, the strain will be the same for all temperatures. However, as shown in Figure 4.1(a), the stiffness of the SRPP is reduced at higher temperatures. This affects several important forming parameters and will have an effect on the surface strain distribution. The lower stiffness at higher temperatures will result in a reduced punch force and therefore friction at the contact surface between the specimen and the punch. This acts to increase the strain at the

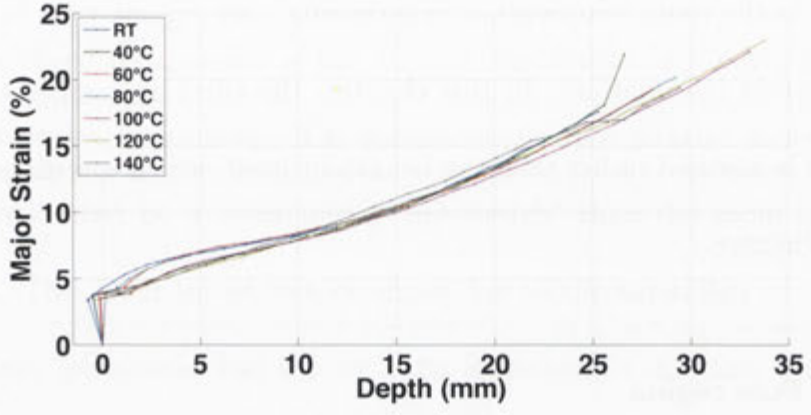

(a) 25mmHG

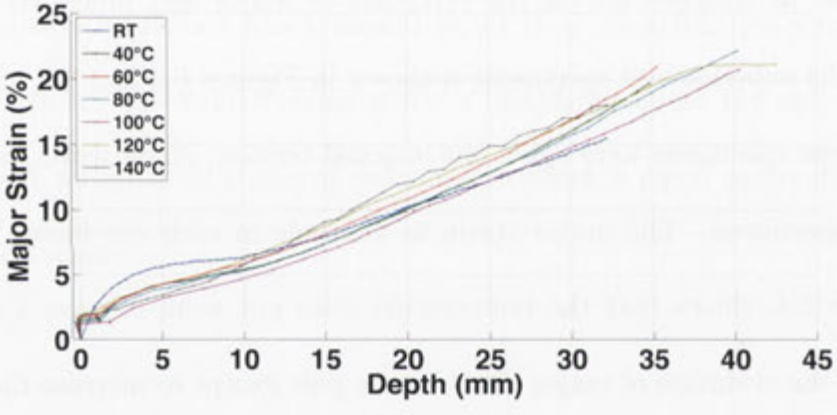

(b) 70mmHG

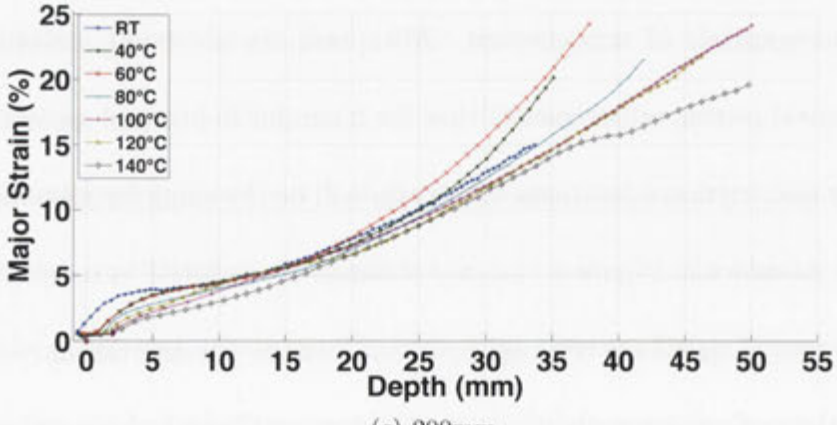

(c) 200mm

Figure 6.4: Effect of temperature on major strain evolution at the pole

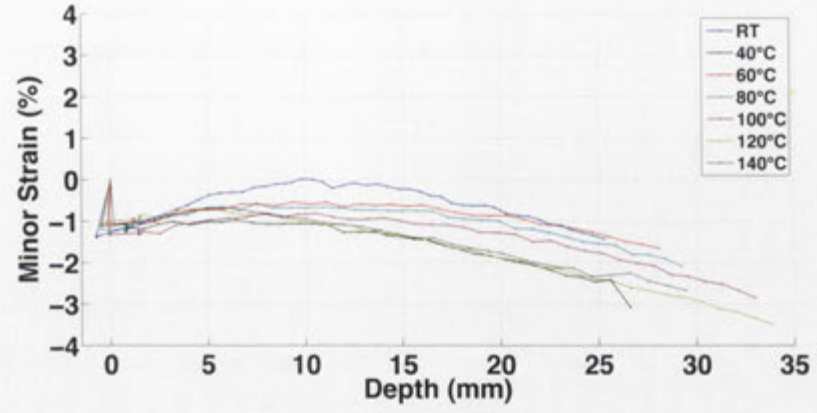

(a) 25mmHG

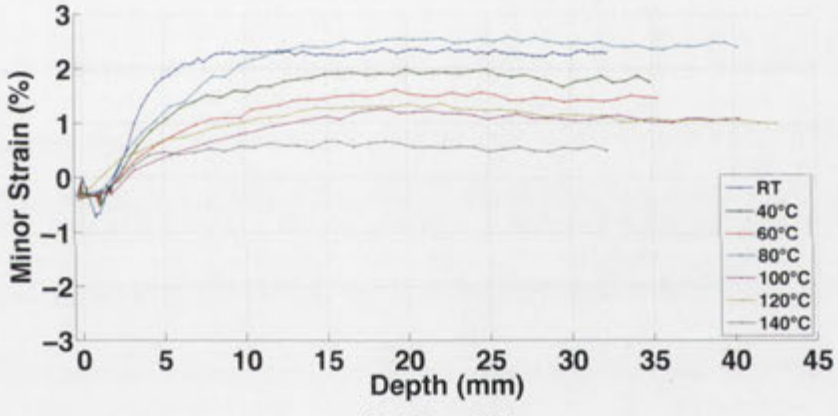

(b) 70mmHG

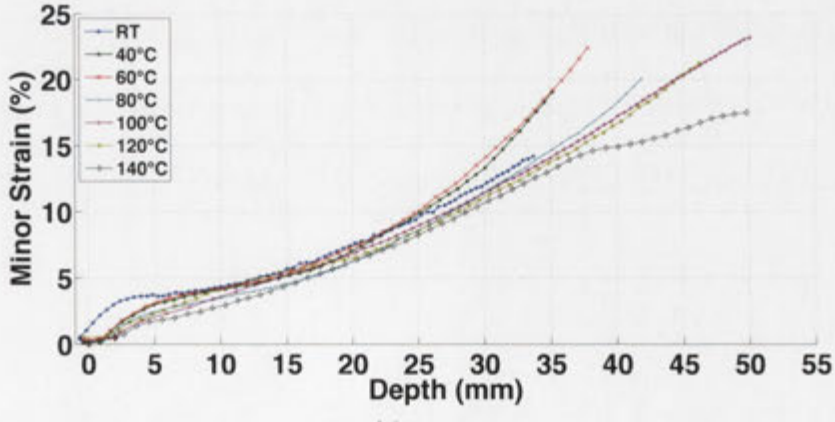

(c) 200mm

Figure 6.5: Effect of temperature on minor strain evolution at the pole

pole. This effect is counteracted by the softer composite material, which makes it easier to stretch the specimen rather than overcome friction at the pole. This reduces strain at the pole and increases the strain in the unsupported regions of the specimen. These conflicting effects and the similar deformation process are the reason that the strain evolution is similar for all specimens. This finding is significant because it shows that, for the desired shape and boundary conditions in this study, material stiffness affects the strain distribution only so far as it can affect friction.

Figure 6.5 shows that there is a possible trend in the minor strain evolution. In the 25mmHG and 70mmHG specimens, the lower temperature specimens exhibit more positive minor strain values. However, the 40°C 25mmHG specimen exhibits a more negative minor strain than some of the higher temperature specimens and the 80°C 70mmHG specimen has a more positive minor strain than the room temperature, 40°C, and 60°C specimens. This trend in the minor strain is due to the contact condition with the pole. The effect on the minor strain is identical to the effect on the major strain; the reduced stiffness of the material at higher temperatures lowers the contact pressure and therefore the friction. This allows the lateral direction to experience larger strain magnitudes which, depending on the specimen geometry, will be negative. Unlike the longitudinal direction, the lateral direction does not have an unsupported region where the reduced stiffness allows easier deformation (which counteracts the increased deformation at the pole). However, this is not the case for the 200mm specimen; this is why it shows

no discernible trend in the minor strain compared to the major strain. Here, the major and minor strain each act as a longitudinal strain and are therefore dictated by the boundary conditions, friction, and material stiffness.

It can be seen in Figures 6.4(c) and 6.5(c) that the strain in the 40°C and 60°C 200mm specimens at the pole begins to rapidly increase in the final stages before failure. The failure in these particular specimens occurs at the pole rather than the side wall, similarly to some of the aluminium hourglass specimens in the previous chapter. This result shows an improved (lower) state of friction with the punch compared to the other experimental specimens, and is the expected failure behaviour for specimens experiencing very low or nil friction with the punch at the pole. However, to reduce friction, all specimens used sheets of PTFE film, and these were the only 200mm specimens to exhibit this failure behaviour. This could be due to the effect of stiffness on the strain distribution: high stiffnesses act to increase strain at the pole and lower stiffnesses act to increase strain in the unsupported region. The low temperature specimens, such as the RT, 40°C, and 60°C specimens, have greater stiffnesses than the higher temperatures and therefore the pole region should experience higher strains than the unsupported regions for a similar contact condition with the pole. One of the 80°C 200mm specimens showed this failure behaviour, but, due to poor lighting, gave no usable strain results at greater forming depths. Other 80°C 200mm specimens did not repeat this behaviour. This indicates that the effect of the Teflon release film on friction at the pole varied from sample to sample in this study. Analysis of

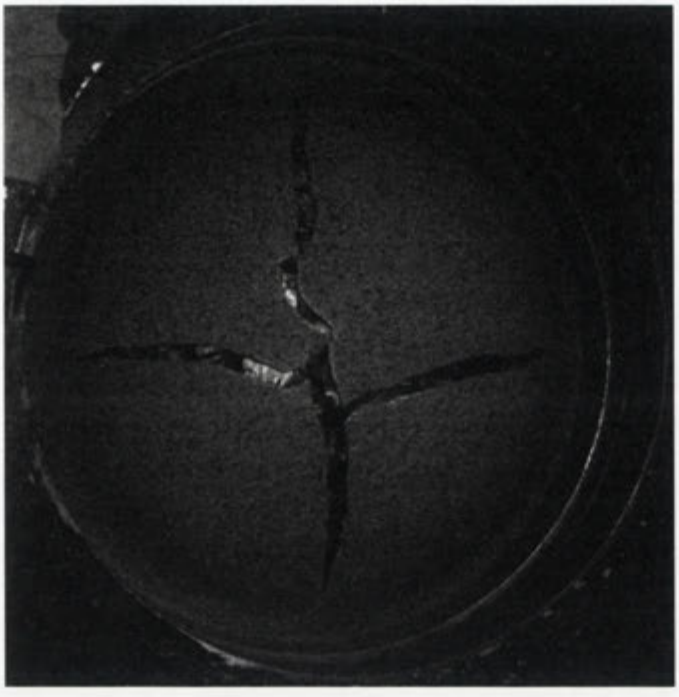

Figure 6.6: Failure behaviour exhibited by the 40°C and 60°C 200mm specimens

the strain contours and meridian strain distributions is required to determine why failure occurs in the different regions for the different temperatures. This will show the areas where the strain is increasing the fastest (either the pole or the unsupported region) and give a qualitative and quantitative indication of the friction effect in the specimens. Figure 6.6 shows the failure behaviour exhibited by the 200mm 40°C and 60°C specimens. It can be seen that failure initiated at the pole and occurred simultaneously in the longitudinal and lateral fibre directions.

The strain path of the pole region for each specimen at varying temperatures is shown in Figure 6.7. This shows that, in general, the temperature does not have an effect on the overall strain path of the specimen. There are changes in the pre-stretch (due to new deformation introduced by the preheating) and biaxial

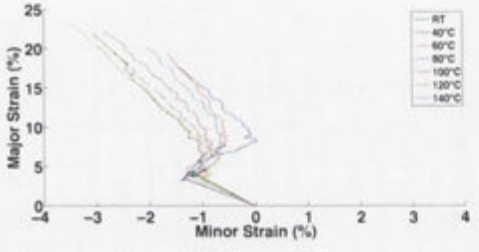

(a) 25mmHG

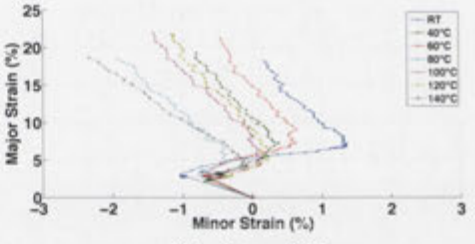

(b) 40mmHG

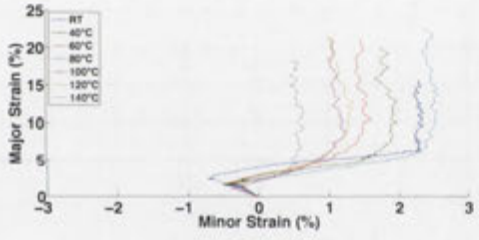

(c) 70mmHG

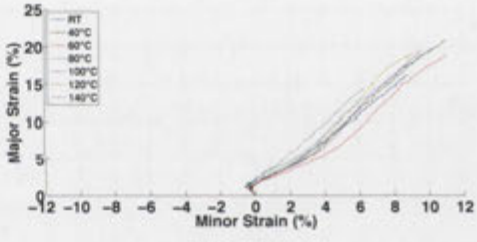

(d) 150mm

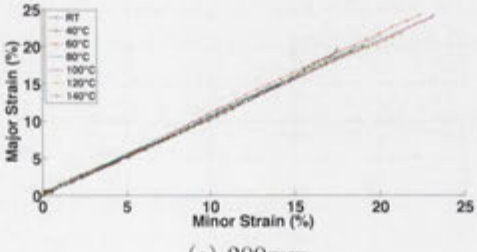

(e) 200mm

Figure 6.7: Effect of temperature on strain evolution at the pole

deformation behaviours (observed in Chapter 5), but the slope of the line during the final stages remains constant. The major difference occurs in the initial biaxial stretch region of deformation where the higher temperatures lead to a reduced amount of biaxial stretch. This explains the trend in the minor strain at the pole, shown in Figure 6.5, indicating that the stiffness of the composite layer also has an effect on this behaviour. It cannot be stated with absolute certainty, however, that temperature is the only effect on the initial biaxial stretch region. Future studies should investigate holding the temperature constant and varying the lubrication to determine the cause of the reduced biaxial stretch. Holding the temperature constant would remove the effect of reduced contact pressure and different stiffness in the unsupported region. If varying the friction at a constant temperature had no effect then the temperature of the laminate is the principal cause of the reduced biaxial stretch; otherwise, it is friction.

It can be seen that if the strain ratio of this point is calculated using only the strain at a given depth, the strain ratio will be affected by temperature, as shown in Figure 6.8. This is because the magnitude of the minor strain is a consequence of the initial biaxial stretch deformation and therefore specimens with the most negative minor strain and strain ratio experience the lowest amount of initial biaxial stretch. The trend in the 25mmHG and 70mmHG specimens is a reduced (more negative) strain ratio with increased temperature and forming depth, which is consistent with the lower initial biaxial stretch with increased temperature. However, the 5mm depth shows a lower strain ratio than the 10mm

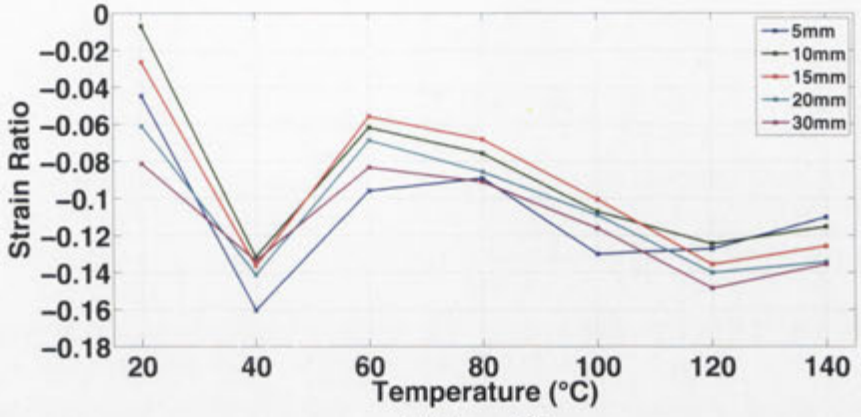

(a) 25mmHG

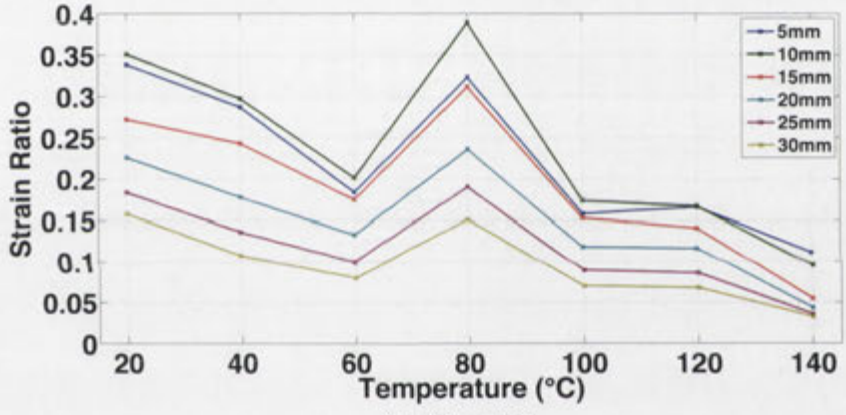

(b) 70mmHG

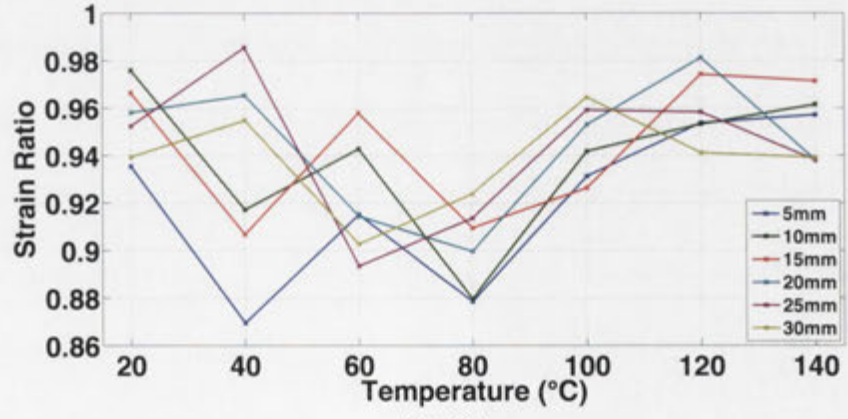

(c) 200mm

Figure 6.8: Effect of temperature on the strain ratio at the pole in selected specimens

	RT	40°C	60°C	80°C	100°C	120°C	140°C
25mmHG	–0.15	–0.14	–0.12	–0.12	–0.14	–0.16	–0.16
40mmHG	–0.1	–0.1	–0.09	–0.11	–0.09	–0.08	–0.16
70mmHG	0	–0.01	0	0	0	–0.02	0
150mm	0.56	0.5	0.58	0.53	0.45	0.52	0.52
200mm	0.94	0.96	0.91	0.95	0.97	0.97	0.88

Table 6.2: Strain ratio of the pole calculated using the evolution of strain to failure

in the 25mmHG and 70mmHG specimens. This would mean that it is within the biaxial stretch region prior to transition to the strain path to failure as the strain ratios would begin to go more negative. The figures show that the change in strain ratio with temperature is a maximum of 0.1 in the 25mmHG specimens, 0.35 in the 70mmHG specimens, and 0.1 in the 200mm specimens. The large variance in the 70mmHG is caused by the values observed in the 80°C experiment which does not follow the trend of the other specimens. In addition, no trend is seen in the 200mm specimens because, as seen in Figure 6.7, the pole exhibits approximately balanced biaxial stretch throughout the entire process.

However, the slope of the strain path in each specimen, and at each temperature, during the final deformation behaviour remains constant and therefore the strain ratio behaviour can be described in this region. Table 6.2 contains the calculated slope of the evolution of strain in the final strain path, and it is evident that the variance in the strain ratio calculated using the strain evolution is low. This was expected, as the strain behaviour of the specimens depends on the specimen geometry, not the material.

Finally, the major and minor strain at the pole are again completely comprised

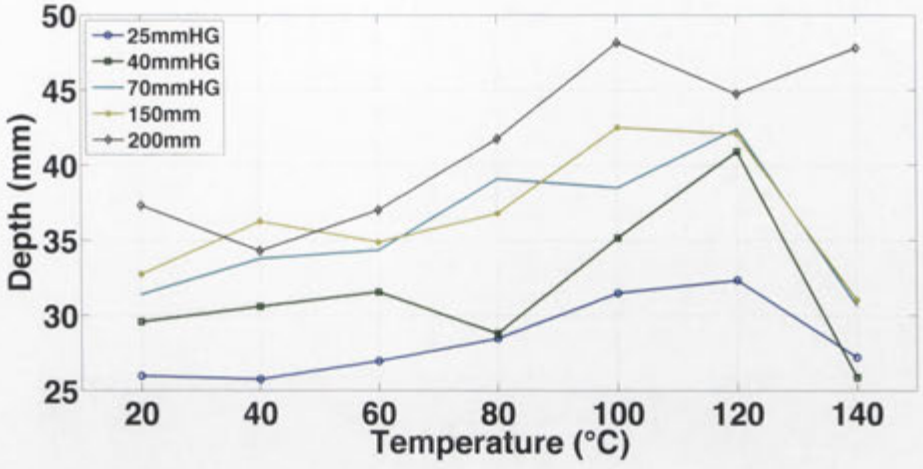

Figure 6.9: Effect of temperature on the failure depth of the specimens

of the longitudinal (ϵ_y) and lateral (ϵ_x) strain respectively.

6.2.2.2 Region of failure

Figure 6.9 shows the effect of temperature on the failure depth of the experimental specimens. The trend in the failure depths for all specimens is an increased forming depth for increased temperature until a sudden drop in forming depth at 140°C. This increased forming depth lends credence to the finding in the previous chapter that the failure of the SRPP FML specimens is triggered by the failure of the composite layer. This is because the forming temperature primarily affects the stiffness and failure strain of the composite. However, this cannot explain the drop in failure depth at 140°C. The major effect occurring at or above this temperature is the melting of the adhesive layer, as shown in the DSC curves provided in Figure 3.3. In all specimens (other than the 25mmHG specimen) failure at 140°C occurred only in the aluminium layer. Figure 6.10 shows the failed 140°C 70mmHG specimen where failure is observed in the adhesive and the

Figure 6.10: Failure of the adhesive bond and aluminium at 140°C

	RT	40°C	60°C	80°C	100°C	120°C	140°C
25mmHG	13mm	5.8mm	6.7mm	9.5mm	12.4mm	5.5mm	33.4mm
40mmHG	17mm	5.4mm	13.5mm	36.2mm	16.4mm	34.4mm	19mm
70mmHG	27mm	17.5mm	22.5mm	46.6mm	36.8mm	26.3mm	31.4mm
150mm	31mm	29.9mm	32.5mm	33.4mm	40.8mm	43.6mm	35.4mm
200mm	33.7mm	0mm	7mm	30.2mm	41.8mm	46.1mm	50.8mm

Table 6.3: Distance from the pole of the failure point in the experimental specimens

aluminium, and no failure occurs in the SRPP layer. This implies that while the fracture of the SRPP layer is the precursor for failure at the lower temperatures, it is also providing support to the aluminium layer through dispersion of strain and reducing the effect of friction on the bottom layer through transverse shear.

Table 6.3 shows the distance from the pole at which failure occurs. Due to the conflicting effects of reduced stiffness and friction at the pole, it is difficult to predict the variation of the distance of failure from the pole with increasing temperature. All specimens used the same lubrication scheme with the punch and should therefore have similar values for the friction coefficient (μ). This should lead to the distance of failure from the pole increasing with increasing temperature as the material becomes easier to deform in the unsupported region rather than overcome friction with the punch. However, the lower stiffness also reduces the contact pressure at the pole and can therefore lead to higher strains in this region. The results in Table 6.3 provide qualitative information about the state of friction at the pole: that is, the distance of failure gives an indication of both the coefficient of friction and the contact pressure at the punch. If the failure distance is high this means that friction at the pole must be high – or the

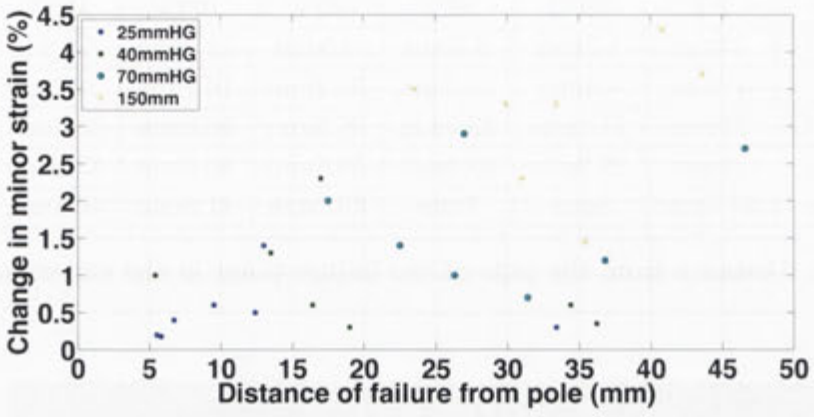

Figure 6.11: Effect of friction on the biaxial stretch at the pole

specimen is deforming more easily in the unsupported region. *Either way, there is less deformation in the pole region.* By plotting the magnitude of the initial biaxial stretch at the pole against the failure distance from the pole it is possible to determine whether there is an effect of reduced pole deformation (arguably friction). Figure 6.11 shows the correlation between the distance of failure and range of minor strain experienced in the initial biaxial region at the pole. This shows that there is a slight trend for increased biaxial stretch as the failure moves further from the pole. This implies that as the region of highest strain moves away from the pole region, which is the consequence of increased friction, the initial biaxial stretch increases. However, this effect will require further research including a full tribological investigation to determine which factor contributes more to the strain distribution and evolution – the ease of deformation or the lowered contact pressure. What is interesting is that the initial biaxial stretch in the specimens is undesirable since the aim of formability experiments is to achieve proportional loading throughout the entire test. In addition, a tensile test using

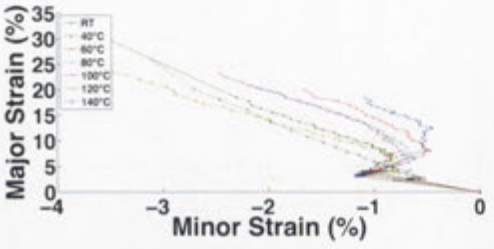

(a) 25mmHG

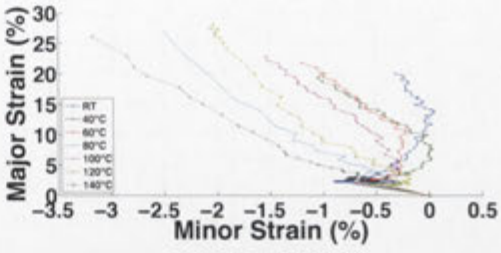

(b) 40mmHG

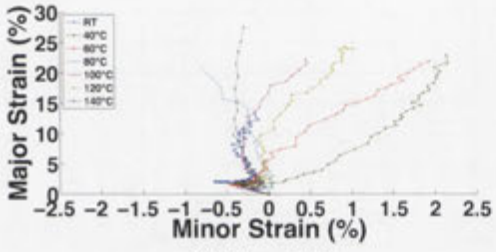

(c) 70mmHG

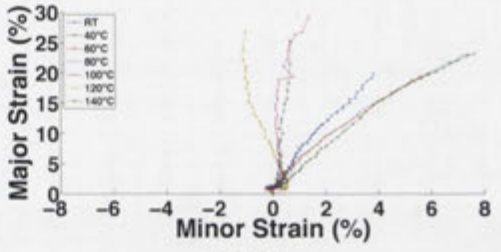

(d) 150mm

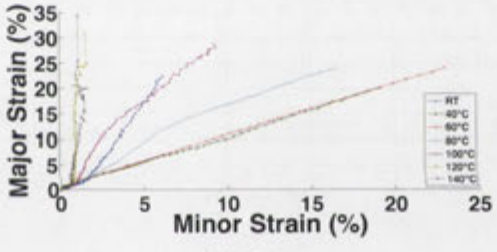

(e) 200mm

Figure 6.12: Effect of temperature on the strain evolution at the point of failure

standard test specimens would not exhibit an initial biaxial stretch behaviour. It is probable that it is caused by the hemispherical punch, and so other punch shapes should be investigated.

Figure 6.12 shows the effect of temperature on the strain evolution at the point of failure in the experimental specimens. It is possible to relate the strain behaviour at this point to the distance at which failure occurs from the pole. This can be seen in the 25mmHG, 40mmHG, and the 40°C and 60°C 200mm specimens where, due to the proximity of failure to the pole, the deformation behaviour is

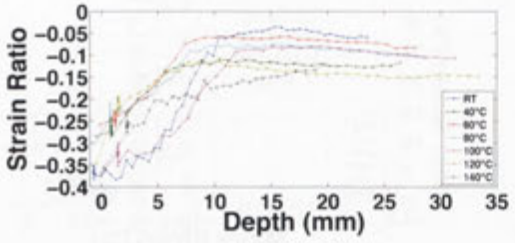

(a) 25mmHG

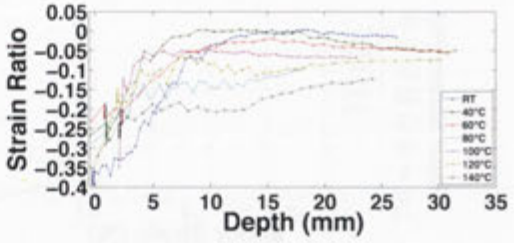

(b) 40mmHG

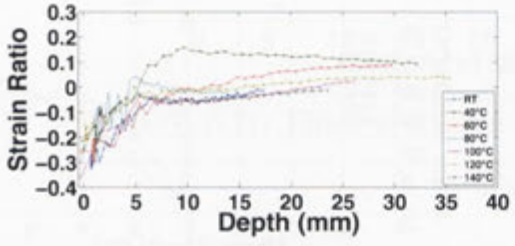

(c) 70mmHG

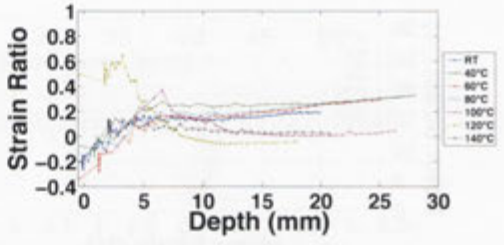

(d) 150mm

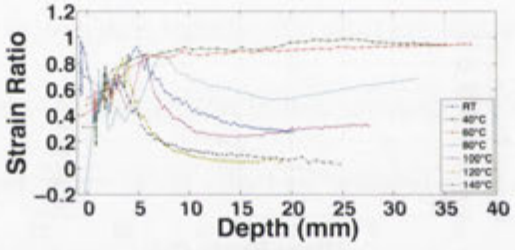

(e) 200mm

Figure 6.13: Evolution of the strain ratio at the failure region vs forming depth

similar to that in Figure 6.7. Those specimens which exhibited deformation modes closer to plane strain also had their failure occurring further from the pole. Figure 6.13 shows the evolution of the strain ratio at the point of failure at all forming depths. These figures show that, in general, the failure region of the specimens goes through three separate deformation behaviours. These include:

- an initial strain ratio for the pre-stretch and preheat,
- a positive or negative change, and finally,
- a straight line.

The second deformation behaviour is where the failure region is different from the pole (in cases where they do not coincide). In the pole, the change is always positive due to the biaxial stretch induced by the hemispherical punch. There are a few interesting specimens. Firstly, the 120°C 150mm specimen shows significantly different strain ratios in the first and second deformation regions where, unlike the other temperatures, the strain ratio for the pre-stretch is positive and the trend of the second region is negative. Also, the 40°C and 60°C specimens highlight the fact that they are at the pole by exhibiting strain ratios of approximately 1.

Figures 6.14 and 6.15 show the evolution of the major and minor strain at the failure point. One of the key features in these figures is the very metal-like behaviour of the 140°C specimens, where the strain begins to rapidly increase compared to the non-failed regions. This is not seen in any of the lower temperature specimens. This indicates a preferential localisation of strain in the failure region as opposed to the generally uniform increase in the other specimens, with the failure determined by a fracture initiated in the composite. This early localisation of strain in the aluminium layer of the 140°C specimen shows that, in the lower temperature specimens, the fibres in the composite layer prevent localised necking in the aluminium layers. This explains why the 140°C specimens exhibit reduced forming depths, why the composite layer is not distributing the deformation across a larger area of the aluminium layers, and why they are necking earlier. This is a significant finding as it means that the metal, as part of a laminate, is showing better formability than its monolithic formability. This could be

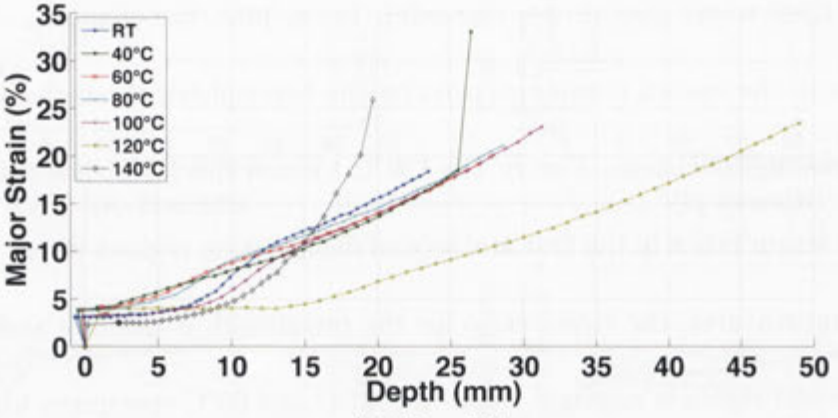

(a) 25mmHG

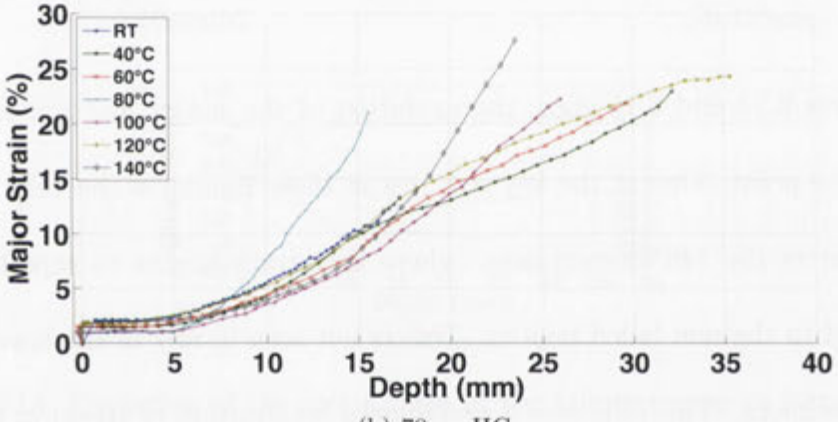

(b) 70mmHG

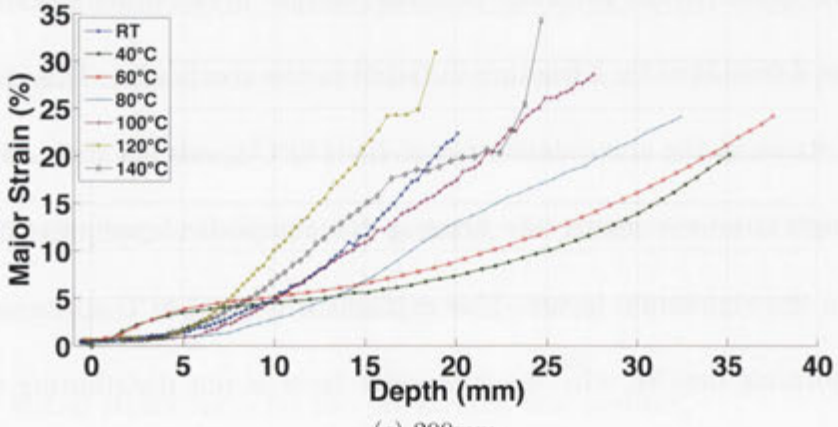

(c) 200mm

Figure 6.14: Effect of temperature on the major strain evolution at the failure point vs. the forming depth

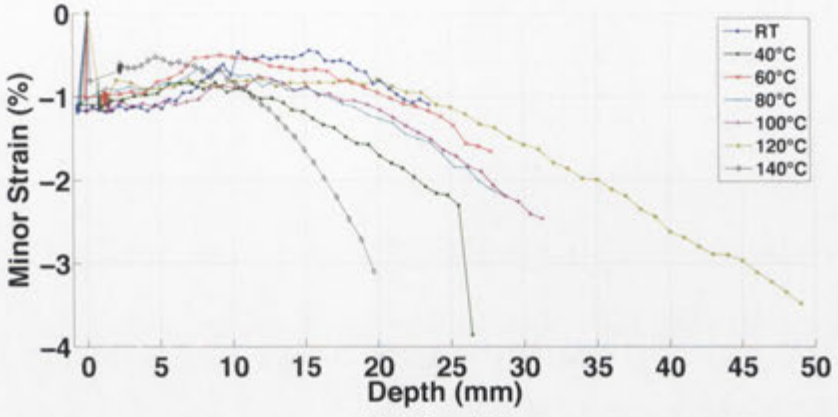

(a) 25mmHG

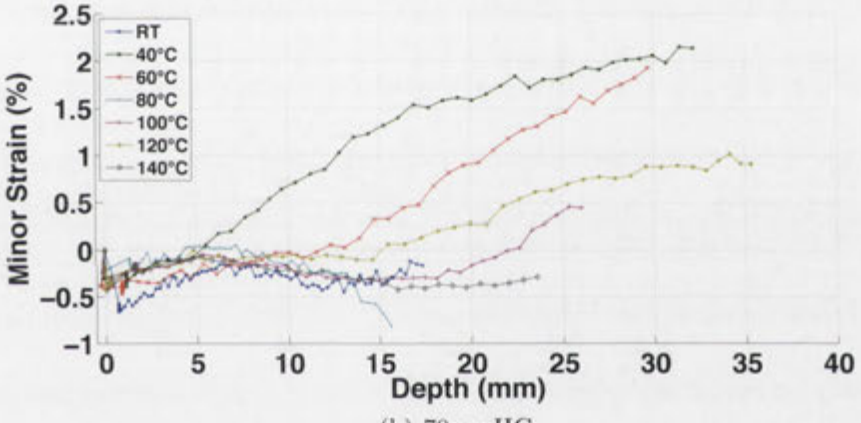

(b) 70mmHG

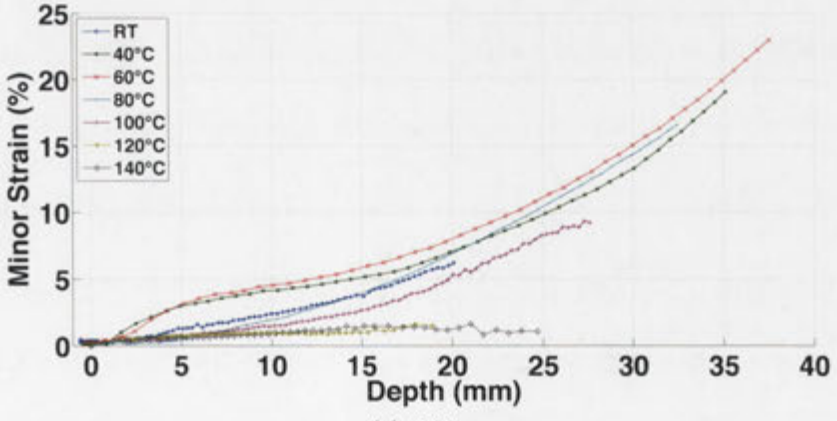

(c) 200mm

Figure 6.15: Effect of temperature on the minor strain evolution at the failure point vs. the forming depth

extended to the use of a low cost composite or polymer whose only purpose is to allow the formation of more complex shapes, not providing added reinforcement after forming.

6.2.3 Surface strain behaviour

The previous sections in this chapter show that the strain behaviour of the pre-stretch, pole, and failure region is similar across all temperatures, with the variations occurring not in the overall behaviour but in the strain values around which the behaviour occurs. Shown in Figures 6.16 , 6.17 , and 6.18 are the surface stain contours for the uniaxial tension (25mmHG), plane strain (70mmHG), and biaxial stretch (200mm) specimens at various temperatures. These figures show that the overall strain distribution for each of the experimental specimens is relatively unchanged by temperature. An interesting aspect of these images is the difference in the apparent strain variation between the room temperature and high temperature specimens, particularly Figures 6.17(b) and (c) and Figures 6.20(c) and (d). This behaviour was especially prevalent in the GFRP specimens which will be presented in Chapters 7 and 8. However, this behaviour also appears in the room temperature GFRP specimens, which used the same resolution measurements as the room temperature SRPP, indicating that the effect is much more pronounced in those specimens. The textured behaviour indicates that the surface strain is affected by the unit cell of the composite layer, shown in Figure 6.19. This shows that, in the area of the unit cell containing the lateral fibre in

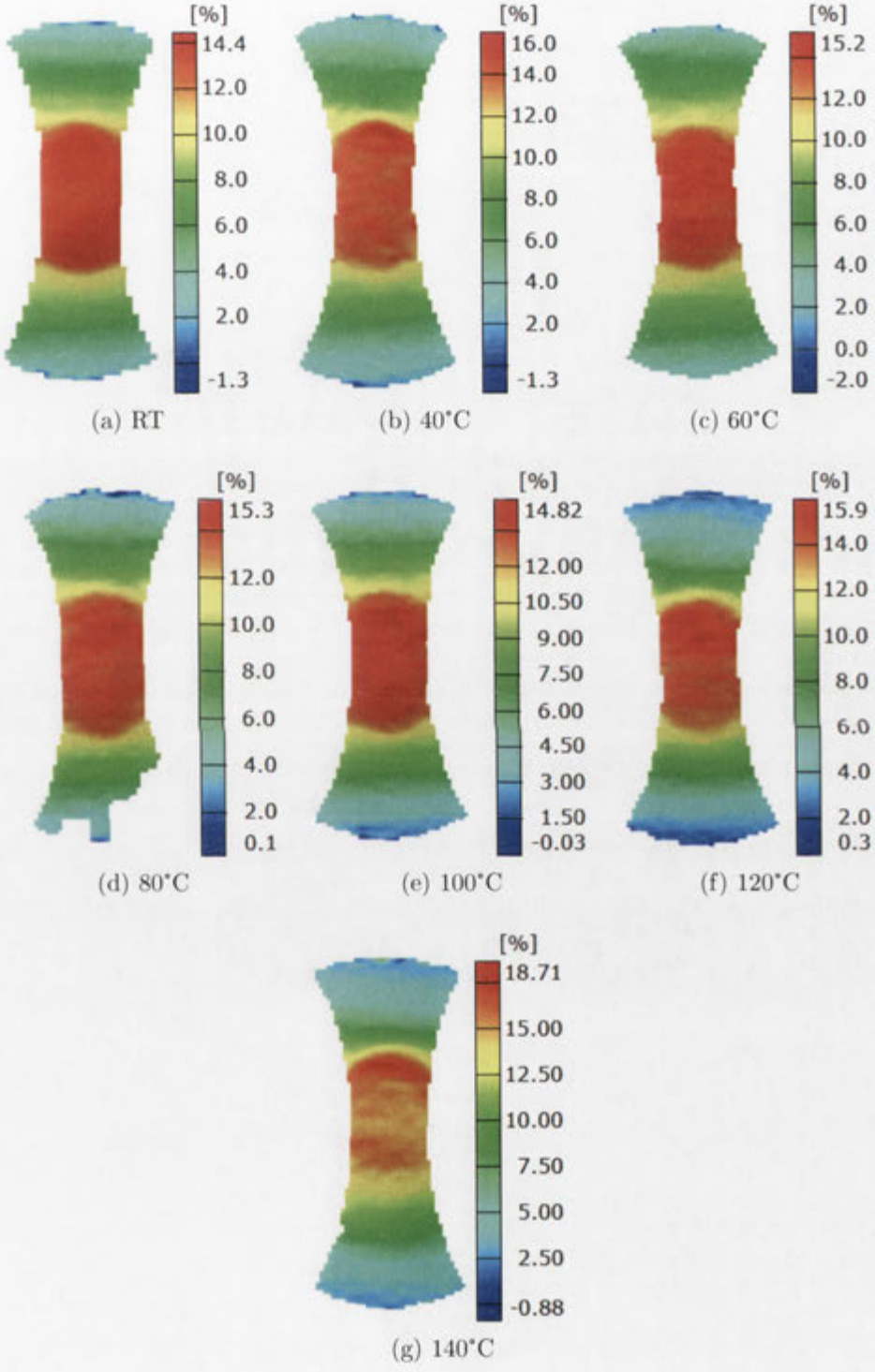

Figure 6.16: Surface strain contours of the 25mmHG specimens at a depth of 20mm

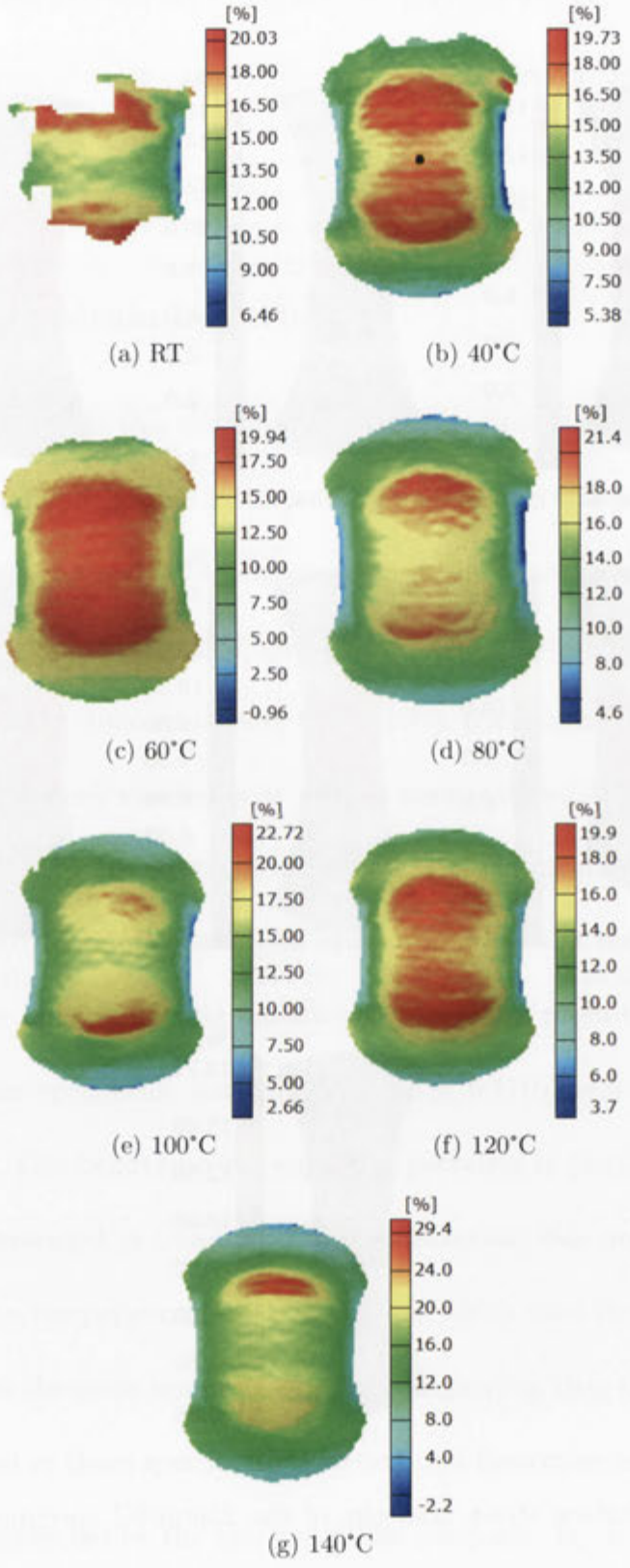

Figure 6.17: Surface strain contours of the 70mmHG specimens at a depth of 30mm

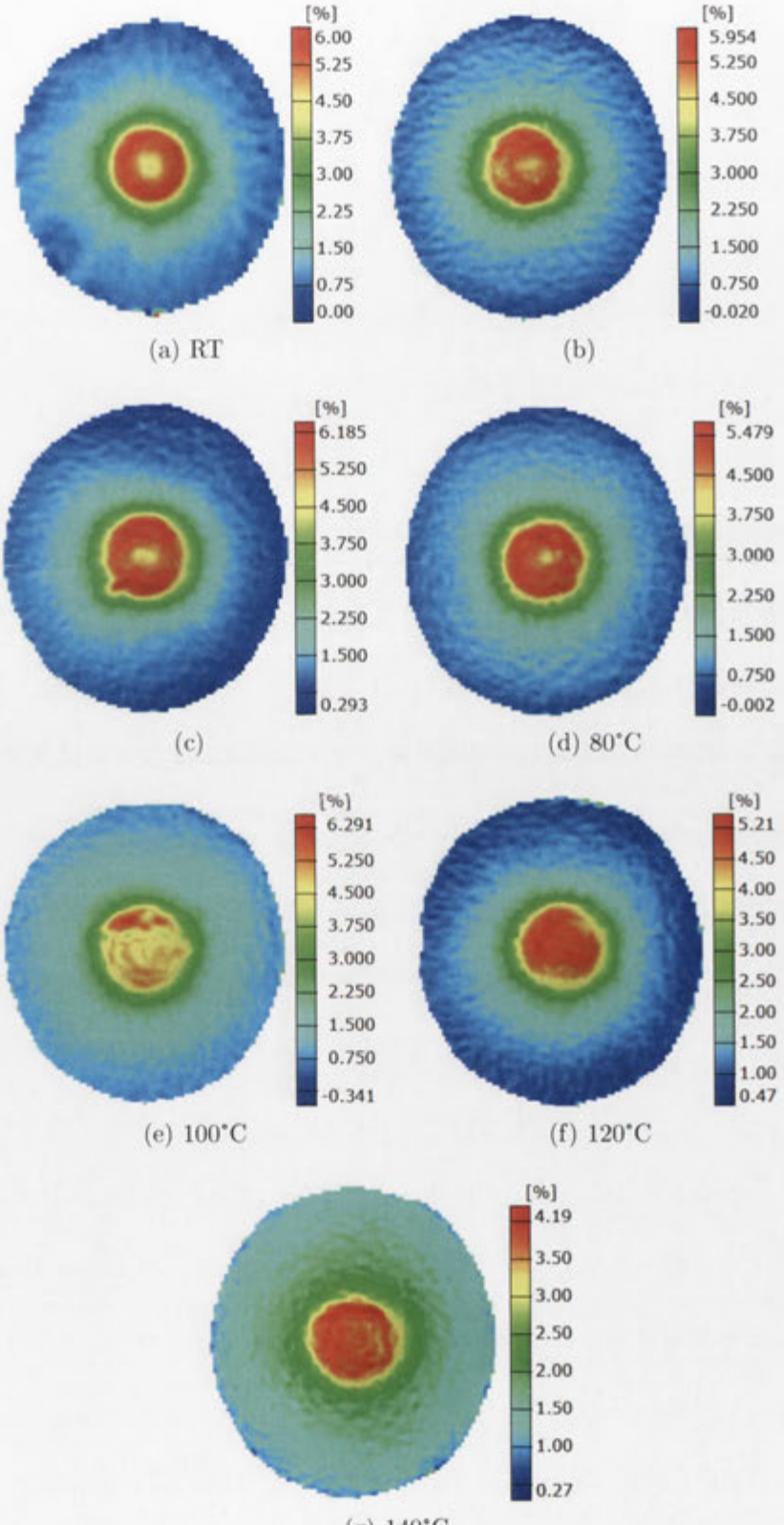

(a) RT (b)

(c) (d) 80°C

(e) 100°C (f) 120°C

(g) 140°C

Figure 6.18: Surface strain contours of the 200mm specimens at a depth of 10mm

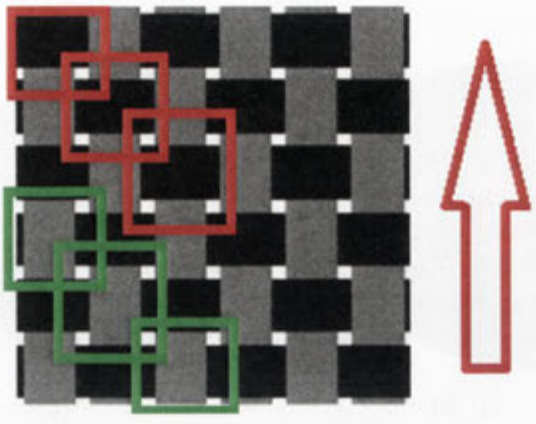

Figure 6.19: Cause of the textured surface strain

the foreground (highlighted in red), the strain will be higher than the areas where the longitudinal fibre is in the foreground (highlighted in green). This is due to the higher proportion of stretching in the matrix direction compared to the fibre direction, an effect which was found by Dhar Malingam [77] and Venkatesan [64] to significantly improve the formability of composite materials. However, those studies found that the improved formability was due, at elevated temperatures, to extension occurring at 45° to the fibre direction through fibre trellising in the softened matrix, whereas the higher resolution in this study shows that preferential stretch occurs in the matrix even in the 0/90° directions. This also has major implications for the strain in a material. If the strain through the thickness of the composite layer is considered, then it is clear that the linear bending strain distribution is not due to the different properties of the fibres in the local longitudinal and transverse directions (i.e. the distribution of bending strain through the thickness is in different directions for the warp and weft fibres).

In addition to the specimens in Figures 6.16, 6.17, and 6.18 the surface strain

contours are also provided for the 150mm specimen in Figure 6.20. This specimen was chosen for review because unlike the thinner specimens, which are not restricted in the lateral direction, and the 200mm specimen, which is forcibly restricted in the lateral direction, the 150mm specimen has the capability to preferentially draw in the lateral (fibre) direction and stretch in the 45° direction (in a similar manner to that observed by Dhar Malingam [77] and Venkatesan [64]. In this work it was thought that even with the enforced boundary conditions in the experimental specimens that there might be some effect of a difference in stiffness. Figure 6.20 shows that this behaviour is not evident. The strain in the lateral direction, especially close to the edge, is much lower than in the 45° and longitudinal directions. However, it is not clear from these images exactly how much of the strain is due to the longitudinal strain, which is always high due to the boundary conditions, and how much is due to stretching in the matrix. After further investigation it was found that the shear strain in the 150mm laminates is negligible compared to the lateral and longitudinal strains, indicating that the enforced boundary conditions have more of an effect than the softened matrix.

Figures 6.21, 6.22, and 6.23 show the effect of temperature on the FLD of selected specimens. The 25mmHG hourglass specimens show no significant change in forming behaviour at any selected depth. Similarly, the 200mm specimen shows only a limited effect of temperature on the overall strain behaviour of the specimen. There are some differences such as the increased biaxiality of the 60°C specimen and the lower strain magnitudes in the 140°C specimen. The 70mmHG

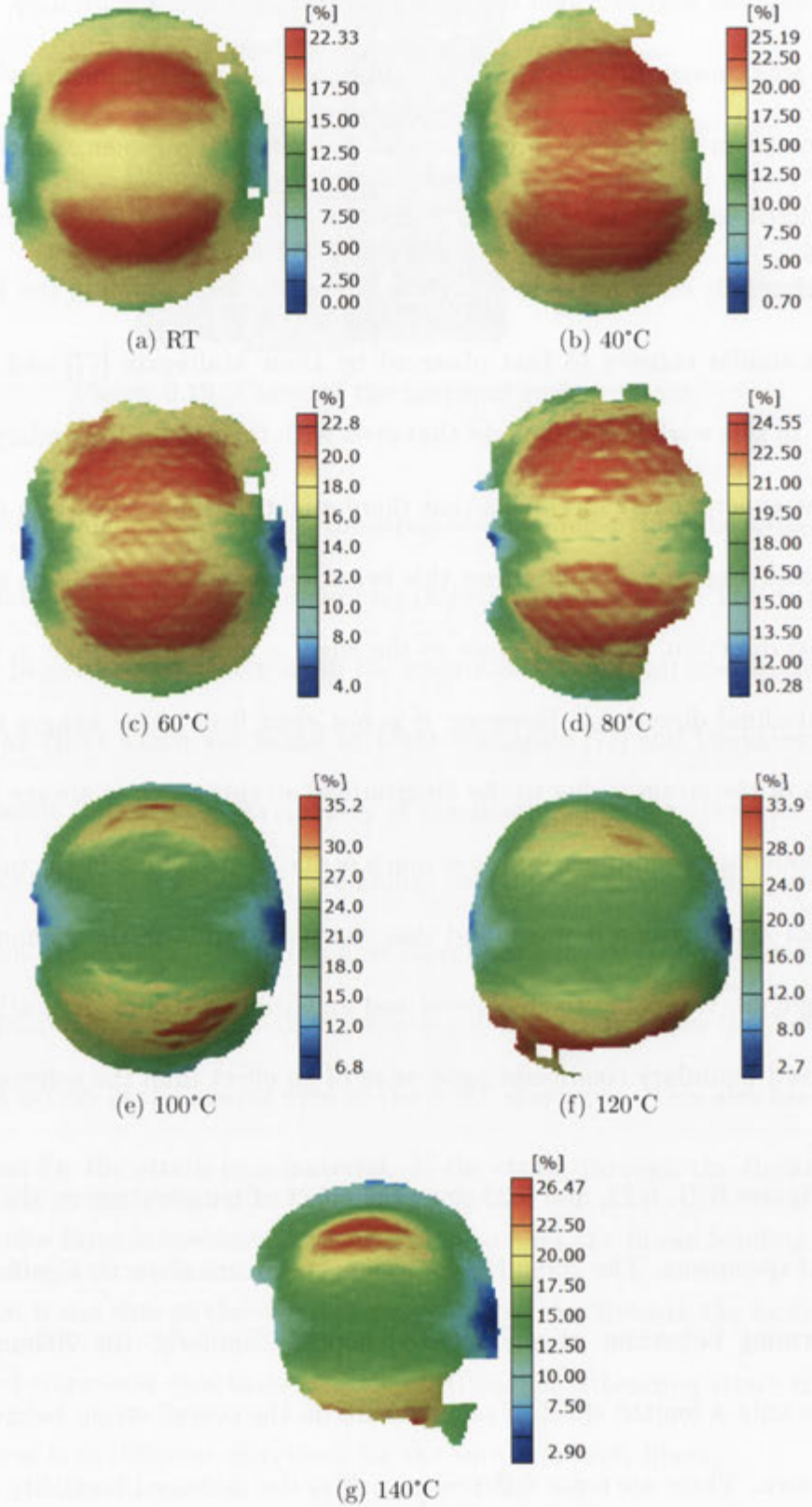

Figure 6.20: Surface strain contours of the 150mm specimens at the depth of failure

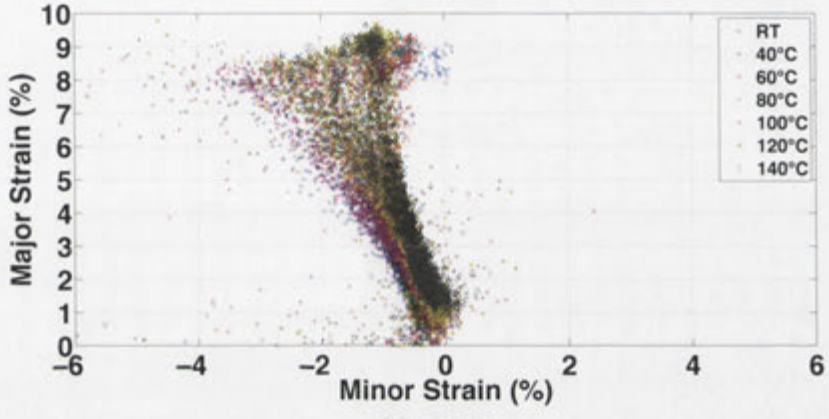

(a) 10mm

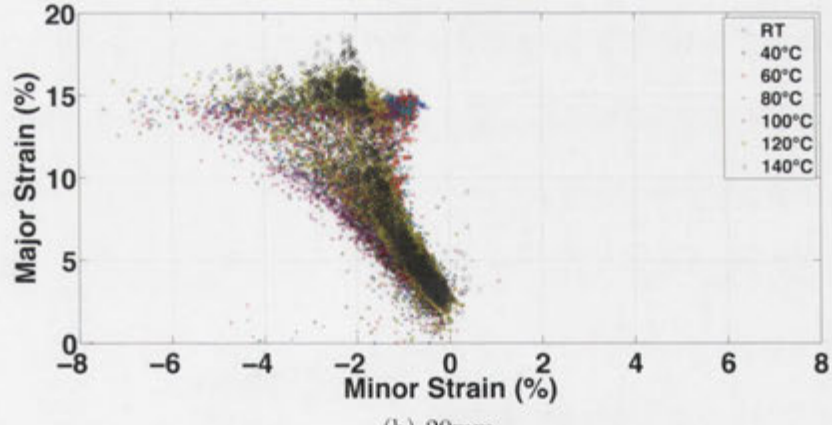

(b) 20mm

Figure 6.21: Effect of temperature on the FLD for the 25mmHG specimens

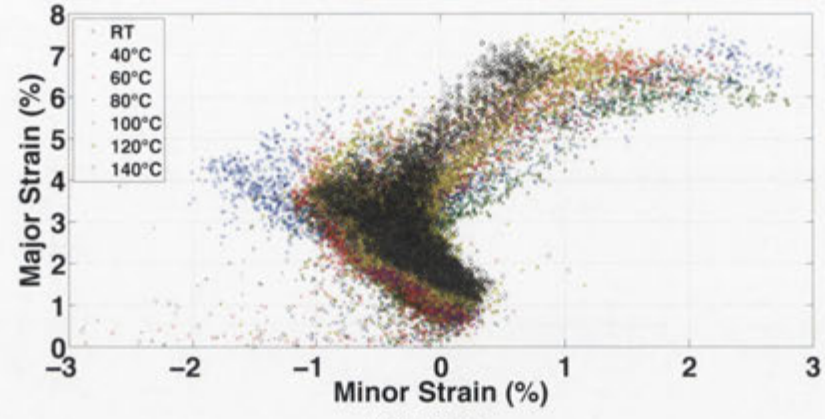

(a) 10mm

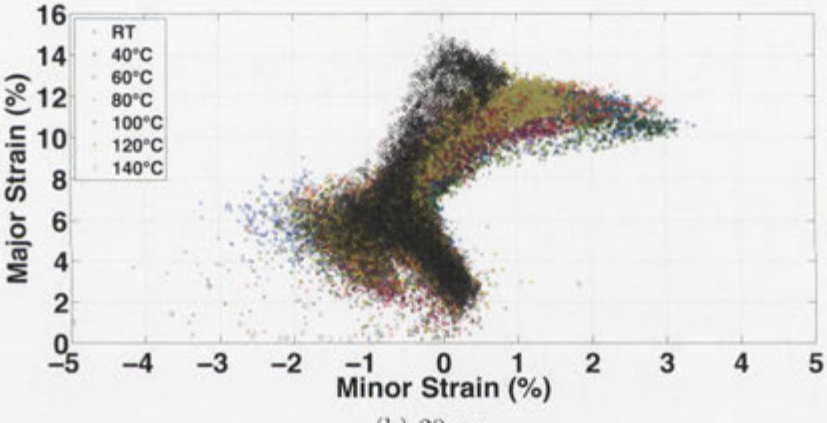

(b) 20mm

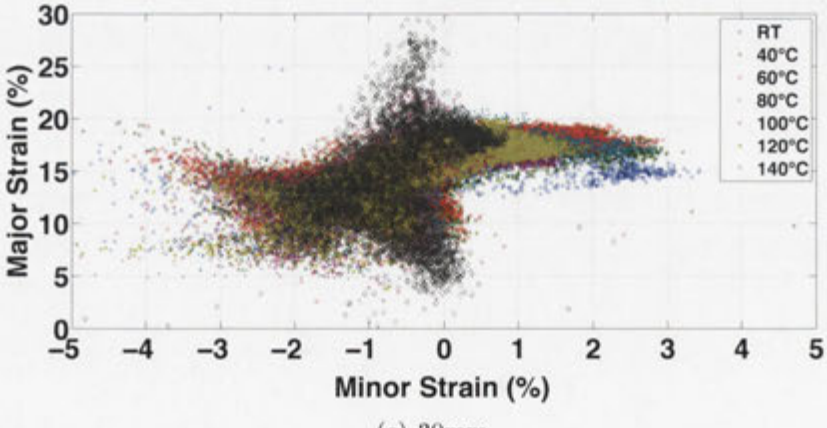

(c) 30mm

Figure 6.22: Effect of temperature on the FLD for the 70mmHG specimens

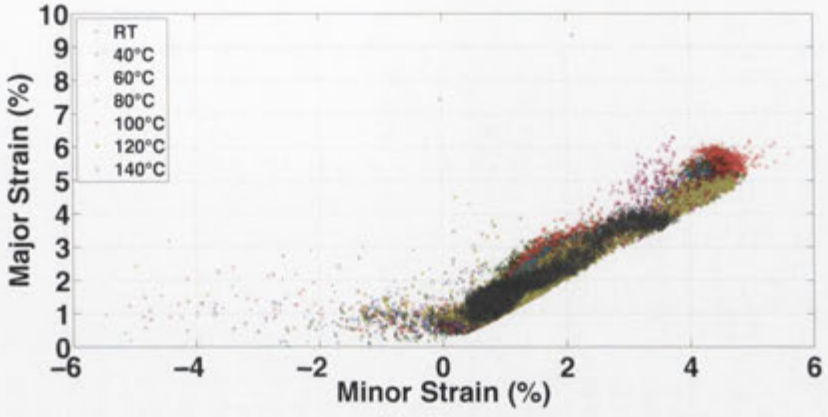

(a) 10mm

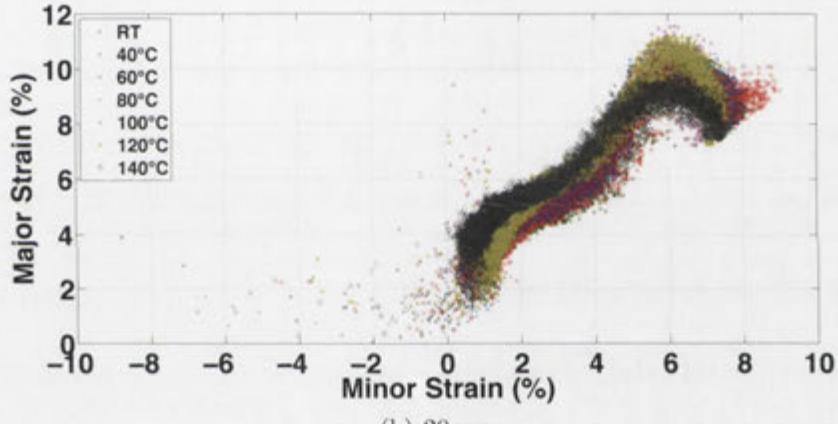

(b) 20mm

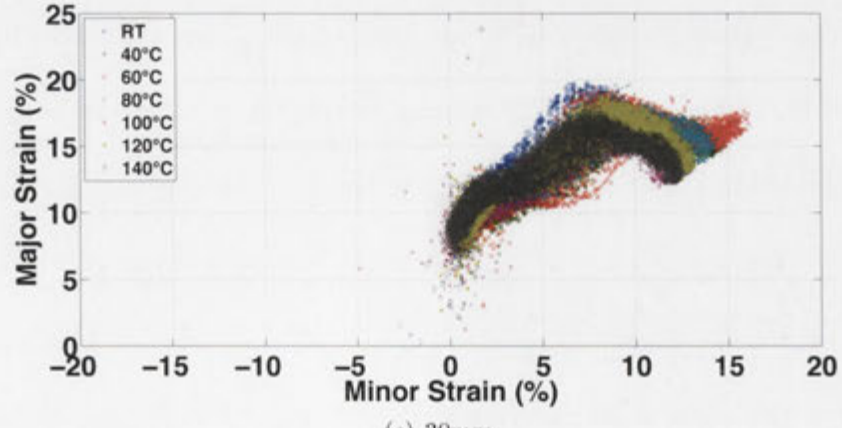

(c) 30mm

Figure 6.23: Effect of temperature on the FLD for the 200mm specimens

shows significant differences in the strain behaviour as the temperature increases. It appears as if the FLD rotates toward a more plane strain deformation mode as the temperature increases. At 140°C the strain behaviour in the 70mmHG specimen closely resembles the behaviour of the room temperature aluminium specimen.

Figure 6.24 shows, for all temperatures, the FLD of the experimental specimens at the final stage of deformation before failure. There is an improvement in the uniformity of the strain distribution as the temperature increases, in addition to the increase in the final major strain. The figure shows that the highest and most uniform strain distribution occurs at 120°C. This is shown through analysis of the strain data: the 25mmHG hourglass specimen shows a 51.6% increase in the maximum major strain and a 44.7% increase in the mean major strain, the maximum major strain in the 70mmHG specimen increases by 44.5% and the mean major strain by 62.9%, and in the 200mm specimen the maximum and mean major strains increase by 66.5% and 44.3%. This demonstrates the improved forming behaviour of the laminate at this temperature as both the mean and maximum major strain magnitudes increase at similar speeds. In contrast, at 140°C the maximum and mean major strain increases (compared to room temperature) are 45.4% and 10.6% for the 25mmHG specimen, 50.25% and –10.3% for the 70mmHG specimen, and 87.4% and 42.4% for the 200mm specimen. The differences in the strain increases show that the failure in the specimen is occurring due to a localised area of deformation in the failure region. As this is

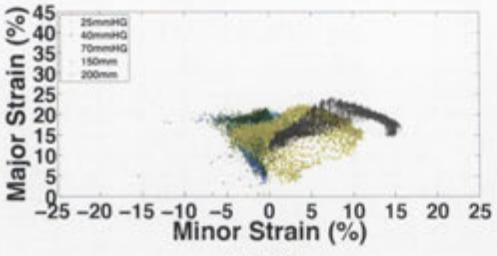

(a) RT

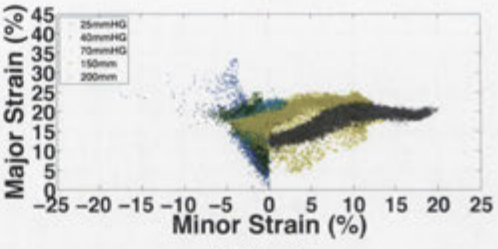

(b) 40°C

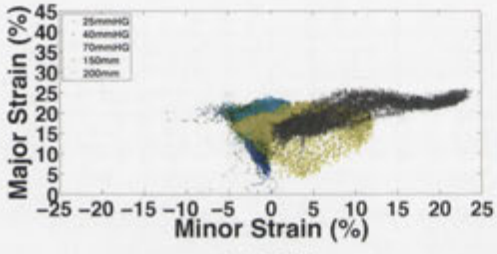

(c) 60°C

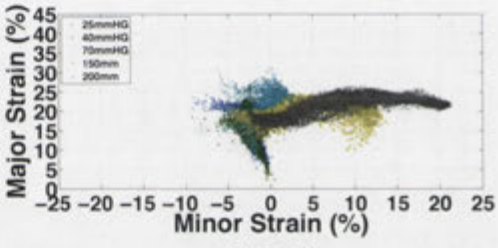

(d) 80°C

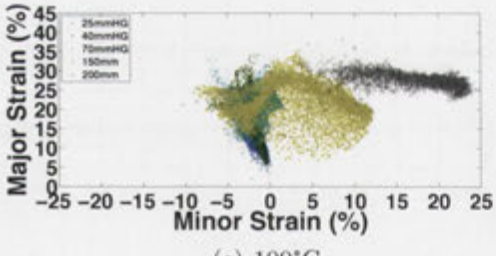

(e) 100°C

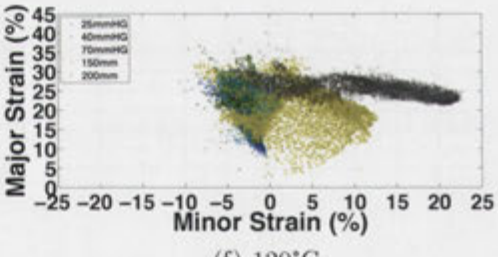

(f) 120°C

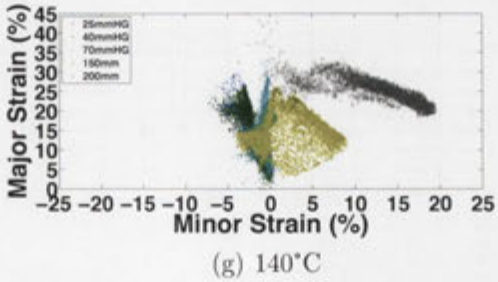

(g) 140°C

Figure 6.24: Final FLDs for each temperature

not exhibited at lower temperatures, and is indicative of monolithic aluminium failure, it can only be caused by a failure of the adhesive bond due to melting of the adhesive layer.

Another interesting behaviour is the minor strain values for the 200mm specimens. These specimens should not show any negative strain as the entire specimen is stretched. However, due to the large forming depth at failure, the edges of the specimen begin to show negative minor strains as a result of bending around the die radius. It is not exhibited by the 100°C specimen due to a difficulty in obtaining strain results at the die edges (caused by lighting and paint issues).

6.2.4 Meridian strain

A comparison of the meridian strain distribution at the various temperatures for the experimental specimens is shown in Figure 6.25. These figures show that, as expected, the state of major strain along the meridian is the same for each specimen at similar depths. Variability in the strain magnitudes is due to the strain results being taken at a forming depth of 15±0.3mm. Additionally, vibrations and movement of the stamping press relative to the cameras causes fluctuations in the centre and length of the meridian plots. However, the most interesting aspect of these images is the 40°C and 60°C results for the 200mm specimens which show higher strain in the centre compared to the other temperatures. This is due to the low friction contact condition between the specimen and the punch which also leads to failure occurring in the centre.

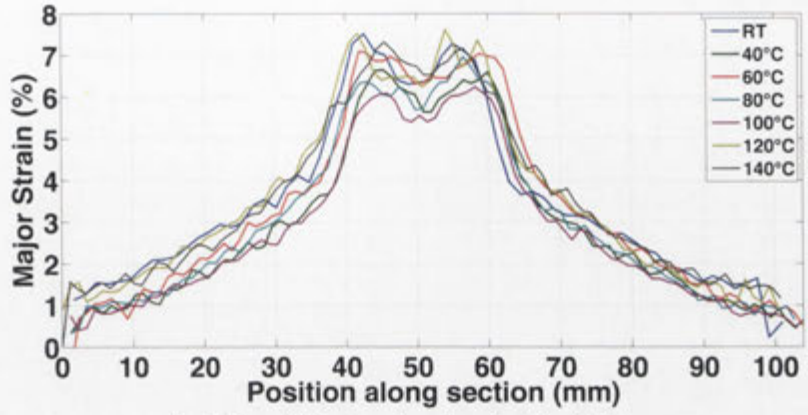

(a) 70mmHG at a forming depth of 10mm

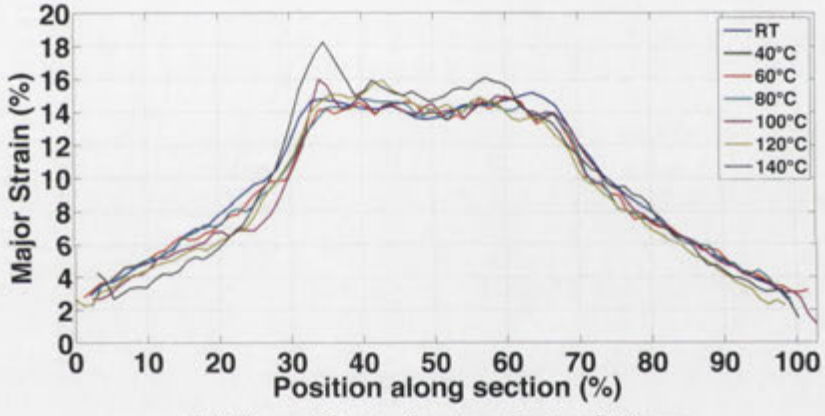

(b) 25mmHG at a forming depth of 20mm

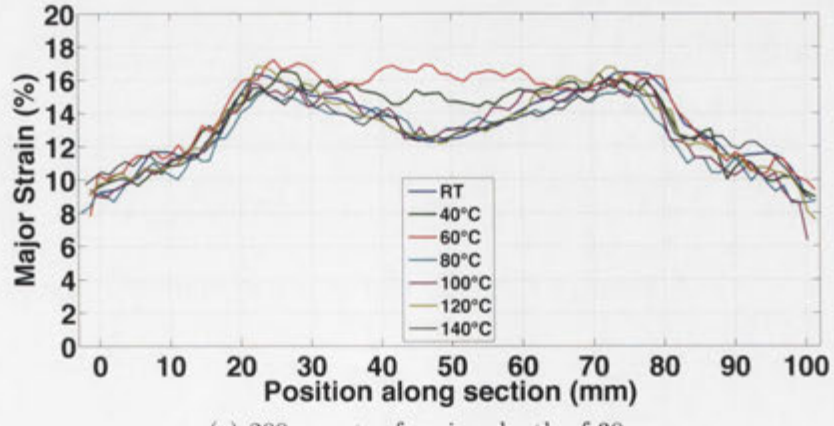

(c) 200mm at a forming depth of 30mm

Figure 6.25: Effect of temperature on the surface strain

In order to observe the effect that greater forming depths have on the strain behaviour of the specimens, the meridian strain plots for the uniaxial tension, plane strain, and biaxial stretch specimens which were formed at the greatest depths are shown in Figure 6.26. These meridian strain plots show that the strain behaviour of the experimental specimens continues in a fairly consistent manner. However, the 25mmHG and 70mmHG show asymmetrical behaviour beginning at a forming depth of 25mm. It is possible that this was caused by localised failure in the composite layer; however, this was not observed in the force–displacement curves produced by the stamping press. This means that some other mechanism was causing the difference in strain – possibly differential cooling rates on each side of the punch. This is plausible because the colder region of the specimen would have a higher stiffness and therefore would not deform as easily as the hot region, given that failure in these specimens did not occur at the point of highest major strain. In fact, failure in the 25mmHG specimen occurred on the opposite side of the punch to the high strain region, which provides further evidence of differential cooling (since strain to failure is lower at lower temperatures). The 70mmHG specimen did show failure in the region of maximum major strain, but it occurred in the trough between the two highest major strain values. The 200mm specimen does not show this behaviour and shows a uniform strain distribution until failure. However, this could be due to deterioration in the calculable region of strain due to lighting problems at higher forming depths.

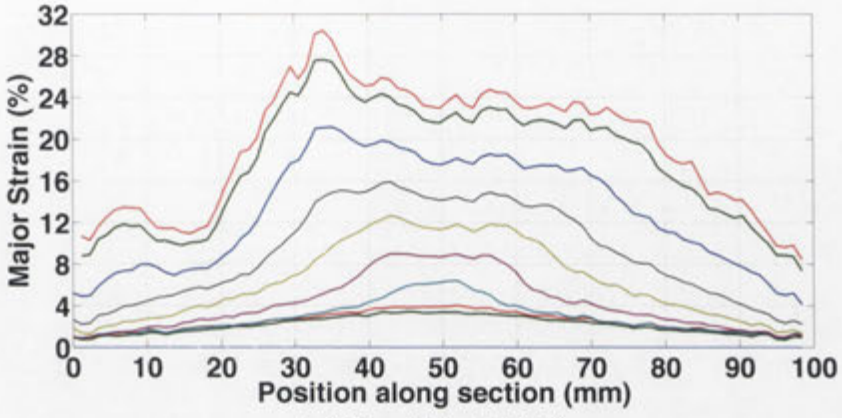

(a) 25mmHG at 120°C

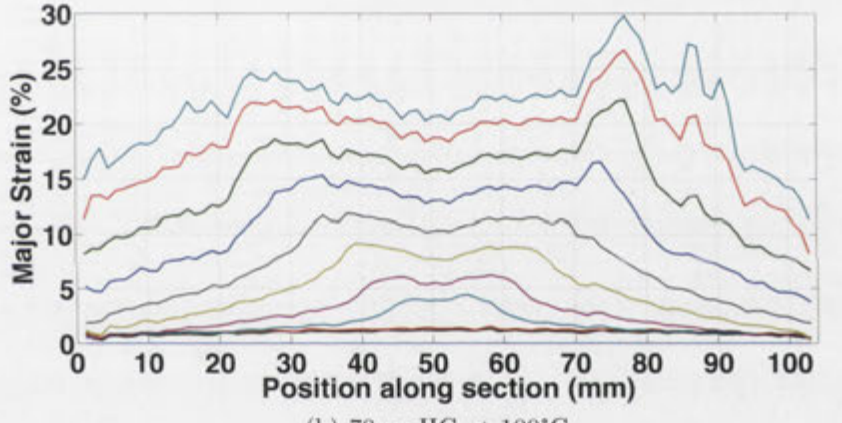

(b) 70mmHG at 100°C

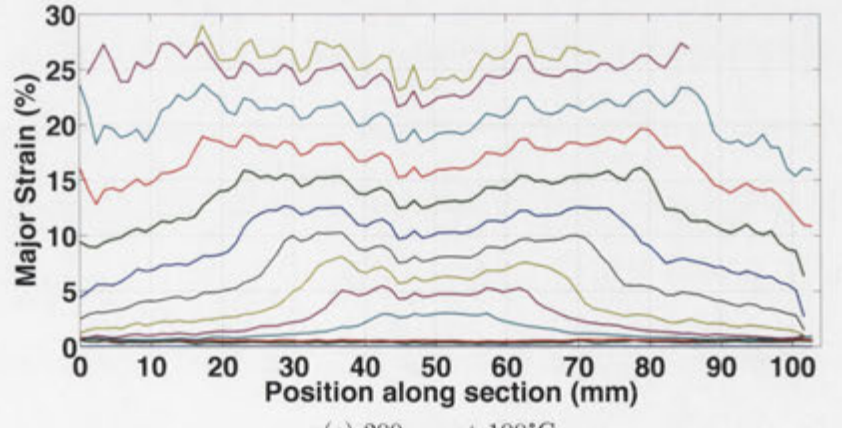

(c) 200mm at 100°C

Figure 6.26: Meridian major strain for specimens that achieved the largest forming depths

	25mmHG		40mmHG		70mmHG		150mm		200mm	
	Min	Maj	Min	Maj	Min	Maj	Min	Maj	Min	Maj
RT	-1.09	18.4	-0.319	20	-0.163	13.3	3.83	19.9	6.23	22.4
40°C	-2.304	18.49	-0.99	20.01	2.138	22.96	7.651	23.17	19.07	20.14
60°C	-1.655	19.91	-1.2	21.74	1.935	21.95	5.886	19.88	23	24.21
80°C	-2.177	21.1	-2.5	26.85	-0.815	21.06	7.434	23.18	16.62	24.17
100°C	-2.462	23.06	-1.538	22.8	0.4484	22.28	1.393	29.37	9.26	28.6
120°C	-3.478	23.49	-2.037	28.02	0.9108	24.33	-1.014	26.79	1.515	30.91
140°C	-2.71	20.12	-3.18	26.04	-0.291	27.58	0.6835	25.34	1.078	34.39

Table 6.4: Major and minor strain values at the point of failure in the experimental specimens

6.2.5 Forming limit curve

The final FLDs for all temperatures are shown in Figure 6.24 and the strain at the points of failure are shown in Figure 6.12. It is from these figures that the FLC can be determined. Similarly to the room temperature specimens, the high temperature specimens (other than the 140°C specimens) showed no localisation of strain prior to catastrophic failure of all three layers of the laminate.

Table 6.4 shows, for all temperatures, the major and minor strains at the point of failure in each specimen. These results, as well as the strain ratio, are also plotted in Figure 6.27. It can be seen from Figure 6.27 that the major strain at failure of the specimens increases with increasing temperature. This is expected because the tensile characterisation experiments show a significant positive influence of increased temperature on the elongation at failure in the SRPP composite. These characterisation experiments were conducted with the fibres oriented along the direction of loading, showing that the polypropylene fibres are also affected by an increase in temperature. The studies by Dhar Malingam [77] and Venkatesan

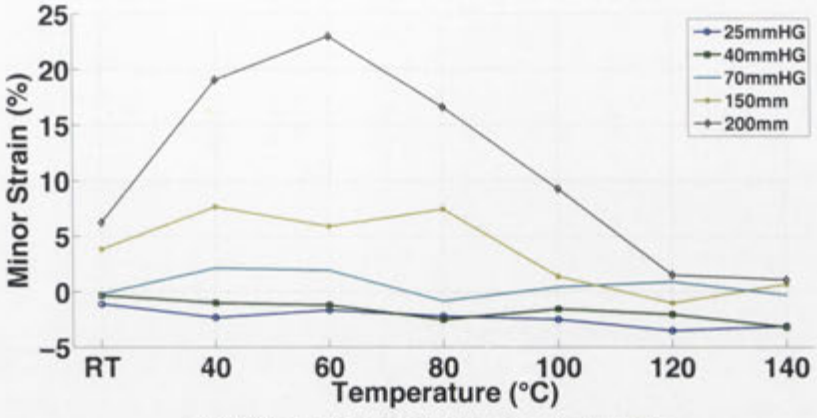

(a) Effect of temperature on minor strain

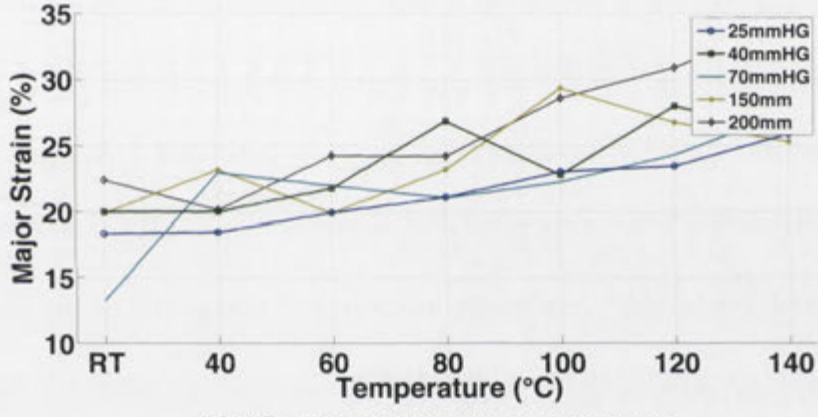

(b) Effect of temperature on major strain

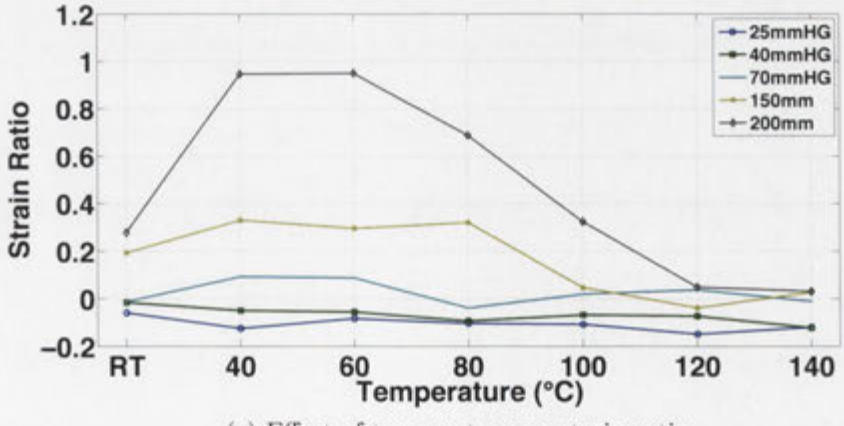

(c) Effect of temperature on strain ratio

Figure 6.27: Effect of temperature on the minor and major strain and the strain ratio at the depth of failure

	40°C	60°C	80°C	100°C	120°C	140°C
25mmHG	0.49%	8.21%	14.67%	25.33%	27.66%	9.35%
40mmHG	0.05%	8.7%	34.25%	11.4%	40.1%	30.2%
70mmHG	72.36%	65.04%	58.35%	67.52%	82.93%	107.37%
150mm	16.43%	-0.1%	16.48%	47.59%	34.62%	27.34%
200mm	-10.09%	8.08%	7.9%	27.68%	37.99%	53.53%

Table 6.5: Change in the major strain at failure at each temperature compared to room temperature

[64] found that improved formability was primarily due to an increase in matrix shear, with some deformation added through increased elongation in the fibres. However, matrix shear provided no benefit in this study as the boundary conditions did not change for different temperatures; this means that different levels of stretch and draw in different directions, which was observed by Dhar Malingam [77] and Venkatesan [64], could not be achieved. However, there is an increase in the strain at failure, which is due to the increased elongation of the fibres in the longitudinal direction. The change in the failure major strain is shown in Table 6.5. It can be seen that above 80°C there is always an increased major strain at failure in the experimental specimens which is due to the increased strain at failure in the SRPP at elevated temperatures.

The elevated temperature does not appear to have a large effect on the minor strain at failure, with only a small negative trend present. The results of the 200mm specimen at 40°C and 60°C minor strain at failure, and the location of the failure point (discussed in Section 6.2.2.2), indicate that other process parameters may affect the minor values more significantly than temperature. The deformation process for similarly shaped specimens (at similar depths) should be

the same regardless of temperature. However, two factors will have an effect on the minor strain at failure: the forming depth at failure and the position of failure. The forming depth affects the minor strain by allowing the specimen to deform further along the path to failure. In the 25mmHG and 40mmHG specimens this causes the minor strain to be more negative; in the 70mmHG the minor strain should be approximately the same, and for the 150mm and 200mm specimens the minor strain at failure should be more positive. However, if the position of failure changes then the minor strain is dependent on the deformation mode of that particular region of the specimen. For example, the unsupported region tends to exhibit deformation behaviour closer to plane strain than does the pole.

These results also present something of a paradox in that the strain ratio at failure is not constant for similar specimens at all temperatures. For example, the failure in the 200mm 40°C specimen occurs at a strain ratio of 0.95, while failure in the 200mm 120°C specimen occurs at a strain ratio of 0.03. This makes it difficult to directly assess the change in the FLC with temperature.

6.3 Finite Element Simulation

The objectives of the finite element analysis at elevated temperatures are the same as those presented in Chapter 5. Hence, the first step of the finite element simulation is to ensure that the results agree with those found in experiments.

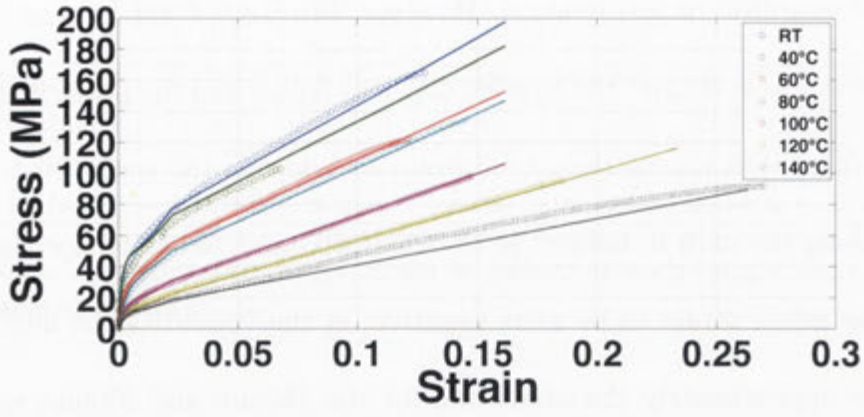

Figure 6.28: Verification of the stress-strain behaviour in the finite element model

6.3.1 Model Verification

An additional step is required in the verification of elevated temperature models: ensuring that the mechanical behaviour of the constituent materials agree at all temperatures. Shown in Figure 6.28 is a comparison of the stress–strain behaviour of the SRPP layer at various temperatures. The circles represent the experimental data and the solid lines represent the simulated tensile specimens. It can be seen that the simulated stress–strain curves show, at all temperatures, excellent agreement with those found in the characterisation experiments. The FE models do not contain failure criteria and therefore continue to predict deformation at strains greater than experienced in the tensile experiments. However, the isothermal FEA results show that the extrapolated behaviour aids in simulating the FML forming behaviour, as the failure limits observed in the forming experiments exceed those determined from the characterisation experiments.

Figure 6.29 and Figure 6.30 compare the surface major strain contours of the FEA and the experimental 25mmHG and 70mmHG specimens at three temper-

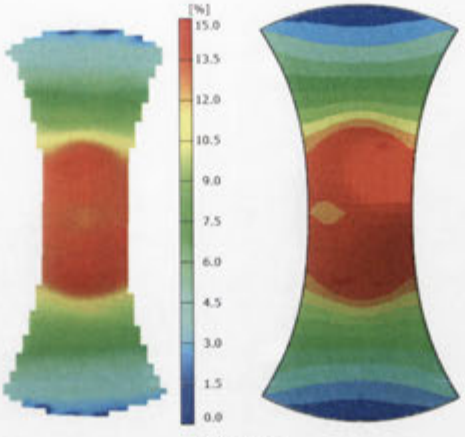

(a) RT

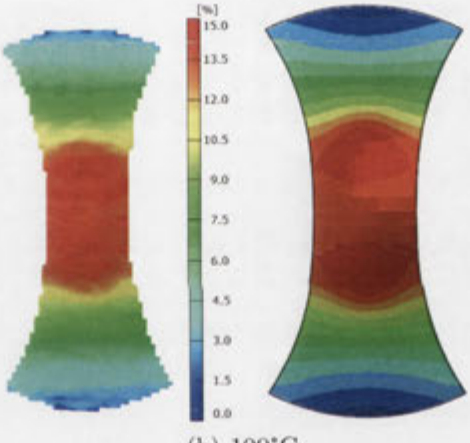

(b) 100°C

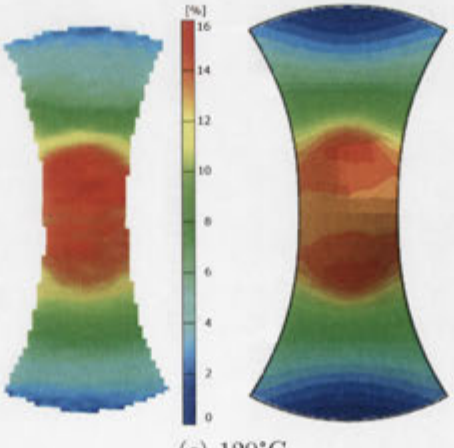

(c) 120°C

Figure 6.29: Comparison of the surface strain contours at different temperatures in the 25mmHG specimen: FEA vs Experiment

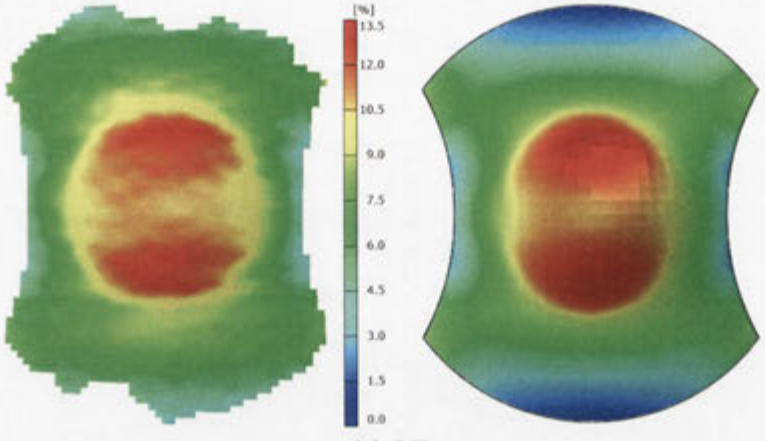

(a) RT

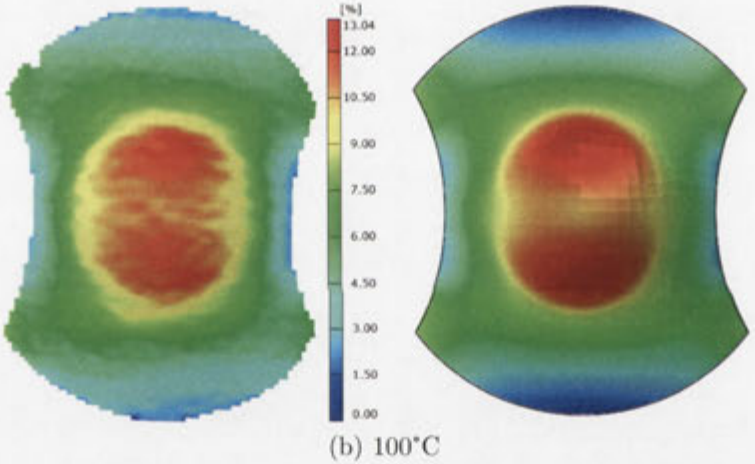

(b) 100°C

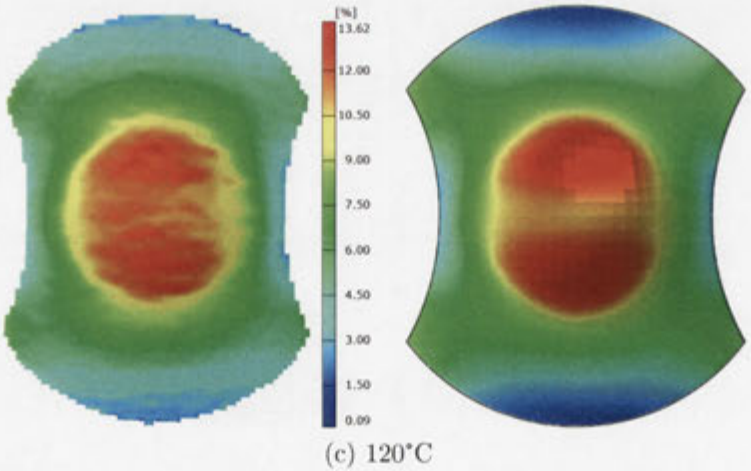

(c) 120°C

Figure 6.30: Comparison of the surface strain contours at different temperatures in the 70mmHG specimen: FEA vs Experiment

atures. It can be seen that temperature has a limited effect on the surface major strain distributions in both the experimental and the FE simulation. Again, this is expected due to the similar deformation processes occurring at each temperature. However, this only shows the result at one strain stage, and it is more useful to consider the evolution of strain across the surface.

Figure 6.31 shows the comparison of the experimental and FE simulation meridian strain plots. It can be seen that the FE simulation results begin to diverge from the experimental results as the depth increases. The strain behaviour in the FE simulation appears similar to the effect of friction, where the unsupported regions exhibit higher strains than the pole. Additionally, the pole region of the specimen also experiences a larger decrease in temperature than the unsupported region due to contact with the punch, which results in a lower stiffness in the unsupported region compared to the pole. This also acts to increase strain in the unsupported region. Reducing friction in the FE model would act to reduce the strain in the unsupported region; however, this would also increase the strain in the pole region, which currently shows excellent correlation with the experimental result. Figure 6.32 shows the major cause of the difference between the FEA and experiments. The pole region of the specimen experiences significantly greater temperature reductions than the unsupported regions, resulting in a 33.65% increase in stiffness at 40mm. Unlike the studies by Venkatesan [64] and Dhar Malingam [77], the die and blankholder are both heated in this study, which results in different temperature profiles. The heat transfer coefficients were

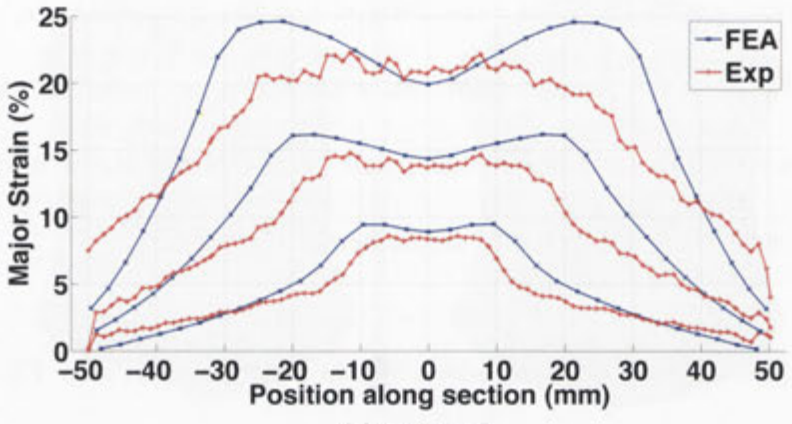

(a) 25mmHG

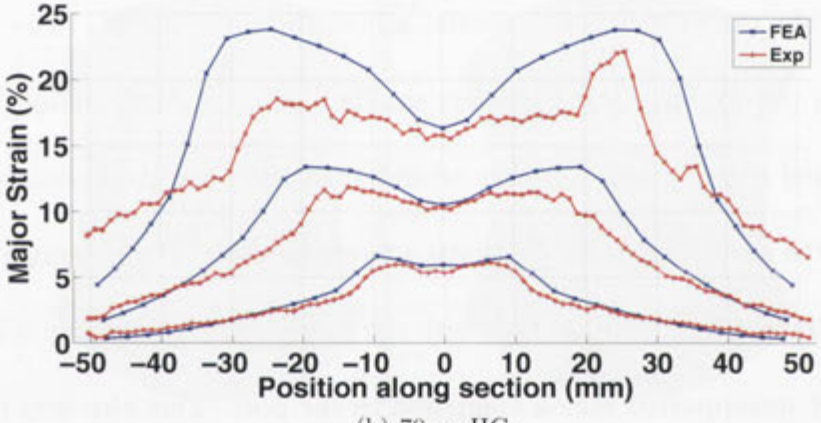

(b) 70mmHG

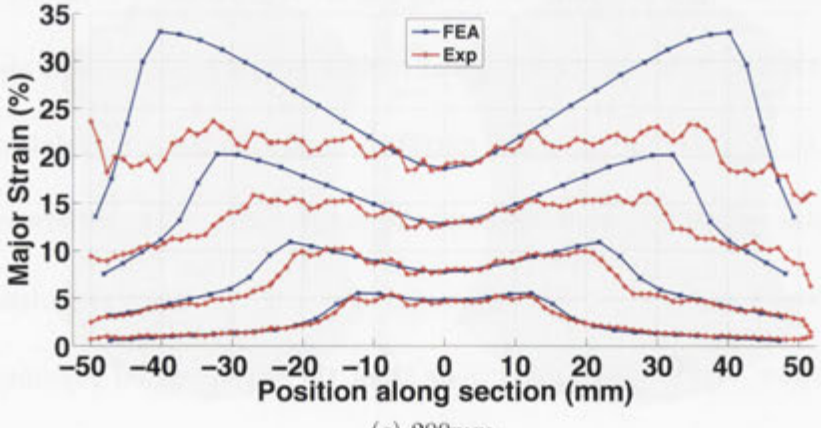

(c) 200mm

Figure 6.31: Comparison of the meridian major strain at 10mm depth increments at 100°C

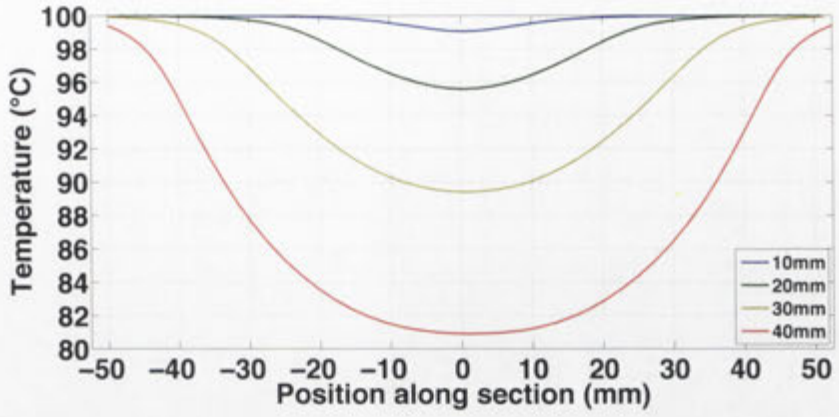

Figure 6.32: Variation of temperature along the meridian in the 100°C 200mm specimen

developed and verified in these studies using thermocouples inserted in the experimental specimens, as was done by Mosse [73]. Therefore, it is expected that the temperature profiles in this study are, due to the similar contact conditions, also valid. However, the high temperature tools and the presence of the lock ring could affect the contact conditions. That is, the lock ring may prevent intimate contact between the blankholder and the top surface of the specimen.

Figure 6.33 shows a comparison of the FLD in the experimental and FEA 70mmHG specimens. It can be seen that the solutions begin to diverge at increasing forming depths, which is consistent with the findings of the meridian strain plots. This is particularly apparent at a forming depth of 30mm where the experimental specimen minor strain shows a range of –4.88% to 1.6% compared to the FE range of –6.80% to 2.43%. The FE major strain also has a higher mean, 14.67% compared to 13.44%. Figure 6.34 shows the comparison of the major and minor strain contours at the 30mm forming depth and elucidates the reason for the difference in the FLD. The major strain magnitudes in the FE simulation

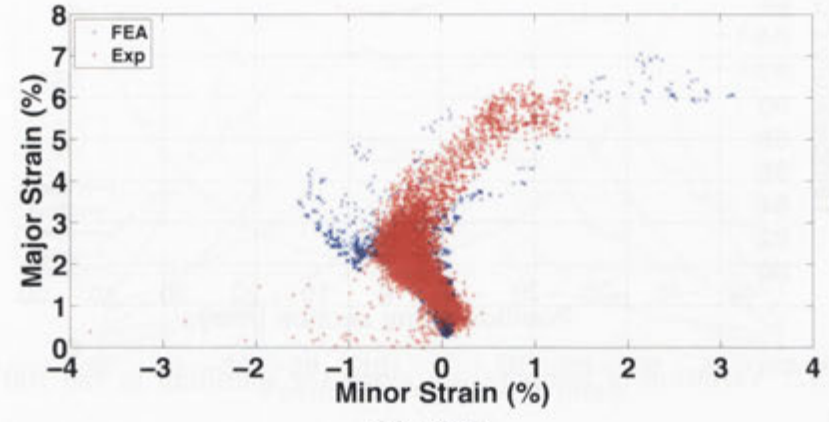

(a) 10mm

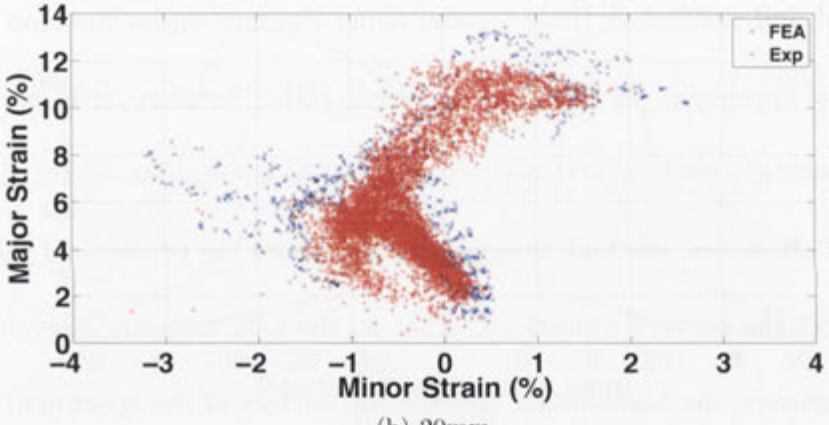

(b) 20mm

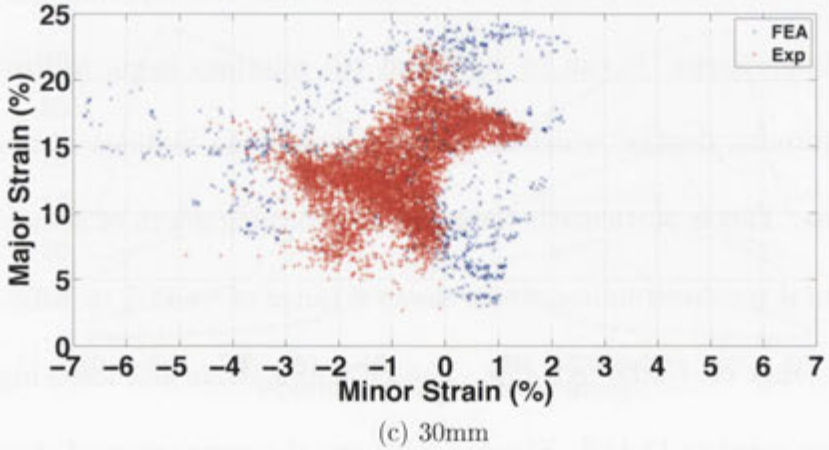

(c) 30mm

Figure 6.33: Comparison of the experimental and FEA results for the 100°C 70mmHG FLD at various depths

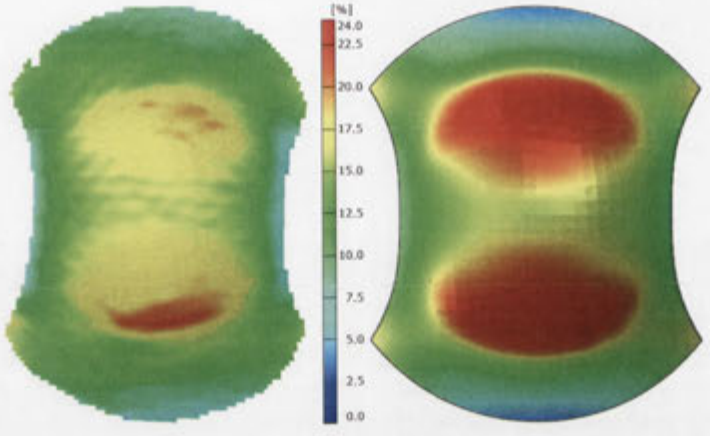

(a) Major Strain

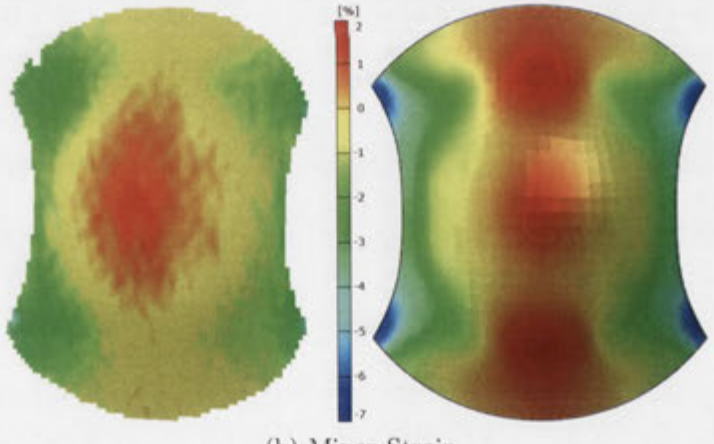

(b) Minor Strain

Figure 6.34: Comparison of the surface strain contours in the 70mmHG 100°C specimen at a forming depth of 30mm

show a larger distribution of high major strain values across the unsupported region than in the experimental specimen. This could be considered an indicator of failure in the laminate, but the strain evolution in this region, shown in Figure 6.14, exhibits no sudden rise in strain at any depth which would signal a failure of one of the laminate layers. Due to the larger area exhibiting elevated major strain, there is a greater range of minor strain, which prevents clustering around the maximum major strain in the experimental FLD. The minor strain at the edges of the FE simulated specimen are also more negative than the experimental specimens, indicating that more draw occurred in this region than was simulated.

Figure 6.35 shows the evolution of minor and major strain and the strain path at the pole in the 25mmHG, 70mmHG and 200mm specimens at 100°C. This shows an excellent match for the major strain at the pole but the minor strain values do not show similar agreement. The FE simulation continues to exhibit a biaxial stretch deformation mode in the 25mmHG and 70mmHG specimens longer than seen in the experimental specimens. This could be due to the lack of information about the interaction between major and minor strain or the lateral boundary conditions. It could also indicate more complex contact conditions with the punch. The trend of the minor strain is also different in the FE simulation, with a strong negative trend in both the 25mmHG and 70mmHG specimens; this could be due to incomplete mechanical properties for the composite material under compression. Figure 6.35(a) also shows that the 25mmHG

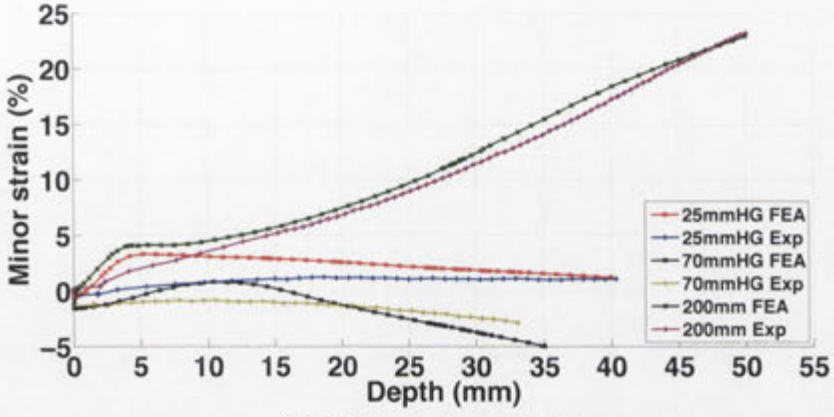

(a) Minor strain evolution

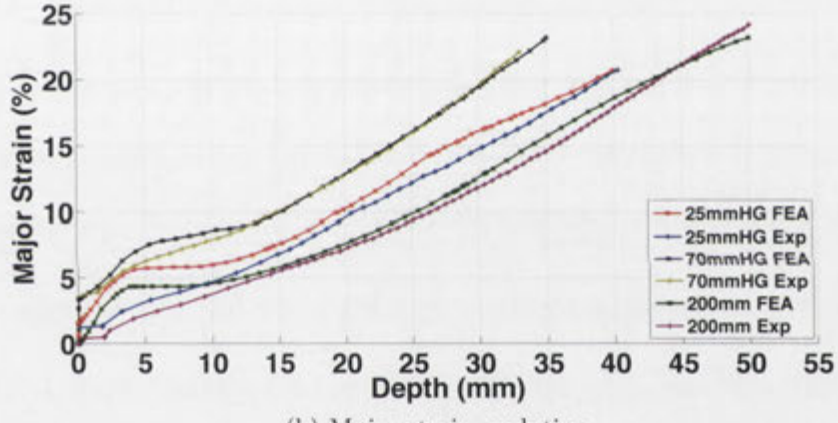

(b) Major strain evolution

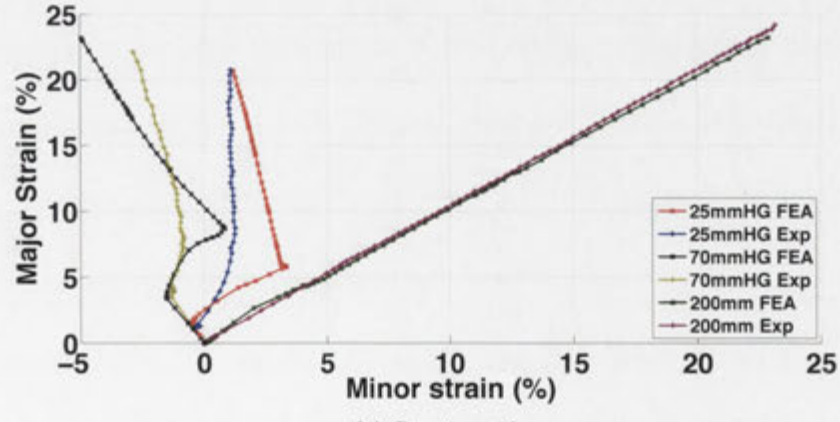

(c) Strain path

Figure 6.35: Comparison of pole strain evolution in the FEA and experimental specimens at 100°C

and 200mm FE specimens display similar minor strain behaviour in the initial stages of deformation.

6.3.2 Strain behaviour in the laminate

The good agreement between the experimental and FE specimens across a range of temperatures allows analysis of the strain through the thickness of the laminate. Figure 6.36 shows the evolution of the simulated strain through the thickness of the SRPP FML at the pole for the 100°C specimen. The major strain plots show that the bending strain equation is still valid for this region at the elevated temperature. This is because the bond between the layers of the laminate has not been broken since the shear strength of the adhesive has not been exceeded. The shear strength determined by Mosse [73, 97] in Figure 4.3 and Equations 4.30 and 4.31 is calculated to be 8.3MPa, 7.5MPa, and 0.74MPa for RT, 100°C, and 120°C. Figure 6.37 shows that the shear stress at the pole of the experimental specimens at 100°C never exceeded 0.3MPa (the sign in Figure 6.37 only indicates the direction of stress) at any forming depth. Similar values were found for the RT and 120°C specimens.

What is interesting about Figure 6.36 is the strain path of the top aluminium in the 25mmHG and 70mmHG specimens. This layer of the FML does not show the same magnitude of biaxial stretch as the bottom aluminium layer or the composite layer. As this is only seen in the top aluminium layer it must be due to the contact conditions with the punch. Figure 6.38 shows the effect of

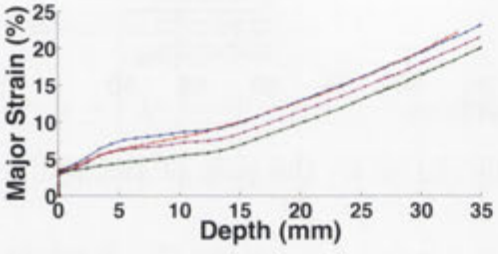

(a) Major strain evolution for the 25mmHG 100°C specimen

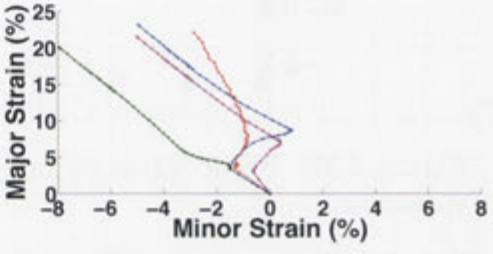

(b) Strain path for the 25mmHG 100°C specimen

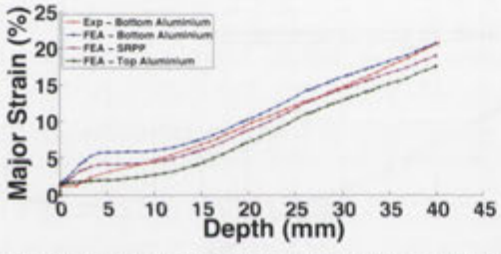

(c) Major strain evolution for the 70mmHG 100°C specimen

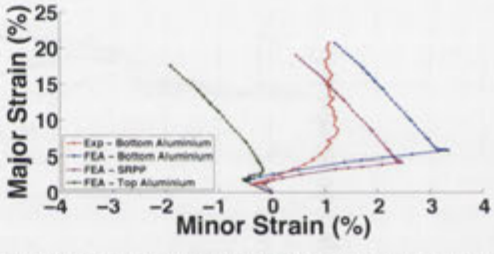

(d) Strain path for the 70mmHG 100°C specimen

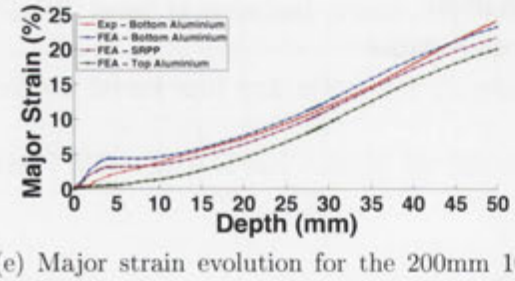

(e) Major strain evolution for the 200mm 100°C specimen

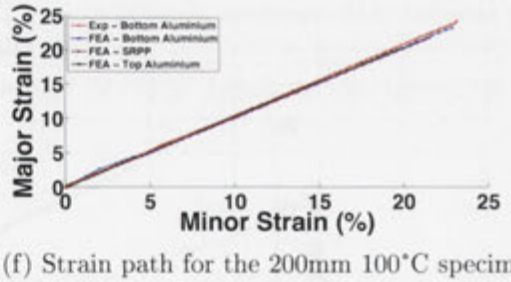

(f) Strain path for the 200mm 100°C specimen

Figure 6.36: Strain through the thickness at the pole of the FE simulated specimens

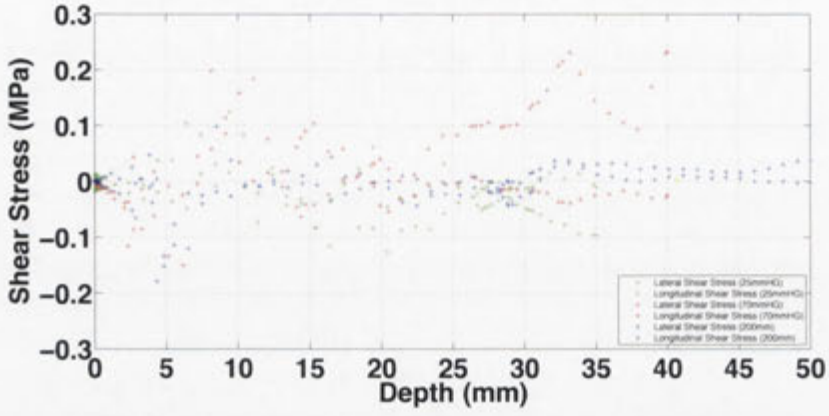

Figure 6.37: Shear stress in between the layers at the pole of the 100°C FE specimens

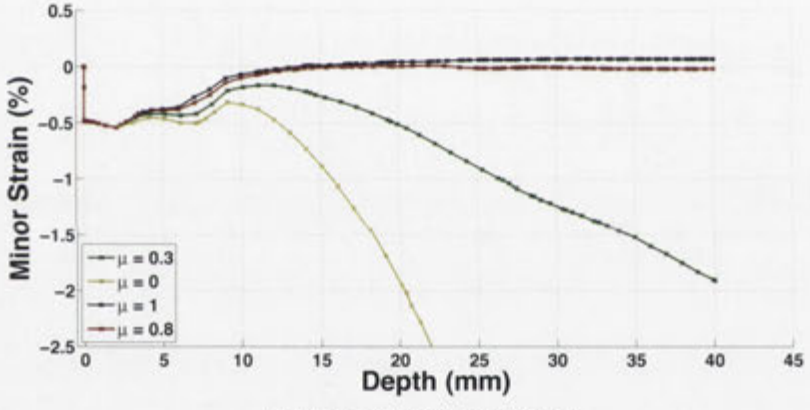

(a) Minor strain evolution

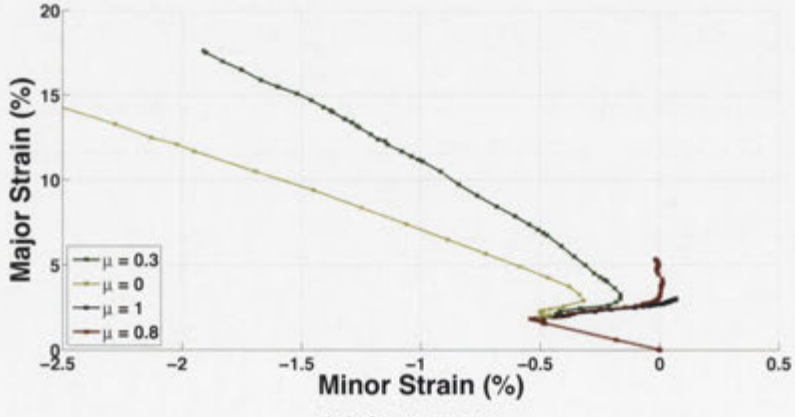

(b) Strain path

Figure 6.38: Effect of friction on the strain evolution in the top aluminium layer of the simulated 70mmHG 100°C specimen

friction on the evolution of strain in the top aluminium layer of the simulated 70mmHG 100°C specimen. It can be seen that increasing the friction between the top aluminium and the punch causes an increase in the biaxial stretch behaviour in the top aluminium layer. However, there is no effect on the biaxial stretch behaviour in the bottom aluminium layer due to increased friction at the pole. This is a significant finding as it implies that the contact condition with the layer above is responsible for the biaxial deformation behaviour of the layer being considered. Therefore, a reduced biaxial stretch deformation behaviour in the bottom aluminium layer is achievable by altering the contact state between it and the composite layer. However, failure of the adhesive was not observed in either the experiments or the FE simulation (as shown by the shear stress magnitudes in Figure 6.37). What was observed in the experiments was that the SRPP layer had suffered intra-ply failure. This means that a more complex model for the SRPP layer is required which can model the interactions between the various woven layers and can allow for a certain amount of "slip" between the layers of the FML which is not caused by the adhesive.

Figure 6.39 compares the FLDs of the SRPP layer at a depth of 10mm. Again, no major effect of temperature is seen in the major strain except that the higher temperature layers appear to exhibit lower minor and major strain magnitudes. This is caused by the different pre-stretch at each temperature. Figure 6.40 shows the FLD for the SRPP layer at various temperatures at their corresponding failures depths. The failure strain of the tensile characterisation specimens for

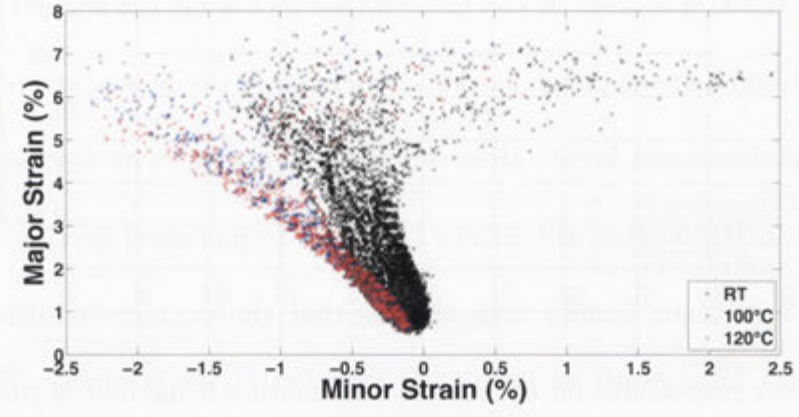

(a) 25mmHG

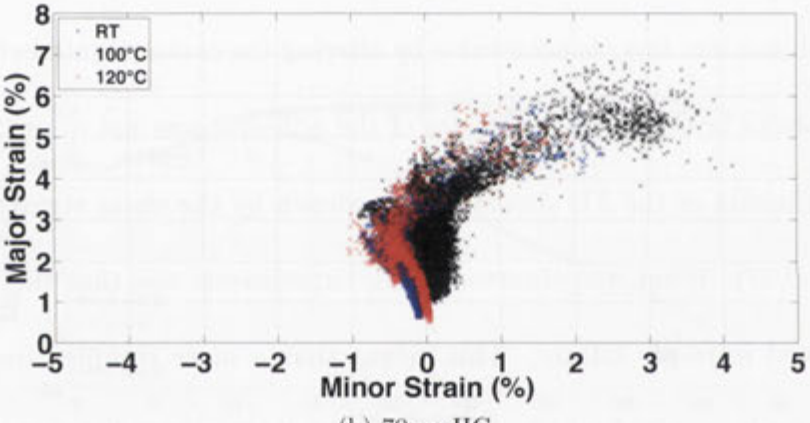

(b) 70mmHG

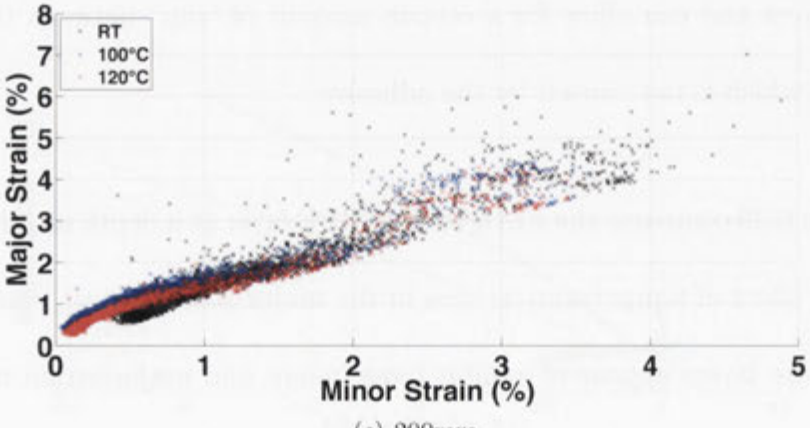

(c) 200mm

Figure 6.39: Comparison of the FLD in the SRPP layer at various temperatures at 10mm forming depth

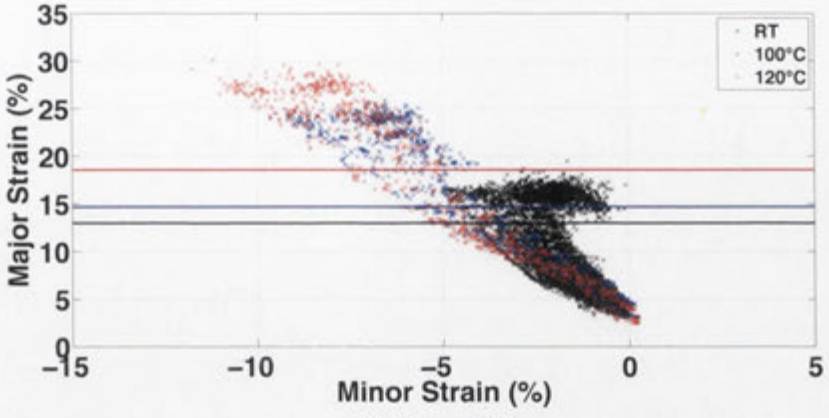

(a) 25mmHG

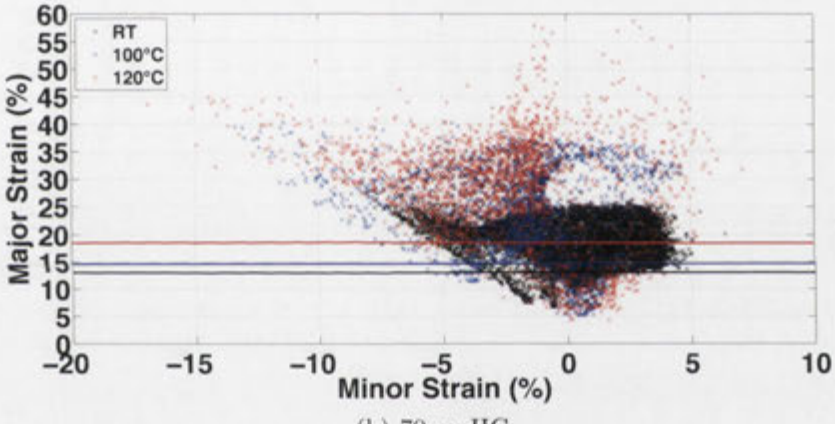

(b) 70mmHG

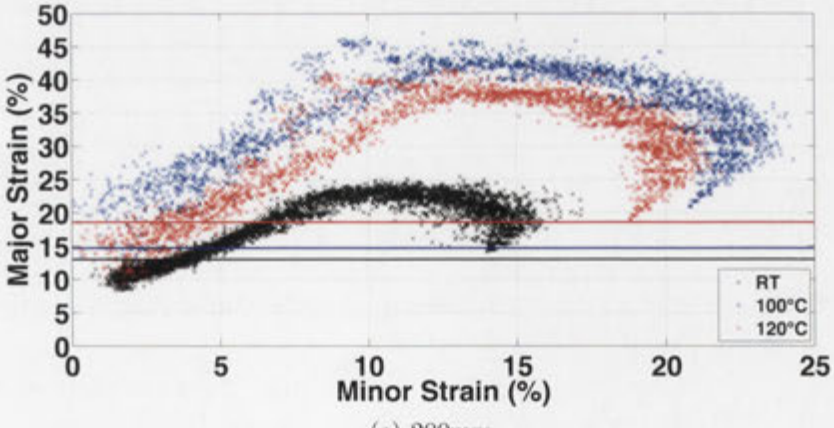

(c) 200mm

Figure 6.40: FLD in the SRPP layer at various temperatures at the failure depth for each specimen. The failure strain of the tensile experiments is also shown

each temperature is also shown. It can be seen that the failure strain determined by the tensile characterisation specimens is incorrect for all temperatures. This strain value was found to be 13%, 14.7%, and 18.6% for the RT, 100°C, and 120°C specimens respectively, which is significantly lower than the strain values experienced by the FE simulated specimens at failure depth. Using the simulated specimens it is possible to determine the failure strain in the SRPP laminate. This was found in a similar manner to Chapter 5 where the position of failure is determined from Table 6.3. The minor and major failure strain values for the 25mmHG specimens were found to be –1.61% and 16.4% at room temperature, –5.8% and 22% at 100°C, and –6.75% and 24% at 120°C. The minor and major failure strain values for the 70mmHG specimens were found to be 3.9% and 25.7% at room temperature, 3.95% and 31.5% at 100°C, and 0% and 38% at 120°C. The minor and major failure strain values for the 200mm specimens were found to be 7.9% and 22.5% at room temperature, 13% and 46.5% at 100°C, and 7% and 31.3% at 120°C. At the elevated temperatures there are again points in the specimens which exhibit major strain values that are higher than the determined failure strain. This is because the major strain in these regions is oriented along the matrix direction, which can undergo much larger deformation than the fibres. Finally, the failure minor and major strains determined above are only indicative values due to the differences found in Figure 6.31 in the unsupported region. Therefore, to correctly determine the failure properties of the SRPP FML it is necessary to conduct stretch forming experiments on the SRPP in isolation to

determine the failure values across all deformation modes.

6.4 Summary

The effect of temperature on the forming behaviour of the SRPP FML was assessed in this chapter. Five specimens were used to elicit deformation behaviours ranging from uniaxial tension to biaxial stretch.

It was found that the temperature of the specimens had a non-uniform effect. In the case of the pre-stretch strain it was found that the thermal expansion of the die and blankholder had the greatest effect on the pre-stretch strain in the specimen.

Assessment of the strain in the SRPP FMLs at elevated temperatures showed that the strain in the specimens was generally the same across all temperatures for similar forming depths. This was expected as the specimen geometry and boundary conditions were consistent and the experiments were designed to reproduce the same deformation modes regardless of material properties. The only differences found between the experimental data was due to the variability of the contact conditions with the tools and the differential cooling rates of regions of the specimens. However, this appeared to have no significant effect on the evolution of strain in the laminates, the FLDs, the meridian strain, or the contours. It was expected that as the SRPP became softer that the unsupported region would become easier to deform and the contact pressure from the punch would reduce. These factors effectively negate each other, ensuring that the strain behaviour of

the laminates was similar at all temperatures.

The failure behaviour was affected by the specimen temperature. Due to the increased strain at failure in the SRPP layer at elevated temperatures, these specimens experience greater forming depths than the lower temperature specimens. As the failure of the SRPP layer triggered the failure of the entire laminate, the failure strain of the high temperature specimens was also higher than the low temperature ones. An interesting finding was that at 140°C, when the adhesive had melted, the specimens exhibited lower forming depths than at 120°C, even though the SRPP layer had not failed. This finding is significant because it shows that the SRPP layer improves the formability of the aluminium layer. This means that any cheap low-stiffness, high-extension material can be used to improve the forming of metallic parts.

The finite element simulation showed good agreement for the stress–strain behaviour of the SRPP compared to the experiments. It was decided that no failure limits should be imposed on the SRPP as it was found in both the room temperature experiments and simulations that the SRPP exhibited forming limits greater than the failure point in the tensile characterisation specimens. The behaviour was again modelled as a two-part polynominal extrapolated from the experimentally determined tensile behaviour of a linear elastic material. The forming simulations were in generally good agreement with the experimental specimens. The major difficulty was matching the meridian major strain because balancing the material stiffness and contact conditions is essential to obtaining correct strain

values. It is believed that the SRPP layer may be undergoing intra-ply shear, a condition which cannot be modelled when the layer is represented by a single shell. It was also found that the shear stress in the simulations never exceeded the shear stress limits determined for the adhesive layer, which means that relative slip never occurred between the layers of the laminate. Finally, more detailed information about the SRPP layer is required to correctly model the interaction between the major and minor strain and to accurately predict the forming limits. These include forming experiments on the SRPP layer, tribological investigations of the tooling, and a micro-level model of the fibre–matrix interactions.

The following chapters will assess the formability of fibre–metal laminates comprised of a composite layer with higher stiffness but lower extension.

Chapter 7

Isothermal forming of a glass-fibre reinforced polypropylene fibre–metal laminate

7.1 Introduction

This chapter investigates the forming behaviour of a FML based on a GFRP composite. The effect of specimen geometry and temperature on the strain behaviour of the laminate during forming is investigated and the safe forming limits are determined. The methods developed in Chapter 3 and the areas of interest determined in Chapter 5 are used in this chapter to analyse the experimental results. The results from the GFRP laminate are compared to the results of the aluminium and the SRPP laminate to elucidate the effect of composite material stiffness and extensibility on the forming behaviour of FML systems. In addition, the forming behaviour of selected specimen geometries is analysed using FEA software to provide information about the behaviour of the adhesive and of the non-visible regions such as the composite and top aluminium layer.

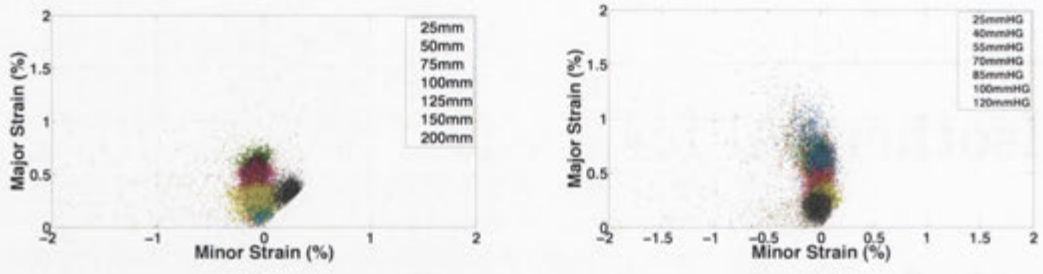

(a) (b)

Figure 7.1: The effect of the lock ring on the surface strain for the rectangular (a) and hourglass (b) geometries

7.2 Experimental Work

7.2.1 Effect of the lock ring

The GFRP FML specimens were subjected to a "pre-stretch" prior to forming. Figure 7.1 shows the effect of the lock ring on the surface strain of the specimens. The effect of the "pre-stretch" in the GFRP laminates was more severe than in the SRPP laminates, primarily due to the low extensibility of the glass fibres. Therefore, generally lower blankholder forces were used to secure the specimens compared to the SRPP FML. This can be seen by comparing Figure 7.1 with Figure 5.2; the major strain in the GFRP laminates never exceeds 2% whereas in the SRPP laminate major strain values of 4% can be supported. The strain behaviour of the GFRP specimens is also significantly different from the SRPP specimens, with the strain behaviour more closely aligned with plane strain, a trend which is visible in all results observed in the GFRP specimens. The range of minor strain is also smaller, with more clustering around 0% minor strain at all major strain values. It can be seen that the only geometry which does not

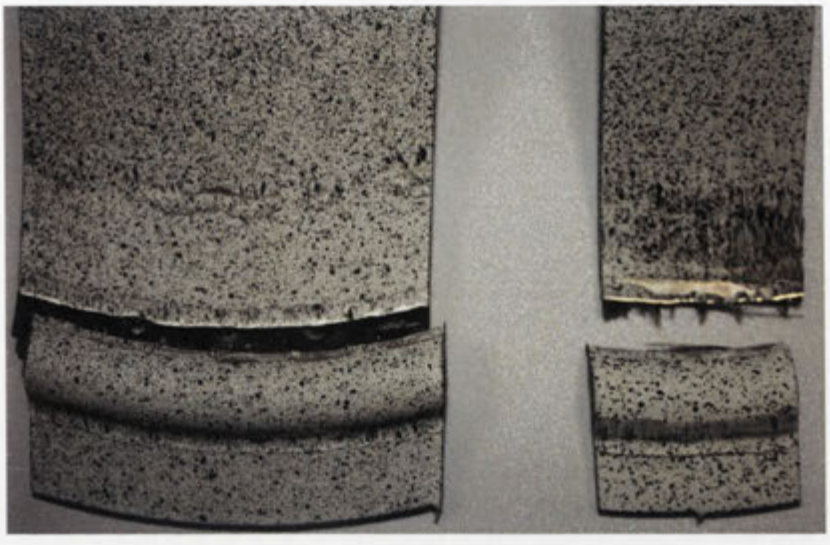

Figure 7.2: Failure at the lock ring in the 50mm (left) and 25mm (right) specimens

approximate plane strain is the 200mm specimen which undergoes biaxial stretch.

Figure 7.2 shows the failure at the lock ring of the 25mm and 50mm specimens. Contrary to the SRPP specimens, it was found that only the 25mm and 50mm GFRP FML specimens failed at the lock ring, with all other rectangular specimens showing significant strain increases or fracture in the centre of the specimen. Premature failure at the lock ring limits the ability for the smaller rectangular specimens to provide accurate information about the forming limits in their respective deformation modes; however, due to failure occurring prior to any failure in the centre of the specimen, it is expected that the failure limits generated by these specimens will be more conservative. In addition, as this work was performed after the SRPP specimens, no tearing in the hourglass specimens was observed.

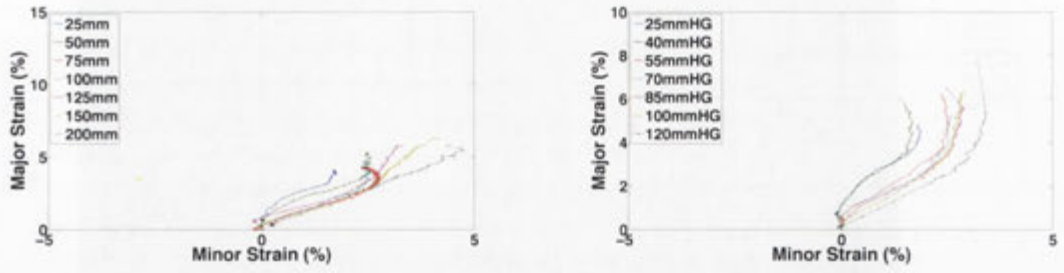

(a) (b)

Figure 7.3: Evolution of strain in the pole region for the rectangular (a) and hourglass (b) geometries

7.2.2 Evolution of strain in selected regions

7.2.2.1 Pole region

Figure 7.3 shows the evolution of surface strain at the pole of both the rectangular and hourglass experimental specimens. Similarly to the SRPP FML specimens there are three distinct regions for the evolution of strain at the pole of the GFRP specimens: the pre-stretch, biaxial, and proportional loading regions. However, there are significant differences in the behaviour of the material systems. The GFRP FML specimens fail at much lower major strain values due to low extensibility of glass fibres. This causes significant difficulty when determining whether the experimental specimens are inducing the expected deformation mode (as for the SRPP and aluminium specimens). It can be seen in the figure that a transition from biaxial stretch is occurring in the specimens; however, failure occurs before any meaningful results can be obtained for this deformation mode.

It can be seen in Figures 7.3(a) and 7.3(c) that the transition from the biaxial strain behaviour in the GFRP laminates is far more gradual than observed in the

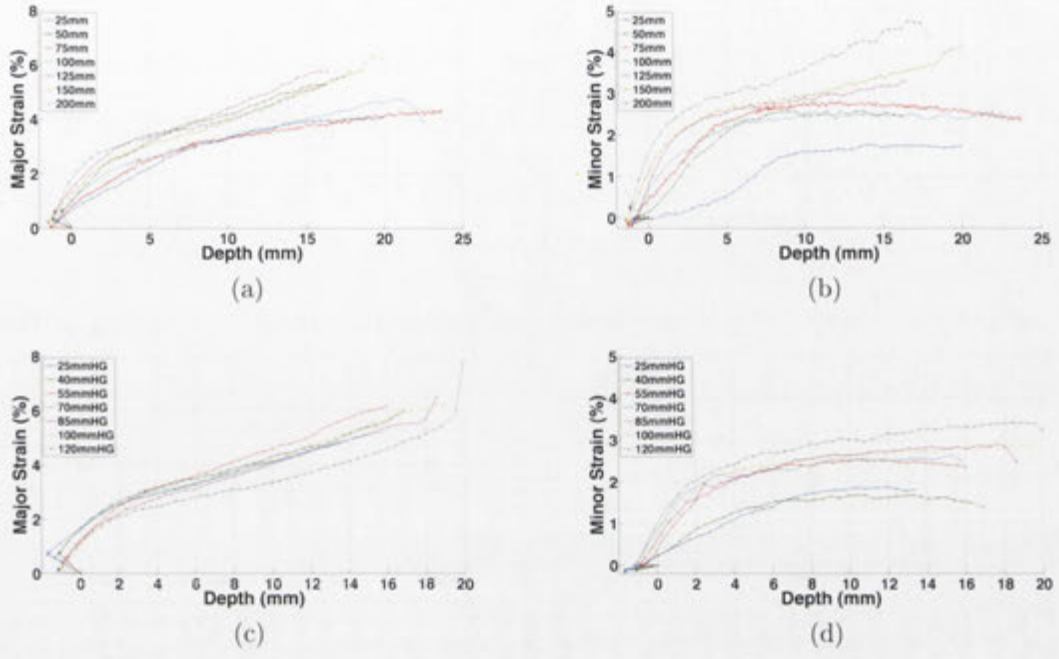

Figure 7.4: Evolution of the strain in the GFRP FML specimens with increasing forming depth

SRPP FML and aluminium specimens. The depth of the transition from biaxial stretch to the deformation behaviour occurs at approximately 3–5mm. Figure 7.4 elucidates the nature of the change in deformation behaviour at this depth which is caused by a change in the evolution of the minor strain. When Figures 7.4(b) and 7.4(d) are compared to the equivalent SRPP figures from Chapter 5,it can be seen that the evolution of the minor strain in the GFRP specimens does not exhibit the same trend as the SRPP specimens. The minor strain for each specimen does not diverge as significantly as in the SRPP specimens, with the wider specimens experiencing more positive minor strain and decreasing values as the specimen width decreases; instead, the GFRP FML specimens split according to specimen width and failure occurs before any divergence emerges. Figure 7.5

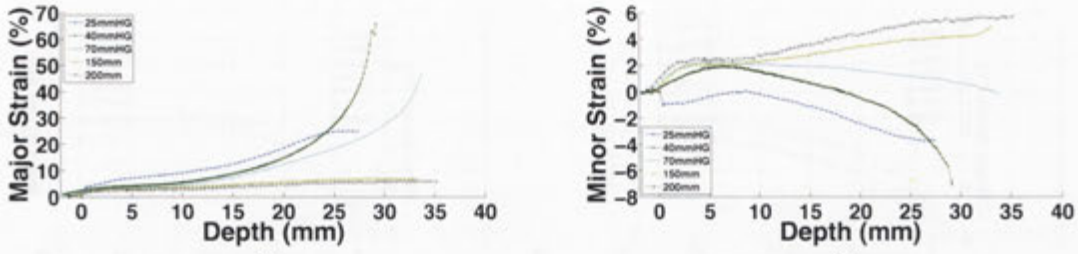

(a) (b)

Figure 7.5: Evolution of major (a) and minor (b) strain with depth in the aluminium

Specimen	25mm	50mm	75mm	100mm	125mm	150mm	200mm
Strain ratio (β)	0.24	–0.06	–0.19	0.01	0.25	0.42	0.9

(a)

Specimen	25mmHG	40mmHG	55mmHG	70mmHG	85mmHG	100mmHG	120mmHG
Strain ratio (β)	–0.27	–0.06	–0.12	0.05	0.15	0.18	0.1

(b)

Table 7.1: Strain ratios for the rectangular (a) and hourglass (b) geometries

shows the evolution of strain in selected aluminium specimens where it can be seen that when failure occurs very close to the pole, as in the 40mmHG and 70mmHG specimens, that the strain increases exponentially as the localised neck forms. The onset of this rapid increase is when the aluminium is considered to have failed, but the figures show that it is difficult to determine the exact start of the localisation of strain. It can be seen in the 25mmHG, 150mm, and 200mm results that these specimens have ceased to deform at the pole.

The strain path to failure allows the determination of the strain ratio in the specimens, which can be used to identify the approximate deformation mode experienced by each specimen. These strain ratios are shown in Table 7.1. As with the SRPP specimens these strain ratios were calculated using the evolution of

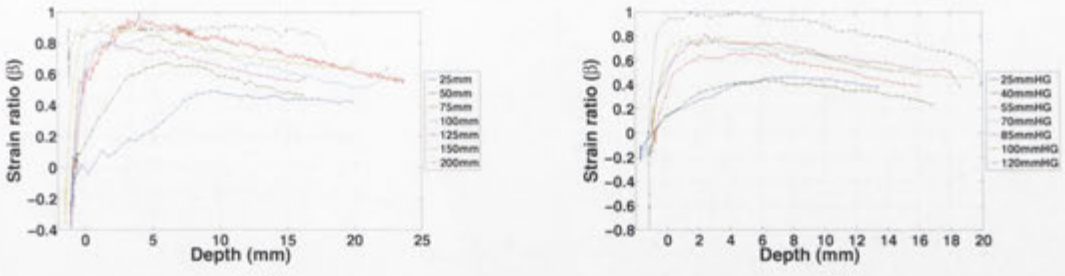

(a) (b)

Figure 7.6: Evolution of the strain ratio (β) at the pole of the rectangular (a) and hourglass (b) specimens

strain and not only the strain at failure. However, due to the limited deformation of the specimens it was very difficult to determine the strain ratio in the expected final deformation behaviour. Therefore, Figure 7.6 shows the strain ratio at the pole for all forming depths. This shows that the strain ratio is not constant at all forming depths. It is important to note that the strain ratio reported for the deformation modes occurring after the pre-stretch do not necessarily correspond to the deformation mode experienced by the specimen. This is because, due to the three distinct regions of deformation observed during forming at the pole, the starting points of the biaxial stretch and strain path to failure do not intersect the strain space at (0,0). This means that the strain ratio, calculated as β, only accounts for the current state of major and minor strain and not the behaviour over a period of time.

Significantly, the strain ratio for all specimens at the pole is never negative. This contradicts the expectation that the thinner specimens such as the 25mmHG and 25mm would experience uniaxial tension; however, Figure 7.6 shows that the strain ratio of all specimens (other than the 200mm specimen which remains

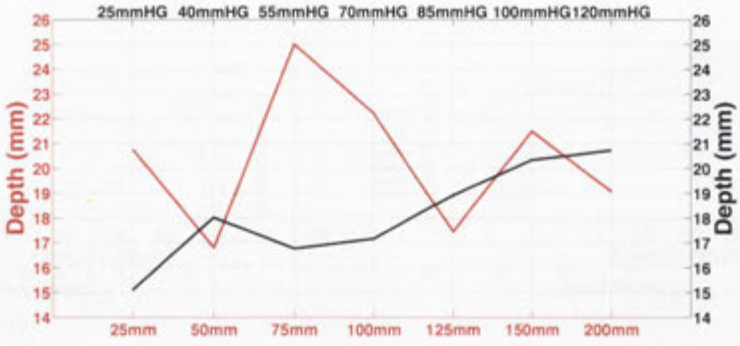

Figure 7.7: Failure depths of the experimental GFRP FML specimens

Figure 7.8: Delamination in the 75mm GFRP FML specimen

relatively constant) is decreasing as the forming depth increases.

7.2.2.2 Failure region

Figure 7.7 shows that the GFRP FML specimens all begin to fail prior to a depth of 26mm. This depth is measured at the pole of each specimen and is therefore the distance travelled by the punch. It can also be seen that all specimens, other the 75mm rectangular specimens, failed before 21mm. This could be due to the 75mm rectangular specimen exhibiting delamination as its failure mode, shown in Figure 7.8. This delamination did not immediately cause a drop in punch force, which would have halted the process, or reduced the major strain on the surface,

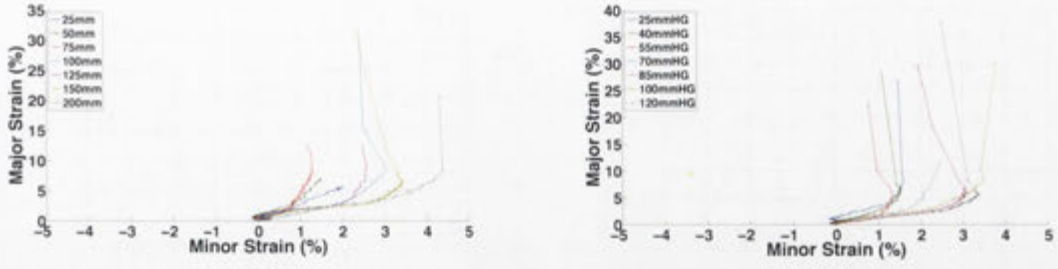

(a) (b)

Figure 7.9: Evolution of strain in the failure region for the rectangular (a) and hourglass (b) geometries

which would have signalled the onset of failure when processing the results. In all other specimens, failure is due to fibre breakage and subsequent tearing in the aluminium. The advantage of using specimens which have an hourglass geometry is that, compared to rectangular specimens, failure of the specimen can be induced in the region which is visible to the optical strain measurement system. Higher levels of friction at the pole prevent that region from deforming completely and therefore increase the amount of strain experienced by the regions surrounding the punch. This region is where failure generally occurs. The Teflon sheets used in this study were intended to prevent high levels of friction at the pole. Figure 7.9 shows the strain path in the specimens at the region where failure occurs. The 25mm, 50mm, and 75mm failure strain was taken from the location of highest major strain. It can be seen that the failure region in all specimens that had visible failure shows a significant increase in major strain prior to the appearance of a tear in the surface aluminium. These strain magnitudes exceed the maximum extensibility of the glass fibres in the GFRP, which therefore indicates a fracture in the GFRP followed by a rapid yielding and failure of the aluminium as the

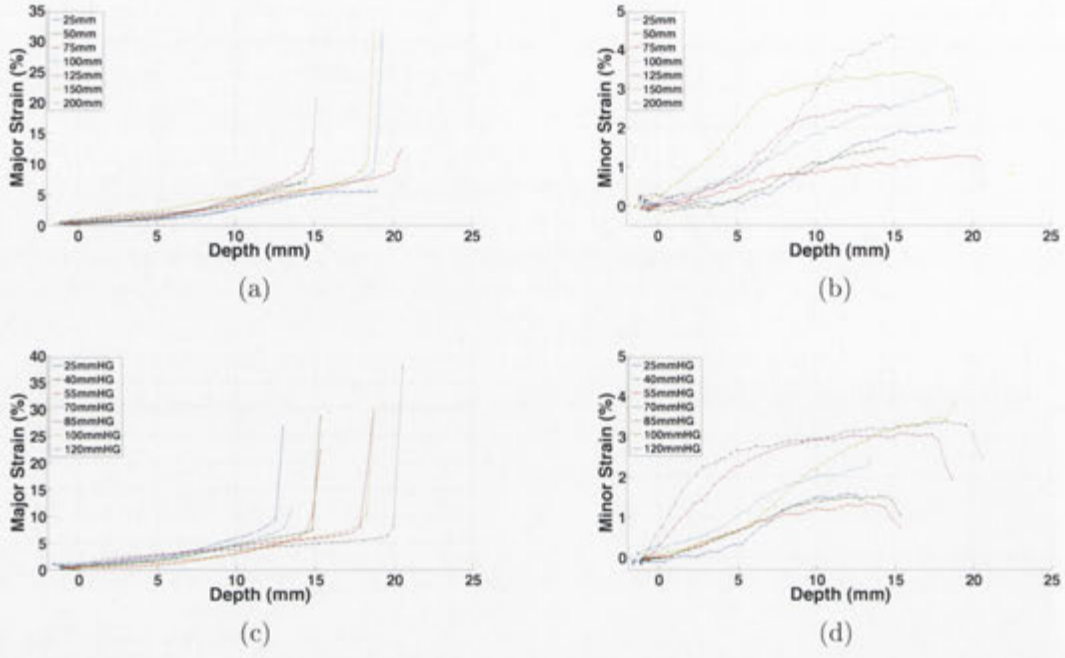

Figure 7.10: Evolution of the strain with increasing forming depth

load is transferred.

Figure 7.10 shows the evolution of the major and minor strain at the point of failure in the FML specimens, which further highlights the rapidity of the strain increase prior to failure. The increase in major strain occurs in either one or two ARAMIS images which, as stated previously, correspond to an approximately 0.5–1mm increase in forming depth. Table 7.2 shows the difference in the hourglass specimens between the increase in major strain at approximately 10mm forming depth and at the failure depth in the hourglass specimens. It can be seen that the increase in major strain is similar to the increase in forming depth until the last stage whereupon the increase in the major strain is orders of magnitude higher than the increase in depth. This failure begins at a major strain of 6–10%, which is slightly higher than the failure strain of the glass fi-

Specimen	Change in depth (%)	Change in ϵ_1 (%)
25mmHG	5.12	6.55
40mmHG	4.25	6.21
55mmHG	3.62	6.19
70mmHG	5.23	9.55
85mmHG	4.19	1.88
100mmHG	4.31	9.13
120mmHG	4.20	3.00

(a)

Specimen	Change in depth (%)	Change in ϵ_1 (%)
25mmHG	3.75	180.46
40mmHG	3.58	287.03
55mmHG	6.53	217.63
70mmHG	3.76	42.55
85mmHG	5.01	267.08
100mmHG	4.71	249.15
120mmHG	5.12	493.61

(b)

Table 7.2: Increase in major strain at 10mm (a) and immediately prior to failure (b)

bres as reported by the manufacturer. However, this strain is measured on the outer surface of the lower aluminium, which experiences a higher strain than the GFRP layer due to combined bending and stretching. Similarly to the SRPP FML specimens it is possible to predict the sub-surface strain using the bending equation. This is especially useful for the GFRP FML specimens, where there is obvious initial failure in the composite laminate followed by necking and tearing in the aluminium layer, as it allows the strain at failure of the GFRP layer to be determined.

Figure 7.11 shows the meridian displacement of deformed specimens with the punch superimposed to allow the radius of curvature around the failure region to be determined. These figures show that in the pole region the radius of curvature is equal to the radius of the punch, and that outside this region the specimen is effectively straight. Therefore, to determine the effect of bending on the failure strain in the specimen, the exact position of failure must be determined. The position at which failure occurs, the radius of curvature, and the calculated strain

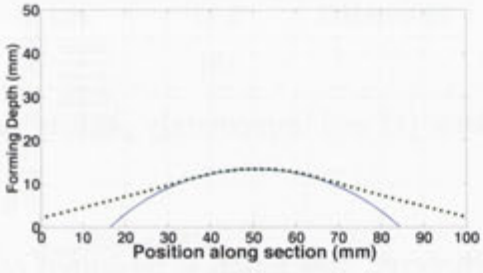

(a) 25mmHG

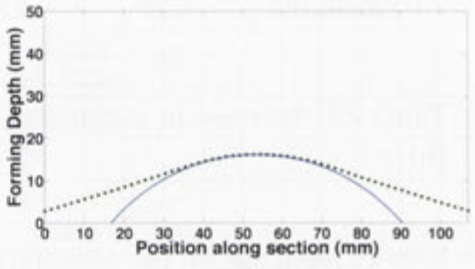

(b) 40mmHG

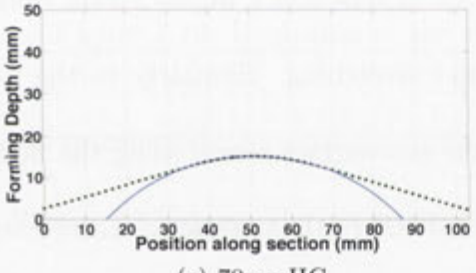

(c) 70mmHG

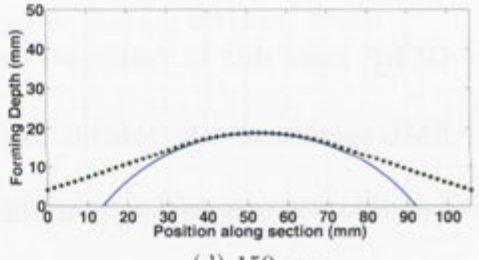

(d) 150mm

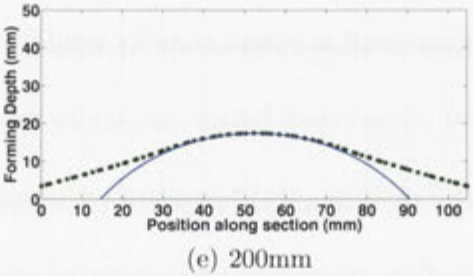

(e) 200mm

Figure 7.11: Deformed meridian of the experimental GFRP FML specimens

Specimen	Distance of failure from pole (mm)	Radius of curvature (κ) (mm)	Mid Surface Strain (ϵ_0) (%)
25mmHG	12	50	7.338
40mmHG	10	50	5.2
70mmHG	12	50	5.776
150mm	6	50	7.346
200mm	17	50	6.13

Table 7.3: Radius of curvature around the failure region in the hourglass specimens

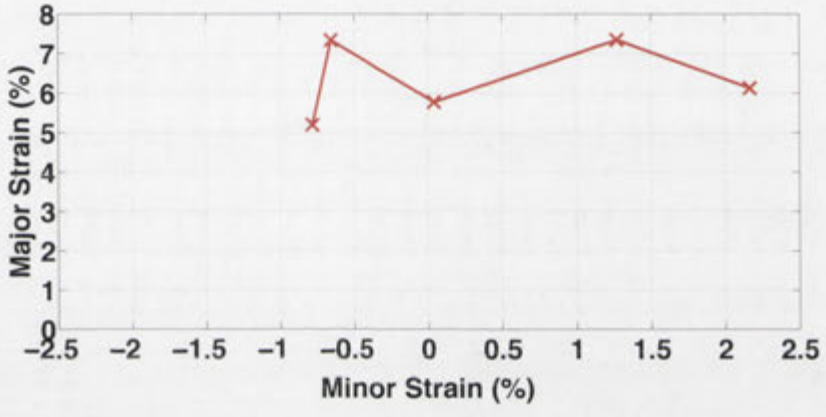

Figure 7.12: Preliminary failure criteria for the GFRP layer

in the GFRP layer for the experimental hourglass specimens is shown in Table 7.3. This table shows that the strain in the middle of the GFRP layer at failure was 4–8%, which is inside the expected failure strain region for a glass fibre composite. Using Table 7.3 and Figure 7.11 it can be seen that the failure of the GFRP FML specimens occurs in the region in contact with the punch, where the radius of curvature at this point is equal to the radius of the punch. The bending strain is therefore 2.2%. The minor strain for the region of failure is found using the radius of curvature in the minor strain direction. Figure 7.12 shows the determined failure limits in the GFRP layer using the bending strain equation. This figure shows that the average failure strain across all specimens,

Figure 7.13: Comparison of failure in the GFRP FML (left), SRPP FML (centre), and aluminium (right)

and therefore deformation modes, is approximately 6.3%. In contrast, Wilson [16] found a tensile failure strain of 2–2.5% for the GFRP; Reyes and Kang [79] found a failure strain of approximately 5%; and the results of the characterisation experiments showed a failure strain of 0.6%. This shows that there could be significant variability in the GFRP supplied by the manufacturer and illustrates the difficulty in determining definite failure limits.

Figure 7.13 shows a comparison of the failed isothermal GFRP, SRPP, and aluminium biaxial stretch (200mm) specimens. The figure shows that the failure in the GFRP FML occurs much earlier than in the SRPP and aluminium specimens. The failure of the two FML systems were similar: a tear following two perpendicular lines across the fibre direction in each specimen; in comparison, the aluminium showed an almost uniform circular tear.

7.2.3 Surface strain behaviour

Figures 7.14 and 7.15 show the surface strain contours for the uniaxial tension, plane strain, and biaxial stretch specimens. These specimens show an interesting tessellated pattern compared to the isothermal SRPP specimens. This behaviour

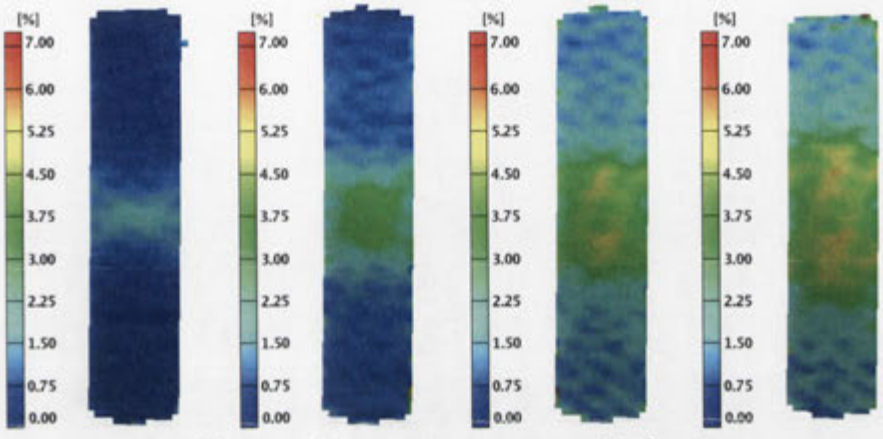

(a) 25mm (5mm, 10mm, 15mm and failure)

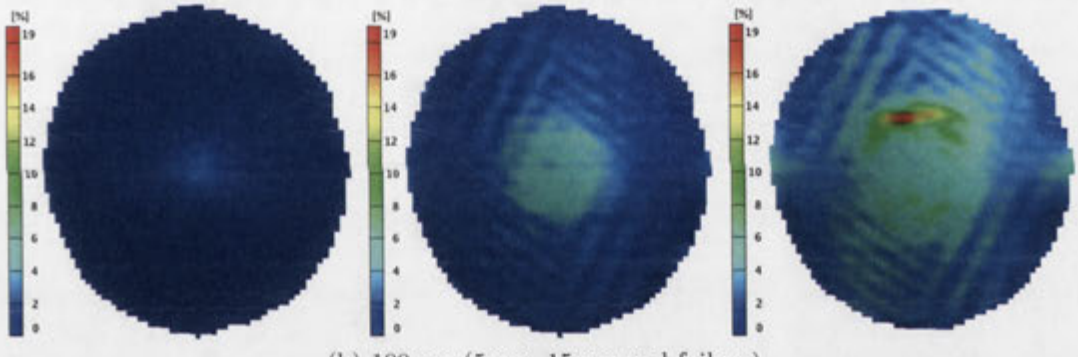

(b) 100mm (5mm, 15mm and failure)

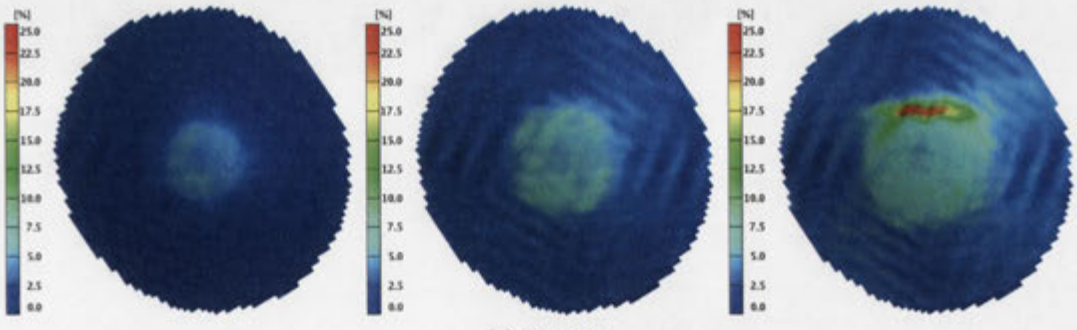

(c) 200mm

Figure 7.14: Surface strain contours

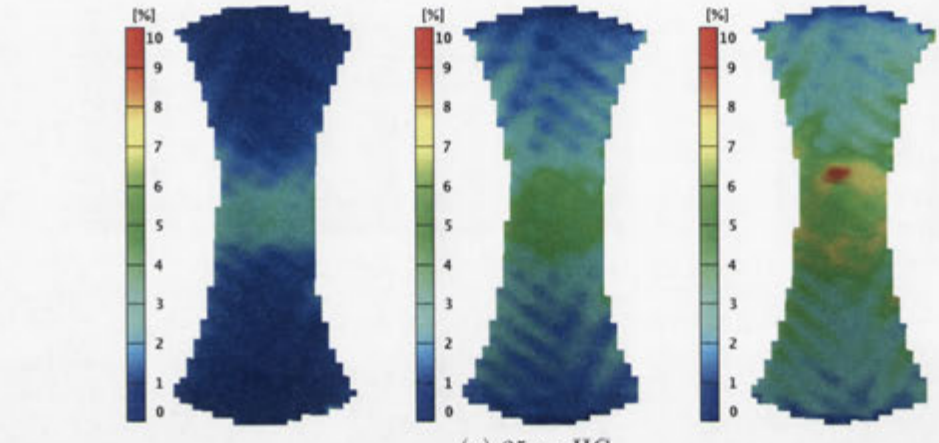

(a) 25mmHG

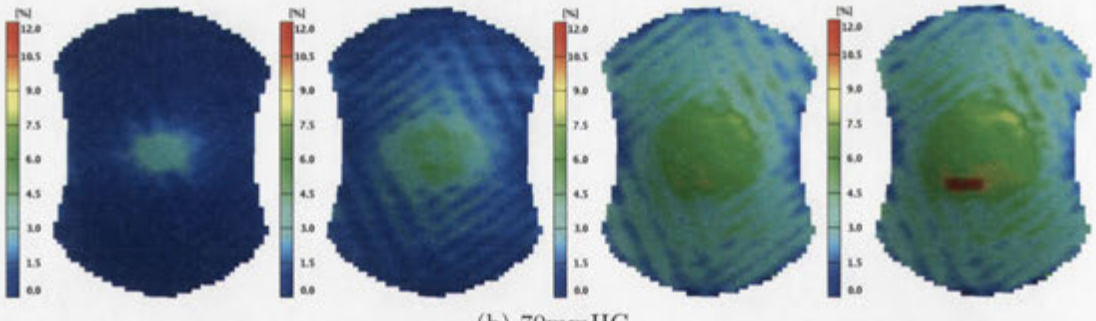

(b) 70mmHG

Figure 7.15: Strain contours for the selected hourglass specimens at different forming depths

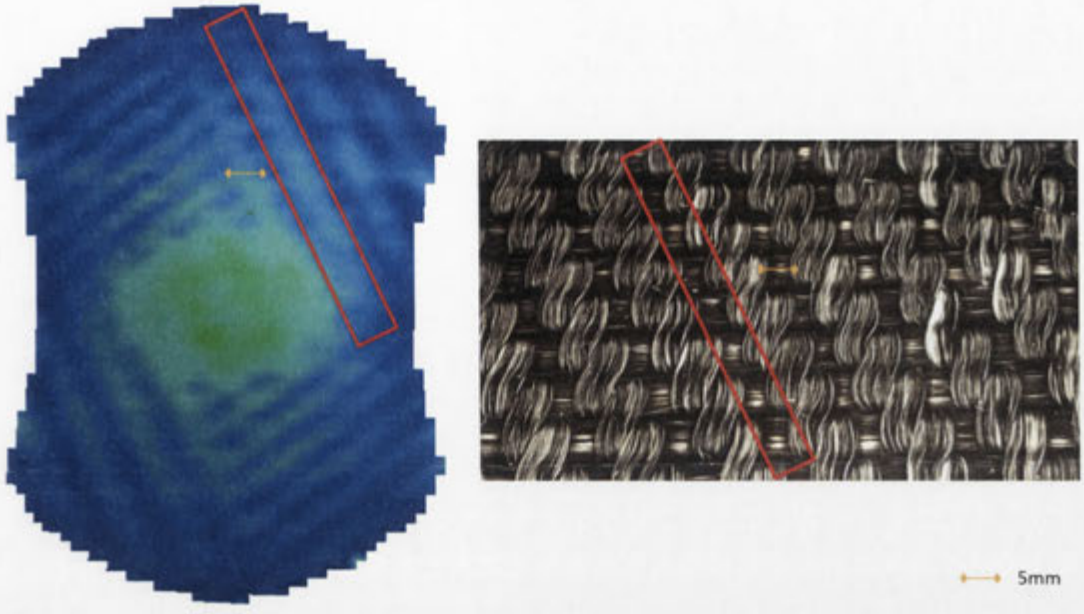

Figure 7.16: Effect of twill weave on surface strain measurements and in-plane waviness apparent in the glass fibre bundles

is caused by the twill weave, shown in Figure 7.16. In a twill weave, each weft floats across the warp yarns in a progression of interlacings to the right or left, forming a distinct diagonal line known as a wale. Figure 7.16 shows the orientation of the wale, which corresponds to the non-highlighted section or the "raised" warp yarns, and the floating weft yarns (highlighted) where higher strains are seen. Higher strains occur in this region as the weft yarns are oriented in the lateral direction, which means that the load is being applied perpendicular to the glass fibres causing the lower stiffness matrix to deform. The lower stiffness provides greater extensibility.

The other main result shown in these figures is the increase in strain on the surface of the specimen in the failure region. As stated in the previous section, failure of the GFRP layer initiates the failure of the laminate. It can be seen that

the strain in the non-failed regions does not generally exceed 10%, which, when considering the bending strain, means that the sub-surface strain in the GFRP does not exceed 8%. Only the 25mm specimen does not show the increase in strain on the surface as failure occurred at the lock ring. It can be seen that the failure strain is much larger than the strain at other regions.

Figure 7.17 shows the strain ratio on the surface of the 25mmHG, 70mmHG, and 200mm specimens immediately prior to failure. The tessellated pattern appears again in the strain ratio contour where the wale, which contained the lower major strain values, has a more positive strain ratio than weft yarns identified in Figure 7.16. This indicates that the area around the warp yarns (wale) is experiencing a deformation mode more closely aligned with biaxial stretch and the weft region is experiencing plane strain–uniaxial tension deformation. This result is not unexpected: the shape of the specimens and the boundary conditions of the process force the major strain to occur in the longitudinal direction and the stiffness and weave of the GFRP affect the minor strain. The minor strain in the warp yarns (wale) is more positive because it occurs in the transverse (lateral) direction, where the warp yarn's superior stiffness cannot significantly restrict the strain in that direction. Conversely, the major strain occurs in the transverse direction of the weft yarns, and therefore the laterally aligned fibres resist an increase in the minor strain. If the GFRP FML specimens were capable of withstanding higher strain values then it is expected (and shown in the trend of the strain at the pole) that the minor strain in the 25mmHG specimen will start

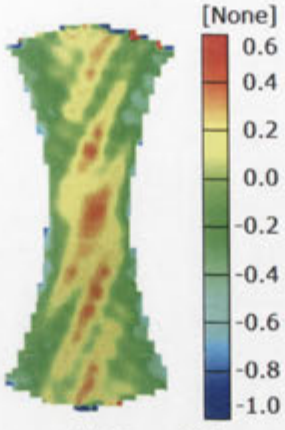

(a) 25mmHG

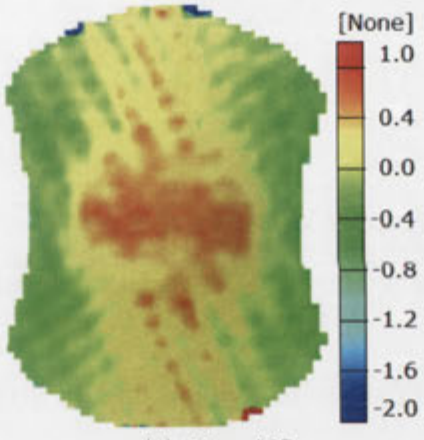

(b) 70mmHG

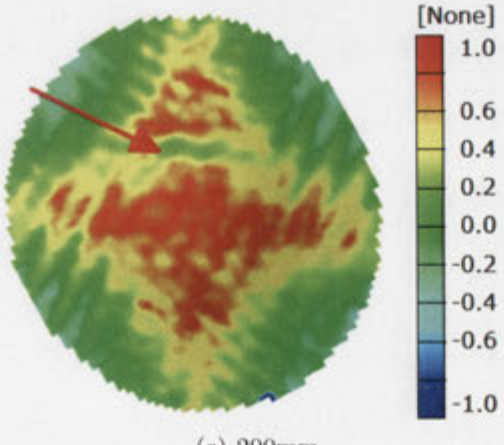

(c) 200mm

Figure 7.17: Strain ratio on the surface of selected specimens

to trend negative and the 70mmHG specimen major strain will cease to change, resulting in the expected deformation modes. When compared to the SRPP and aluminium specimens, shown in Figure 5.16, it can be seen that the GFRP specimens exhibit significant differences in strain ratio behaviour. The 200mm and 25mmHG specimens, unlike the SRPP FML, contain negative and positive strain ratios on the surface respectively.

Finally, the strain ratio at failure also highlights where failure is going to occur: due to the rapid increase in strain in the aluminium caused by the failure of the GFRP the strain ratio becomes much lower than the surrounding regions. The failure regions of the specimens are indicated by the red arrows in the figure.

7.2.3.1 Forming limit diagram at various depths

Figure 7.18 shows the FLDs for the experimental GFRP FML hourglass specimens. These figures show that GFRP FML shows similar behaviour to the SRPP FML specimens shown in Chapter 5 with a few significant differences. Firstly, the strain is lower in the GFRP than the SRPP for similar forming depths. For example, it can be seen in Figure 5.18 that the 25mmHG SRPP FML specimen has a major strain range from 0–9.07% and a mean major strain of 3.46% compared to the GFRP specimen which has values of 0–6.03% and 2.27% respectively. One of the main reasons for this difference is the difference in "pre-stretch" between the SRPP and GFRP FML specimens; for the SRPP FML strain values reached 4%, whereas for the GFRP the strain never exceeded 2% and was centred below 1%.

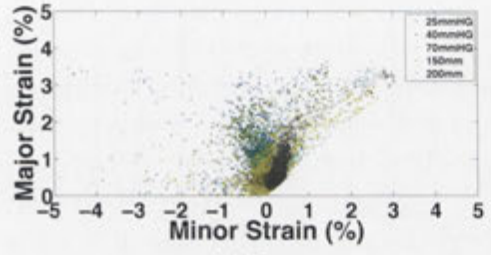

(a) 5mm

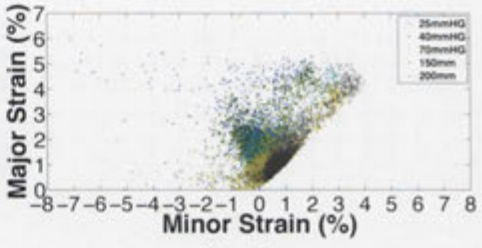

(b) 10mm

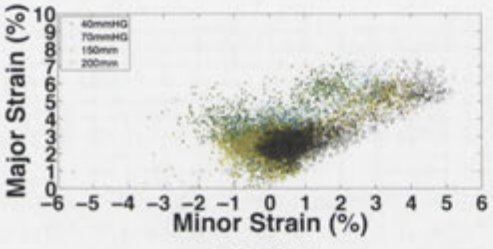

(c) 15mm

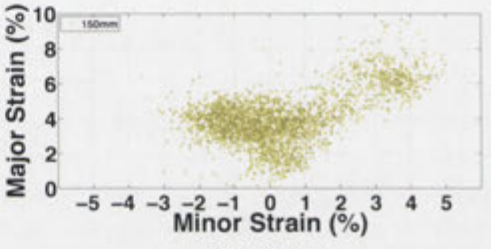

(d) 20mm

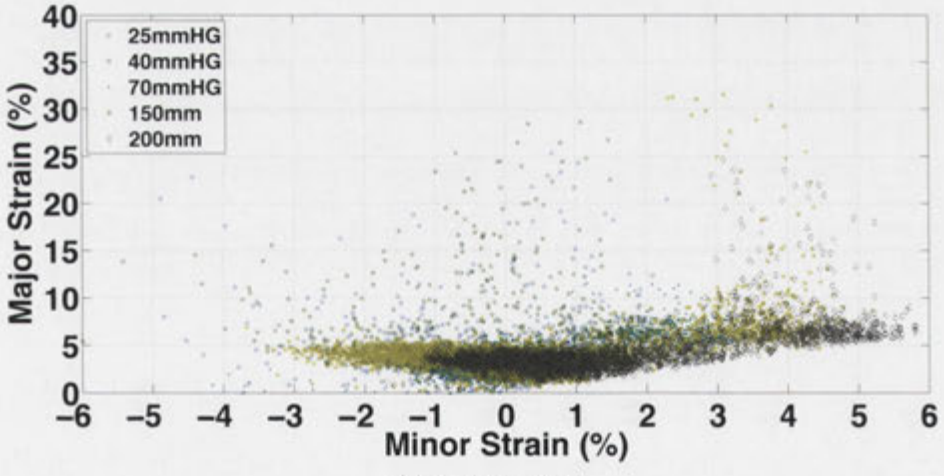

(e) Failure depth

Figure 7.18: Experimental forming limit diagrams for the hourglass geometries at various depths

This means that for all depths the strain in the GFRP FML specimens will be lower. However, another parameter which affects the surface strain distribution is the stiffness of the specimen being formed. High stiffness materials require a higher punch force which increases the contact pressure between the specimen and the punch. If the friction between the punch in the low and high stiffness cases are the same then the surface strain in the high stiffness material will be more evenly distributed than in the low stiffness case. This is because it is easier to overcome the friction force than deform the specimen in the unsupported region and therefore the overall strain is lower and more uniform. For a softer material the unsupported region is easier to deform and therefore experiences more strain and the pole region undergoes rigid body motion. However, if a material exhibits plastic deformation then the effects of the high stiffness are superseded by the plastic deformation in the unsupported region which again leads to higher strains in this area.

It should be noted that the 25mmHG specimen reaches a forming depth of 15mm but this also corresponds to its failure depth; therefore the 15mm FLD for the 25mmHG specimen is shown in Figure 7.18(e). However, only one of these GFRP specimens reaches a depth of 20mm, whereas all the SRPP FML specimens reach this depth. In total, only the 100mm, 150mm, 100mmHG, and 120mmHG exceed 20mm forming depth while still exhibiting fibre failure.

Figure 7.18(e) shows the FLD for the hourglass specimens at their respective failure depths. Here the maximum major strain in the specimens approaches 40%,

whereas the SRPP FML specimens showed only 25–30% major strain at failure, due to the failure of the GFRP layer and subsequent load transfer. Figure 7.18(e) also shows that the FLC for the GFRP should approximately lie directly above the cluster of data at around 8–10%, with the values above this indicating failure in the GFRP layer.

Figures 7.19 and 7.20 show the comparison of the aluminium, SRPP, and GFRP FML specimens at a depth of 15mm. These figures show the major differences between the different material systems are the magnitudes of strain they experience. As discussed previously, the primary reasons for the difference are the stiffness of the laminate and the amount of pre-stretch applied to the specimen. Another behaviour that can be seen in the GFRP FML specimens is the clustering of minor strain about 0% in an inverted triangular shape. This clustering around 0% is also caused by the weave pattern, and for the reasons detailed previously.

7.2.4 Meridian strain

Figure 7.21 shows that the GFRP FML also exhibited a more uniform major strain distribution along the fibre direction than the aluminium specimens. Again the meridian line is oriented along the longitudinal axis, the pole region occurs at the 50mm distance, and the edge of the die is at 0 and 100mm. However, there appears to be more noise in the major strain along the meridian of the GFRP specimens compared to the SRPP FML specimens. This apparent behaviour is

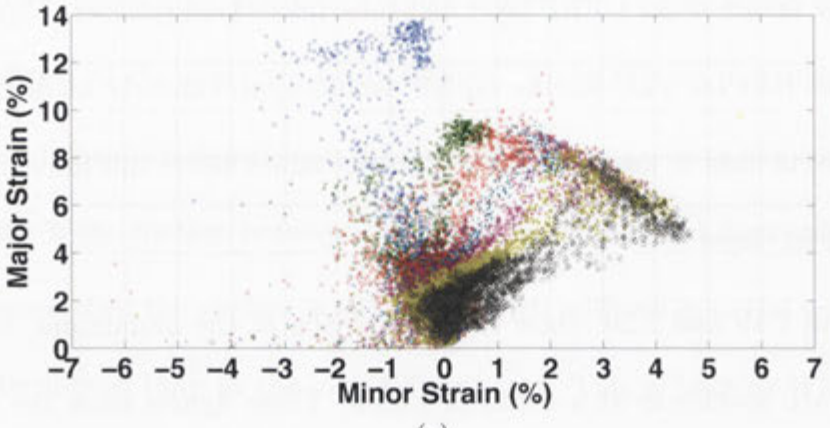

(a)

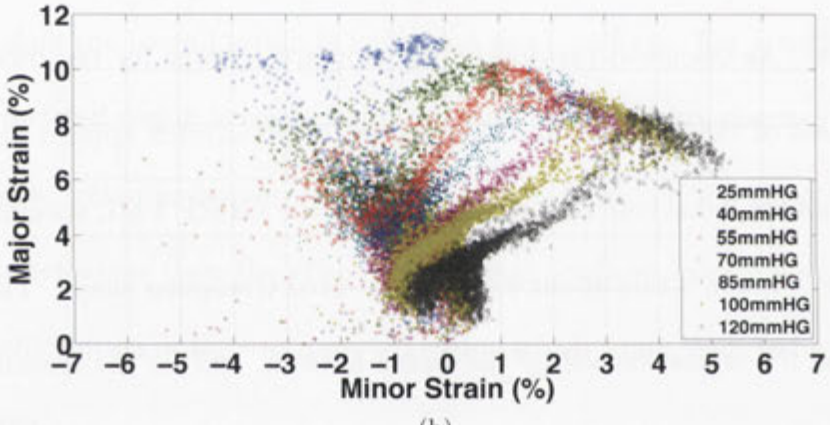

(b)

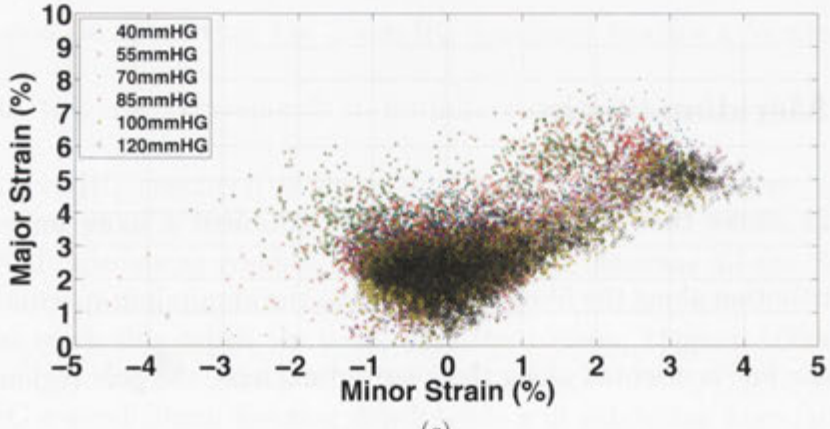

(c)

Figure 7.19: Comparison of the aluminium (a), SRPP FML (b), and GFRP FML (c) hourglass FLDs at 15mm forming depths

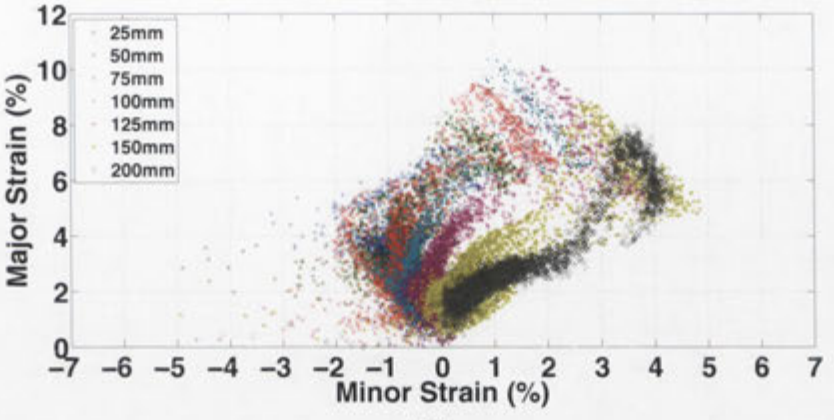

(a)

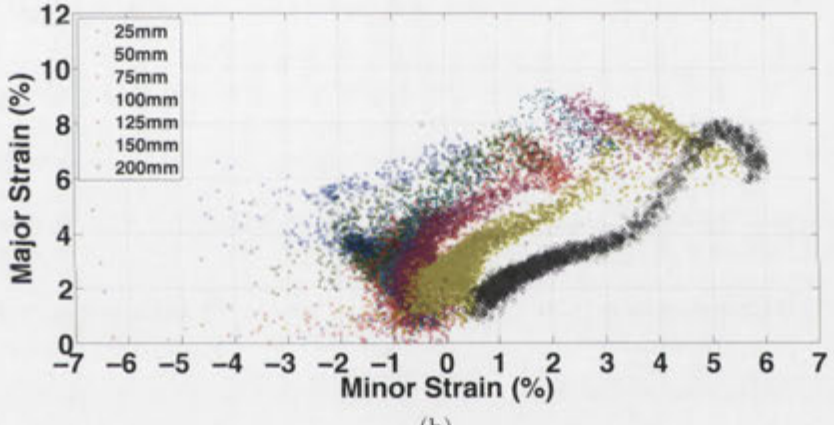

(b)

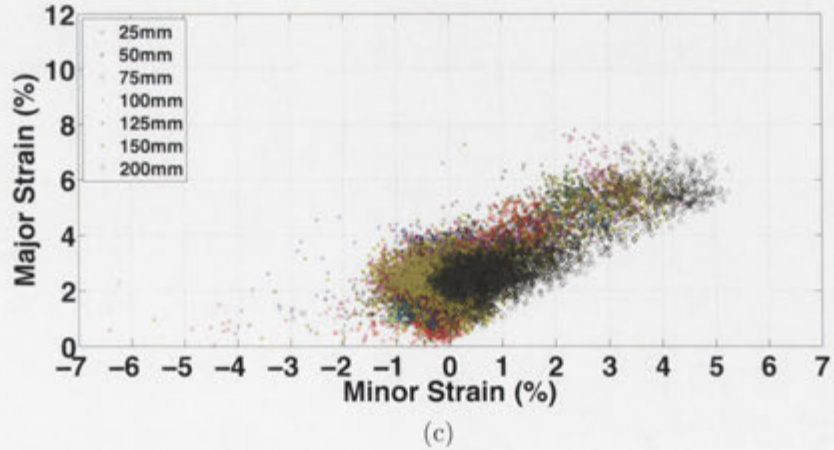

(c)

Figure 7.20: Comparison of the aluminium (a), SRPP FML (b), and GFRP FML (c) rectangular FLDs at 15mm forming depths

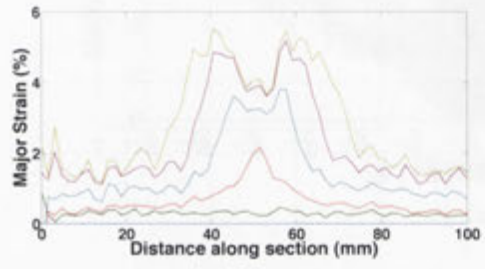

(a) 25mm

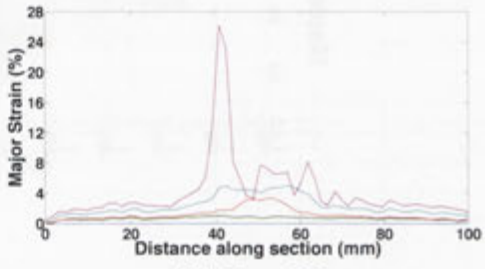

(b) 25mmHG

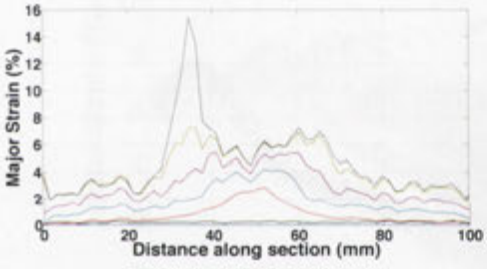

(c) 100mm

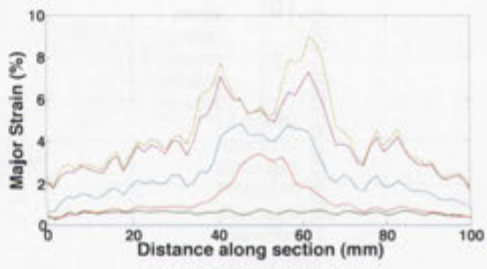

(d) 70mmHG

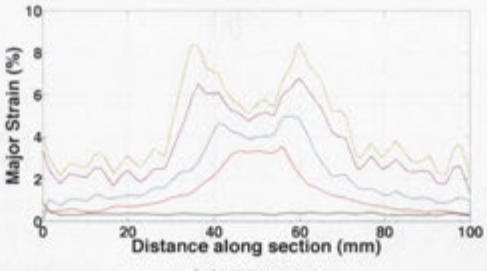

(e) 200mm

Figure 7.21: Meridian major strain at 5mm depths for the specimens corresponding to uniaxial tension, plane strain, and biaxial stretch

caused by the twill weave pattern discussed previously. In addition, the more uniform strain behaviour compared to aluminium only applies until the onset of fracture in the GFRP layer, when a sudden increase in the surface strain appears at the failure region. This rapid strain increase is similar to the behaviour of the aluminium specimens with one significant difference: whereas the aluminium strain begins with an accelerating trend towards failure in the sidewall with limited deformation at the pole, the GFRP FML shows approximately equal strain increases along the meridian with a sudden increase in strain in only one region (as shown in Section 7.2.2.2).

7.2.5 Forming limit curve

The failure of the experimental specimens was dependent on the specimen geometry. The thinner rectangular specimens such as the 25mm and 50mm failed at the lock ring, the 75mm appeared to delaminate, and the larger specimens such as the 100, 125, 150, and 200mm and all the hourglass specimens displayed failure which was visible to the optical measurement system.

The failure which occurred in the visible regions occurred to the side of the pole and along the longitudinal axis, and that failure occurred in the 200mm specimen in both the warp and weft fibre directions simultaneously. It has been discussed previously that the failure of the laminate is initiated by the failure of the GFRP layer. Supporting this assertion is that, contrary to previous studies on the forming of composite and FML systems [111, 112], the GFRP FML exhibited

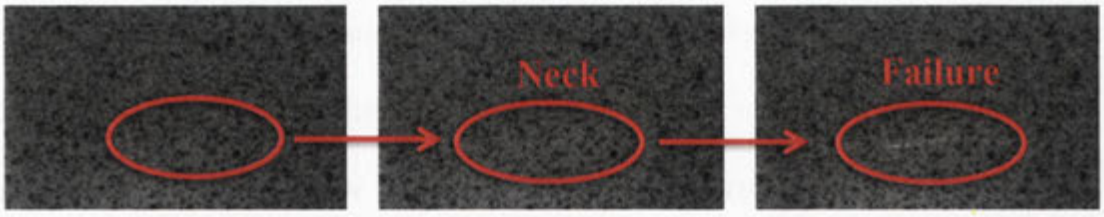

Figure 7.22: Appearance of localised neck prior to failure

some strain localisation, where none existed previously, prior to the appearance of a tear. Figure 7.22 shows the final three images of the surface of a FML specimen before failure. These figures show the rapid evolution of a neck in the aluminium layer leading to failure of the FML. This process occurs in 1/10th of a second, at 20fps, meaning that immediately after the fibres in the composite layer have failed the entire load is transferred to the aluminium layer which causes it to neck and subsequently tear.

Therefore, the forming for the GFRP FML specimen is much easier to determine than for either the aluminium or the SRPP FML specimens. This is because the high strain in the failed region allows for ready determination of safe points (outside the failed region), marginal/necked points (the localised strain region prior to the localistion of strain), and failed points (the localised high strain). The forming limit curves constructed for the rectangular and hourglass specimens are shown in Figure 7.23. These FLCs agree with the theory that the glass fibre will fail at a strain of approximately 4–8%, with the marginal region occurring in the region between these strain values. The localised necking in the FML specimens can be seen from the failed points in the figure, which are at much higher strain values than can be sustained by a glass fibre composite. In

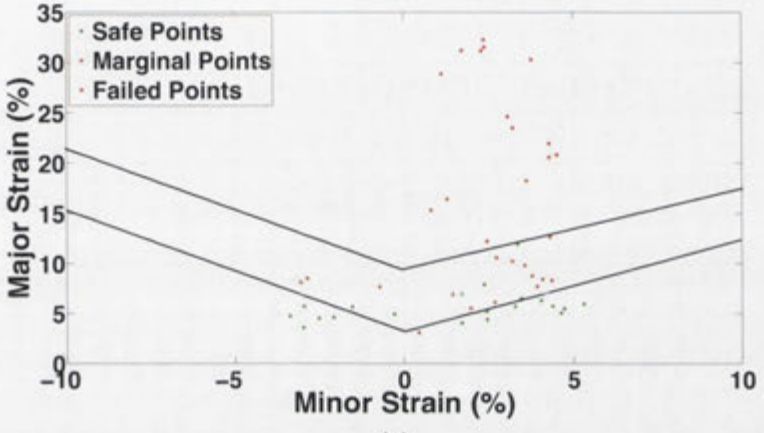

(a)

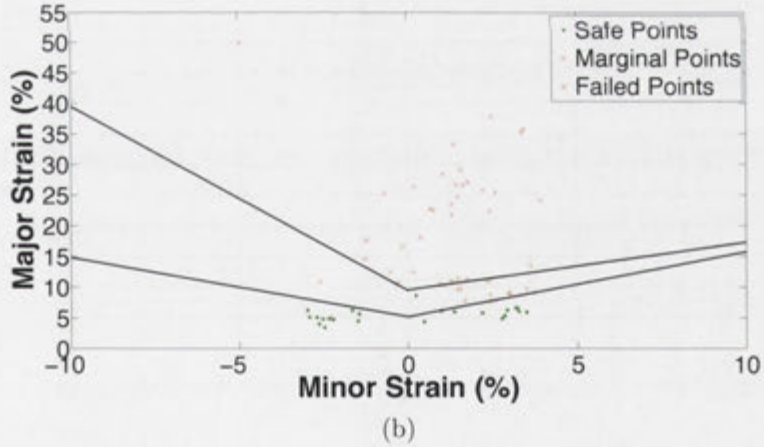

(b)

Figure 7.23: FLC for the GFRP laminate at room temperature. (a) shows the FLC determined using the rectangular specimens and (b) shows the FLC for the hourglass specimens

addition, they display significantly higher strain results than the marginal data points which were taken prior to an observation of a neck, such as in Figure 7.22. The FLC for the FML shows that, at room temperature, the strain in the glass fibre limits the ability of the FML to deform using the stamp forming process.

7.3 Finite element simulation

Similarly to the SRPP based laminate, the first step in the simulation of the GFRP laminate was the verification of the constitutive model by comparing the strain on the surface of the lower aluminium layer with that recorded in the experimental work.

7.3.1 Verification of the model

There were more difficulties in verifying the simulation for the GFRP FML than for the SRPP FML, primarily due to the surface strain behaviour caused by the twill weave and exhibited in Figures 7.14 and 7.15.

Figure 7.24 shows the pre-stretch applied to the specimens. It can be seen that FE results do not exactly match the experimental results, particularly because the minor strain does not match and there are more regions of low strain than in the experimental specimens. This is again the result of the pre-stretch in the FE simulation being an in-plane force rather than a forced deformation of the specimen into the lock ring. Figure 7.25 shows why the pre-stretch in the FEA does not match the experiments. The fibres in the experimental specimen distribute

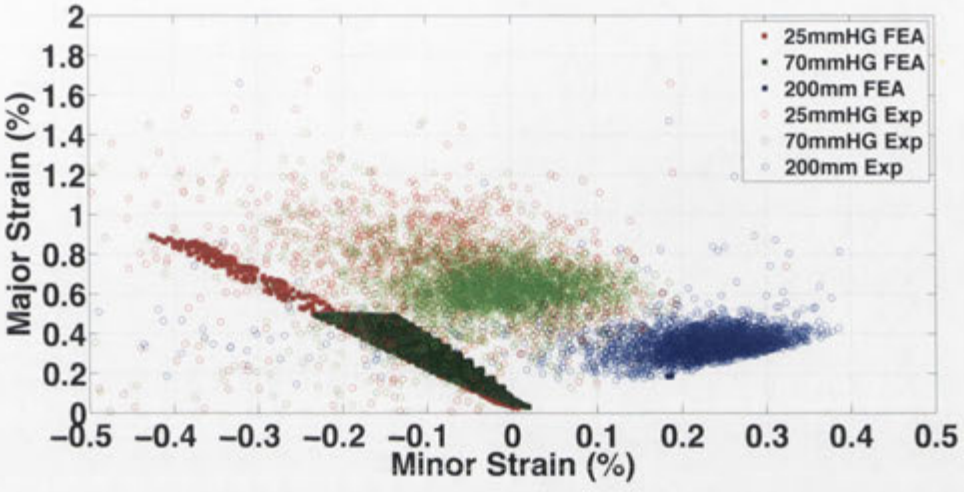

Figure 7.24: Verification of the pre-stretch in the FEA

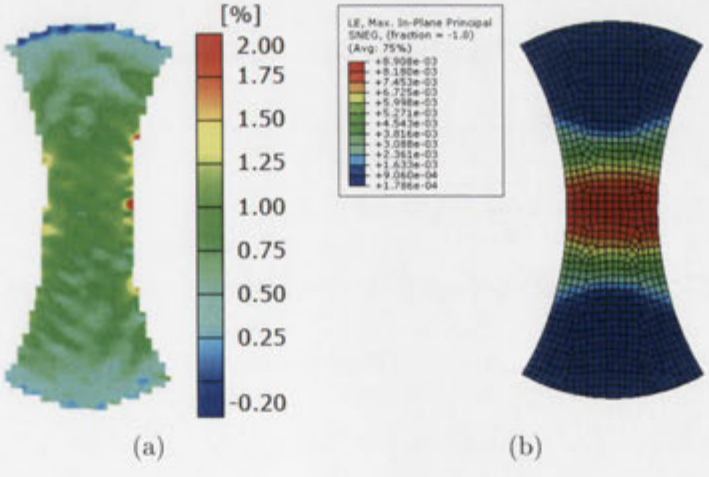

Figure 7.25: Comparison of the surface strain contours for pre-stretch in the experimental (a) and FEA (b) specimens

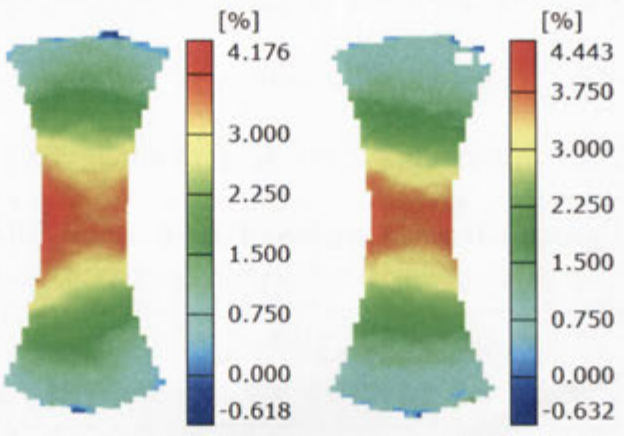

Figure 7.26: Pre-stretch major strain contours in the SRPP FML (a) and aluminium (b) specimens

the strain more efficiently than modelled by the simulation because the weave pattern results in a more textured strain distribution. The weft fibre regions distribute the strain and prevent the low strain region occurring by providing a region of low longitudinal stiffness which preferentially deforms compared to the warp fibres. This region, as stated previously, is called the wale. Contrasting this is the strain distribution in the SRPP FML and aluminium specimens, shown in Figure , which show the expected strain distribution where the highest strain occurs in the thinnest part of the specimen.

Figure 7.27 shows the evolution of the strain at the pole of the 25mmHG, 70mmHG, and 200mm specimens. This shows that the pre-stretch major strain in the FEA matches the experiments in this region within 0.8% in the 25mmHG, 0.5% in the 70mmHG, and 0.2% in the 200mm specimen. In contrast to the SRPP FML results, the FE simulation of the GFRP FML at the pole does not match in the initial biaxial region, not because it is too high but because it is too

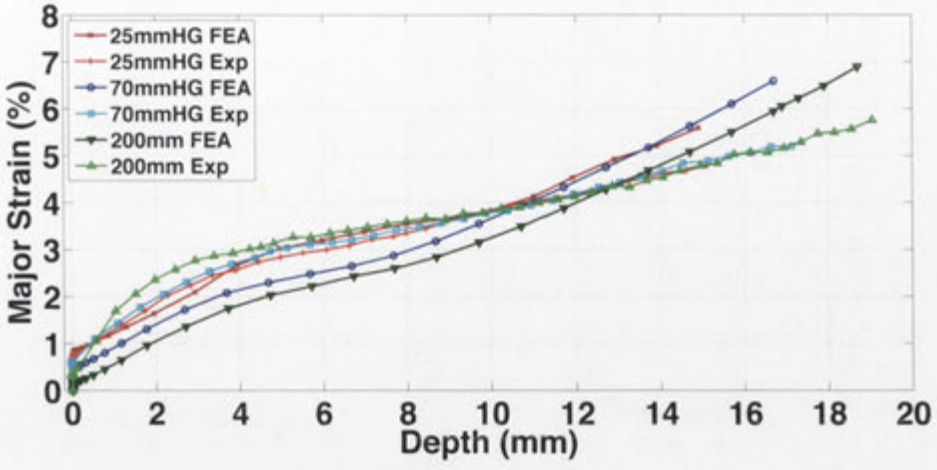

Figure 7.27: Comparison of the experimental and simulated pole strain evolution

low.

Figure 7.28 shows the comparison between the FEA and experimental meridian major strain at forming depth increments of 5mm. These figures show that the oscillation in the major strain is unachievable in the FE simulation due to the fact that the weave pattern is not simulated. However, the overall shape of the strain behaviour shows good agreement. This agreement worsens at higher forming depths, primarily because it appears that the pole deformation slows significantly in the experimental specimens (this was also discussed in the pole strain evolution). Figure 7.29 shows the effect of the weave on the surface roughness of the GFRP FML specimens. It can be seen that the uneven surface is caused by the pressure applied by the punch, forcing the aluminium layer to conform to the surface structure of the GFRP and resulting in a "wavy" appearance. This surface condition drastically affects the tribological system between the punch and the specimen and therefore the ability to correctly match the strain behaviour

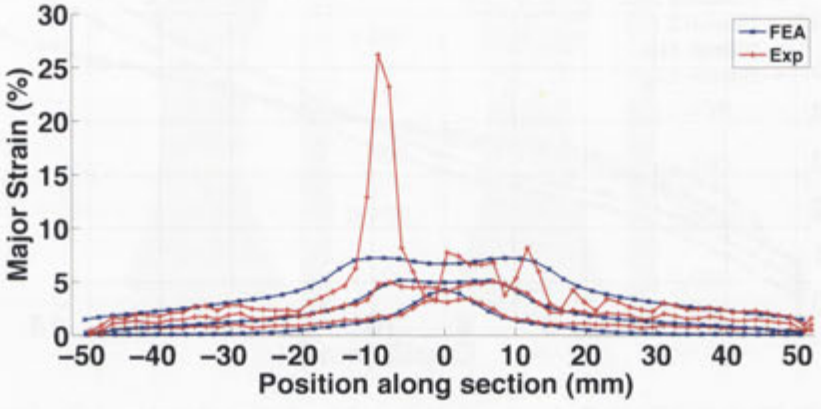

(a) 25mmHG

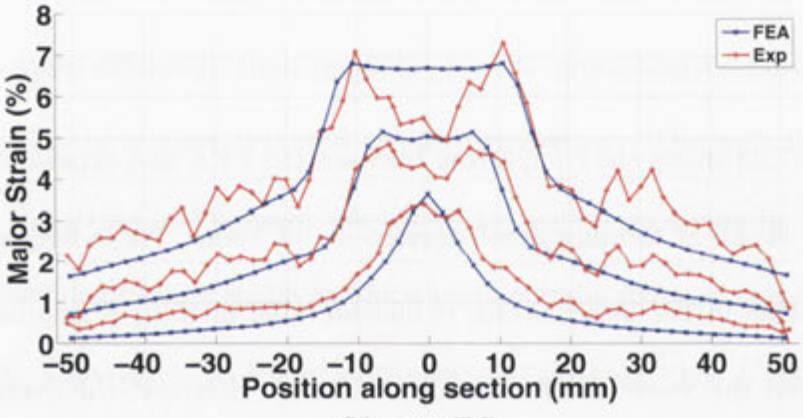

(b) 70mmHG

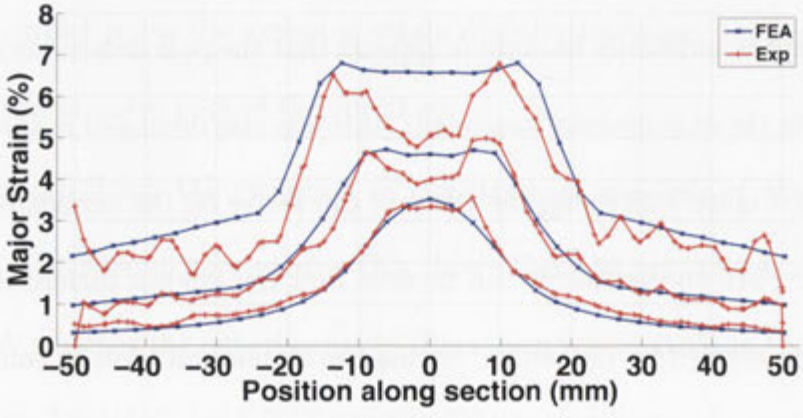

(c) 200mm

Figure 7.28: Comparison of the experimental and FEA meridian major strain

Figure 7.29: Effect of weave on the surface of the GFRP specimens

using FEA. For example, it can be seen that the major strain at the pole of the FE simulation is higher than that exhibited in the experiments, which leads to the conclusion that the friction between the punch and upper surface is too low. However, the strain unsupported region exhibits excellent correlation. Figure 7.30 shows the effect of the friction coefficient between the punch and the 25mmHG specimen at two forming depths. It can be seen that by raising the coefficient of friction the strain at the pole decreases and that at μ=15 a good match can be obtained for the major strain in the pole region. However, all of the simulated specimens do not show good agreement at distances greater than 20mm from the pole. There are three ways to achieve higher strain in desired areas which have been discussed previously: change the punch friction, change the die/blankholder friction, and/or change the material stiffness. A first thought in this model was to increase the die/blankholder friction as there is a small chance that material is stretching in the flange region which lowers the overall strain in the die region;

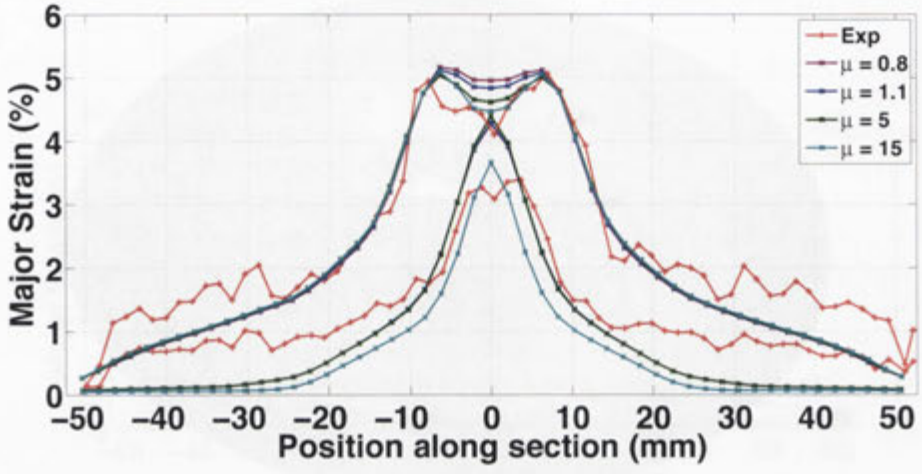

Figure 7.30: Effect of punch friction on the meridian major strain distribution in the 25mmHG GFRP FML specimen at 5mm and 10mm forming depths

however, this was found to have limited effect on the strain distribution. Therefore, the only remaining aspect which has not been altered is the stiffness of the GFRP layer. As discussed previously, an increase in stiffness leads to increased strain at the pole (more even across the entire surface) whereas lowered stiffness leads to reduced strain at the pole (much higher in the unsupported region). This is the reverse effect of the punch friction, indicating that a specific combination of friction and material stiffness is needed to achieve a perfect match. However, the stiffness data used for the material, shown in Figure 4.1, was the result of tensile experiments. Figure 7.31 compares the stress–strain curve in the tensile experiments and a verification simulation created in ABAQUS. This figure shows that a slightly higher stress is reported in the FE simulation, but if the tangent modulus is considered (which is how the the stiffness is calculated in the model) then the match with the results is very good. Therefore, this indicates that a Coulomb friction approach to simulating the interaction between the punch and the GFRP

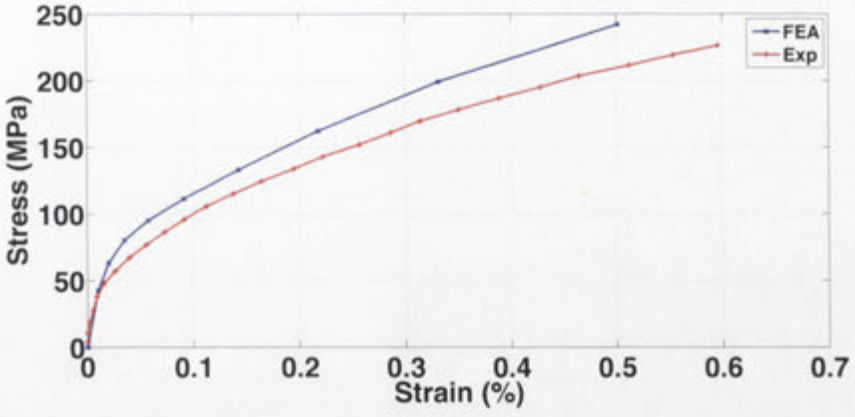

Figure 7.31: Comparison of the uniaxial tension data in the FE simulation with the tensile test results used for model development

FML specimen is not complex enough to accurately model the behaviour.

However, when matching FEA to experimental results it is very difficult to match the results at particular points. This is primarily due to noise in the experiments and the fact that it is impossible to perfectly model the material and process. Figure 7.32 shows the comparison of the simulated and experimental FLDs at a forming depth of 10mm. It can be seen that the overall strain distribution shows good agreement with a large cluster of data at low strain and some regions of increased strain. It can be seen that the most biaxial strain data is higher in the FE simulation than in the experiments. This region corresponds to the pole region which, as shown in the strain evolution and meridian strain distributions, is higher than the experimental data. Figure 7.33 shows the comparison between the experimental and simulated FLDs at the failure depth. In these figures the strain at the pole in the FEA is shown to have accelerated away from the experimental results. This indicates that, as the forming depth increases, the effect of friction at the pole also increases in the experimental specimens. This is

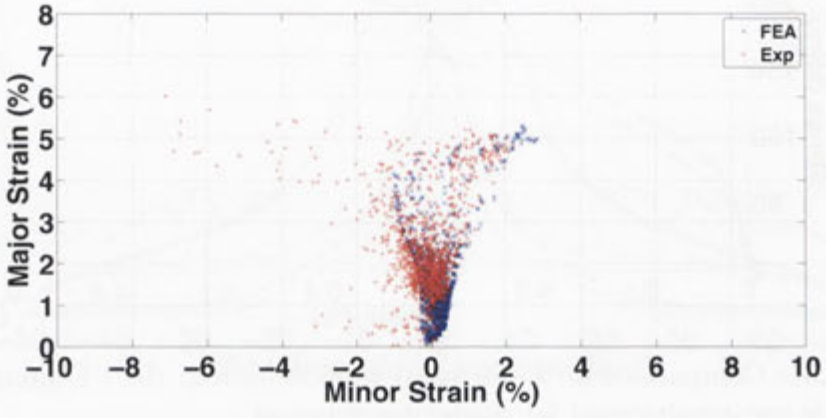

(a) 25mmHG at a forming depth of 10mm

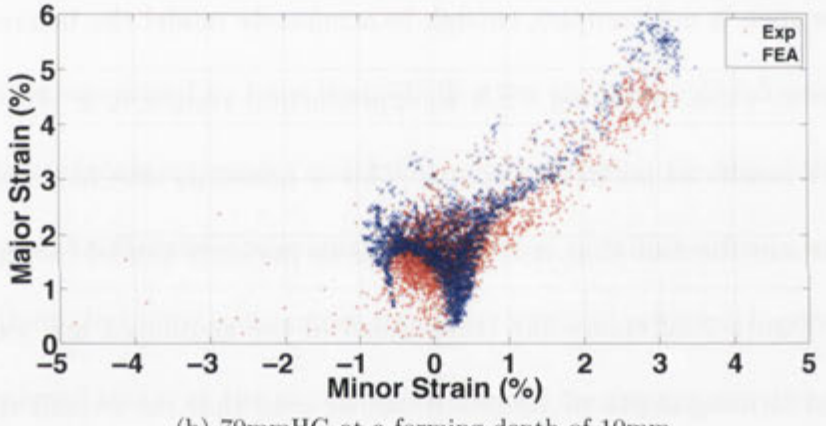

(b) 70mmHG at a forming depth of 10mm

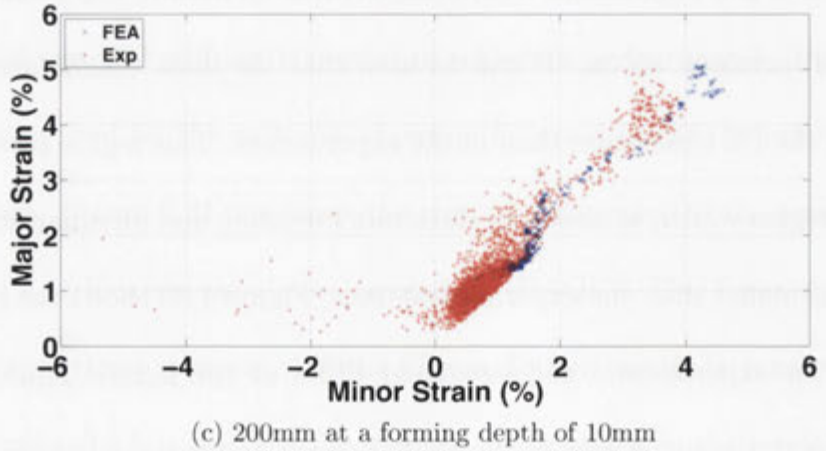

(c) 200mm at a forming depth of 10mm

Figure 7.32: Comparison of the experimental and FEA FLDs at a 10mm forming depth

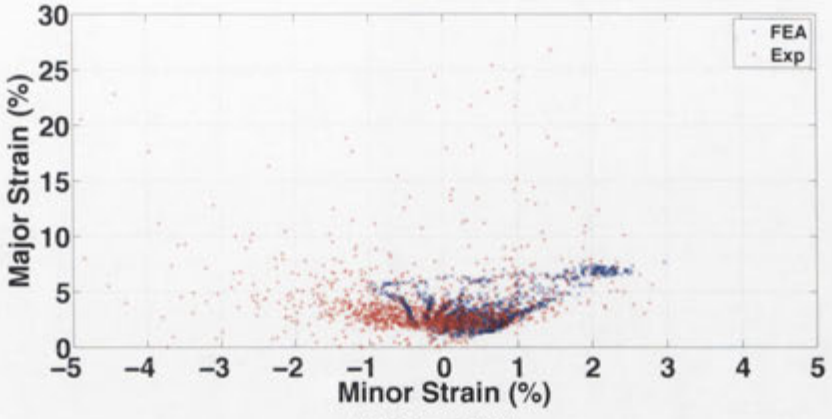

(a) 25mmHG

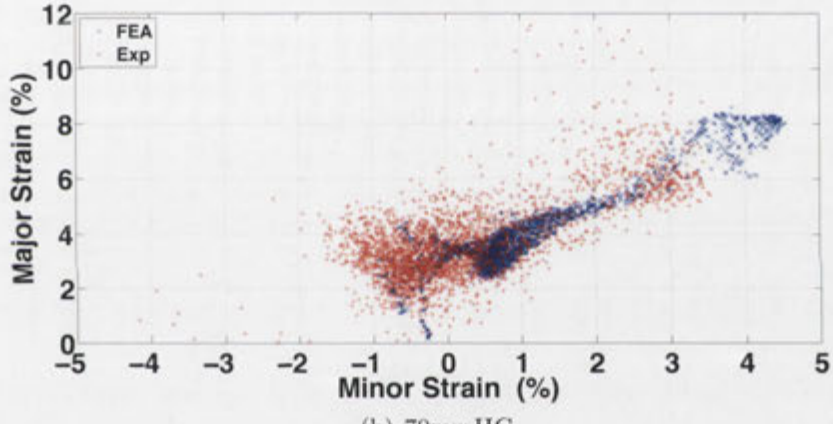

(b) 70mmHG

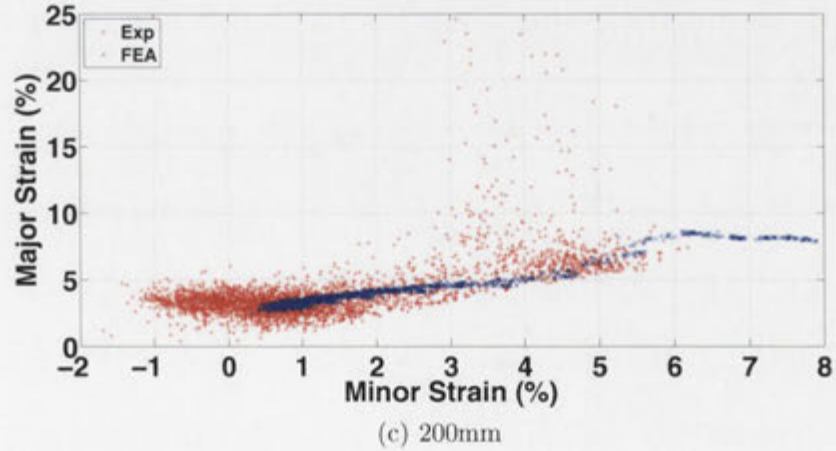

(c) 200mm

Figure 7.33: Comparison of the experimental and FEA FLDs at the final forming depth

explained by the increased punch force and contact pressure; however, as the FEA also simulates these increases it is therefore probable that the contact condition between the surfaces is dependent on the contact pressure as is the representative coefficient of friction (μ).

Figure 7.34 shows the major strain contours on the surface of the experimental and FE selected specimens; the limits of the FE and experimental strain contours are the same in each specimen. The tessellated pattern exhibited by the experimental specimens cannot be replicated by the homogenised macro-level model used in the FE simulation. The general strain behaviour shows good agreement; however, the lateral edges of the simulated 70mmHG specimen show greater levels of compressive strain than the experimental specimen, and the longitudinal edges show a modest tensile strain compared to the compressive strain in the experimental specimen.

7.3.2 Behaviour of the fibre–metal laminate layers

Again, the main purpose of the FE simulation is to assess the behaviour of the internal layers of the FML. Figure 7.35 shows the major strain in each layer along the longitudinal axis in the selected specimens. It is again evident that the strain in the inner layers of the FML follows the expected bending strain equation in regions in contact with the punch. The top aluminium layer, which is in direct contact with the punch, shows the greatest effect of friction on the strain distribution. This effect should appear constant along the region in contact with

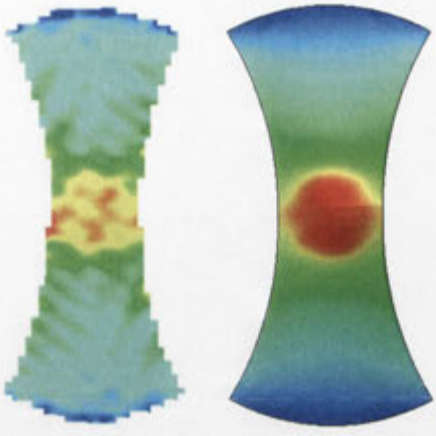

(a) 25mmHG at a forming depth of 10mm

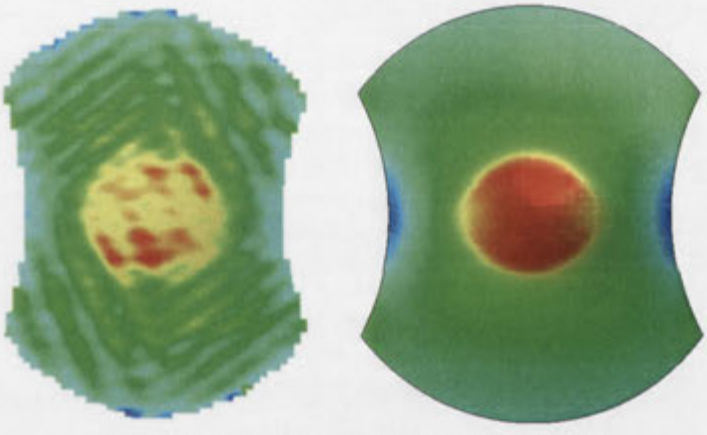

(b) 70mmHG at a forming depth of 15mm

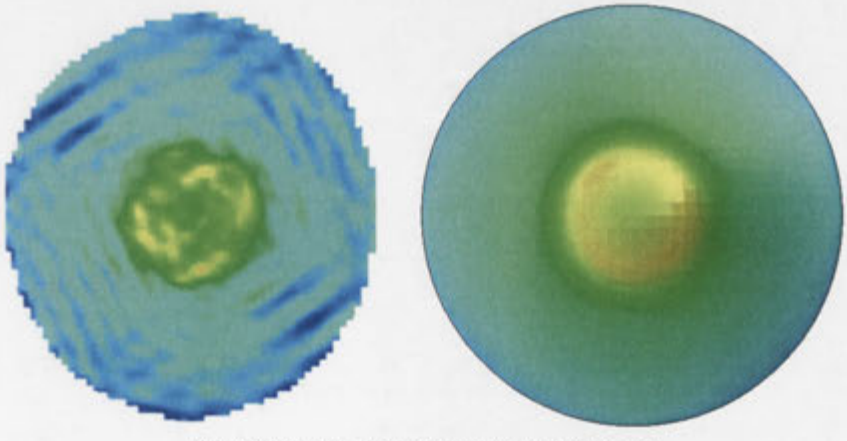

(c) 200mm at a forming depth of 15mm

Figure 7.34: Comparison of the experimental and simulated strain contours for selected specimens

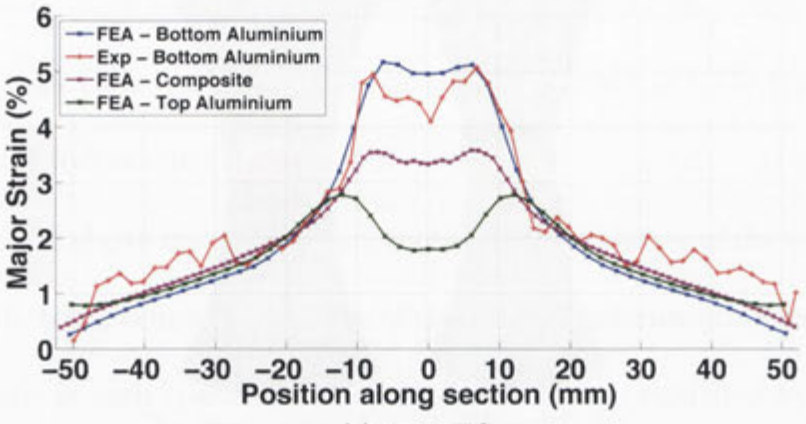

(a) 25mmHG

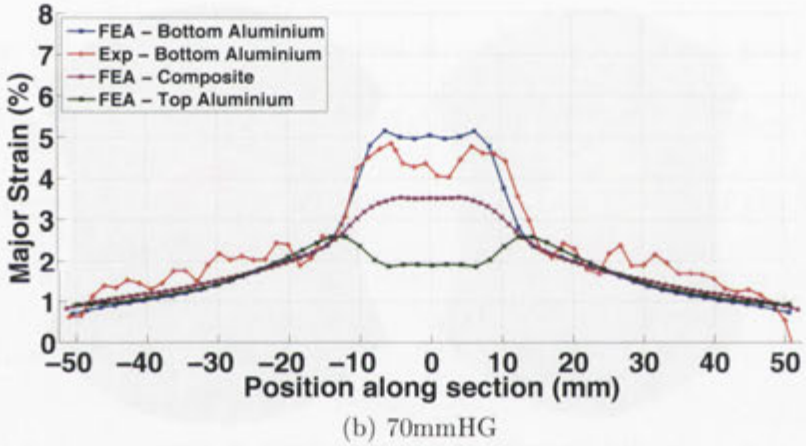

(b) 70mmHG

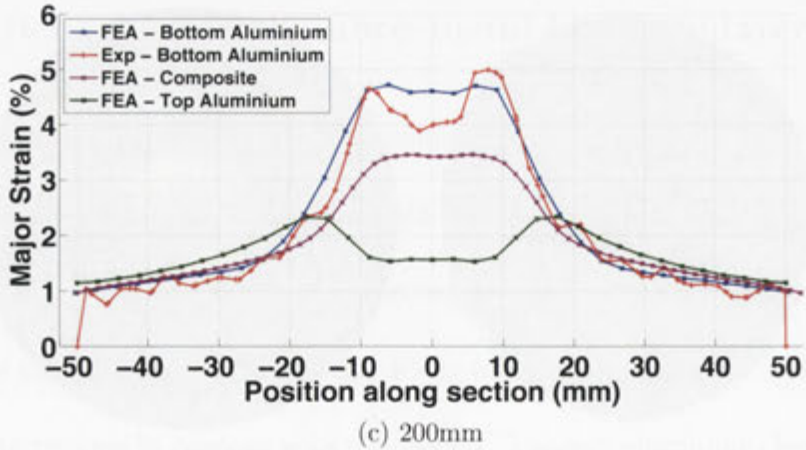

(c) 200mm

Figure 7.35: Meridian strain determined by the FEA simulation in all three layers of the GFRP FML

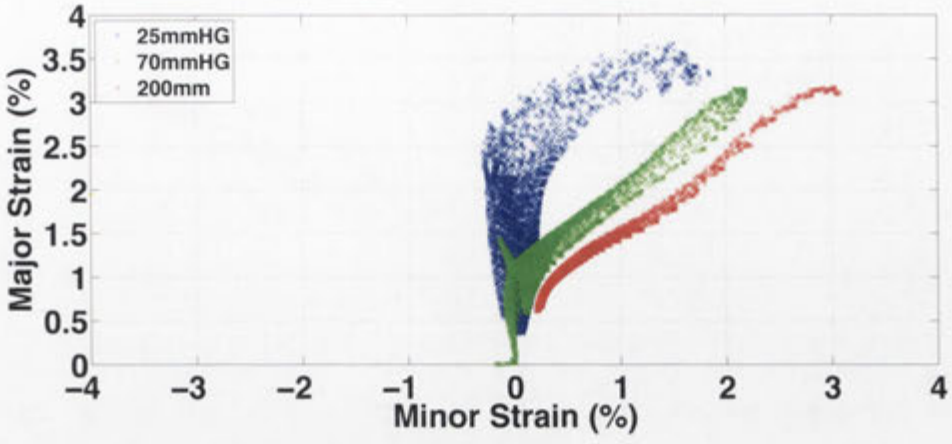

Figure 7.36: FLDs for the GFRP layer in the selected specimens at a forming depth of 10mm

the punch, as long as the laminate retains integrity. The only reason this effect does not appear is the transverse shear in the composite layer.

Figures 7.36 and 7.37 show the FLDs for the GFRP layer in the FE simulations at a depth of 10mm and the failure depth respectively. These figures show significant difference from the behaviour observed in the SRPP layer in the FE simulation shown in Chapter 5. Figure 7.37 also shows the failure limits of the GFRP composite as determined by the characterisation experiments (purple line) and by the manufacturer (gold line). This shows that the strain in the GFRP layer is in the expected range as determined by the manufacturer. However, the failure strain determined by the characterisation experiments is much lower than observed in the FEA and in the experiments. This is most likely caused by either the failure region not occurring inside the gauge length during the characterisation, or the deformation induced by the mechanical grips. Again, the failure of the composite layer can be directly determined from the finite element model

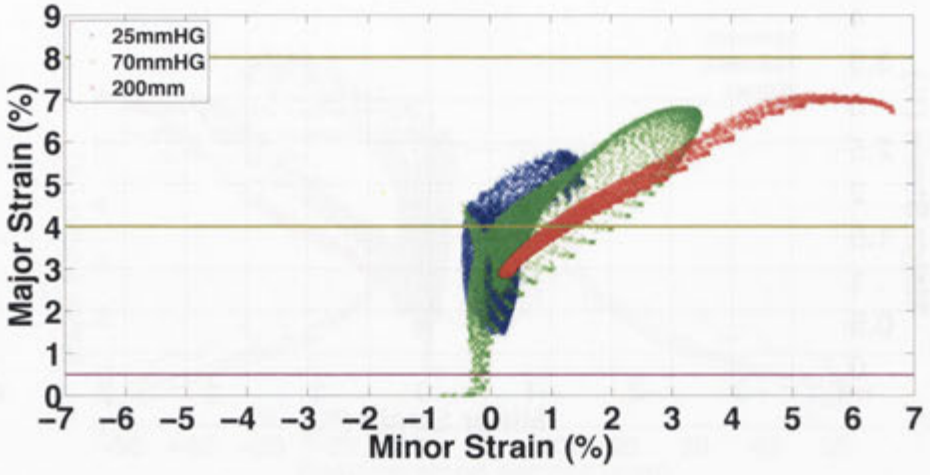

Figure 7.37: FLDs for the GFRP layer in the selected specimens at the failure depth

using the location of failure determined in the previous sections. It was found that, according to the FEA, the 25mmHG (uniaxial tension) specimen had minor and major failure strains of 1.22% and 7.03% respectively; the 70mmHG (plane strain) specimen had minor and major failure strains of 2.64% and 6.16%; and the 200mm (biaxial stretch) specimen had minor and major failure strains of 5% and 6.77%. Similarly to the isothermal SRPP FML specimens, the major strain values for failure match well with the experimental values but the minor strain values do not. There is a 4.3%, 6.4%, and 9.9% difference for the major strain at failure in the 25mmHG, 70mmHG, and 200mm specimens respectively, compared to a 661%, 193%, and 79% difference for the minor strain values. The reason for the difference in the strain values could be due to the manner in which the characterisation experiments were conducted; only the strain in the 1st principal direction was measured and the effect of deformation in the other directions was ignored. Other possibilities are: that the aluminium layer is affecting the

ability of the GFRP to behave as expected, the interface model is not adequate, there is an anisotropic friction condition, or at this location the fibre weave is affecting the results. This will need to be investigated through stretch forming and simulation of the monolithic GFRP.

It can be seen from the failure strain values and Figure 7.37 that, unlike the isothermal SRPP FML specimens, there are no unfailed points in the 70mmHG GFRP FML specimen above the failure limit determined by the 25mmHG specimen. However, it can be seen that a meso-level model, which can replicate the behaviour of the warp and weft fibres, is required to more accurately predict the behaviour of the GFRP composite.

7.4 Summary

This chapter has assessed the formability of a glass-fibre reinforced fibre–metal laminate under isothermal conditions. Similar to the SRPP FML specimens, this was performed using 14 specimen geometries.

The major and minor strain were measured at key locations (such as the pole and failure region and along the meridian line) and using a general overview of the behaviour across the entire surface. These results were used to assess the forming behaviour of the GFRP FML and subsequently develop a forming limit curve.

In contrast to the SRPP based FMLs shown in Chapter 5 and the monolithic aluminium specimens, it was difficult to obtain the expected deformation be-

haviour in the GFRP FML specimens using the varied specimen geometry. This is because the failure of the specimens occurred before the expected deformation modes could significantly progress. The strain evolution behaviour of the GFRP FML is similar to the SRPP FML and the aluminium until the final strain path to failure and then appears to change, indicating that the behaviour would follow the expected path if the failure strain of the GFRP was higher.

The failure of the GFRP FML highlights the effect that a composite with low strain to failure has on the forming of a FML. Unlike the SRPP FML, there was a noticeable localisation of major strain prior to the appearance of a tear in the FML. This can only be caused by failure of the GFRP layer, which than transfers load to the aluminium, causing high strains and rapidly leading to tearing. This localisation also occurs in the monolithic aluminium specimens; however, this is due to the formation of a localised neck in the aluminium which does not immediately proceed to failure. As expected, failure occurs in the fibre direction due to the lower extensibility of the fibres. However, failure did not always occur along the longitudinal meridian line. Due to the weave and unit cell of the GFRP layer, failure occurred in the fibre direction where the fibre was in the lower half of the composite; this did not always coincide with the meridian line. This was also highlighted in the surface strain contours and meridian strain plots of the FML, which showed the effect of the fibre weave more clearly. The surface strain contours showed a tessellated pattern appearing on the surface and the meridian showed peaks and troughs in the major strain magnitudes. Until the failure of

the composite layer, the FML showed greater uniformity in the surface strain which could be indicative of better formability.

The FLC for the GFRP FML closely followed the expected ranges of failure of the GFRP. This was a failure strain of 4–10% on the surface of the laminate which corresponds to a strain of 2–8% in the GFRP layer. This shows that the GFRP FML does not have comparable forming limits to the SRPP FML or the monolithic aluminium. However, temperature may improve the forming of the laminate. In addition, the direction of the major and minor strain was not as significant a factor in failure as in the case of the SRPP FML. This is because the failure of the GFRP layer occurred before the shear strain magnitude became significant.

The finite element model for the specimens, corresponding to the uniaxial tension, plane strain, and biaxial stretch deformation modes, showed good agreement with the experimental results. The evolution of the major strain with depth, the FLD, and the meridian major strain were used to determine the accuracy of the finite element model. It was found that the major parameter affecting the agreement was the contact between the punch and the specimen. The surface characteristics of the GFRP FML may be causing a contact condition which cannot be modelled using Coulomb friction; extremely high values for the friction coefficient result in more accurate strain predictions. In addition, the effect of the fibre weave cannot be simulated using the homogenised material model used for the GFRP. The GFRP layer of the laminate was analysed using the FE model and

it was found that the failure conditions in the GFRP agreed with the expected failure limits of the material. It is expected that if the major strain was oriented at an angle from the fibre direction the failure limits of the laminate would be higher.

This study has shown that the forming of the GFRP FML under isothermal, low temperature conditions is not advisable. Further study on the effect of temperature is required to determine if forming of the GFRP FML can be improved.

Chapter 8

Effect of temperature on the forming of a glass-fibre reinforced polypropylene fibre–metal laminate

8.1 Introduction

This chapter investigates the effect of temperature on the forming behaviour of the FML based on a GFRP composite. This work continues from the previous chapter and uses the significant findings of Chapter 6 to assess the effect of temperature. Hence, as the GFRP FML showed relatively poor forming at room temperature compared to the SRPP FML, and temperature will have a less significant effect on glass fibres, only five temperatures will be considered: RT, 80 °C, 100°C, 120°C, and 140°C. In addition, the analysis of results from the formability testing will be streamlined to cover only the significant aspects of the GFRP FML. The effect of specimen geometry and temperature on the strain behaviour of the laminate during forming is investigated and the safe forming limits determined. The methods developed in Chapter 3 and used in Chapter 5 are again

	25mmHG		70mmHG		200mm	
	Mean ϵ_1	Mean ϵ_2	Mean ϵ_1	Mean ϵ_2	Mean ϵ_1	Mean ϵ_2
RT	0.72%	0.34%	0.63%	–0.056%	0.36%	0.203%
80°C	0.69%	–0.006%	0.93%	–0.027%	0.41%	0.2%
100°C	1.47%	–0.072%	0.73%	0.121%	0.45%	0.24%
120°C	0.98%	–0.004%	1.15%	0%	0.45%	0.26%
140°C	1.35%	0.066%	1.02%	0.162%	0.29%	0.19%

Table 8.1: Effect of temperature on the mean major and minor strain induced by the lock ring

used in this chapter to analyse the experimental results. In addition, the results from the GFRP laminate are compared to the results of the SRPP laminate to elucidate the effect of composite material stiffness on the forming behaviour of FML systems.

8.2 Experimental work

8.2.1 Surface strain behaviour

Figure 8.1 shows the effect of temperature on the induced "pre-stretch" strains in the GFRP FML. Table 6.1 shows that the mean major and minor strain in the uniaxial tension, plane strain, and biaxial stretch specimens exhibit similar behaviour to the SRPP specimens, with small increases in strain at increased temperatures of 0.2–0.3% major strain, reinforcing the hypothesis that expansion in the specimens is caused by thermal expansion in the die and blankholder.

The analysis of the SRPP based FML at elevated temperatures showed that there was no significant effect of temperature on the FLD at lower forming depths. This is because the specimens had the same boundary conditions, and therefore

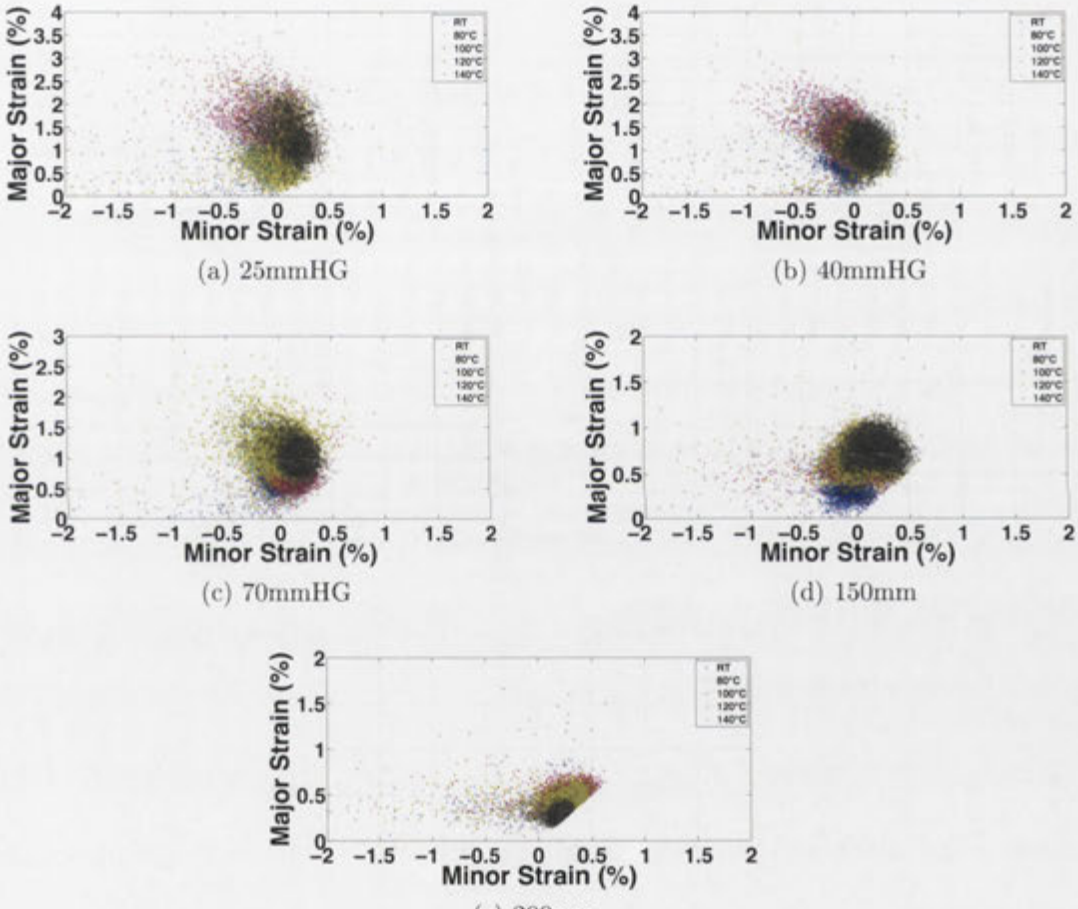

(a) 25mmHG

(b) 40mmHG

(c) 70mmHG

(d) 150mm

(e) 200mm

Figure 8.1: Effect of temperature on "pre-stretch" strain in the specimens

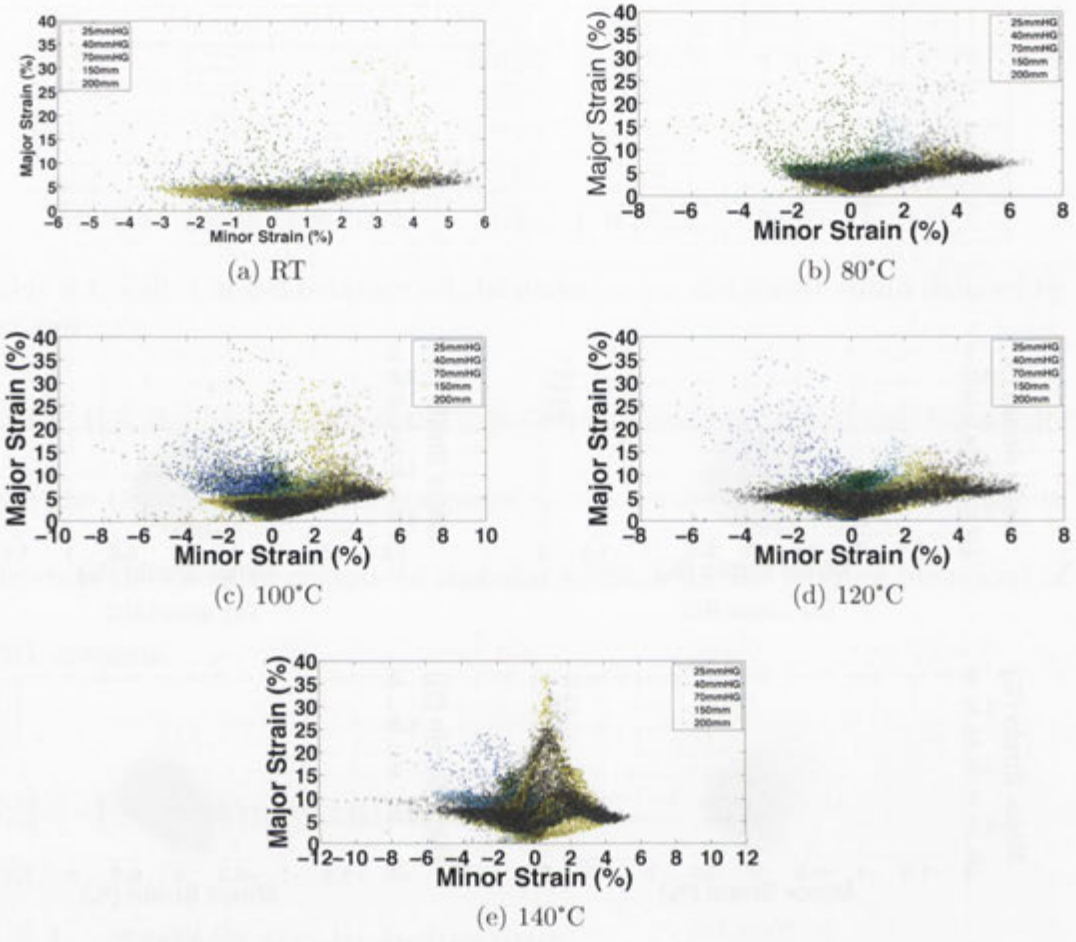

(a) RT

(b) 80°C

(c) 100°C

(d) 120°C

(e) 140°C

Figure 8.2: FLDs for the experimental specimens at the failure depth

deformation behaviour, for similar forming depths. Therefore, for the GFRP specimens which exhibit lower forming depths than the SRPP specimens, only the FLD at the depth of failure will be presented. Figure 8.2 shows the FLD for the GFRP specimens at the failure depth. These figures show that, unlike the SRPP specimens, there is little change in the FLD at the failure depth at elevated temperatures compared to room temperature, other than the effect of the melted adhesive observed at 140°C. This highlights the fact that, as will be discussed later, elevated temperatures do not significantly increase the depth of

	RT		80°C		100°C		120°C		140°C	
	Mean	Median	Mean	Median	Mean	Median	Mean	Median	Mean	Median
25mmHG	3.9	2.96	3.38	3	7.12	6.89	4.73	2.73	5.25	3.76
40mmHG	4.46	3.43	5.92	4.89	4.96	3.68	5.78	5.49	5.88	5.47
70mmHG	3.8	3.51	4.61	3.95	4.2	3.86	5.19	4.69	7.16	7.46
150mm	4.34	3.95	3.64	3.38	4.77	4.12	4.57	4.21	7.39	6.14
200mm	4.09	3.52	4.61	4.05	3.88	3.25	5.17	5.15	8.32	7.03

Table 8.2: Effect of temperature on the mean and median major strain values at the depth of failure

failure in the GFRP FML specimens.

The 140°C specimens are the exception. Due to the melting of the adhesive, these specimens can show different surface strain behaviours since the laminate is no longer acting as a continuous material. As shown previously, this loss of support from the composite layer leads to a localisation of strain in the aluminium layers. This is harder to assess in the GFRP FML specimens due to the brittle failure of the glass fibres, which leads to localisation of strain at all temperatures. The localised failure in the GFRP FML specimens causes a skew in the major strain results. It is therefore useful to discuss both the mean and median major strain values to determine the central tendency of the strain behaviour at failure. Table 8.2 shows the mean and median major strain values at the depth of failure. There appears to be no trend in either the mean or median strain values as a function of temperature; however, it can be seen that the mean strain values are generally larger than the median values. This occurs in specimens where a localisation in strain occurs due to the failure of the GFRP layer, so that the large strain values in the failure area skew the mean strain results to higher values. It can be seen that the mean and median major strain failure values still remain

in the 4–8% range indicating that, in the case of stretch forming, temperature provides no benefit to the forming limits. This does not disagree with the previous findings of Mosse [73], Dhar Malingam [77], or Venkatesan [64] where the high temperature GFRP specimens were found to have improved formability through mechanisms of trellising (and stretching) of the weave and drawing of the fibres. In this study, the fibre weave still trellised more easily at elevated temperatures compared to lower temperatures, but, due to the boundary conditions, the high temperature specimens were still required to deform in the same way as the low temperature specimens. This shows that it is always preferable to allow some drawing of GFRP based composites and laminates so that the fibres do not experience strain magnitudes comparable to the matrix.

In addition to the FLD, the surface strain contours were also assessed. Figure 8.3 shows the surface major strain contours for the 25mmHG specimens at all experimental temperatures. Figures 8.3(d) and (e) show an interesting behaviour which was occasionally seen in the specimens. This is a more extreme version of the tessellated strain pattern observed in the other GRFP specimens and some SRPP specimens. The surface quality of the GFRP sheets made it more difficult to bond than the SRPP specimens. It is posited that this surface strain behaviour is a result of the weave pattern of the composite leading to bonding difficulties. Figure 8.4 shows the mechanism causing this effect. The peaks and troughs in the fibre weave cause certain areas of the composite to be preferentially bonded compared to others. As the fibre weave begins to flatten under load the straight

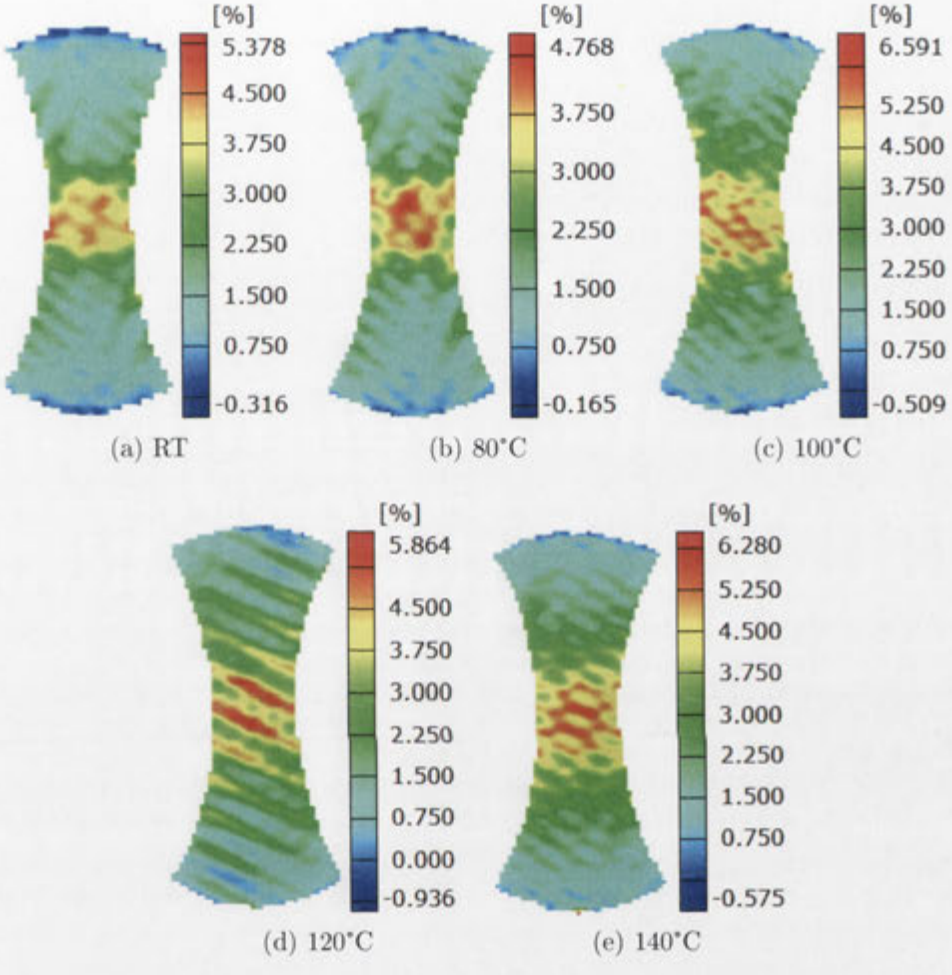

Figure 8.3: Major strain contours for the 25mmHG experimental specimens at a depth of 10mm

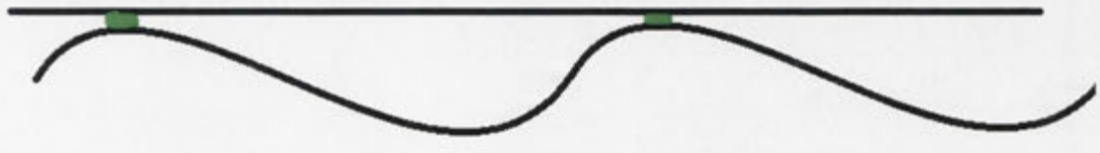

Figure 8.4: Effect of the GFRP fibre weave on the quality of the adhesive bond

aluminium in the unbonded region must experience a relatively higher strain. This is very similar to the regions of transverse fibres causing preferential strain seen in the isothermal GFRP specimens. It can also be noticed in the figures that the specimens with the highest maximum major strain are also the specimens with the most defined tessellated pattern. This most likely means that those specimens have the most trouble bonding in the trough regions. This does not affect the failure of the experimental specimens, as even though the aluminium is experiencing higher strains the failure of the laminate is still initiated by failure of the GFRP layer. The surface strain contours of the GFRP FML specimens were similar to those shown in Figure 7.14 and Figure 7.15 where the strain localised prior to the appearance of a tear in the aluminium layer.

Finally, the meridian strain in the 70mmHG specimens is shown in Figure 8.5. These figures show that similar deformation processes, and the variability in the strain due to the weave pattern, make it difficult to differentiate the behaviour of the various specimens. As stated previously, the deformation behaviour is not controlled by temperature but by the boundary conditions at the lock ring, the specimen geometry, and the contact conditions with the punch.

8.2.2 Effect of temperature on the evolution of strain at the pole

The effect of temperature on the major and minor strain evolution at the pole of the uniaxial tension, plane strain, and biaxial stretch specimens is shown in

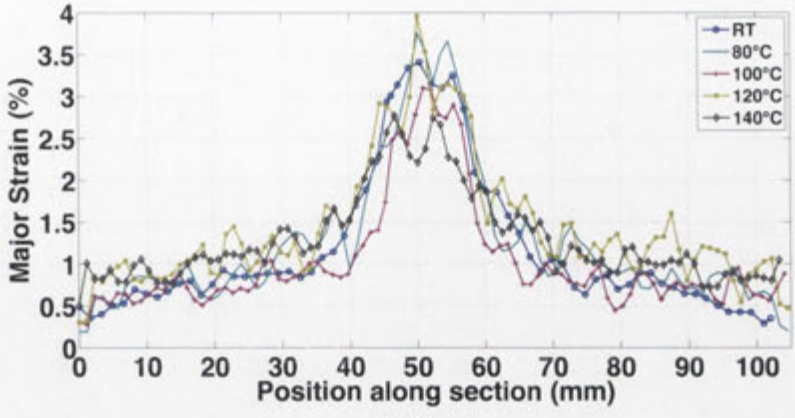

(a) 5mm

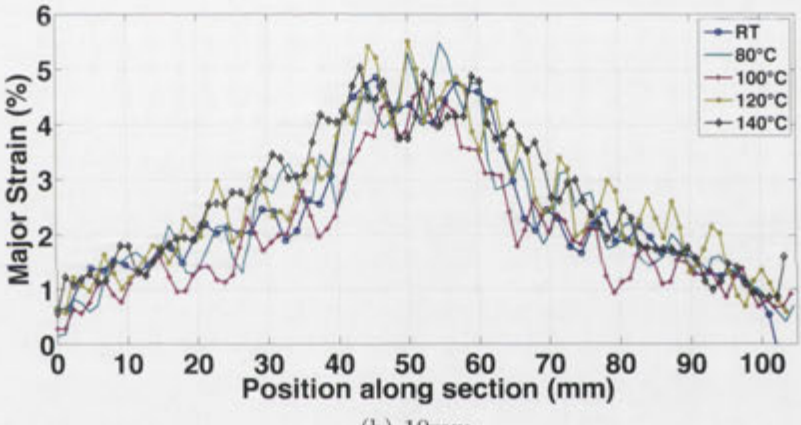

(b) 10mm

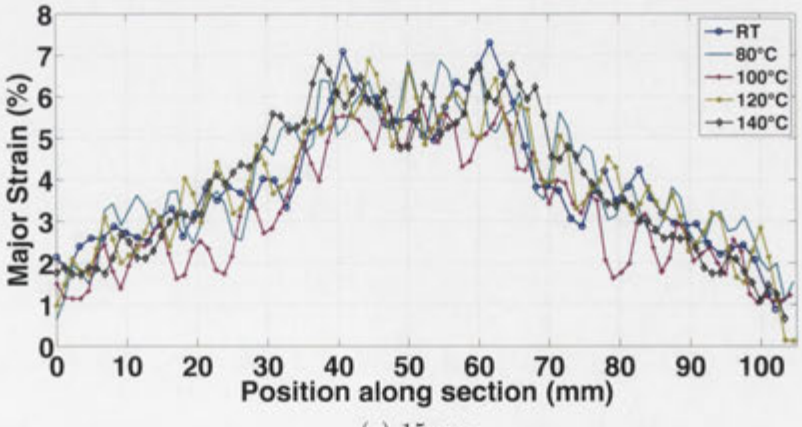

(c) 15mm

Figure 8.5: Effect of temperature in the 70mmHG specimens at 5mm, 10mm, and 15mm forming depths along the longitudinal axis

Figures 8.6 and 8.7 respectively. The effect of temperature on the major strain is shown to be fairly minimal in cases where the behaviour before failure is the same across all temperatures. This is identical behaviour to the SRPP specimens where the temperature also had minimal effect on the major strain. This is because the strain in the longitudinal direction is controlled by boundary conditions at the lock ring and the punch displacement, not by material. The significant effect of temperature is an effect on the minor strain; this is obvious since the altered material behaviour can have an effect as the lock ring is not enforcing a pure stretch condition in the lateral direction of specimens smaller than 200mm. This is also because the minor strain values for all 200mm (biaxial stretch) specimens (other than the 140°C specimen) show similar behaviour. The 25mmHG specimens show the greatest sensitivity of minor strain to temperature. The low temperature specimens show positive minor strains, the 100°C and 120°C specimens exhibit almost plane strain, and the 140°C specimen shows negative minor strain.

When the major and minor strains are combined to create the strain path for the experimental specimens, the effect of temperature can be seen more readily. Figure 8.8 shows the strain paths for all experimental specimens. This shows that for the 40mmHG, 70mmHG, 150mm, and 200mm specimens, all temperatures show very similar overall behaviour except for the 140°C specimens. The individual strain values do not match, but the trend in the specimens is the same. It is interesting to note the behaviour in the 40mmHG specimen shows compa-

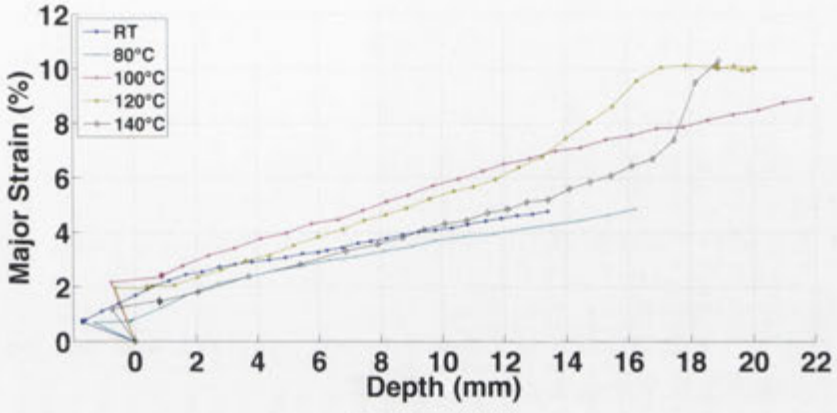

(a) 25mmHG

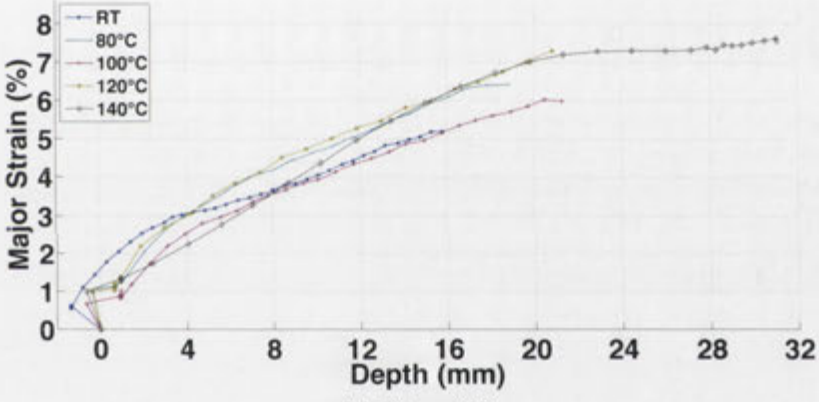

(b) 70mmHG

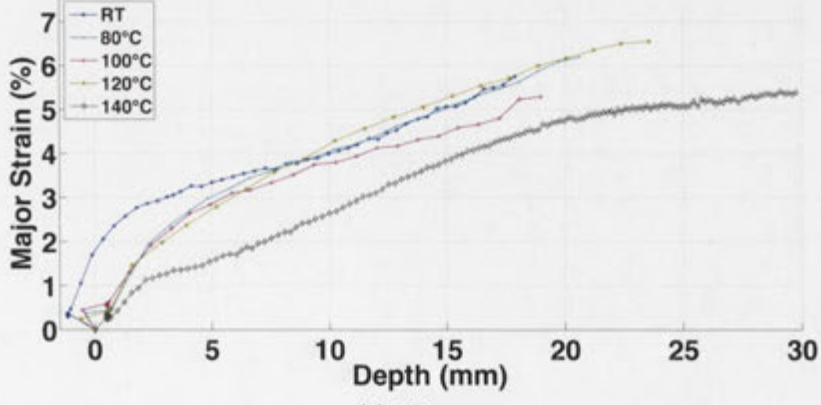

(c) 200mm

Figure 8.6: Effect of temperature on major strain evolution at the pole

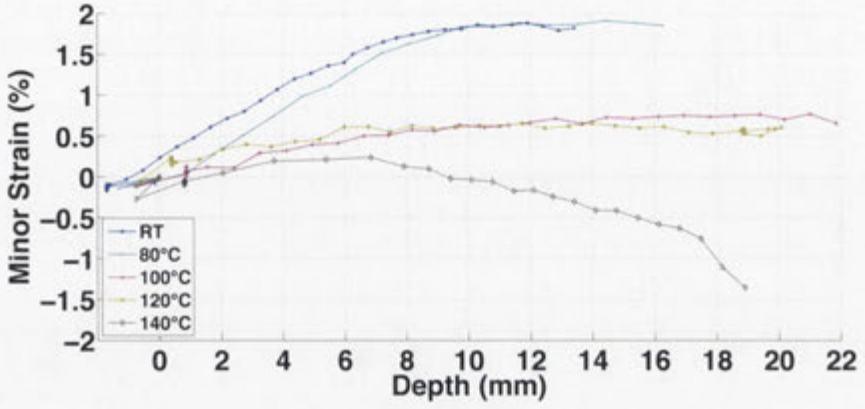

(a) 25mmHG

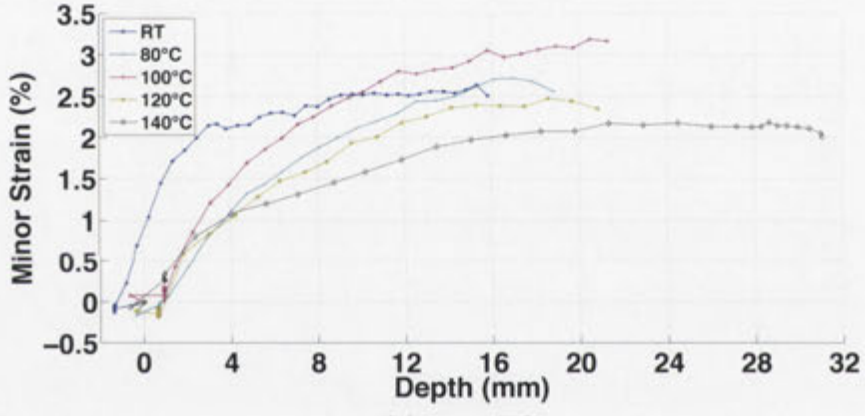

(b) 70mmHG

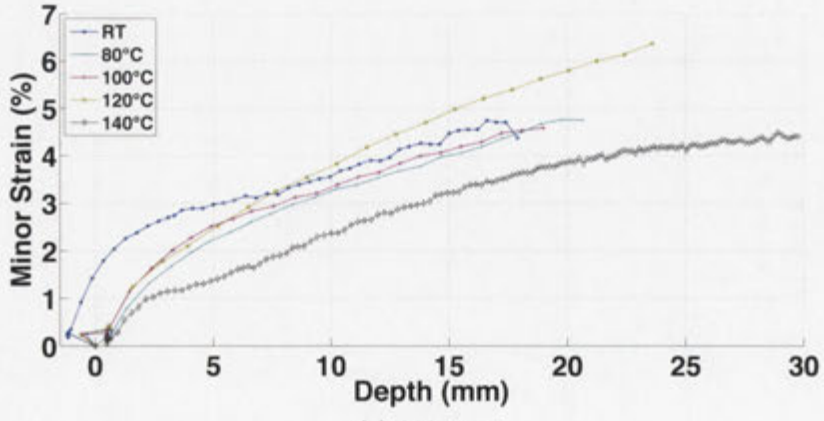

(c) 200mm

Figure 8.7: Effect of temperature on minor strain evolution at the pole

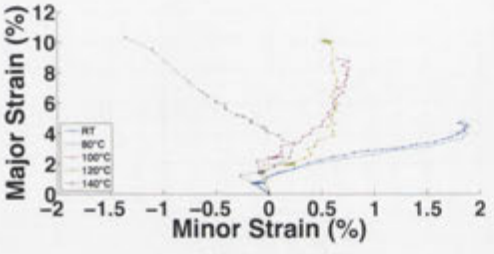

(a) 25mmHG

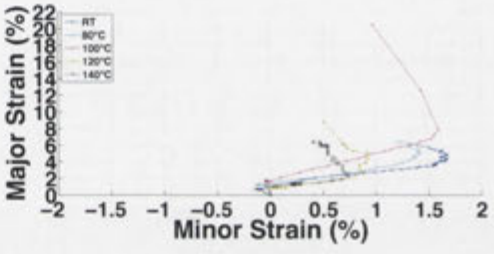

(b) 40mmHG

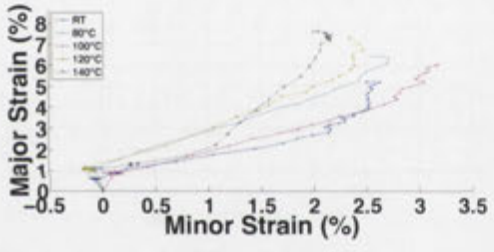

(c) 70mmHG

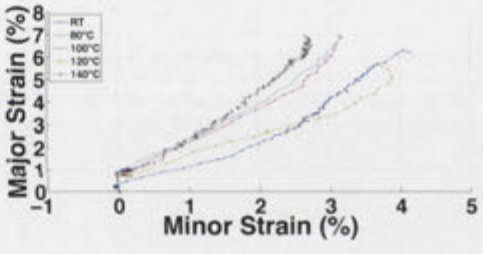

(d) 150mm

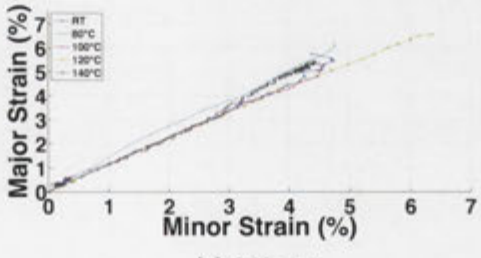

(e) 200mm

Figure 8.8: Effect of temperature on strain evolution at the pole

rable behaviour to the SRPP specimens, where the initial "biaxial" deformation region reduces with increasing temperature. This behaviour was also exhibited in the 25mmHG and 70mmHG SRPP FML specimens but it is not clear it occurs in the 25mmHG and 70mmHG specimens. Both these specimens do show a trend for more negative minor strain as the temperature is increased, but it is not clear that the initial biaxial stretch region is being truncated to begin the strain path to failure. Instead, there is a more gradual transition to a different deformation behaviour. This could be because the strain values in the GFRP specimens are too low to convincingly determine the final strain path to failure; the behaviour could be starting but the failure of the GFRP prematurely halts the process. This is plausible as the change in the SRPP specimens begins at a major strain of approximately 5%, which is when failure in the GFRP layer is imminent. It could also be that the GFRP layer has already started a failure mechanism in some regions which alters the strain behaviour.

The 25mmHG specimens exhibit the most interesting behaviour of all the GFRP specimens, showing three significantly different strain behaviours. There are different behaviours for the RT and 80°C specimens, the 100°C and 120°C specimens, and the 140°C specimen. It is particularly interesting that the 100°C and 120°C specimens show similar behaviour, as the surface strain contours such as those shown in Figure 8.3 display a profound difference in surface strain behaviour. However, it was noticed that the points corresponding to the pole in both of these specimens occupy a high strain region (red areas in Figure 8.3) –

that is, where the bond is poor or the transverse fibres offer reduce support to the aluminium layer. This finding shows that the reduced bonding between the layers does not significantly affect the strain behaviour of the specimens, and also shows that most of the differences in strain behaviour between specimens could be due to the chosen analysis regions coinciding with different areas of the composite. For example, the pole in the 80°C 25mmHG specimen coincides with a low strain region, indicating a possible cause of the strain differences. Therefore, it could be that the temperature has only minimal effect on the minor strain at the pole and that the most important parameter is the weave. Further study with careful control of the weave is required. Finally, the 140°C 25mmHG specimen shows the behaviour expected from a monolithic aluminium specimen, indicating complete failure of the adhesive bond.

8.2.3 Effect of temperature on the failure of the specimens

The failure behaviour of the GFRP FML laminates was consistent across all temperatures up to 120°C, with the failure being initiated by failure in the glass fibres. This caused a localisation of strain in the aluminium layers and subsequently led to the appearance of a tear in these layers. The effect of temperature on the SRPP laminates was to increase the depth at which failure occurs through an increase of the strain at failure in the SRPP fibres. Generally, as shown in Figure 4.1(b), it is not expected that temperature will have a strong effect on the strain at failure. While this figure appears to show a large relative increase in strain at failure, and

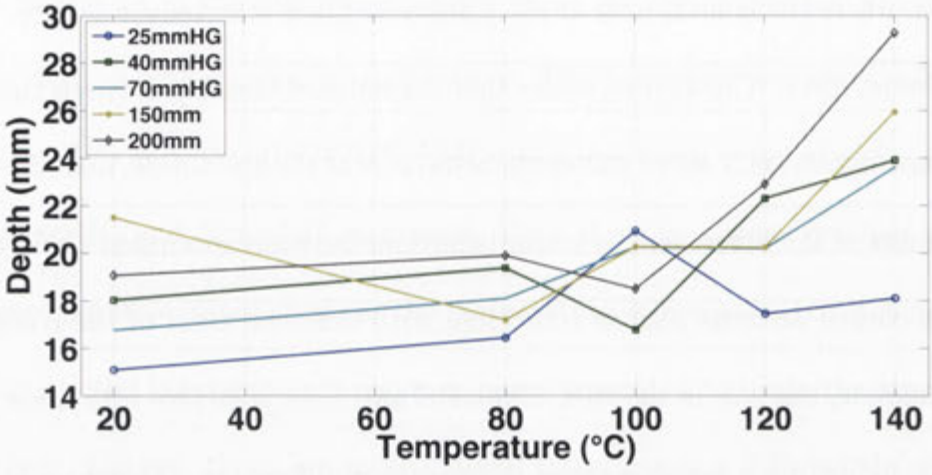

Figure 8.9: Effect of temperature on the failure depth of the specimens

	80°C	100°C	120°C	140°C
25mmHG	8.94%	38.68%	15.63%	19.87%
40mmHG	7.5%	-6.93%	23.68%	32.56%
70mmHG	7.93%	20.81%	20.45%	40.73%
150mm	-20%	-5.72%	-5.86%	20.65%
200mm	4.35%	3%	20.1%	53.5%

Table 8.3: Change in maximum forming depth with increasing temperature compared to room temperature

decrease in stiffness, for the GFRP composite as temperature is increased, the strain to failure in the tensile specimens was still below 2% (which is much lower than the strain values experienced in the forming experiments). The effect of temperature on the failure depth of the GFRP FML specimens is shown in Figure 8.9. It can be seen that temperature has a small effect on the failure depth of the GFRP FML. There is a slight positive trend in most of the specimens. The comparative changes in forming depth (compared to room temperature) for all specimens and temperatures are shown in Table 8.3. This table shows that no real trend appears at higher temperatures, only that in the 25mmHG, 40mmHG,

70mmHG, and 200mm specimens the higher temperatures generally give higher failure depths than room temperature. The 150mm specimen showed unexpected behaviour: it had the highest forming depth at room temperature but experienced significant reduction in forming depth with increased temperature. This could be because the failure depth at room temperature is an outlier and the values reported at 80°C, 100°C, and 120°C are more realistic for the material. In addition, Table 8.3 shows the validity of not including the 40°C and 60°C experiments, as the change in failure depth from RT (20°C) to 80°C for almost all specimens is less than 10%.

Unlike the SRPP FML specimens, the greatest failure depths occur at 140°C. However, this was due to a failure of the lock ring to restrict the drawing of material at this temperature. At 140°C the bottom aluminium and GFRP layers (but not the top aluminium layer) drew in from outside the lock ring, indicating a failure of the adhesive bond in the material. It was not anticipated that the lock ring would fail to secure the specimens at this temperature. The failure of the 140°C specimen was still a result of tearing in an aluminium layer; however it was in the top layer which is in contact with the punch, and there was no observable failure in the GFRP and bottom aluminium layers (other than the draw from outside the lock ring). A higher blankholder force could be used to restrict this draw of material; however, as discussed in Chapter 7, high blankholder forces cause failure of the GFRP FML specimens through strain induced in the fibres. It may be possible to increase the blankholder force after heating the specimen,

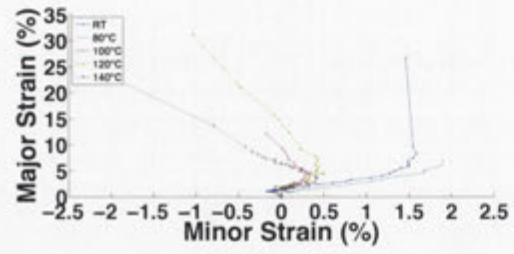

(a) 25mmHG

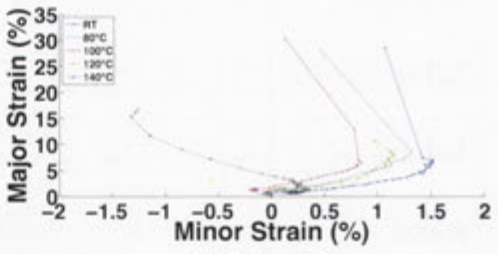

(b) 40mmHG

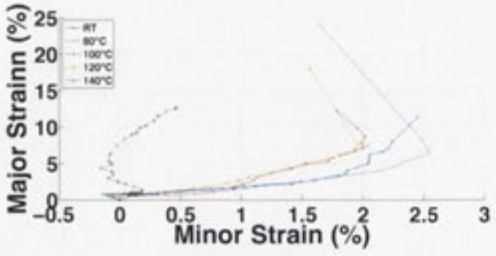

(c) 70mmHG

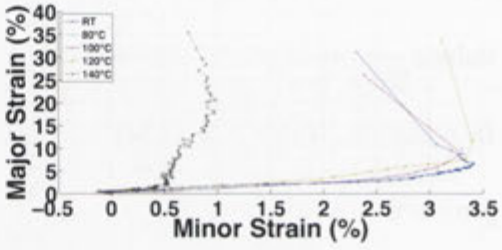

(d) 150mm

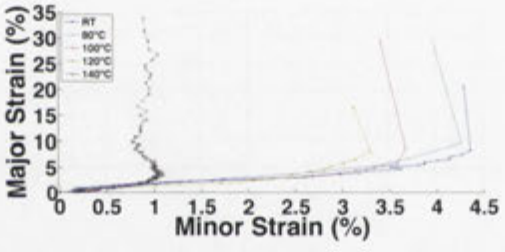

(e) 200mm

Figure 8.10: Effect of temperature on strain evolution at the point of failure

which could reduce the probability of failure, but this was not considered for this study. In future work the use of a blankholder without lock rings, which still restricts draw, would be preferable as it would not induce a "pre-stretch" strain in the specimens and therefore not risk premature failure. Therefore, the greatest forming depth for the GFRP FML specimens can be found by assessing the 100°C and 120°C experiments, as these temperatures correspond to contiguous laminates.

Figure 8.10 shows the effect of temperature on the strain path at the point of

	RT	80°C	100°C	120°C
25mmHG	11.4mm	10.4mm	25.1mm	11.6mm
40mmHG	9.5mm	20.6mm	0.3mm	7mm
70mmHG	11mm	16mm	20mm	15mm
150mm	10mm	5.4mm	17.2mm	11mm
200mm	16.4mm	21.8mm	12.1mm	13.3mm

Table 8.4: Distance of the failure point from the pole

failure in the GFRP FML specimens. It can be seen that the 40mmHG, 70mmHG, 150mm, and 200mm specimens show consistent behaviour up to 120°C, and vastly different behaviour at 140°C. This is caused by melting of the adhesive layer which affects the strain on the surface of the laminate as it is no longer affected by the GFRP layer. It can be seen that some of the 25mmHG specimens below 140°C exhibited similar behaviour to the 140°C specimen. As discussed previously, it is likely that this is caused by a weakness of the bond in these specimens, which is highlighted in Figures 8.3 and 8.4.

It is also important to consider the distance from the pole at which failure occurs, as, in the absence of other information, it provides the best qualitative result for the effect of friction on the surface strain and failure behaviour. There was a slight positive trend in the SRPP laminates which, as discussed in Chapter 6, is caused by the reduction in modulus of the SRPP composite which makes the unsupported region easier to deform. The effect of temperature on the distance of failure from the pole is shown in Table 8.4. The table shows that there is no trend in the GFRP FML specimens. Without more information it is difficult to draw many conclusions from this data. Primarily, what is needed is more accurate force–displacement information about the forming process. This data

was obtained during the experiments, but it was found that the output from the equipment was unreliable. Repeat specimens of the same geometry, temperature, and material, and which exhibited identical strain and failure behaviour, would report completely different force–displacement diagrams. According to Mosse [73], elevated temperatures do not have an effect of the elastic stiffness of GFRP composites in the fibre direction, the only effect is on the shear modulus which is dominated by the polypropylene matrix. This would explain the lack of a trend in Table 8.4 because if the stiffness in the longitudinal (fibre) direction is unchanged by temperature then the force applied by the punch should be the same at all temperatures. All specimens had the same friction condition with the punch, which, when combined with a similar punch force, would lead to failure occurring in the same position for each specimen. This reinforces the finding in Chapter 6 that, in the case of stretch forming, the stiffness of the material has an effect on the friction which in turn is the principal driver of behaviour differences.

Figure 8.11 shows the final FLDs for the experimental specimens, with the FLC drawn at the lower levels of the localised and outlying strain values. Due to failure of the 140°C specimens in the upper aluminium layer it was not possible to construct an FLC for this temperature. Even if failure had occurred in the bottom aluminium layer first, and could be readily identified, it would still not be valid as the specimen had ceased to act as a continuous laminate. It can be seen from the figure that with an increase in temperature there is some increase in strain values at the failure limit. At room temperature the failure limit ranges from 4–8%,

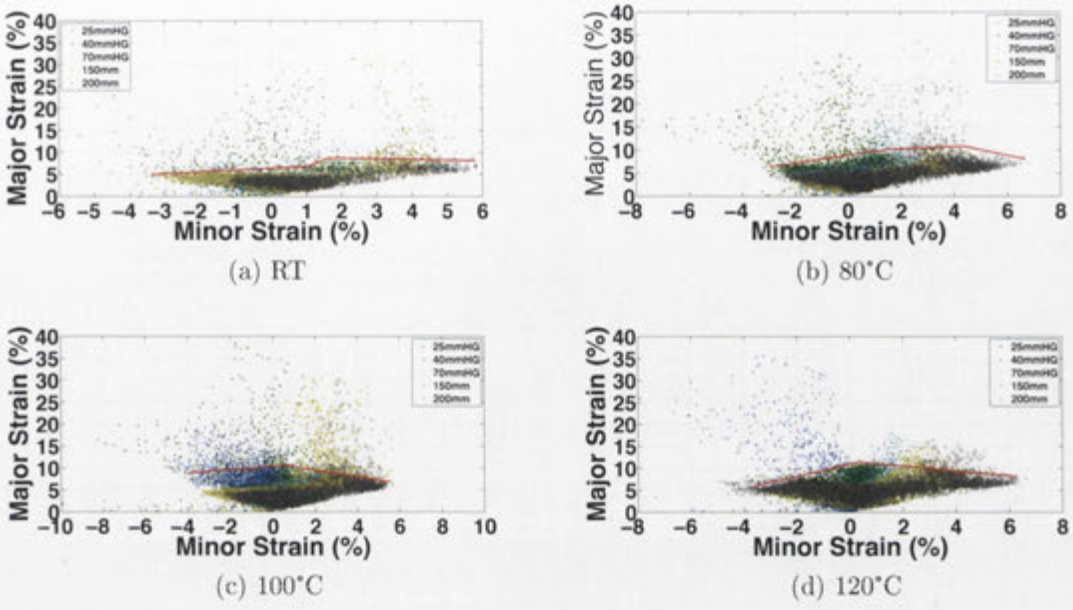

(a) RT (b) 80°C

(c) 100°C (d) 120°C

Figure 8.11: Forming limits of the GFRP FML specimens at various temperatures

whereas the limit in the 80°C, 100°C, and 120°C ranges from 5–10%, 6–10%, and 6–12% respectively. However, when the exact points of failure in each specimen at each temperature are compared, such as shown in Figure 8.12,it can be seen that there is no major advantage from elevated temperatures. The mean safe major strain values are 5.67%, 6.18%, 7.22%, and 7.82% for the RT, 80°C, 100°C, and 120°C specimens respectively. The mean marginal major strain values are 10.05%, 6.83%, 7.96%, and 7.56% for the RT, 80°C, 100°C, and 120°C specimens respectively. The mean major failed strain values are 25.57%, 18.38%, 22.32%, and 19.21% for the RT, 80°C, 100°C, and 120°C specimens respectively. It is interesting to see that the marginal values for the specimens can have a lower average than the "safe" points. The marginal points were considered to be the areas of failure at a depth prior to the localisation of strain, and the safe points

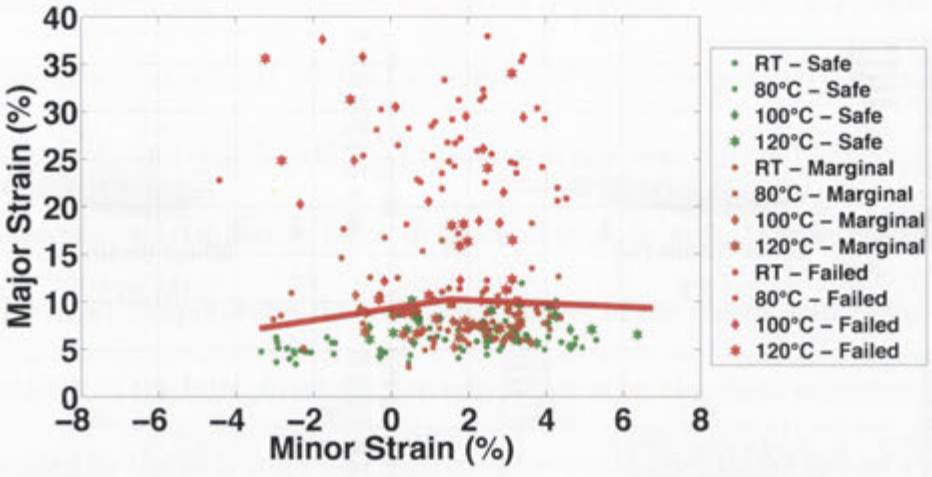

Figure 8.12: Comparison the failed, marginal, and safe strain points for all specimens at each temperature

were determined from regions far from the failure at the failure depth. Therefore, these "safe" points should also be considered marginal because, even if the GFRP does not fail, they still carry a high chance of failure. The most important finding from Figure 8.12 is that the most reliably safe forming limit for all temperatures in 4–5%. In addition, unlike metals, the GFRP FML shows a higher forming limit in the plane strain deformation mode.

The results from analysis of the failure region of the GFRP FML show that temperature does not improve the formability of the laminate when the fibres are oriented in the direction of highest stretch (longitudinal). Previous studies by Mosse [73], Dhar Malingam [77], and Venkatesan [64] showed improved formability due to the mechanism of trellising. Therefore, future studies should investigate the formability of the laminate when the fibres are oriented at an angle from the direction of highest stretch.

8.3 Finite element simulation

A finite element simulation was also conducted for the high temperature GFRP FML specimens, the only changes from the high temperature SRPP FML models being the material properties of the laminate and the friction condition with the tools. The change in friction was highlighted in the isothermal simulations, and experiments where high friction coefficients in the model provided better matches for strain values and the weave of the composite were shown to generate a macro level surface variability. Figure 8.13 shows a comparison of the evolution of major strain at the pole of the experimental specimens at RT, 80°C, and 120°C. It can be seen that all specimens exhibit a good match between the experimental and simulated results. An interesting finding was that the longitudinal (major) strain in the 80°C 200mm specimen does not match the experimental strain as well as the lateral (minor) strain. The simulated specimen shows a greater degree of biaxial stretch than the experimental specimen, reinforcing the hypothesis that the weave of the fibre affects the local deformation of the laminate.

One of the major differences at the pole occurs in the final stages of deformation, where the experimental pole regions exhibit lower deformations than the simulated ones. However, Figure 8.14 shows that the strain in the simulated 120°C specimens starts to increase in the unsupported regions, which means the behaviour is being correctly modelled. As discussed previously, there are two conditions at the pole which can make it easier for the specimen to be deformed in the unsupported region. Firstly, there is friction between the punch and the

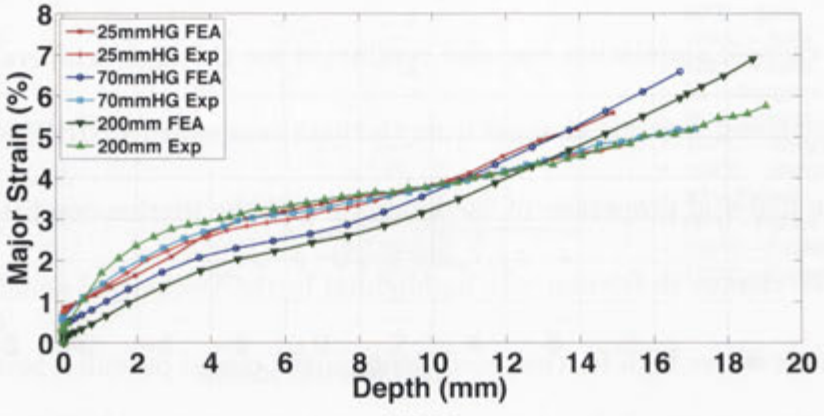

(a) RT

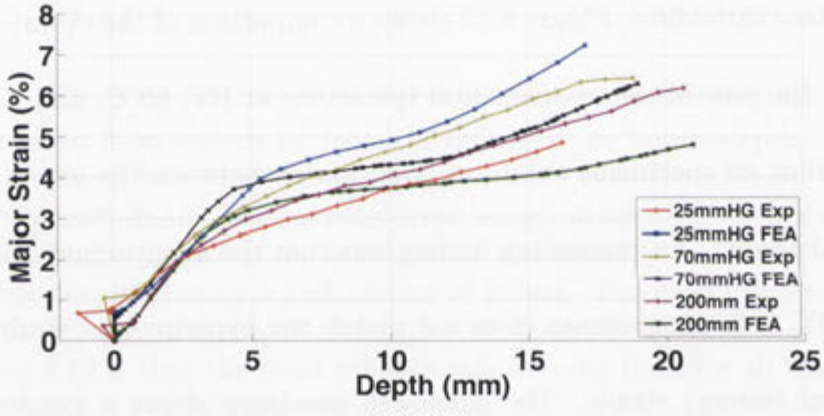

(b) 80°C

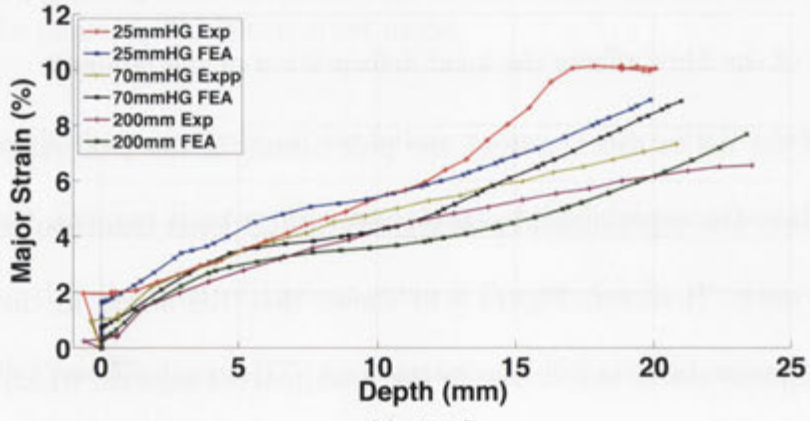

(c) 120°C

Figure 8.13: Comparison of the strain evolution at the pole of the experimental specimens at various temperatures

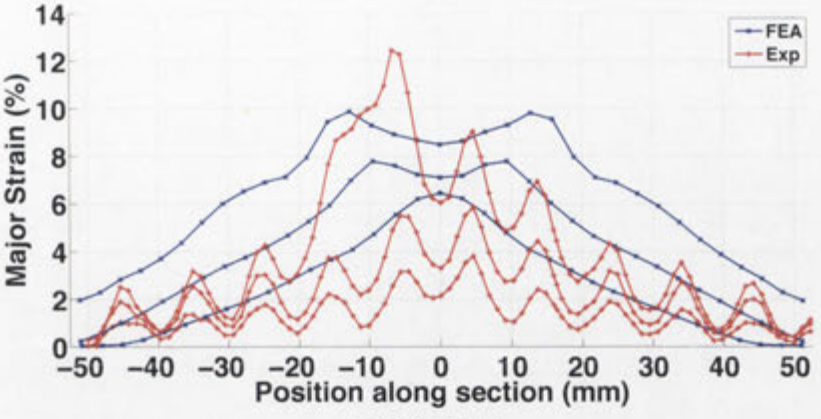

(a) 25mmHG

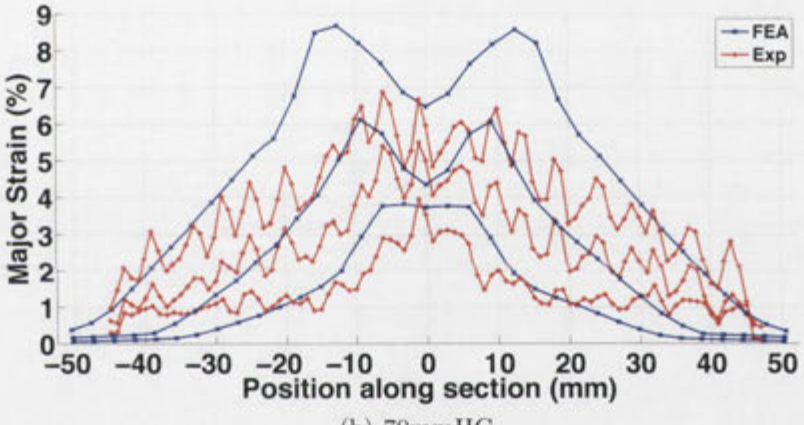

(b) 70mmHG

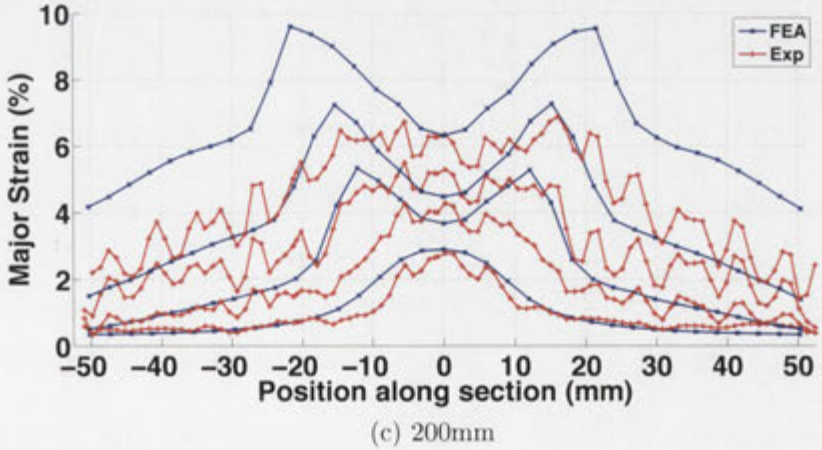

(c) 200mm

Figure 8.14: Comparison of the meridian major strain at 5mm depths in the FE and experimental specimens at 120°C

specimen, and secondly, heat transfer increases stiffness in the lower temperature regions. However, the effect of temperature on the stiffness of the GFRP is lower than that on the SRPP. For example, the change in stiffness from RT to 80°C in the GFRP is 2.56%, whereas the change in the SRPP is 19.95%. Hence, in the simulated specimens reduced temperatures at the pole make the specimen not much more difficult to deform than the higher temperature unsupported region, particularly when the temperature reduction is less than 15°C. Therefore, it is likely that the friction between the specimen and punch is more complex, or the material model requires refinement. This should be investigated in future research. Figure 8.14 also highlights the difficulty in matching the strain behaviour of the GFRP FML specimens. Variability in strain along the meridian line of the specimens highlights the main difficulties with modelling the GFRP FML specimens using the property homogenisation method: local effects of the fibre weave on the bonding of the layers (mentioned previously), the interaction between the matrix and the fibres, and interaction between the longitudinal and lateral fibres.

Figure 8.15 compares the strain paths at the poles of the high temperature specimens. It can be seen that the 70mmHG and 200mm specimens show excellent agreement, but the 25mmHG specimens do not. The simulated specimens show behaviour almost identical to that of the monolithic aluminium specimens. The 25mmHG specimen was difficult to match in all cases, including the SRPP FML specimens. It appears that the composite layer has a limited effect on the minor strain in the simulated 25mmHG specimens. It is believed that this is also caused

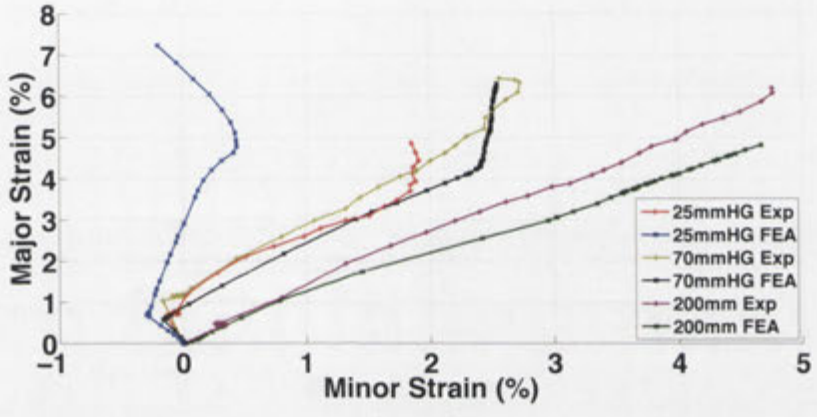

(a) 80°C

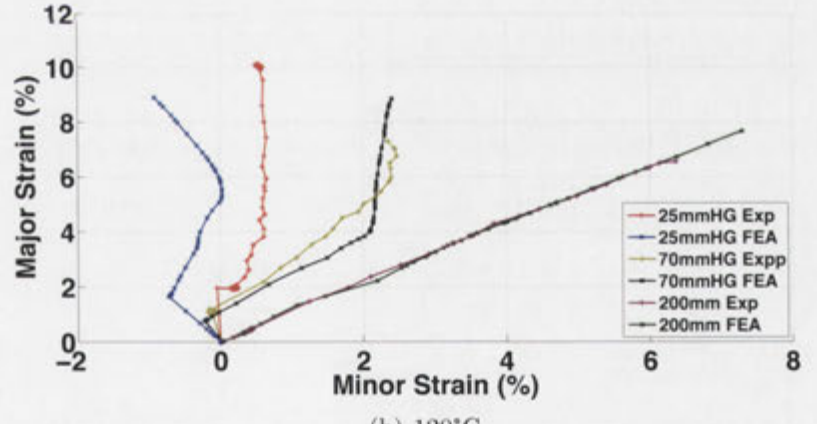

(b) 120°C

Figure 8.15: Comparison of the strain path at the pole in the 80°C and 120°C specimens

by the lack of information about fibre interactions and compressive stiffness. Additionally, the strain pattern observed in the 120°C 25mmHG specimen, shown in Figure 8.3, limits the ability to accurately reproduce the material behaviour.

Figure 8.16 compares the experimental and simulated FLDs for the 70mmHG specimen at 120°C. It can be seen that the overall strain behaviour of the simulated specimens matches the experimental results. Similar results were found for the 25mmHG and 200mm specimens, including the 80°C specimen. This is a recurring theme across all simulated specimens including the SRPP FML. The overall deformation behaviour, shown by the FLDs, can be replicated with accuracy, but individual points and regions are difficult to match. The overall behaviour of the specimen is controlled by its dimensions and the boundary conditions of the experiments. The primary difficulty when replicating the individual regions is the minor strain in the 25mmHG and 70mmHG, where the strain shows a negative or zero trend. If the material data for Poisson's ratio or compressive stiffness is not adequate then it will always be difficult to match these results. This should be able to be rectified with more comprehensive and refined material models which account for fibre/matrix interactions and which have better compressive stiffness data for the composite layer, particularly where the specimen exhibits deformation modes consisting of a negative minor strain.

Finally, Figure 8.17 compares the surface strain contours between the simulated and experimental specimens. Here the localised effects of the fibre weave on the strain distribution on the surface of the GFRP specimens can be seen in the

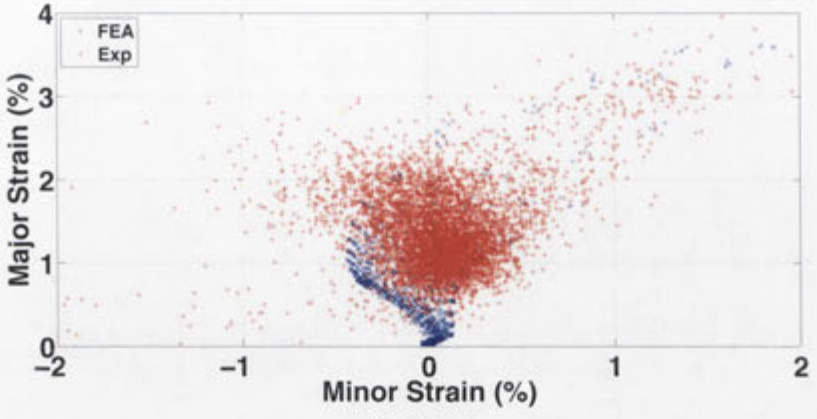

(a) 5mm

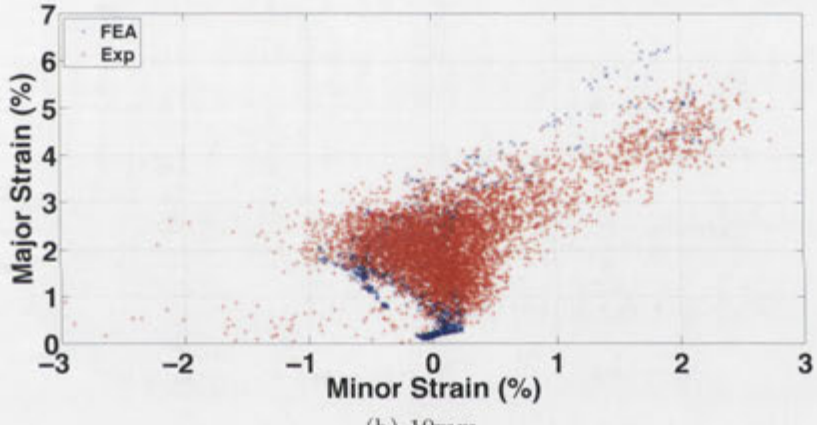

(b) 10mm

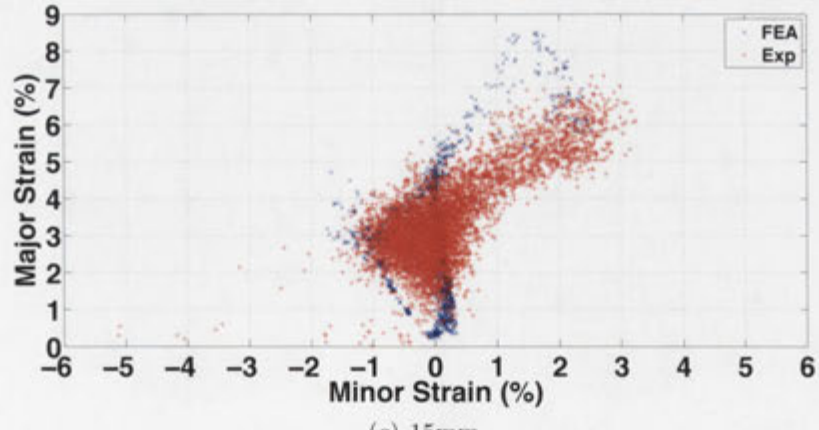

(c) 15mm

Figure 8.16: Comparison of the experimental and simulated FLDs for the 70mmHG 120°C specimen

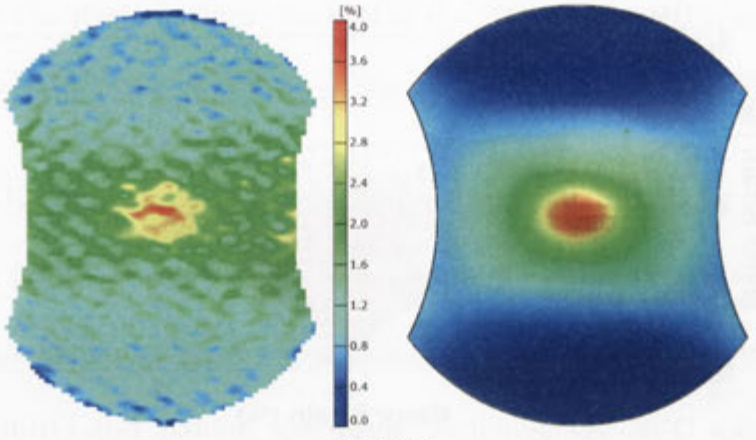

(a) 5mm

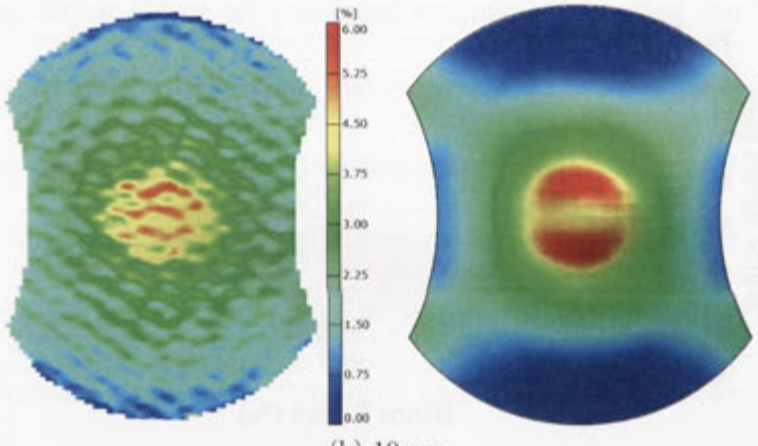

(b) 10mm

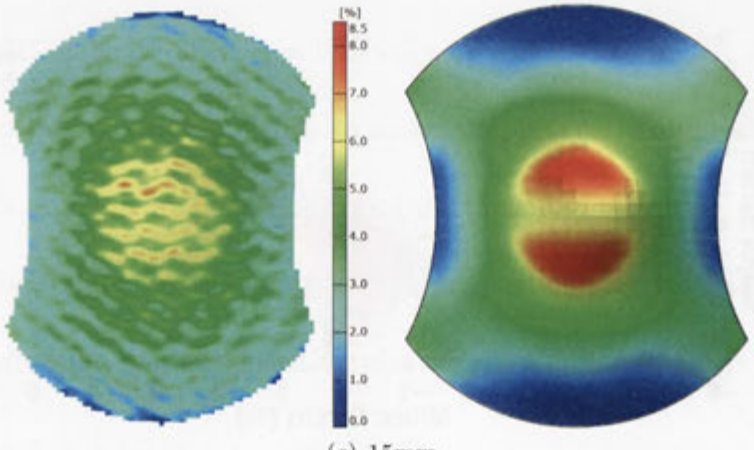

(c) 15mm

Figure 8.17: Comparison of the surface strain contours at different depths in the 120°C 70mmHG specimen: FEA vs Experiment

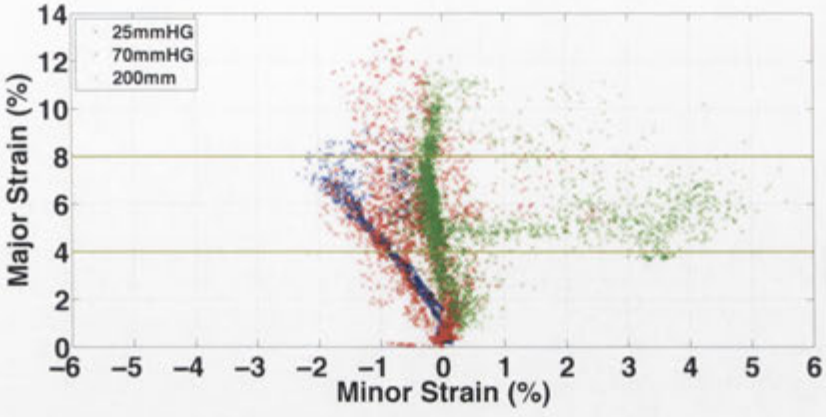

(a) 80°C

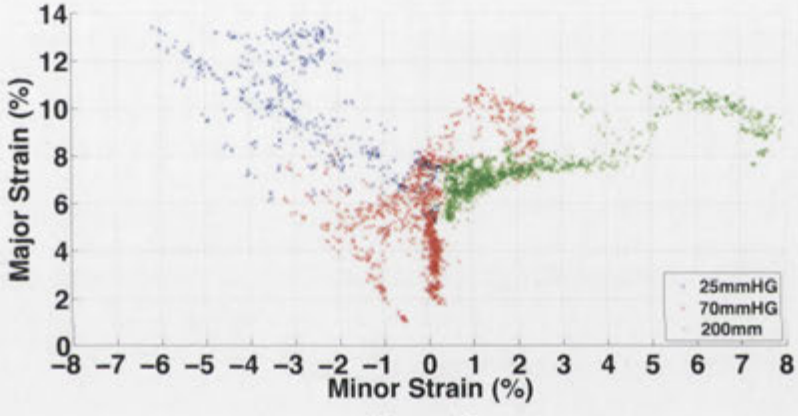

(b) 120°C

Figure 8.18: FLD of the simulated SRPP layer at the failure depth

experimental specimen but not in the simulated one. While the simulated specimens show similar strain contours, and the strain magnitudes agree, the local deformation behaviour of the specimens cannot be replicated.

Figure 8.18 shows the FLDs for the simulated GFRP layers at 80°C and 120°C. Here it can be seen that, unlike the experimental specimens shown in Figure 8.12, there are points in the GFRP layer which experience strains higher than 8%. This is primarily due to the effect seen in the meridian strain plots shown in Figure 8.14, where the unsupported region begins to experience very

large strain magnitudes. As these areas are also where failure generally occurs, no valid information can be determined for the failure behaviour of the GFRP layer from these simulated specimens.

It was particularly difficult to accurately model the deformation of the GFRP FML specimens. Whereas multiple layers and densely packed fibre weave tend to endow the SRPP with a homogeneous behaviour, the single layer of larger weave fibres in the GFRP leads to the variable strain pattern seen in the experimental results. This becomes apparent as the forming depth increases. At lower forming depths the composite layer can be represented as a linear elastic material. As the forming depth increases the lateral fibres begin to affect the stiffness of the longitudinal fibres (and vice versa), the matrix begins to deform (which leads to fibres no longer aligning with the longitudinal and lateral axes), and various damage mechanisms alter the performance of the material. Meso-level or micro-level models, which can account for this behaviour, are required to simulate the material behaviour more accurately.

8.4 Summary

This chapter has investigated the effect of temperature on the forming behaviour of a GFRP FML. In a similar way to the high temperature SRPP FML, elevated temperatures had a marginal effect on the laminate's strain behaviour. At comparable forming depths there was no significant change in the strain behaviour of the specimens; this includes the pre-stretch, FLD, strain contours, and strain

evolution. The pole strain evolution in the high temperature specimens followed the behaviour of the RT specimens, where it was difficult to obtain the expected deformation modes. Again, this was caused by the relatively low strain at failure in the specimens which prevented a transition to the expected behaviour.

The significant finding of this chapter was that, with increased temperature, the GFRP FML showed no appreciable improvement in failure depth. Unlike previous studies [73, 77, 64], no draw of the GFRP layer was permitted, nor was any preferential trellising of the fibres at high temperatures. Trellising was still easier at elevated temperatures, but due to the boundary conditions these specimens could only undergo the same amount of trellising as the RT specimens. Whereas the laminates were found to show some increase in forming depth (due to the softened polypropylene matrix allowing greater fibre displacement), the largest increase generally came after melting of the adhesive at 140°C. At this temperature it was found that no failure occurred in the composite layer, and the large forming depths were primarily caused by draw-in of the GFRP and bottom aluminium layer. This implies that the glass fibres did not experience large strains. This also highlights the fact that the GFRP layer, when bonded as a laminate, *reduces* the formability of aluminium in stretch forming (unlike the SRPP composite). Therefore, it is recommended that the GFRP composite only be used in structures which can be manufactured using the method of draw forming, which has been shown to allow greater formability of the GFRP laminates [73, 77, 64].

The FE simulation of the high temperature GFRP FML specimens was relatively successful. At lower forming depths, excellent agreement could be found with the experimental specimens; however, as the strain in the specimens increased the results began to diverge. The minor strain and the tessellated strain behaviour were particularly difficult to match.

This chapter primarily identified that more comprehensive models are required to simulate the behaviour of GFRP specimens. Due to large fibre bundles and weave, GFRP has a more pronounced effect on the behaviour of a specimen. The large weave leads to a noticeable waviness of the surface of the external aluminium layers, which in turn makes modelling the interaction between the specimens and the tools more complex, since friction models are inadequate. Additionally, interactions between the warp and weft fibres, the matrix, and the adhesion to the aluminium must be better characterised. We conclude that the bonding of some specimens was non-homogeneous, with bonding only occurring along the wale of the fibre weave.

Chapter 9

Conclusions and Future Work

9.1 Introduction

This work investigated the deformation behaviour of fibre–metal laminates based on thermoplastic composites. The aim was to determine whether existing methods could be used to elicit a wide range of forming modes in an advanced material and to derive the forming limits. Two different composite materials were used to investigate the effect of stiffness and elongation at failure on the formability of the laminate. An optical strain measurement system was used to obtain the material behaviour during the experimental forming process. Finite element analysis software was used to simulate the forming process to ascertain the strain behaviour of components not capable of being determined experimentally. This chapter presents the most significant conclusions of this thesis and provides recommendations for future studies.

9.2 Conclusions

- Analysis of strain evolution at the pole, together with forming limit diagrams, confirmed the expected deformation behaviour in the SRPP FML

specimens. The full range of deformation modes from uniaxial tension to biaxial strech were obtained using specimens of varying width. The GFRP FML specimens exhibited similar forming behaviour to the SRPP specimens at lower forming depths but failed prior to a transition to the expected behaviour at the pole. Additionally, the FLDs showed little correlation with the expected deformation modes. The transition to this behaviour occurred at a depth of 3–5mm in the SRPP FML. This is lower than the failure depth of the GFRP specimens which appeared to maintain the early biaxial stretch type behaviour until the failure depth was reached. This is an important finding in that conventional stretch forming experiments to obtain the deformation behaviour of materials may need to be modified for FMLs containing a high-stiffness low-extensibility composite. Further study should be conducted to determine whether a transition to the expected behaviour would have occurred if greater forming depths were achieved.

- The deformation behaviour of the laminates was assessed in multiple ways: at two points, one at the centre (pole) and one at the region of failure, at the meridian line along the longitudinal axis, with the FLD of the specimens, and with the surface strain contours.

  - The strain at the pole identified three deformation behaviours during the forming process: the strain induced by the lock ring, a period of biaxial stretching, and finally a strain path corresponding to an expected deformation mode until failure occurred.

- The region of failure highlighted that no localisation of strain occurred in the SRPP FML specimens, whereas the aluminium and GFRP FML specimens showed rapid increases in the major strain prior to failure.
- The meridian strain also showed localisation of strain at the failure region in the aluminium and GFRP specimens. Additionally, it displayed the effect of friction on the surface strain in all specimens. These results showed that as the forming depth increased the pole deformation slowed compared to the unsupported region due to the restriction of movement from frictional contact with the punch.
- The FLDs of the specimens and the surface strain contours were used to examine the behaviour across the entire surface of the laminate. These results allowed rapid determination of unusual strain behaviour such as the tessellated strain pattern in the GFRP FML specimens. The strain contours were particularly helpful in this case as it was possible to identify the characteristics of the woven fibre, primarily the wale of the twill weave. It also showed that the behaviour of the GFRP composite is not homogeneous, as regions where the lateral fibres were at the surface exhibited higher strains than regions of longitudinal fibres.

• The failure of the FML specimens is initiated by failure of the composite layer. That is, failure will not occur in the aluminium layers prior to the failure of the composite layer, unless the temperature is sufficiently high

as to cause a high strain to failure in the composite and melting of the adhesive.

- The failure limits of the SRPP based FML are significantly higher than those of the monolithic aluminium and the GFRP specimens. This was also accompanied by absence of a localised neck in the SRPP FML specimens prior to failure.
- In the case of the SRPP, failure occurred as a simultaneous catastrophic failure of the entire laminate which originated in the composite fibres. Significantly, it was found that ***the SRPP composite layer also provided support and allowed the aluminium to achieve greater forming depths than can be achieved as a monolithic metal***. This was shown by the reduced forming depth at a temperature of 140°C where the specimens behaved as three independent layers and failure occurred only in the aluminium layer. This is significant as it indicates that ***any low-cost high-extensibility material could be used to improve the forming of metals***.
- The GFRP composite ***reduced*** the forming depth of the aluminium owing to a rapid transfer of load to the aluminium layers and the loss of support in a single region, which led to rapid failure of the aluminium in that region.

• The forming limits for the fibre–metal laminates predicted by the experi-

mental work do not take the fibre orientation into account, meaning that regions of the FML could safely withstand strains higher than those in the FLC. Therefore unlike metals and other isotropic materials, the forming limit curve for composites and orthotropic laminates depends not only on the deformation mode described by the major and minor strain, but also the direction of the principal strains.

  - The FE simulations underlined the fact that the failure limits of the composite layer in the FML depended not only on the state of major and minor strain but also the composition of these strains. It was shown that where the major strain is heavily comprised of shear strain in the composite that the state of strain can appear to exceed the determined forming limits. It is proposed that the principal strain angle be used as a third parameter to represent this effect.

- Elevated temperatures were found to have small effects on the deformation behaviour of the experimental specimens. The strain behaviour of the specimens is controlled by the specimen geometry so alterations in stiffness have only a limited effect on the strain. The lower stiffness would also reduce the load required to deform the specimen which therefore reduces the contact pressure at the punch interface. This decreases the frictional force and therefore allows greater deformation at the pole. However, this also makes the unsupported region easier to deform, particularly as this region holds the elevated temperature longer than the pole region. These two effects act

to cancel each other out.

- The major effect of elevated temperature is to increase the strain at failure of the SRPP composite and therefore the forming depth achievable by the laminate. This is because the fibres in the SRPP are high temperature dependent. This effect is not seen in the GFRP specimens as the glass fibres do not benefit from these temperatures, but some increase is observed due to easier fibre movement through the softer matrix.

- The best temperature for deformation of the laminates was found to be the 120°C SRPP laminate where the temperature was high enough for a large strain at failure in the composite but not so high that the adhesive had melted. Therefore, the SRPP layer allowed the aluminium to reach the greatest forming depth.

- The finite element simulation of the materials used a user-defined material for the composite layers which operated on the principle of property homogenisation. For the SRPP FML this technique was extremely successful and allowed validation of the models and the ability to draw conclusions about the materials, which was not possible using the experimental data. This allowed determination of the preliminary failure limits for the composite layer. It should be noted that due to the effect of the fibre weave on the local strain evolution, only the general trend of the strain can be obtained. At lower temperatures and low forming depths, the behaviour

could be accurately represented but the ability of the model to predict the behaviour was limited as the high stiffness fibres began to trellis, fail, and extend. More comprehensive and complex models are needed in the future to obtain greater detail about deformation of composites.

- For both FMLs used in this work, one of the most significant findings from the FE simulation of the forming behaviour was that, apart from material selection, ***friction between the tools and the specimen is the most important parameter detracting from the veracity of the simulation***.

  - This is particularly important for the high temperature specimens, where the lowered stiffness and friction between the tools are closely related. Even though the friction and lubrication in this study were carefully considered, the effect of friction at the pole led to variability in the results.

9.3 Future Work

- The effect of fibre orientation on the forming limits of the FML should be investigated. In this study the fibres in the composite layer were aligned along the longitudinal and lateral axes of the specimens. This means that the fibres, which generally have a lower strain to failure than the matrix, were oriented along the axis of greatest stretch. This is also important for

the determination of failure limits as the failure strain at an angle is greater than along the fibres.

- The mechanical behaviour of the composite requires more extensive investigation. The shear properties of the composites are required to determine a more detailed shear modulus for simulation, including the effect of trellising and fibre locking on deformation of the composites. The compressive behaviour of the composite should be investigated as the negative trend in the minor strain highlights the need for accurate properties of the material under compression. Finally, the biaxial deformation of the composite needs to be evaluated to provide information about Poisson's ratio and the effect of longitudinal strain on the lateral stiffness (and vice versa).

- A comprehensive investigation into the tribology of the forming process (including the punch, die, and blankholder) and the effect that the paint may have on the interaction between the specimens and the tools. In addition, this study should examine different lubrication mechanisms to determine the best lubrication system for the forming of FML specimens.

  - Particularly, the lubrication/friction condition between the specimen and the tooling must be carefully controlled. Experiments should be repeated until failure is achieved in the same spot to produce less variability in the results.

Bibliography

[1] A.B. Lovins and D.R. Cramer. Hypercars, hydrogen and the automotive transition. *International Journal of Vehicle Design*, 35:50–85, 2004.

[2] S. Das. The cost of automotive polymer composites: a review and assessment of doe's lightweight materials research. Technical Report ORNL/TM-2000/283, Energy Division, Oak Ridge National Laboratory, 2001.

[3] J. Patterson. New large aircraft composite fire fighting, June 2012.

[4] C.A.J.R. Vermeeren. An historic overview of the development of fibre metal laminates. *Applied Composite Materials*, 10:189–205, 2003.

[5] J.F. Laliberté, C. Poon, P.V. Straznicky, and A. Fahr. Applications of fiber-metal laminates. *Polymer Composites*, 21:558–567, 1999.

[6] P. Xue, P. Xiongqi, and J. Cao. A non-orthogonal constitutive model for characterizing woven composites. *Composites: Part A*, 34:183–193, 2003.

[7] S. Kalpakjian and S. Schmid. *Manufacturing Engineering and Technology*. Prentice Hall, 2006.

[8] R.E. Sanders Jr., P.A. Hollinshead, and Simielli E.A. Industrial development of non-heat treatable aluminium alloys. *Materials Forum*, 28:53–64, 2004.

[9] K.G. Budinski and M.K. Budinski. *Engineering Materials: Properties and Selection*. Pearson Prentice Hall, 2005.

[10] M.T. Abadi, H.R. Daghyani, and S. Fariborz. Finite element analysis of thermoplastic composite plates in forming temperature. *Composites Science and Technology*, 66:306–313, 2006.

[11] Arnt R. Offringa. Thermoplastic composites – rapid processing applications. *Composites: Part A*, 27A:329–336, 1996.

[12] J.D. Muzzy and A.O. Kays. Thermoplastic vs. thermosetting structural composites. *Polymer Composites*, 5:169–172, 1984.

[13] M.D. Wakeman and C.D. Rudd. Compression molding of thermoplastic composites. In *Comprehensive Composite Materials*, pages 915–963. Pergamon, 2000.

[14] X. Tang and J.D. Whitcomb. Progressive failure behaviors of 2d woven composites. *Journal of Composite Materials*, 37:1239–1259, 2003.

[15] J. Launay, G. Hivet, A.V. Duong, and P. Boisse. Experimental analysis of the influence of tensions on in plane shear behaviour of woven composite reinforcements. *Composites Science and Technology*, 68:506–515, 2008.

[16] Martin Wilson. *Finite Element Analysis of Glass Fibre Reinforced Thermoplastic Composites for Structural Automotive Components*. PhD thesis, University of Nottingham, 2003.

[17] A. Jambor and M. Beyer. New cars - new materials. *Materials & Design*, 18:203–209, 1997.

[18] S.S. Krishnakumar. Fiber metal laminates - the synthesis of metals and composites. *Materials and Manufacturing Processes*, 9:295–354, 1994.

[19] J. Schijve, H.T.M. Van Lipzig, G.F.J.A. Van Gestel, and A.H.W. Hoeymakers. Fatigue properties of adhesive-bonded laminated sheet material of aluminium alloys. *Engineering Fracture Mechanics*, 12:561–579, 1979.

[20] J.K. Kim and P.F. Thomson. Forming behaviour of sheet steel laminate. *Journal of Materials Processing Technology*, 22:45–64, 1990.

[21] J.K. Kim and P.F. Thomson. Separation behaviour of sheet steel laminate during forming. *Journal of Materials Processing Technology*, 22:147–161, 1990.

[22] T. de Jong. *Forming of Laminates.* PhD thesis, Technische Universiteit Delft, 2004.

[23] Igor Burchitz, Roel Boesenkool, Sybrand van der Zwaag, and Marc Tassoul. Highlights of designing with hylite - a new material concept. *Materials and Design*, 26:271–279, 2005.

[24] Marissen R. Vogelesang, L.B. and J. Schijve. A new fatigue resistant material: Aramid reinforced aluminium laminate (arall). In *Proceedings of the 11th ICAF Symposium*, Noordwijkerhout, The Netherlands, May 1981.

[25] L.B. Vogelesang. Development of a new hybrid material (arall) for aircraft structures. *Industrial and Engineering Chemistry Product Research and Development*, 22:492–496, 1983.

[26] A. Vlot, L.B. Vogelesang, and T.J. de Vries. Towards application of fibre metal laminates in large aircraft. *Aircraft Engineering and Aerospace Technology*, 71:558–570, 1999.

[27] A. Vlot, R.C. Alderliesten, P.A. Hooijmeijer, J.L.C.G. de Kanter, J. Sinke, and M.S. Ypma. Fibre metal laminates: a state of the art. *International Journal of Materials and Product Technology*, 17:79–98, 2002.

[28] H.F. Wu, L.L. Wu, W.J. Slagter, and J.L. Verolme. Use of the rule of mixtures and metal volume fraction for mechanical property predictions of fibre-reinforced aluminium laminates. *Journal of Materials Science*, 29:4583–4591, 1994.

[29] P. Cortés and W.J. Cantwell. The prediction of tensile failure in titanium-based thermoplastic fibre-metal laminates. *Composites Science and Technology*, 66:2306–2316, 2006.

[30] J.G. Carrillo and W.J. Cantwell. Mechanical properties of a novel fiber-metal laminate based on a polypropylene composite. *Mechanics of Materials*, 41:828–838, 2009.

[31] G. Reyes and W.J. Cantwell. The mechanical properties of fibre-metal

laminates based on glass fibre reinforced polypropylene. *Composites Science and Technology*, 60:1085–1094, 2000.

[32] J.G. Carrillo and W.J. Cantwell. Scaling effects in the tensile behaviour of fiber-metal laminates. *Composites Science and Technology*, 67:1684–1693, 2007.

[33] J.G. Carrillo and W.J. Cantwell. Scaling effects in the low velocity impact response of fiber-metal laminates. *Journal of Reinforced Plastics and Composites*, 27:893–907, 2008.

[34] J. Sinke. Development of fibre metal laminates: concurrent multi-scale modeling and testing. *Journal of Materials Science*, 41:6777–6788, 2006.

[35] T. Sinmazcelik, E. Avcu, M. Bora, and O Coban. A review: Fibre metal laminates, background, bonding types and applied test methods. *Materials and Design*, 32:3671–3685, 2011.

[36] J. L. Duncan, Z. Marciniak, and S.J. Hu. *Mechanics of Sheet Metal Forming.* Butterworth-Heinemann, 2002.

[37] S. Keeler. Determination of forming limits in automotive stampings. Technical Report 650535, Society of Automotive Engineers, 1965.

[38] G. Goodwin. Application of strain analysis to sheet metal forming problems in the press shop. Technical Report 680093, Society of Automotive Engineers, 1968.

[39] S.P. Keeler and W.A. Backofen. Plastic instability and fracture in sheets stretched over rigid punches. *ASM Transactions Quarterly*, 56:25–48, 1963.

[40] Joel Gresham. Influence of temperature on the stamp forming of fibre-metal laminate systems. Master's thesis, Australian National University, 2006.

[41] K. Nakazima, T. Kikuma, and K Hasuka. Study on the formability of steel sheets. Technical Report Yawata Technical Report 264, Technical Research Institute, Yawata Works, 1968.

[42] Siegfried S. Hecker. Simple technique for determining forming limit curves. *Sheet Metal Industries*, 52:671–676, 1975.

[43] K.S. Raghavan. A simple technique to generate in-plane forming limit curves and selected applications. *Metallurgical and Materials Transactions A*, 26A:2075–2084, 1995.

[44] D.R. Shouler and J.M. Allwood. Design and use of a novel sample design for formability testing in pure shear. *Journal of Materials Processing Technology*, 210:1304–1313, 2010.

[45] V. Buakaew, S. Sodamuk, S. Sirivedin, and S. Jirathearanti. Formability prediction of automotive parts using forming limit diagrams. *Journal of Solid Mechanics and Materials Engineering*, 1:691–698, 2007.

[46] Daoming Li and Amit K. Ghosh. Biaxial warm forming behavior of aluminum sheet alloys. *Journal of Materials Processing Technology*, 145:281–

293, 2004.

[47] Emilie Hsu, John E. Carsley, and Ravi Verma. Development of forming limit diagrams of aluminium and magnesium sheet alloys at elevated temperatures. *Journal of Materials Engineering and Performance*, 17:288–296, 2008.

[48] Zdzislaw Marciniak and Kazimierz Kuczyński. Limit strains in the processes of stretch-forming sheet metal. *International Journal of Mechanical Sciences*, 9:609–620, 1967.

[49] T. Foecke, S.W. Banovic, and R.J. Fields. Sheet metal formability studies at the national institute of standards and technology. *JOM*, 53:27–30, 2001.

[50] C.M. O'Brádaigh and P.J. Mallon. Effect of forming temperature on the properties of polymeric diaphragm formed thermoplastic composites. *Composites Science and Technology*, 35:235–255, 1989.

[51] M. Hou and K. Friedrich. Stamp forming of continuous carbon fibre/polypropylene composites. *Composites Manufacturing*, 2:3–9, 1991.

[52] M. Hou. Stamp forming of fabric-reinforced thermoplastic composites. *Polymer Composites*, 17:596–603, 1996.

[53] M. Hou. Stamp forming of continuous glass fibre reinforced polypropylene. *Composites: Part A*, 28A:695–702, 1997.

[54] K. Friedrich and M. Hou. On stamp forming of curved and flexible geometry components from continuous glass fibre/polypropylene composites. *Composites: Part A*, 29A:217–226, 1998.

[55] U. Breuer and M. Neitzel. High speed stamp forming of thermoplastic composite sheets. *Polymers and Polymer Composites*, 4:117–123, 1996.

[56] J.H. Lee, J.H. Vogel, and K.Y. Rhee. An analysis of stretch forming of thermoplastic composites. *Polymer Composites*, 23:442–453, 2002.

[57] Norbert Cabrera. *Recyclable all-polypropylene composites: Concept, properties and manufacturing.* PhD thesis, Technische Universiteit Eindhoven, 2004.

[58] N.O. Cabrera, C.T. Reynolds, B. Alcock, and T. Peijs. Non-isothermal stamp forming of continuous tape reinforced all-polypropylene composite sheet. *Composites: Part A*, 39:1455–1466, 2008.

[59] D. Trudel-Boucher, B. Fisa, J. Denault, and P. Gagnon. Experimental investigation of stamp forming of unconsolidated commingled e-glass/polypropylene fabrics. *Composites Science and Technology*, 66:555–570, 2006.

[60] R. Nakamura, K. Goda, J. Noda, and J. Ohgi. High temperature tensile properties and deep drawing of fully green composites. *eXPRESS Polymer Letters*, 3:19–24, 2009.

[61] S. Venkatesan and S. Kalyanasundaram. Finite element analysis and optimization of process parameters during stamp forming of composite materials. In *Proceedings of 9th World Congress on Computational Mechanics and 4th Asian Pacific Congress on Computational Mechanics*, Sydney, Australia, July 2010.

[62] S. Venkatesan and S. Kalyanasundaram. A study on the real time strain evolution in glass fibre reinforced composites during stamp forming. In *Proceedings of 6th Australasian Congress on Applied Mechanics*, Perth, Australia, December 2010.

[63] S. Venkatesan and S. Kalyanasundaram. Effect of preheat temperature on formability of consolidated all-pp composite materials during stamp forming. In *Proceedings of 6th Australasian Congress on Applied Mechanics*, Perth, Australia, December 2010.

[64] Sudharshan Venkatesan. *Stamp Forming of Composite Materials: An Experimental and Analytical Study*. PhD thesis, Australian National University, 2012.

[65] H. Takuda, H. Fujimoto, and N. Hatta. Formabilities of steel/aluminium alloy laminated composite sheets. *Journal of Materials Science*, 33:91–97, 1998.

[66] K.J. Kim, D. Kim, S.H. Choi, K. Chung, K.S. Shin, F. Barlat, K.H. Oh, and J.R. Youn. Formability of aa5182/polypropylene/aa5182 sandwich sheets.

Journal of Materials Processing Technology, 139:1–7, 2003.

[67] M. Weiss, M.E. Dingle, B.F. Rolfe, and P.D. Hodgson. The influence of temperature on the forming behaviour of metal/polymer laminates in sheet metal forming. *Journal of Engineering Materials and Technology*, 129:530–537, 2007.

[68] O. Sokolova, A. Carradó, and H. Palkowski. Metal-polymer-metal sandwiches with local metal reinforcements: A study on formability by deep drawing and bending. *Composite Structures*, 93:1–7, 2011.

[69] N. Asnafi, G. Langstedt, C.H. Andersson, N. Östergren, and T. Håkansson. A new lightweight metal-composite-metal panel for applications in the automotive and other industries. *Thin-Walled Structures*, 36:289–310, 2000.

[70] L. Mosse, W. Cantwell, M.J. Cardew-Hall, P. Compston, and S. Kalyanasundaram. A study of the effect of process variables on the stamp forming of rectangular cups using fibre-metal laminate systems. *Advanced Materials Research*, 6-8:649–656, 2005.

[71] L. Mosse, P. Compston, W. Cantwell, M.J. Cardew-Hall, and S. Kalyanasundaram. The effect of process temperature on the formability of polypropylene based fibre-metal laminates. *Composites: Part A*, 36:1158–1166, 2005.

[72] Luke Mosse, Paul Compston, W. Cantwell, M.J. Cardew-Hall, and Shankar Kalyanasundaram. Stamp forming of polypropylene based fibre-metal laminates: The effect of process variables on formability. *Journal of Materials Processing Engineering*, 172:163–168, 2006.

[73] Luke Mosse. *Stamp Forming of Fibre-Metal Laminates*. PhD thesis, Australian National University, 2006.

[74] P. Compston, W.J. Cantwell, M.J. Cardew-Hall, S. Kalyanasundaram, and L. Mosse. Comparison of surface strain for stamp formed aluminium and an aluminium-polypropylene laminate. *Journal of Materials Science*, 39:6087–6088, 2004.

[75] Joel Gresham, W. Cantwell, M.J. Cardew-Hall, Paul Compston, and Shankar Kalyanasundaram. Drawing behaviour of metal-composite sandwich structures. *Composite Structures*, 75:305–312, 2006.

[76] S. DharMalingam, P. Compston, and S. Kalyanasundaram. Forming analysis of metal-composite sandwich structures. In *Proceedings of the 14th European Conference on Composite Materials*, Budapest, Hungary, June 2010.

[77] Sivakumar Dhar Malingam. *An Investigation into the Forming Behaviour of Metal Composite Hybrids*. PhD thesis, Australian National University, 2011.

[78] A. Carradó, J. Faerber, S. Niemeyer, G. Ziegmann, and H. Palkowski. Metal/polymer/metal hybrid systems: Towards potential formability applications. *Composite Structures*, 93:715–721, 2011.

[79] G. Reyes and H. Kang. Mechanical behavior of lightweight thermoplastic fiber-metal laminates. *Journal of Materials Processing Technology*, 186:284–290, 2007.

[80] K.P. Jackson, J.M. Allwood, and M. Landert. Incremental forming of sandwich panels. *Journal of Materials Processing Technology*, 204:290–303, 2008.

[81] S.P. Edwardson, P. French, G. Dearden, K.G. Watkins, and W.J. Cantwell. Laser forming of fibre metal laminates. *Lasers in England*, 15:233–255, 2005.

[82] T. Schmidt, J. Tyson, K. Galanulis, D. Revilock, and M. Melis. Full-field dynamic deformation and strain measurements using high-speed digital cameras. In *Proceedings of SPIE - The International Society for Optical Engineering*, volume 5580, pages 174–185, 2005.

[83] John Tyson and Timothy Schmidt. Advanced photogrammetry for robust deformation and strain measurement. In *Proceedings of SEM 2002 Annual Conference*, Milwaukee, WI, June 2002.

[84] E. Carasusan and F. Canal. Determination of forming limit strains in sheet metals using an automated optical procedure. In *IEEE International*

Conference on Industrial Technology, 2006. ICIT 2006., pages 2943 –2948, 2006.

[85] GOM mbh. Determination of forming limit diagrams using aramis.

[86] M. Geiger and M. Merklein. Determination of forming limit diagrams - a new analysis method for characterization of materials' formability. *CIRP Annals - Manufacturing Technology*, 52:213–216, 2003.

[87] D.J. Lewison and D. Lee. Determination of forming limits by digital image processing methods. In *Proceedings of the International Body Engineering Conference (IBEC'99)*, Detroit, MI, September 1999.

[88] Shankar Kalyanasundaram, Paul Compston, and Joel Gresham. A methodology for real time surface strain measurement for stamping through non-contact optical strain measurement system. *Key Engineering Materials*, 344:855–861, 2007.

[89] J. Fan, Z. Guan, and W.J. Cantwell. Structural behaviour of fibre metal laminates subjected to a low velocity impact. *Science China*, 54:1168–1177, 2011.

[90] Fahrettin Ozturk and Daeyong Lee. Experimental and numerical analysis of out-of-plane formability test. *Journal of Materials Processing Technology*, 170:247–253, 2005.

[91] W.R. Yu, F. Pourboghart, K. Chung, M. Zampaloni, and T.J. Kang. Non-

orthogonal constitutive equation for woven fabric reinforced thermoplastic composites. *Composites: Part A*, 33:1095–1105, 2002.

[92] Jian Cao, Pu Xue, Xionqi Peng, and Neil Krishnan. An approach in modeling the temperature effect in thermo-stamping of woven composites. *Composite Structures*, 61:413–420, 2003.

[93] F. Hashagen, J.C.J. Schellekens, R. de Borst, and H. Parisch. Finite element procedure for modelling fibre metal laminates. *Composite Structures*, 32:255–264, 1995.

[94] Z. Guan, W.J. Cantwell, and R. Abdullah. Numerical modeling of the impact response of fiber-metal laminates. *Polymer Composites*, 30:603–611, 2009.

[95] Z. Guan and W.J. Cantwell. Numerical modeling of fibre metal laminates subjected to blast loading. In *AIP Conference Proceedings*, Hong Kong-Macau, China, December 2009.

[96] J. Fan, Z. Guan, and W.J. Cantwell. Modeling perforation in glass fiber reinforced composites subjected to low velocity impact loading. *Polymer Composites*, 32:1380–1388, 2011.

[97] Luke Mosse, W. Cantwell, M.J. Cardew-Hall, Paul Compston, and Shankar Kalyanasundaram. The development of a finite element model for simulating the stamp forming of fibre-metal laminates. *Composite Structures*, 75:298–304, 2006.

[98] T.P. Vo, Z.W. Guan, W.J. Cantwell, and G.K. Schleyer. Low-impulse blast behaviour of fibre-metal laminates. *Composite Structures*, 94:954–965, 2012.

[99] A.K. Ghosh. A method for determining the coefficient of friction in punch stretching of sheet metals. *International Journal of Mechanical Science*, 19:457–470, 1977.

[100] M. Javadi and M. Tajdari. Experimental investigation of the friction coefficient between aluminium and steel. *Materials Science-Poland*, 24:305–310, 2006.

[101] J.F. Guillén and W.J. Cantwell. The influence of cooling rate on the fracture properties of a thermoplastic-based fibre-metal laminate. *Journal of Reinforced Plastics and Composites*, 21:749–772, 2002.

[102] N.A. Zanjani and S. Kalyanasundaram. The effect of fibre orientation on the forming behaviour of a self-reinforced polypropylene composite. In *Proceedings of the International Conference on the Mechanics of Nano, Micro and Marco Composite Structures*, Turin, Italy, June 2012.

[103] GOM mbh. Aramis user manual v5.4.1, 2005.

[104] N. Rebelo, J.C. Nagtegaal, L.M. Taylor, and R. Passmann. Comparison of implicit and explicit finite element methods in the simulation of metal forming processes. In *Proceedings of the 4th International COnference*

on Numerical Methods in Industrial Forming Processes, Valbonne, France, September 1992.

[105] K. Mattiasson, L. Bernspang, A. Samuelsson, T. Hamman, E. Schedin, and A. Melander. Evaluation of a dynamic approach using explicit integration in 3-d sheet forming simulation. In *Proceedings of the 4th International Conference on Numerical Methods in Industrial Forming Processes*, Valbonne, France, September 1992.

[106] K-J. Bathe. *Finite Element Procedures*. Prentice Hall, 1996.

[107] F.J. Harewood and P.E. McHugh. Comparison of the implicit and explicit finite element methods using crystal plasticity. *Computational Materials Science*, 39:481–494, 2007.

[108] J. Kim, Y-H. Kang, S-M. Choi, S-M. Hwang, and B-S. Kang. Comparison of the implicit and explicit finite-element methods for the hydroforming process of an automobile lower arm. *The International Journal of Advanced Manufacturing Technology*, 20:407–413, 2002.

[109] Dassault Systèmes. Abaqus analysis user's guide, 2012.

[110] M.J. Hinton, A.S. Kaddour, and P.D. Soden. *Failure criteria in fibre reinforced polymer composites: the world-wide failure exercise*. Elsevier Science Ltd, 2004.

[111] C. Morrow, S. DharMalingam, S. Venkatesan, and S. Kalyanasundaram.

Stretch forming studies on thermoplastic composite. In *Proceedings of 6th Australasian Congress on Applied Mechanics*, Perth, Australia, December 2010.

[112] A. Sexton, W. Cantwell, and Kalyanasundaram S. Stretch forming studies on a fibre metal laminate based on a self-reinforcing polypropylene composite. *Composite Structures*, 94:431–437, 2012.

Appendix A

Plastic Stress-Strain Behaviour of the 5005-O aluminium

Stress (MPa)	Plastic strain
41.4	0
55.99462506	0.010404145
67.15270561	0.020404145
76.18132772	0.030404145
83.58874756	0.040404145
89.75933037	0.050404145
94.98380203	0.060404145
99.48211278	0.070404145
103.4207173	0.080404145
106.925635	0.090404145
110.0923205	0.100404145
112.9931239	0.110404145
115.6829292	0.120404145
118.203416	0.130404145
120.58628	0.140404145
122.8556674	0.150404145

Table A.1: Stress for the aluminium as a function of plastic strain

SRPP constitutive model coefficients

$$A(T) = \begin{cases} -0.269T + 45.84 & \text{if } T \leq 40 \\ -0.403T + 51.2 & \text{if } T \leq 60 \\ -0.15T + 36.02 & \text{if } T \leq 80 \\ -0.4495T + 59.98 & \text{if } T \leq 100 \\ -0.206T + 35.63 & \text{if } T \leq 120 \\ -0.09185T + 21.932 & \text{if } T \leq 140 \end{cases}$$

$$B(T) = \begin{cases} 0.003T + 30.96 & \text{if } T \leq 40 \\ 0.117T + 26.4 & \text{if } T \leq 60 \\ -0.034T + 35.46 & \text{if } T \leq 80 \\ 0.04T + 29.54 & \text{if } T \leq 100 \\ 0.1055T + 22.99 & \text{if } T \leq 120 \\ -0.06T + 42.85 & \text{if } T \leq 140 \end{cases}$$

$$C(T) = \begin{cases} -0.029T - 32.89 & \text{if } T \leq 40 \\ 0.5305T - 55.27 & \text{if } T \leq 60 \\ 0.061T - 27.08 & \text{if } T \leq 80 \\ 0.4555T - 58.64 & \text{if } T \leq 100 \\ 0.2066T - 33.75 & \text{if } T \leq 120 \\ 0.074T - 17.838 & \text{if } T \leq 140 \end{cases}$$

$$D(T) = \begin{cases} 0.535T - 919 & \text{if } T \leq 40 \\ 19.39T - 1673.2 & \text{if } T \leq 60 \\ 5.315T - 828.7 & \text{if } T \leq 80 \\ -0.745T - 343.9 & \text{if } T \leq 100 \\ -6.665T + 248.1 & \text{if } T \leq 120 \\ -4.09T - 60.9 & \text{if } T \leq 140 \end{cases}$$

$$Y(T) = \begin{cases} -4.1725T + 966.69 & \text{if } T \leq 40 \\ -4.2685T + 970.53 & \text{if } T \leq 60 \\ -0.3705T + 736.65 & \text{if } T \leq 80 \\ -8.02T + 1349 & \text{if } T \leq 100 \\ -5.115T + 1058 & \text{if } T \leq 120 \\ -7.3795T + 1329.87 & \text{if } T \leq 140 \end{cases}$$

Appendix C

GFRP constitutive model coefficients

$$A(T) = \begin{cases} -1.1035T + 138.67 & \text{if } T \leq 40 \\ -9.36T + 468.93 & \text{if } T \leq 60 \\ -2.1665T + 37.32 & \text{if } T \leq 80 \\ 1540.8T - 123400 & \text{if } T \leq 100 \\ -1530T + 183680.05 & \text{if } T \leq 120 \\ -6.9635T + 915.61 & \text{if } T \leq 140 \end{cases}$$

$$B(T) = \begin{cases} 0.385T + 108.1 & \text{if } T \leq 40 \\ -50.975T + 2162.5 & \text{if } T \leq 60 \\ 12.72T - 1659.2 & \text{if } T \leq 80 \\ 27.903T - 2873.84 & \text{if } T \leq 100 \\ 5.4135T - 624.89 & \text{if } T \leq 120 \\ -26.1615T + 3164.11 & \text{if } T \leq 140 \end{cases}$$

$$C(T) = \begin{cases} 0.741T - 113.66 & \text{if } T \leq 40 \\ 9.416T - 460.66 & \text{if } T \leq 60 \\ 1.785T - 2.8 & \text{if } T \leq 80 \\ -1541T + 123420 & \text{if } T \leq 100 \\ 1530.1T - 183689.25 & \text{if } T \leq 120 \\ 6.881T - 903.87 & \text{if } T \leq 140 \end{cases}$$

$$D(T) = \begin{cases} 11T - 1501 & \text{if } T \leq 40 \\ 57.921T - 3377.84 & \text{if } T \leq 60 \\ -5.244T + 412.045 & \text{if } T \leq 80 \\ -3.75925T + 293.285 & \text{if } T \leq 100 \\ -12.483T + 1165.66 & \text{if } T \leq 120 \\ 18.191T - 2515.22 & \text{if } T \leq 140 \end{cases}$$